

Modelling of the gas dynamics in the inner-coma and the composition of comet 67P/Churyumov-Gerasimenko

Inaugural dissertation
of the Faculty of Science,
University of Bern

Presented by
Olga Janeth Pinzón Rodríguez
From Colombia

Supervisor of the doctoral thesis:
Prof. Dr. Nicolas Thomas
Physics Institute

Accepted by the Faculty of Science.

Bern, 26.02.2021

The Dean Prof. Dr. Zoltan Balogh

To my family and friends who shared this path with me.

*She had studied the universe all
her life, but had overlooked its
clearest message: For small
creatures such as we the vastness is
bearable only through love.*

Carl Sagan, Contact

Abstract

This thesis presents a study of the gas dynamics of cometary nuclei with a focus on the target of the Rosetta mission, comet 67P/Churyumov-Gerasimenko. We therefore apply the 3D Direct Simulation Monte Carlo (DSMC) method to different distributions of H₂O and CO₂-ice source on the surface of the nucleus in order to model the inner-coma of 67P/CG. The sublimation rates and temperatures at the surface are calculated using a balance equation that takes into account the solar radiation at the surface and the energy losses due to thermal emission, sublimation of ices and thermal conduction. This has been done for a spherical nucleus comet of 2km, and a comet that takes into account the real shape of 67P/CG.

The ultimate goal of this work is to find a link between remote sensing observations at large distances and the relative abundances of major volatiles in the nucleus. Therefore, for the complex shape of the nucleus, we validate our surface boundary condition by comparing the simulation results with local measurements of the gas properties obtained by ROSINA, MIRO and VIRTIS-M.

The targeted times in this work are May 10, 2015, when the comet was at its spring equinox at 1.67AU; and July 10, 2015, when the comet was at 1.67AU and the global production rates were high enough to study the increasingly emissions from the southern hemisphere of the comet as it approached perihelion.

We have found that different distribution of H₂O and CO₂ sources at the surface are difficult to detect using ROSINA data alone. Comparison with multiple instruments are found to be necessary to better constrain the thermophysical models that link comae measurements with the nucleus near-surface structure and composition. CO₂ has been found to be the most likely candidate for nightside activity in multiple tests that include thermal inertia values between 40 - 80 $J/(m^2K\sqrt{s})$. There is a strong indication that the heat exchange between the dust mantle and the sublimating gas can have a strong effect on the expansion velocities of the gas measured by MIRO on both dates.

Dedication and acknowledgements

I sincerely would like to thank Prof. Nicolas Thomas for his trust and support during the whole project. You gave me space to test my own ideas, but hold my back when things seemed to go out of track. Unusual circumstances made the last year particularly difficult, but thanks to your guidance I felt stronger facing a project that sometimes felt very challenging.

Un enorme agradecimiento a mi familia, que han entendido y apoyado cada una de mis decisiones de vida. Un sueño me ha traído muchos kilómetros y muchos años lejos de casa, pero espero hacerlos sentir orgullosos de quien soy y lo que he logrado. A los nuevos y peludos miembros de la familia: Kira y Loki por ser una fuente de amor y diversión para mis papás, mi hermano y virtualmente para mí. Ya tengo ganas de conocerlos!

Thanks to the comet-dudes: Rapha, Selina-Barbara and Clemence, with whom I always had very constructive conversations that helped me with my project, but also some good laughs that I appreciate pretty much.

Thanks to Antoine for having the door open for questions whenever I was confused about the Lab-side of the World.

Thanks to the generation of space PIGs with whom I spent some quality-time coffee-breaks in a beautiful era when social distancing was not "a thing": Tracy, Rapha, Clemence, Zuri, Yann, Vicky, Olivier, Bernard, Alireza, S-BG, Panagiotis, Pato, Romain, Miguel, Nico, Matt, Holly, Jo-Ann, Camila, Adam, Stefano, Clément, Lea, Caroline, Tatiana, Michael, Luca and Lucas.

Thanks to the Zoo: Michalina, Stefan, Pato and Vero, my small family in Bern, who taught me friendship has no borders and that you can always adopt new and crazy traditions from different parts of the world.

Thanks to the new friends: Andrea, Stefano, Benedetta, Nico and Caroline for the bike rides, for ping pong in Marzili and all other adventures I have loved to share with you.

Gracias a mis amigos de toda la vida: Zaira, Aleja, Laura, David e Ingrid que a pesar de la distancia, siempre he sentido su cariño y apoyo incondicional.

Gracias a mis Kölsche Jungs: Inés y Andrea, a quienes siento conocer de toda la vida y no me explico cómo sobreviví tanto tiempo sin su dulce amistad. A Philip por ayudarme a desliar el nido en mi cabeza.

Thanks to Nick, Rapha, Ladi and Laura for taking the time to read some parts the document and help me with their comments to improve it.

Thanks to Prof. Hubertus Fischer Dr. Ekkehard Kührt for taking valuable time to read and evaluate this work.

Table of Contents

	Page
List of Tables	ix
List of Figures	xi
1 Introduction	1
1.1 Cometary Science before the Rosetta mission	3
1.2 Comet 67P/Churyumov-Gerasimenko and the Rosetta mission	9
1.3 Motivation	15
2 Modelling the gas dynamics: Methods and tools	17
2.1 Mesh generation	18
2.2 Thermal model and selection of model parameters	19
2.2.1 Nucleus coordinate system	19
2.2.2 Calculation of illumination conditions	20
2.2.3 Thermal model	20
2.2.4 Effective active fraction	24
2.3 Collision Model	24
2.3.1 Overview of flow regimes in gas dynamics	25
2.3.2 3D Direct Simulation Monte Carlo	26
2.4 Rosetta Instruments	30
2.4.1 ROSINA	30
2.4.2 MIRO	31
2.4.3 VIRTIS	32
2.5 Model comparison approach	33
2.5.1 Extraction of local number densities from the model results	33
2.5.2 Calculation of multi-beam profiles along the line of sight of MIRO	34
2.5.3 Radiative Transfer calculation	36
2.5.4 Column density integration for artificial IR-images	38
3 Basic studies on gas dynamics	41

TABLE OF CONTENTS

3.1	Spherical Nucleus	41
3.1.1	Uniform outgassing of H ₂ O and CO ₂	41
3.1.2	Insolation-Driven Outgassing and Cometary Plumes	44
3.2	Complex Shape Nucleus	50
3.2.1	Homogeneous ice distribution on comet 67P/CG	50
3.2.2	Inhomogeneous ice distribution on comet 67P/CG	53
3.3	Model comparison with MIRO	56
3.3.1	LTE condition	57
3.3.2	Non-LTE condition	58
4	The effect of thermal conductivity on the outgassing and local gas dynamics from cometary nuclei	65
4.1	Introduction	67
4.2	Model assumptions	67
4.3	Boundary Conditions	68
4.4	Results	70
4.4.1	Diurnal evolution of temperatures at the surface	70
4.4.2	DSMC calculation	71
4.5	Discussion	80
4.6	Conclusions	82
5	3D modelling of the H₂O and CO₂ outgassing from comet 67P/CG	85
5.1	Introduction	87
5.2	Model assumptions and boundary conditions	88
5.3	Results and Discussion	89
5.3.1	Comparison with ROSINA	90
5.3.2	Comparison with MIRO	95
5.3.3	Comparison with VIRTIS-M	99
5.4	Conclusion	103
6	Summary and conclusions	107
6.1	Conclusions	108
A	MIRO comparison with a purely insolation-driven outgassing assuming non local thermal equilibrium	111
B	Mapping of CO₂ sources using VIRTIS-M images	119
	Bibliography	123

List of Tables

TABLE	Page
2.1 Meshes properties.	19
3.1 Purely insolation-driven cases with cometary plumes.	45
4.1 Physical parameters used in the model.	68
4.2 List of tested parameters for model calculations.	69
5.1 List of tested parameters for model calculations.	89
5.2 Dates for MIRO comparison	95
5.3 Selected dates for model comparison with VIRTIS-M IR images.	99
A.1 MIRO dates selected on July 2015 for comparison.	112

List of Figures

FIGURE	Page
1.1 Comet reservoirs	2
1.2 Comet's orbit	3
1.3 Comet Halley as seen by the Giotto mission.	6
1.4 Cometary nuclei observed by spacecraft	7
1.5 Comet 67P/CG orbit (in black) on the J2000 inertial frame.	10
1.6 Comet 67P/CG as seen by the OSIRIS camera on-board of Rosetta	11
1.7 Morphological regions of comet 67P/CG	12
1.8 Abundances relative to water before and after Rosetta	13
1.9 Summary of thermal inertia values	14
2.1 Modelling gas dynamics in 4 steps.	17
2.2 3D view of the nucleus coordinate system	20
2.3 Incidence angle sketch	21
2.4 Sketch of the heat sources and sinks at the surface and sub-surface of a cometary nucleus	23
2.5 Flow regimes given the Knudsen number and the range in which mathematical models are valid. Credit: Yu [2004].	25
2.6 The hard sphere collision model	29
2.7 Percentage of the number density mixing ratios measured by ROSINA/DFMS for the whole mission.	31
2.8 MIRO's field of view	32
2.9 Extracting average gas properties	34
2.10 Definition of the multi-beam profiles inside MIRO's FOV	35
2.11 Viewing geometry of VIRTIS-M, indicating the parameters used for the column integration.	39
2.12 Solar Zenith Angle (SZA) and phase angle.	39
3.1 Change with distance from the nucleus of the normalized number density	42
3.2 Average properties of the uniform emission cases	43

3.3	Ratio between the rotational temperature T_{rot} and the translational temperature T_{trans}	45
3.4	Boundary Conditions for a jet with different outgassing strengths.	46
3.5	Slice of the DSMC results on the yz-plane for the H ₂ O plumes cases	47
3.6	xtracted DSMC results along the +z direction for all cases listed in Table 3.1	48
3.7	Radiality of the flow field for the purely insolation-driven	49
3.8	Slice in the xz-plane of the 3D DSMC results for the uniform outgassing of a sphere and comet 67P/CG.	50
3.9	DMSC results for the uniform outgassing from the complex shape of comet 67P/CG using two Z_{rot}	51
3.10	Boundary conditions for the purely insolation-driven H ₂ O outgassing from a nucleus with a homogeneous ice composition.	52
3.11	First model comparison with ROSINA/COPS data	53
3.12	EAF of inhomogeneous H ₂ O sources	54
3.13	Comparison of DSMC results with local measurements of number density taken by ROSINA/COPS for July 2015.	55
3.14	RMSLE and PCC for July 2015.	57
3.15	Vertical profiles for the purely insolation-driven case along MIRO's FOV	58
3.16	Thermal inputs T_{Front} and $T_{Front+100K \cdot \cos(\theta_i)}$	59
3.17	MIRO comparison for July 2017 using LTE.	60
3.18	MIRO comparison for July 2017 using non-LTE for a purely insolation-driven case.	61
3.19	Vertical profiles along MIRO's FOV for case T_{Front}	61
3.20	MIRO comparison for July 2017 using non-LTE for a case with an artificial dust mantle.	62
3.21	Vertical profiles along MIRO's FOV for case $T_{Front+100K \cdot \cos(\theta_i)}$	62
4.1	Diurnal change of the temperature	72
4.2	Slice of the 3D DSMC simulation domain on the xy-plane	74
4.3	Temporal and longitudinal variation in the H ₂ O and CO ₂ number densities obtained with DSMC	75
4.4	Variation in the CO ₂ to H ₂ O number density mixing ratio obtained with DSMC	76
4.5	Diurnal variation of the heat flux density	77
4.6	Cross section of the temperature and speed calculation on the xy-plane	77
4.7	Averaged temperature and velocity of the gas mixture at 8 km	78
4.8	Profiles of number density, Doppler velocity and temperature with altitude at the 0° phase angle	80
4.9	Profiles of number density, Doppler velocity and temperature with altitude at termi- nator orbits	81
5.1	Comparison of DSMC results with local measurements of number density taken by ROSINA/COPS for the Spring Equinox.	91

5.2	RMSLE and PCC for the time around the spring equinox.	92
5.3	ROSINA/DFMS number density measurements for H ₂ O and CO ₂ gas between May 1 to May 31, 2015.	92
5.4	Mixing ratios n_{CO_2}/n_{H_2O} compared to ROSINA/DFMS data for May 2015.	93
5.5	Goodness of mixing ratios for May 2015	94
5.6	Comparison of DSMC results for a case including inhomogeneous H ₂ O- and CO ₂ -ice sources with ROSINA/COPS	94
5.7	Comparison with MIRO absorption spectra for May 2015	97
5.8	MIRO comparison of model M3 with two different thermal input parameters.	98
5.9	Model M4 compared to VIRTIS-M cube E in Table 5.3.	100
5.10	Model M4 compared to VIRTIS-M cube F in Table 5.3	101
5.11	Model M4 compared to VIRTIS-M cube G in Table 5.3	101
5.12	Models M4 and M6 compared to VIRTIS-M cube A in Table 5.3.	102
5.13	Models M4 and M6 compared to VIRTIS-M cube B in Table 5.3.	103
A.1	Spectra for the H ₂ ¹⁶ O and H ₂ ¹⁸ O absorption bands on 2015-07-10T00:51:51	113
A.2	Spectra for the H ₂ ¹⁶ O and H ₂ ¹⁸ O absorption bands on 2015-07-10T01:01:59	114
A.3	Spectra for the H ₂ ¹⁶ O and H ₂ ¹⁸ O absorption bands on 2015-07-10T01:23:03.	115
A.4	Spectra for the H ₂ ¹⁶ O and H ₂ ¹⁸ O absorption bands on 2015-07-10T01:51:51	116
A.5	Spectra for the H ₂ ¹⁶ O and H ₂ ¹⁸ O absorption bands on 2015-07-10T02:03:20	117
B.1	On the trail of CO ₂ sources using VIRTIS-M IR images.	120
B.2	On the trail of CO ₂ sources using OSIRIS images.	121
B.3	Final count of CO ₂ sources	121
B.4	CO ₂ map at the surface for the time before May 2015	122

Introduction

One can attempt to investigate the history of the Solar System through the study of its main components, planets, moons and asteroids. However, comets, among other small bodies in the solar system, are considered to be special because, compared to larger objects in the solar system, their structure and composition may not have changed significantly since their formation which is widely assumed to have occurred about 4.6 billion years ago [Amelin et al., 2002; Baker et al., 2005; Bouvier and Wadhwa, 2010]. Comets are rocky-icy bodies that revolve around the sun in highly eccentric orbits. Evidence suggests that most of the known comets come from a belt beyond Neptune's orbit [Edgeworth, 1943; Kuiper, 1951; Jewitt and Luu, 1993], or a comet reservoir at the outer boundary of the solar system, named the Oort Cloud [Öpik, 1932; Oort, 1950] (see Figure 1.1). The Oort Cloud has never been observed directly, but it is believed to be a huge spherical shell where a lot of the debris material from the Solar System formation process was thrown out by the giant planets. Most of the long-period comets are thought to come from this region after experiencing forces resulting from galactic tides of passing stars that send them closer to the sun [Vokrouhlický et al., 2019]. The small amount of material, that was not thrown out, was captured through gravitational pull. Neptune and Jupiter exert a strong gravity force over some Trans-Neptunian objects (TNOs), which combined with the gravitational pull of the sun can change their orbits [Fernández, 1980; Duncan et al., 1988]. Subsequent interactions with the giant planets can bring these objects into the inner Solar System with their aphelia tied to Jupiter. These are called Jupiter Family Comets (JFCs) and have low-inclination orbits with orbital periods of up to 20 Earth-years [Lowry et al., 2008].

Comets are comprised of a nucleus that can reach up to 100 km in diameter [Whipple, 1962] and a coma, which is an unbound atmosphere that forms around the nucleus as it is being heated by the solar radiation. In general, cometary nuclei are composed of a mixture of rock, dust and ices. As the comet gets closer to the Sun, these ices heat up and sublimate, creating a coma and tail that, depending on the amount of gas expelled from the nucleus, can reach a distance of

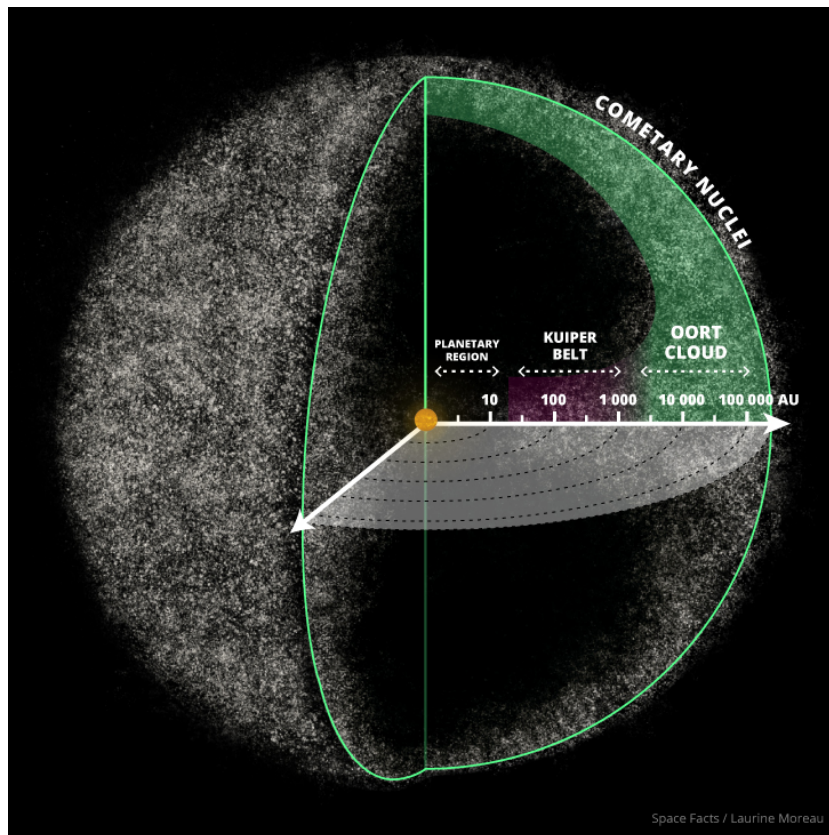


FIGURE 1.1. Illustration of the biggest comet reservoirs: 1) the *Edgeworth-Kuiper Belt* starting at about 30 AU to nearly 1,000 AU from the Sun, and 2) the Oort cloud between 10,000 AU and 100,000 AU from the Sun. Objects from both of these zones are also called *Trans-Neptunian Objects* (TNOs). Source: <https://space-facts.com/oort-cloud/>

1.5AU Vsekhsvyatskii [1969] or even as much as 3.8AU away from the nucleus as determined for comet Hyakutake [Jones et al., 2000]. Gas molecules are subsequently ionized and picked up by the solar wind to form an ion tail, as can be seen in Figure 1.2. There are actually two types of tails, the first one is ionized gas formed by ultraviolet sunlight, while the second one is more diffuse and is composed of small dust particles pushed by solar pressure.

Although the first registered observation of a comet dates back to China 1000 B.C. [Ho Peng Yoke and Ho Ping-Yü, 1962], it was not until the middle of the 16th and the beginning of the 17th century, with the invention of the telescope, that cometary sciences became a new research field. In the more recent times, space technology has allow us to get even closer than ever imagined to these pristine objects and take in situ measurements of their nuclei and comae that, together with numerical models, significantly improved our knowledge of them. Therefore, in the following sections I shall make a small review of cometary research in the modern era before and after the Rosetta mission.

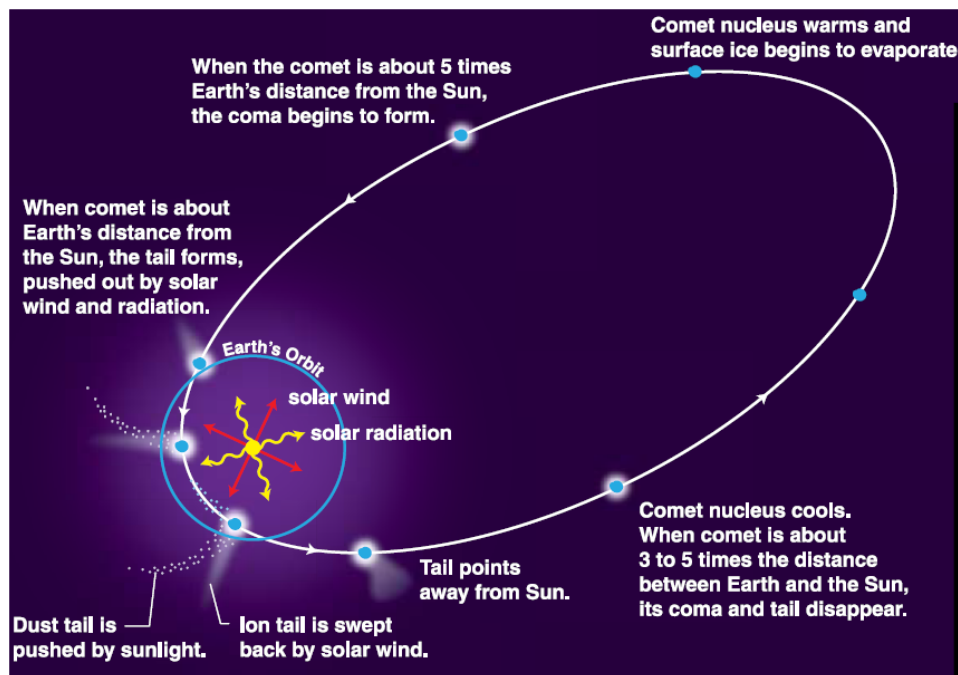


FIGURE 1.2. Illustration of a comet's orbit and the formation of its tails as it gets closer to the Sun. Source: <https://spaceplace.nasa.gov/review/posters/stardust/comets-vs-asteroids.pdf>

1.1 Cometary Science before the Rosetta mission

Before we could send spacecraft and telescopes into space, all we knew of comets was limited to Earth based observations. In 1578, the danish astronomer Tycho Brahe calculated for the first time the parallax of the "Great comet of 1577" (also known as comet C/1577 V1). After this discovery and even though we did not know exactly what comets were made of, astronomers could track their orbits and determined that some of them moved in highly eccentric ellipses as observed by Sir William Lower in 1610. At the same time the astronomers Robert Hooke and Giovanni Borelli determined that some of them would actually move in parabolic orbits. Years later, Isaac Newton would apply his theory of gravity to show that comet C1/1577 V1 also moved in an elliptical orbit and that it passed by about 0.00154AU above the surface of the sun [Festou et al., 2004]. Probably the first person that comes to mind when talking about cometary scientist is the English astronomer Edmund Halley. In 1705, he made an enormous contribution after having studied the orbits of many of the known comets at that time, and predicted the periodic nature of comet 1P/1682 Q1. Halley died before he could confirm his prediction, but when comet 1P/1682 Q1 came back in 1758, it was named after him.

The first spectroscopic observation of comets came in 1864, when Donati [1864] compared the spectra of comets C/1864 N1 and 55P/Tempel–Tuttle with the spectra of a flame and observed three bright bands in its spectra due to emissions of the comet and the continuum due to reflected

sunlight. It was determined that these bands agreed with carbon content in the cometary coma and tail [Huggins, 1868]. This led spectroscopy to become a new and powerful tool in the study of the compositions of comets. In the 1940s, the spectra of several comets was studied and the presence of OH, NH, CN, C₂, CH⁺ and N₂⁺ were identified in their comae, some of which were inferred to be daughter species of the CO, CO₂, C₂N₂, CH₄, N₂ and NH₃ molecules [Swings et al., 1941; Swings, 1942; Wurm, 1949; Festou et al., 2004]. In 1941, the discovery of OH 3090 Å UV emission led to the determination of H₂O as a parent molecule [Festou et al., 2004]. How all these ices could survive in vacuum for so long was difficult to explain at the time if no solid nucleus was assumed. The most fundamental theory for the composition of comets was suggested by Whipple in 1950. He described comets as solid and dirty snowballs and suggested that the icy part of the nucleus sublimates as the comet approaches the Sun. At the same time, dust is released from the nucleus as the gas is ejected. The mixture of ices inside the nucleus was not described in detail, but he assumed that given the high volatility of the ice, there should be a desiccated dust layer at the surface before the comet approached perihelion. Even though we now suspect the reality is more complicated than this, Whipple gave us a good and simple description of what a comet basically is. A few years later, Delsemme and Swings [1952] suggested that H₂O was a major constituent of comets, and that it formed hexagonal lattice structures in which more volatile material was trapped.

The emission of gas and dust is a consequence of an energy balance at the surface that needs to include conduction into the interior. Thermal conductivity is a key physical property for the heat exchange process within any material. In the case of comets, the thermal conductivity has been inferred to be extremely low [Huebner et al., 2006; Fernández et al., 2013]. Observations from comet Kohoutek (1973f) together with a numerical model of the cometary nucleus consisting of a growing non-volatile dust mantle surrounding a volatile icy core revealed that for heliocentric distances below 2 AU, the thermal conductivity of the dust mantle should be quite small and the mantle's thickness should lie in the range of 10-75 cm after a perihelion passage [Mendis and Brin, 1977]. The model results of Mendis and Brin suggest a strong insulation effect caused by a growing dust layer at the surface of the nucleus, which could reduce the gas production rate compared to a case in which the ice is at the surface. Similar studies were performed by Fanale and Salvail [1984], who integrated processes involving heat, gas and dust transport to model cometary activity for an idealized short-period comet. This model was developed in a series of papers applied to comet 1P/Halley in which the effect of the coma, non-gravitational forces and the grain cohesion was taken into account [Fanale and Salvail, 1986, 1987, 1990]. It was determined that thermal conductivity for comet Halley had to be very low and that the ice near the surface had to be in its crystalline form. Regarding CO₂ and CO ice, Fanale and Salvail found that it should always be found within ~ 1 m and 3 m from the surface, respectively. The KOSI (Kometensimulation) experiments for cometary analogues found that the sublimation of volatile ices causes a chemical differentiation of the samples and that some of the sublimed

gas can re-condense in the interior of the nucleus to create a hard layer of ice [Huebner et al., 2006]. Grün et al. [1991] performed an energy analysis of an ice-dust-sample and found that the visible and thermal re-radiation from the sample surface, the sublimation energy of the ices and the increase of internal heat were the most important contributions to the energy balance. Thermal inertia controls the speed at which heat penetrates and leaves the comet surface. It is defined as the squared root of the thermal conductivity, the specific heat and the bulk mass density (see Equation 2.4). Laboratory experiments estimated thermal inertia values (typical units are $J/(m^2K\sqrt{s})$ abbreviated here to TIU) around 73 TIU for a dry and highly porous matrix and 258 TIU for a porous matrix with water vapour [Seiferlin et al., 1995, 1996]. For comets 103P/Hartley 2 and 9P/Tempel 1, observations suggest a thermal inertia lower than 250 TIU and 45 TIU, respectively [Groussin et al., 2013]. However, other studies estimated a thermal inertia for comet 9P/Tempel 1 between 50-150 TIU for scarped/pitted terrain and up to 200 TIU if the terrain is relatively flat [Davidsson et al., 2013].

The growing interest in the scientific community resulted in a series of space missions to these objects. The first visit to a comet was made by the International Cometary Explorer (ICE) spacecraft on 11th of September, 1985. ICE did a flyby near comet 21P/Giacobini-Zinner and took distant observations of comet 1P/Halley. Comet 1P/Halley was visited multiple times after that by the Vega program in 1984, and by the Sakigake spacecraft, the Giotto mission and the Suisei spacecraft in 1985. Figure 1.3 shows a photograph taken by the camera on board of the Giotto spacecraft, which became the first close up observation of a comet's nucleus. These observations confirmed Whipple's hypothesis of a solid and irregular nucleus and were used to constrain cometary models. 1P/Halley was found to be partially active in certain regions, most of which were covered by a very dark material with an albedo of about 4% [Keller et al., 1986]. Water vapour was detected for the first time in a comet thanks to observations taken by the Kuiper Airborne Observatory (KAO) of comet 1P/Halley [Mumma et al., 1986; Reinhard, 1986]. H_2O ejections were mainly observed on the illuminated side of the comet and production rates of up to 2.3×10^{30} molecules per second were determined at its post-perihelion passage [Weaver et al., 1986]. Similar studies also showed that there was an asymmetry in gas production between the pre-perihelion and post-perihelion of the comet, such that the largest amount of gas emissions were a few days after its closest approach to the Sun. Similar findings were reported for comet 19P/Borrelly, after NASA's mission Deep Space 1 approached it in 2001. Comet 19P/Borrelly also seemed to be very dark and with maximum 10% of its surface being actively sublimating [Soderblom et al., 2002; Buratti et al., 2004; Ho et al., 2003]. The formation of dust jets by collimated subsurface gas ejections in the comet were also studied and compared to observations of jets seen in other comets [Keller et al., 1986; Yelle et al., 2004; Sekanina et al., 2004; Li et al., 2007].

So far, we had only observe comets from afar, but with the Stardust mission we could for the first time collect sample material ejected from comet 81P/Wild 2 which was brought to Earth in



FIGURE 1.3. Comet Halley as seen by the Halley Multicolour Camera on-board of the Giotto spacecraft on 14 March 1986. ©ESA/MPAe.

order to study its composition. Organic material was found, which had similarity to interplanetary dust particles and carbonaceous meteorites [Sandford et al., 2006]. This extended the work of Jessberger et al. [1988] who inferred the presence of organics from in situ measurements of elemental abundances in dust at Halley. The surface of comet 81P/Wild 2 was full of craters (see Figure 1.4), which were modeled and inferred to be a result of active sublimation from its nucleus [Ivanova and Shulman, 2005]. Flat-topped mesas bounded by cliffs were also observed and it was determined that gas emissions from the cliff faces could be responsible for such features [Brownlee et al., 2004]. Fink et al. [1999] determined H_2O production rates of 1.5×10^{28} molecules per second for comet 81P/Wild 2, and they found it to be very similar to comet 19P/Borrelly, which was also very depleted in C_2 emissions.

The next big encounter with a comet was made by the Deep Impact mission, which successfully flew by comet 103P/Hartley 2 and comet 9P/Tempel 1, to eventually release a 370 kg *smart impactor* towards 9P/Tempel 1. Comet 103P/Hartley 2 revealed very interesting findings, as most of its activity was primarily caused by CO_2 gas emissions, which drag chunks of water ice out of its nucleus [A'Hearn et al., 2011]. The same studies determined that, even though smaller compared to Tempel 1, comet Hartley 2 was much more active at perihelion, with H_2O production rates of 1.1×10^{28} molecules per second, CO_2 production rates larger than 2.0×10^{27} molecules per second and CO production rates between $2.2\text{-}2.9 \times 10^{25}$ molecules per second [Meech et al., 2011; Weaver et al., 2011]. In terms of comet shape, comet Hartley 2 has a similar bi-lobed shape to

that of comet Borrelly, but its surface seemed to be much smoother as can be seen in Figure 1.4. One of the reasons to study comets is because it is conceivable that they are the responsible for have brought water to Earth. Hartogh et al. [2011] determined that a comet such as Hartley 2 would have the same type of D/H ratio as that seen in Earth oceans, and combined with asteroids could be a potential source of Earth's water.

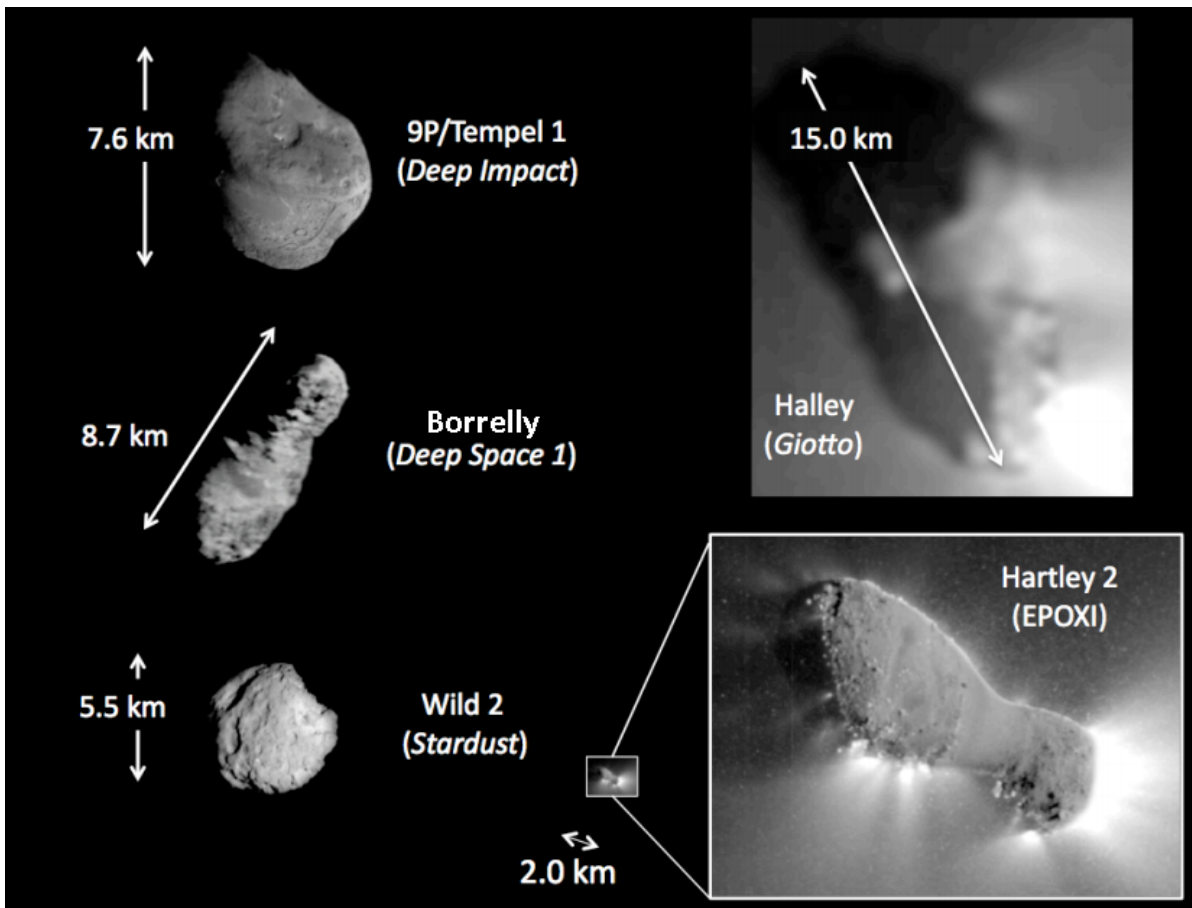


FIGURE 1.4. Dimensions of the cometary nuclei observed by spacecraft before Rosetta. Taken from the Supplementary material of A'Hearn et al. [2011].

On the other hand, the crater produced by Deep Impact in comet Tempel 1 revealed that this comet was covered by a layer of micrometer size dust particles and, even though its coma was found to be very faint, frequent outbursts could be observed near areas of local sunrise [A'Hearn et al., 2005]. Biver et al. [2007] inferred H_2O production rates of up to 1×10^{28} molecules per second before the impact and used radiative transfer calculations to estimate the increase in H_2O production after the impact of about 1×10^{32} molecules or 5000 ± 2000 tons, which was consistent with estimates from other authors [Mumma et al., 2005; Küppers et al., 2005; Schleicher et al., 2006]. Thanks to the high spatial resolution of the HRI-IR spectrometer aboard Deep Impact,

it was possible to produce maps with the distribution of H₂O and CO₂ gas in the inner-coma of Tempel 1, which indicated chemical heterogeneities within the nucleus [Feaga et al., 2007; Finklenburg et al., 2014b]. Moreover, the analysis of the IR-spectra suggested that H₂O ice was depleted in approximately the first 1m from the surface layer of the comet [A'Hearn et al., 2005; Richardson et al., 2007; Schultz et al., 2007; Sunshine et al., 2007].

In parallel with the accomplishments of space exploration, the development of numerical models that allow us to interpret new available data also began to play an important role. The first model to study cometary activity was called the *Fountain model* and it was developed by Eddington [1910]. It assumes the comet to be a point source and the density of its emission decreases with the inverse square of the distance from the source ($1/r^2$). Some years later, Haser [1957] and Wallace et al. [1958] modelled the coma as a free expansion problem, where daughter species were created by photo-dissociation of some parent molecules. Marconi and Mendis [1982, 1983] used multi-fluid models to study H₂O cometary atmospheres. Since the late 1980s a large amount of this work has been done by Jean-François Crifo, Michael Combi and Tamas Gombosi, who used numerical methods to study the expansion of flows in space and apply this to the dynamics of dust and gas in cometary atmospheres. Some of these studies used hydrodynamic models to investigate the outgassing in the coma of comet Halley [Crifo, 1986a, 1988, 1987b, 1990, 1997b; Combi, 1989, 1996; Cravens, 1989; Gombosi et al., 1996; Rubin et al., 2011] and the neutral coma gases around spherical and non-spherical activity sources [Kitamura et al., 1985; Kitamura, 1987; Gombosi et al., 1985, 1986a; Koemle and Ip, 1987; Combi and Smyth, 1988a; Combi, 1988b; Knollenberg, 1994; Crifo and Rodionov, 1997a]. The first 3D computation of a H₂O coma was done by Kitamura [1990], who used the Euler equations to simulate jet interactions and the formation of shock waves at the limit of their interaction regions. Combi [1996] used for the first time the Direct Simulation Monte Carlo (DSMC) method to study comets. Comparisons between Euler and Navier-Stokes equations [Kitamura, 1987; Crifo and Rodionov, 2000] and Navier-Stokes and DSMC results were done for homogeneous and inhomogeneous cometary sources [Crifo et al., 2002, 2003, 2005; Lukyanov et al., 2005; Zakharov et al., 2008, 2009]. In these models, the H₂O flux was derived from surface ice sublimation equations, and the CO flux was set arbitrarily [Crifo et al., 2004]. They found that Euler equations start to fail close to the jet features where rarefied gas appeared. Finklenburg et al. [2014b] also used 3-dimensional DSMC simulations to model the coma of comet Tempel 1 and reproduce the H₂O column densities found by the infrared imaging spectrometer of the Deep Impact spacecraft. In the current work, I use an approach similar to the one Finklenburg et al. [2014b] used to investigate the gas emissions from the target comet of the Rosetta mission. Further information of the DSMC method will be given in Section 2.3.2.

1.2 Comet 67P/Churyumov-Gerasimenko and the Rosetta mission

Comet 67P/Churyumov-Gerasimenko (hereafter 67P/CG) was discovered in 1969 by the Ukrainian astronomer Klim Churyumov, who found it in a photograph taken by his colleague Svetlana Gerasimenko earlier that year [Churyumov and Gerasimenko, 1972]. Comet 67P/CG was found to be a short period comet, which belongs to the JFCs. Due to the close encounters of the comet with Jupiter, it was found that its orbital period is very unstable, as it was determined that after its encounter in 1959, its perihelion distance was reduced from 2.76 to 1.29 AU and its orbital period changed from 8.97 to 6.55 years [Lamy et al., 2007; Thomas, in press]. At the present time, we know comet 67P/CG completes one orbit every 6.45 years, it has an elliptical orbit with an eccentricity of 0.64 and an inclination with respect to the ecliptic plane of about 7° [Lamy et al., 2007]. Comet 67P/CG, as any other comet, is also perturbed by non-gravitational forces that can influence its motion. Cometary activity produces a reaction force in the anti-Sun direction, that can be responsible in a small degree of changes in its orbital period, but big changes in its rotational period. Thanks to observations of the *Hubble* and the *Spitzer* Space Telescopes, it was determined that the rotation period of the nucleus was between 12-12.8 hours [Lamy et al., 2006, 2007; Tubiana et al., 2008, 2011; Lowry et al., 2012]. However, after Rosetta's arrival to the comet's orbit, it was found that its rotation period was 12.4043 ± 0.0007 h [Mottola et al., 2014]. The period changed and reached a peak shortly before the spring equinox and dropped quickly as it approached perihelion [Keller et al., 2015]. The obliquity of the comet's rotational axis is about 52° , which produces a seasonal effect and a strong dichotomy at its surface activity [De Sanctis et al., 2010; Filacchione et al., 2016; Keller et al., 2017].

In 2003, Comet 67P/CG became the destination of the European Space Agency's Rosetta mission, after a launch failure caused a delay in Rosetta's launch, making it impossible to reach the original target, comet 46P/Wirtanen. The Rosetta mission was launched in 2004, and it took 10 years before it reached its destination on the 6th of August 2014. Figure 1.5 illustrates the comet's orbit in the J2000 inertial frame, indicating some relevant dates regarding the mission and others relevant for the studies presented in the present work. The Rosetta mission accompanied comet 67P/CG from August 2014 to September 2016, and observed gas and dust activity in its coma. Thanks to the extensive payload complements, Rosetta collected significant data on the abundances of the major gas species near the nucleus as well as highly resolved spectra of the coma in the infrared and microwave regimes.

The Optical, Spectroscopic, and Infrared Remote Imaging System (OSIRIS) of the Rosetta mission [Keller et al., 2007] photographed the comet nucleus and found it has a bi-lobed shape, that is connected by the so called *neck* region [Sierks et al., 2015]. Studies suggest that these lobes may be the result of two separate objects that formed in the same region and joined through a low-energy collision [Massironi et al., 2015; Jutzi and Benz, 2016; Schroeder et al., 2019].

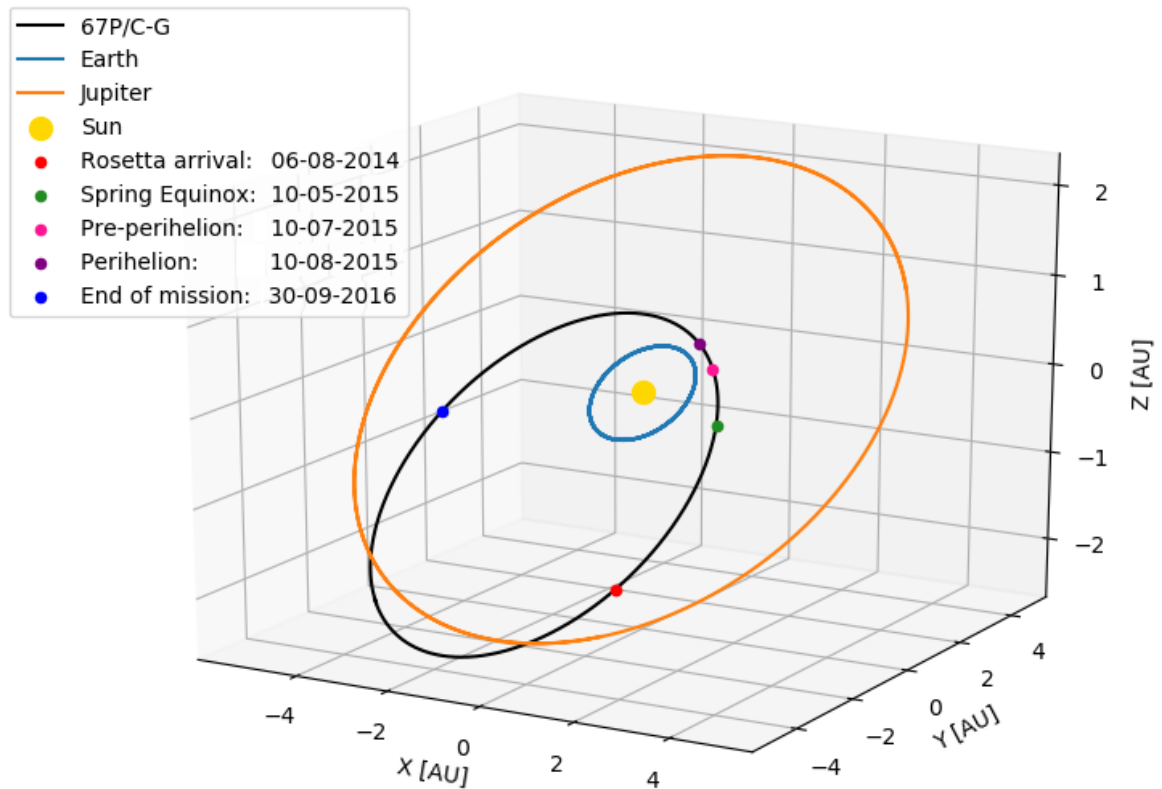


Figure 1.5: Comet 67P/CG orbit on the J2000 inertial frame. The orbit of Earth (in blue) and the orbit of Jupiter (in orange) are shown for comparison. The colored dots indicate relevant dates for the mission and for the some of the simulations performed in the present work.

Compared to other comets visited by spacecraft missions, comet 67P/CG has a similar size to comet Wild 2. The larger lobe of comet 67P/CG measures approximately $4.1 \times 3.2 \times 1.3$ km, while the smaller lobe has dimensions of $2.5 \times 2.5 \times 2.0$ km.

Thanks to the high resolution of the images taken by the OSIRIS camera, Preusker et al. [2015] used DLR's stereo-photogrammetric analysis technique to produce a shape model for comet 67P/CG with a vertical accuracy at the decimeter scale. The last version of the shape model (SHAP7) has a larger coverage of the southern latitudes to produce a shape with a metre scale accuracy [Preusker et al., 2017]. In the current work, I have used SHAP7 to generate the mesh needed for my 3D DSMC simulations (see Section 2.1). Based on the available images at the time, morphological regions (and sub-regions) were defined and mapped onto the 3D shape model [Thomas et al., 2015a,b; El-Maarry et al., 2016; Thomas et al., 2018] which are shown in Figure 1.7.

The Rosetta Orbiter Spectrometer for Ion and Neutral Analysis (ROSINA) [Balsiger et al., 2007] determined H_2O , CO_2 , CO and O_2 to be the most abundant gases in the coma [Hässig et al., 2015; Le Roy et al., 2015; Bieler et al., 2015a], which gives a clear indication of the composition of

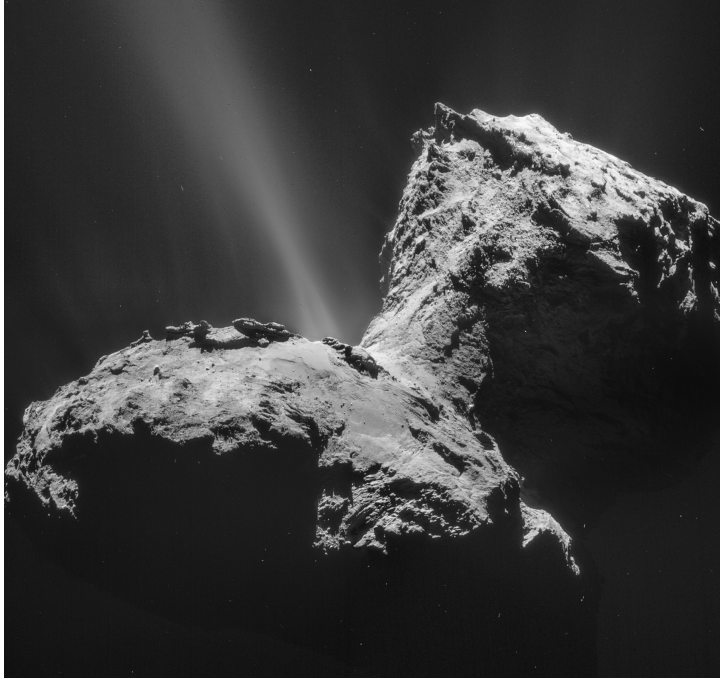


FIGURE 1.6. Comet 67P/CG as seen by the OSIRIS camera on-board of the Rosetta spacecraft in January 2015. It shows dust ejections coming from the *neck* of the comet. ©ESA/Rosetta/NAVCAM.

dominant ices within the nucleus. How these different ices are physically related to each other and distributed within the nucleus is a more intricate issue for which we have no clear answer at this time. Bockelée-Morvan [2011] and Bockelée-Morvan and Biver [2017] have made a summary of the main species detected in comets relative to water from measurements taken up to 2015, which is shown in Figure 1.8. There, we see how ground-based and spacecraft observations have confirmed H_2O to be the most abundant molecule in cometary comae, followed by CO_2 , CO , CH_3OH , C_2H_6 , H_2S and CH_4 .

Although ices have been detected at the surfaces of cometary nuclei through infrared remote-sensing [Sunshine et al., 2006; Oklay et al., 2016; Barucci et al., 2016; Filacchione et al., 2016] and inferred from visual broad-band imaging [Pommerol et al., 2015; Fornasier et al., 2016], the areal extent of the ice exposed on the surface is totally insufficient to explain the total volatile mass loss [Sunshine et al., 2006; Fougere et al., 2016a,b; Marschall et al., 2016]. Furthermore, measured surface temperatures under strong illumination far exceed the free sublimation temperature of water ice (around 200 K) [Emerich et al., 1988; Li et al., 2007; Groussin et al., 2013; Tosi et al., 2019]. In addition, the mass loss per unit surface area is typically well below the free sublimation rate from a pure ice surface leading to the introduction of concepts such as the "effective active fraction" (*EAF*) to reduce the total sublimation rates in models to match those observed [A'Hearn et al., 1995; Lamy et al., 2001]. ROSINA measurements have been used to

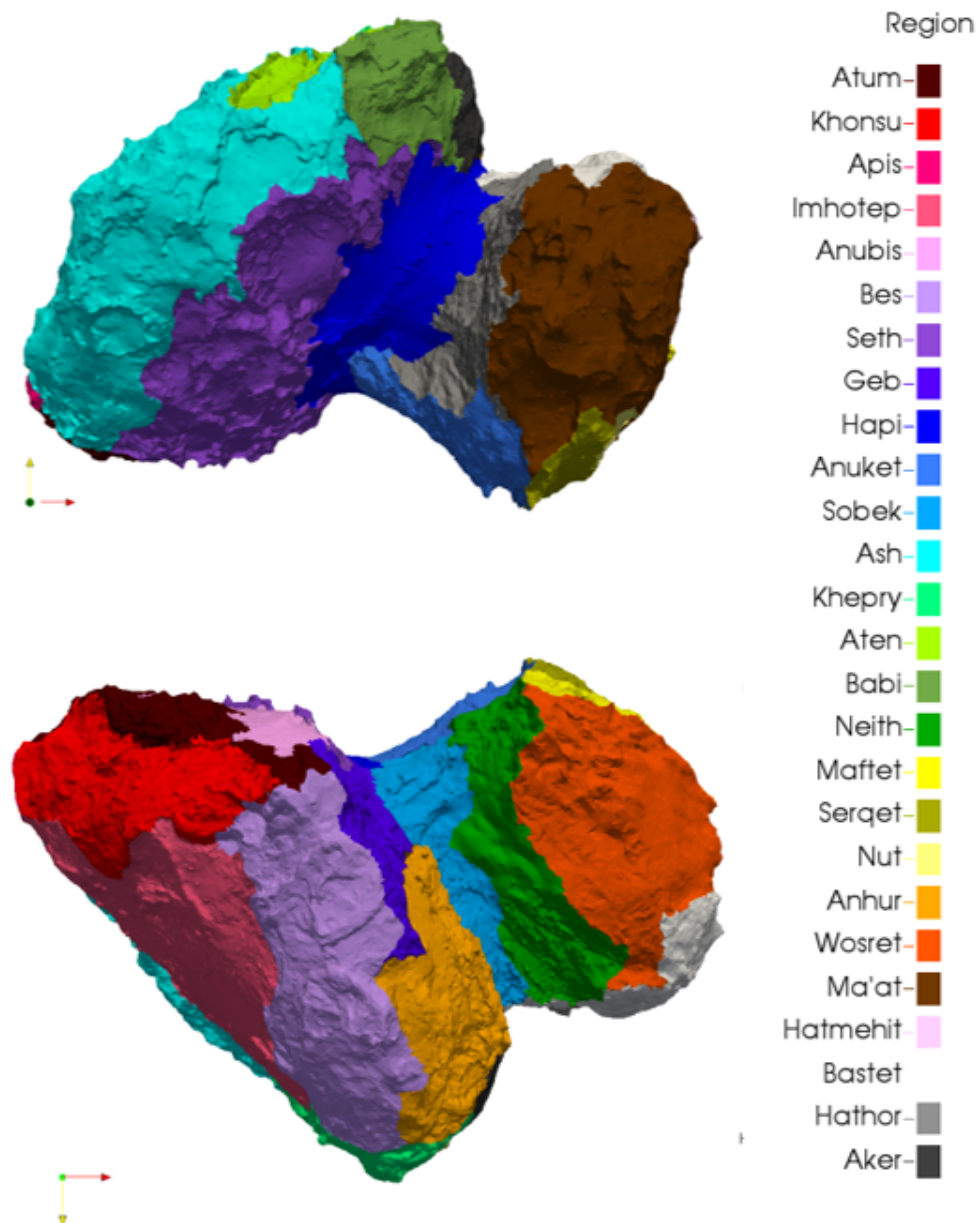


FIGURE 1.7. Morphological regions of comet 67P/CG defined by Thomas et al. [2015a,b]; El-Maarry et al. [2016]. The top panel give us a view of the northern hemisphere of the comet, while the bottom panel shows the southern hemisphere of 67P/CG.

estimate peak production rates between $1.85 - 3.5 \times 10^{28}$ molecules/s for H_2O and about 1.58×10^{27} molecules/s for CO_2 [Hansen et al., 2016; Läuter et al., 2020].

Previous studies have used numerical data inversion methods or kinetic and hydro-dynamical approaches to derive the H_2O activity distribution and evolution of densities observed by ROSINA

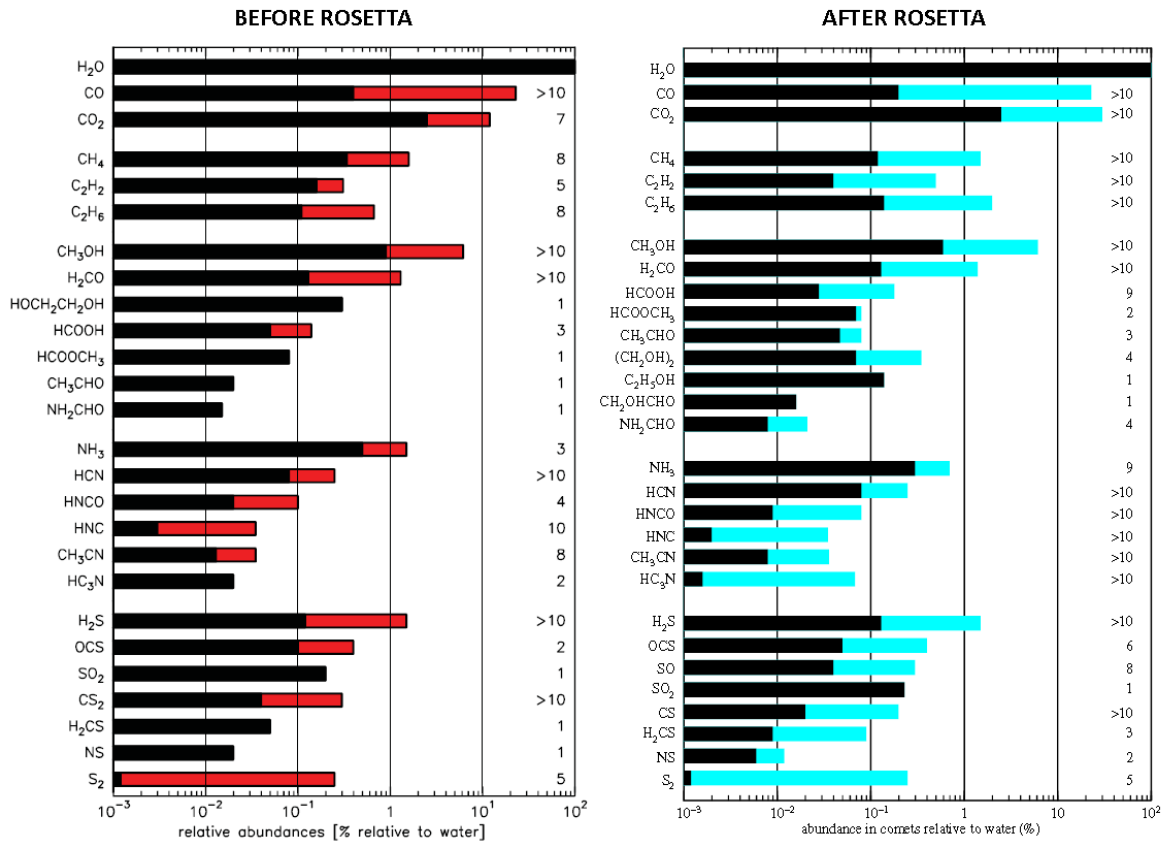


Figure 1.8: Abundances relative to water (black bars) of the main species detected in cometary nuclei before and after the Rosetta mission. Colored bars indicate the range of measured values and the numbers on the right indicate the amount of comets used for the abundance estimation. Taken from Bockelée-Morvan [2011] and Bockelée-Morvan and Biver [2017].

in the coma of comet 67P/CG during different stages of the Rosetta mission [Bieler et al., 2015b; Biver et al., 2015; Marschall et al., 2016, 2019; Fougere et al., 2016a,b; Hoang et al., 2016; Combi et al., 2020]. These studies have identified the heterogeneous distribution of H₂O outgassing from the cometary surface, with strong sources localized in the Hapi region for example [Marschall et al., 2016], but confirmed that, at scales greater than ~ 400 m, it is rather difficult to detect heterogeneity in the distribution of H₂O sources from ROSINA measurements alone [Marschall et al., 2020]. Crudely, the outgassing of H₂O can be assumed to be driven to a large extent by insolation with no significant thermal lag [Bieler et al., 2015b]. However, CO₂ does not seem to follow the same principle, because there are significant changes in the CO₂/H₂O mixing ratio in the coma [Bockelée-Morvan et al., 2015; Hässig et al., 2015; Fink et al., 2016; Fougere et al., 2016a; Migliorini et al., 2016]. Bockelée-Morvan et al. [2015] suggested that observations of the infrared spectrometer for the Rosetta mission (VIRTIS-H) [Coradini et al., 2007] were consistent with nightside outgassing of CO₂, for example, which suggests that heat is still available to

produce sublimation in the absence of insolation, on rotational timescales. The idea of nightside emission has been brought forward on several occasions with most gas dynamics calculations assuming a small but not insignificant amount of gas (2-10 %) emitted from the nightside or non-illuminated areas of the comet [Bockelée-Morvan et al., 2015; Bieler et al., 2015a].

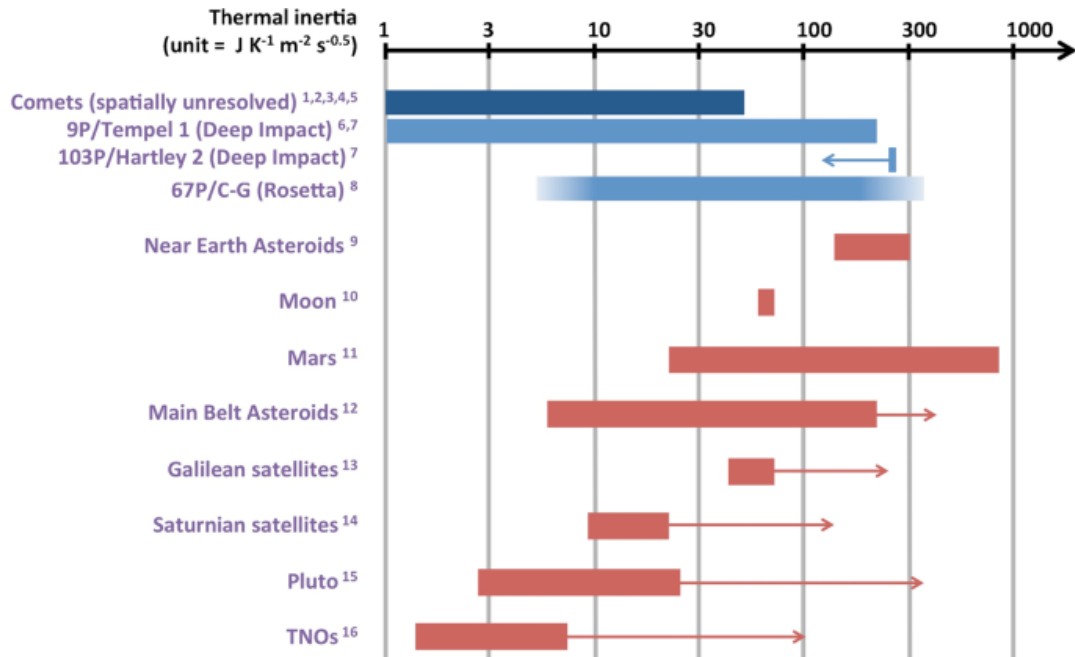


Figure 1.9: Thermal inertia values from Groussin et al. [2019]. For comet Hartley, the arrow indicates that the thermal inertia is < 250 TIU. For comet 67P/CG most estimates indicate a thermal inertia between 10-170 TIU. The colour gradient in this case indicates some extreme values that indicate a thermal inertia < 10 TIU or > 170 TIU.

Regarding the dust composition of 67P/CG, the Optical, Spectroscopic and Infrared Remote Imaging System (OSIRIS) on-board Rosetta observed a very dark surface that, together with COSIMA dust measurements [Kissel et al., 2007], suggested the presence of carbon-rich material mixed with an almost equally amount of silicates [Bardyn et al., 2017]. The OSIRIS observations were used to estimate a geometric albedo of $6.5 \pm 0.2\%$ for its surface [Fornasier et al., 2015], which is in the same range as the albedo estimate of $\sim 4\%$ for other comets [Huebner et al., 2006]. The Comet Nucleus Sounding Experiment by Radio wave Transmission (CONSERT) provided measurements that suggest a porosity between 75% to 85% [Kofman et al., 2015; Brouet et al., 2016]. It is important because the conduction of heat into the interior decreases in highly porous materials [Seiferlin et al., 1996; Shoshany et al., 2002], and it can be used to constrain the properties of the dust mantle in thermophysical models. The Multipurpose Sensors for Surface and Sub-Surface Science (MUPUS) on the Philae lander was used to estimate a thermal inertia of 85 ± 35 TIU on the Abydos area of the nucleus [Spohn et al., 2015]. Further analysis with MIRO data has produced TI values from 10 to 50 TIU and suggests a highly insulating role

for the dust at the surface [Gulkis et al., 2015]. More recent studies using data from MIRO’s mm-channel imply this value is ≤ 80 TIU, while the Visible and InfraRed Thermal Imaging Spectrometer (VIRTIS) data suggests a broader range between 40 - 160 TIU [Marshall et al., 2018]. Such low thermal inertia values would be consistent with the high porosity observed by CONSERT and with inferred values for other comets. Figure 1.9 summarizes the thermal inertia values for some cometary nuclei compared with other objects in the solar system. Taking into account that thermal conductivity is temperature dependent and the temperature increases as the heliocentric distance decreases, thermal inertia depends on heliocentric distance as $r_h^{-3/4}$ [Delbo’ et al., 2007; Rozitis et al., 2018]. Therefore, comets have a large range of thermal inertia values compared to larger objects in the solar system. They also are among the bodies of the solar system with the lowest thermal inertia. Derived thermal inertia values for comet 67P/CG have large discrepancies which could be caused by real differences in the nucleus structure and composition, or could be model dependent [Groussin et al., 2019].

1.3 Motivation

We have a basic understanding of the way gases are released from the nucleus in order to form the gas and dust comae as the comet approaches the Sun. We know that the production of these gases is driven by the incident solar radiation on the nucleus, and this leads to the sublimation of cometary ices that can drag dust particles away, while eroding the comet’s surface. The composition of the coma depends on the composition and thermal properties of the nucleus. However, to what extent we can use coma measurements to derive the composition of the nucleus is a major issue in cometary sciences. The analysis of remote sensing data requires a comprehensive study of the gas emission process and the gas dynamics of the inner coma. After which a comparison with multi-instrument data allows us to better constrain the thermophysical models that link comae measurements with the nucleus near-surface structure and composition.

The present work uses a kinetic method to model the gas dynamics in the inner-coma of comet 67P/CG, which is compared with multi-instrument data from the Rosetta mission. Given that cometary comae are very rarefied flow fields, the most appropriate method is the Direct Simulation Monte Carlo (DSMC). DSMC results are compared with data from three instruments of the Rosetta mission: ROSINA, MIRO and VIRTIS-M that observe different aspects of the cometary coma. The selected times in this study are the spring equinox and pre-perihelion (see Figure 1.5). The first one has been chosen because at that time H_2O emissions measured by ROSINA are relatively well explained, such that to include CO_2 gas and a thin dust mantle can complement the Marschall et al. [2019] analysis of VIRTIS observations and improve the fit with MIRO velocity and temperature profiles retrieved by the DSMC simulation profiles. The second date has been selected to explore emissions from the southern hemisphere one month before perihelion. At this time, the southern hemisphere is fully illuminated, while the gas production

rates are not high enough to increase markedly the computational time and compromise the accuracy of the DSMC calculations.

Based on previous studies [Marschall et al., 2019], I attempt to find activity inhomogeneities of H_2O and CO_2 gases that can lead to different distributions of H_2O and CO_2 -ices at the nucleus. In a first step, I study the gas expansion of H_2O and CO_2 gas in order to understand the main properties governing the adiabatic expansion of both types of gases. This will become important when studying gas mixtures from spherical and complex shape sources, in which I estimate the effect of CO_2 emissions in H_2O gas field and vice versa. I also explore the role of thermal inertia in the distribution of ice sources at the sub-surface and how the presence of a dust mantle can contribute to larger gas temperatures and velocities close to the surface.

Modelling the gas dynamics: Methods and tools

In the following chapter, I discuss the modelling approach used in this work to study the composition and formation of the inner-coma of cometary nucleus, with the focus on comet 67P/CG. Figure 2.1 shows the steps in which the following chapter is divided. The scheme is essentially a subset of the approach used by Marschall et al. [2019]. In the first part, I describe the mesh generation procedure required for our 3D simulations. In the second part, I explain the thermal model and the selection of model parameters to define the boundary conditions at the nucleus' surface. The Direct Simulation Monte Carlo (DSMC) method used in this study is explained in Section 2.3.2. Finally, I provide a brief explanation of the Rosetta instruments I worked with for

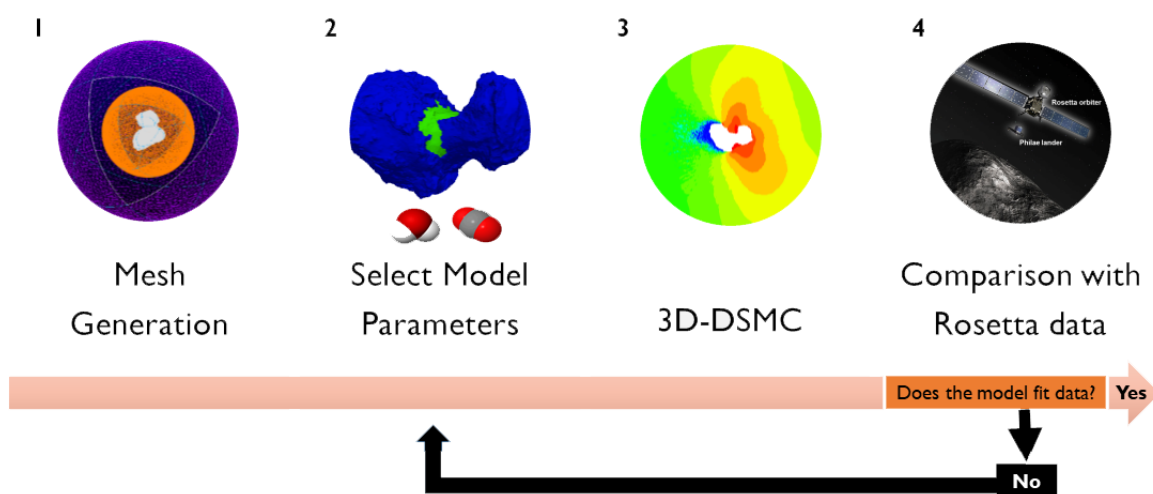


Figure 2.1: Modelling gas dynamics in 4 steps.

this analysis, and the methods used to compare the model results with *in situ* measurements of the coma average properties.

2.1 Mesh generation

The simulation of three-dimensional flows using the DSMC method requires a mesh to sample the inter-molecular collisions within each cell and calculate the macroscopic properties of the gas flow. The DSMC software we work with uses an unstructured mesh to define better gas flows with complex geometries. This mesh is produced using the PointwiseTM software, where one defines important properties such as the:

1. Outgassing source: it can be as simple as a sphere or be produced from any 3D shape available.
2. Mesh's resolution: is the variability of the cell size, which depends on the desired flux density one wants to simulate. Every computation within a mesh has an associated quality parameter given by the ratio between the cell dimension Δs and the average distance travelled by the gas particles between collisions, also called mean free path (*mfp*)

$$\frac{\Delta s}{mfp} \leq 1 \quad (2.1)$$

As the *mfp* increases with distance from the nucleus when the gas expands into vacuum, I have defined a gradual increase in the cell size as the flow moves away from the inlet boundary. Therefore, if the mesh satisfies the condition of equation 2.1 everywhere, we can be sure that the code samples properly every particle collision with its nearest-neighbor and we can rely on the accuracy of the simulation [Bird, 2005]. This also means that the number of cells with such a small dimension becomes very large, which significantly decreases the computational efficiency of our simulations. One of the techniques used to solve this problem is the transient adaptive subcell scheme (TAS) included in our DSMC code (see Section 2.3.2). However, there can be places in the mesh with a large number of collisions where $\Delta s/mfp$ is never smaller than 1. It has been previously calculated that the error associated with $\Delta s/mfp > 40$ corresponds to a mean difference over the whole flow of about 2% [Finklenburg, 2014]. Therefore, we have made a compromise and set a limit of $\Delta s/mfp = 20$ for cases with production rates around 10^{28} molecules/s, which corresponds to about 300 kg/s of H₂O gas. Since we use the same collisional method as Finklenburg, we also estimate that the accuracy of our DSMC calculations is better than 10%.

3. Simulation domain: it is defined as a sphere with a radius of 10 km in all our simulations. A slice of it is shown in Figure 2.9 specifying the mesh's dimension.

In order to study the gas dynamics around a cometary nuclei, I have used the simplest approach to start with, which is a spherical nucleus comet of 2 km radius. It can be used to study

Mesh	Surface Facets	Surface's Δs [m]	Total Cells
Sphere	323'508	20	7'769'109
High-res 67P	440'596	16	13'303'916
Low-res 67P	40'020	70	779'463

Table 2.1: Meshes properties.

the basic physical processes in the gas expansion from the nucleus, without taking into account complexities associated with an irregular nucleus shape. This grid has been used for the studies presented in section 3.1 and chapter 4. For comet 67P/CG, I have used a decimated version of SHAP7 [Preusker et al., 2017] with 125k facets, on top of which I have defined 8 surface domains in which the mesh resolution required for the simulations is set. In a first stage, I have worked with a high-resolution mesh that, compared to SHAP7, has a difference in surface area of $\sim 2\%$ and a vertical elevation difference of maximum 32 cm. Although we estimate the accuracy of these calculations to be good, the computation times for this mesh can take between 3 to 5 days, given the larger amount of cells the DSMC code needs to sample. For lower production rates around 50 kg/s, we have a low-resolution grid that has maximum quality factor $\Delta s/\text{mfp}$ of 10 and requires less computation time. The main characteristics for all meshes used in this work are listed in Table 2.1.

2.2 Thermal model and selection of model parameters

In the following section, I will explain the coordinate system used for comet 67P/CG, how we calculate the input solar energy per surface unit and how we modulate the global production rates by setting a variable that measures the activity at the surface.

2.2.1 Nucleus coordinate system

The coordinate system used in this work is defined with respect to a comet-fixed frame, also known as *Cheops reference frame* for comet 67P/CG. In this frame, the Z -axis corresponds to the comet's axis of rotation. The comet's equator lies in the plane $Z = 0$, such that the northern hemisphere of the comet is given by the $+Z$ -axis and the southern hemisphere by $-Z$ -axis. The 0° longitude in the comet has been set in the $-X$ direction and given that in the comet-fixed frame the sun is moving around the comet in the clockwise direction, we have defined this to be the direction in which the longitude of the comet increases. The definition of the coordinate system (latitude, longitude) = (λ, ϕ) I use in the present work is illustrated in Figure 2.2. On the left side, we have a view of the comet's latitude coordinate from the neck at sub-observer $\lambda_{obs}=0^\circ$ and $\phi_{obs}=280^\circ$. On the right side, we have a view above the northern pole of the comet's longitude coordinate.

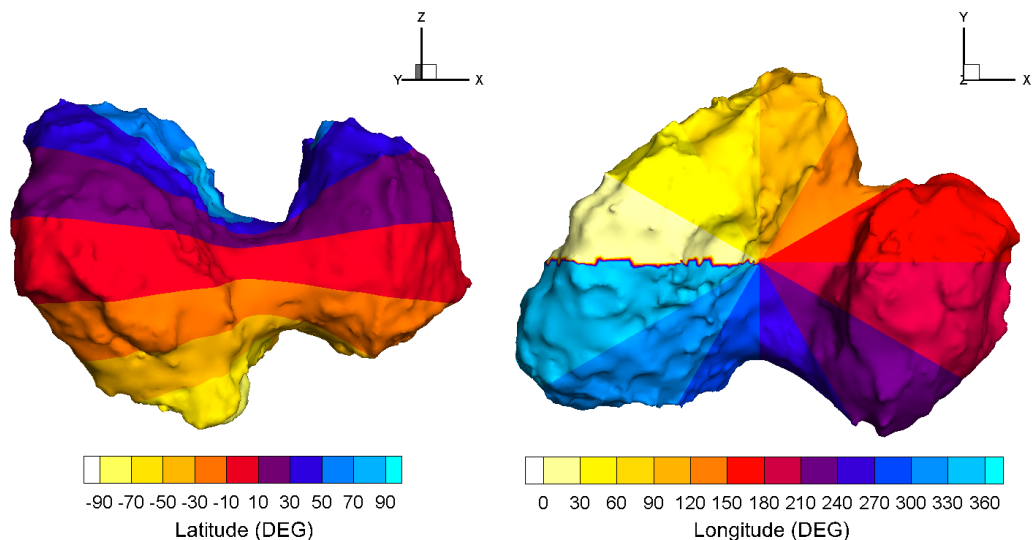


Figure 2.2: 3-dimensional view of the nucleus coordinate system. The cometographic latitude is shown on the left side. The Northern hemisphere goes from 0° to $+90^\circ$ and the southern hemisphere goes from 0° to -90° . The cometographic longitude is shown on the right side. The 0° longitude is set on the $-X$ -axis and increases in the clockwise direction when looking from the northern pole.

2.2.2 Calculation of illumination conditions

The illumination conditions at the surface of the nucleus change very fast. Therefore, we first need to calculate the position of the sun with respect to the comet in the 67P/CG fixed frame for the specific time we want to simulate. For each facet, we calculate the normal vector to the surface (\vec{n}) and the angle θ_i between it and the incidence solar vector (\vec{v}_\odot)

$$\vec{n} \cdot \vec{v}_\odot = \|\vec{n}\| \|\vec{v}_\odot\| \cos \theta_i \quad (2.2)$$

which is illustrated in Figure 2.3. Wherever the incidence angle $\theta_i \geq 90^\circ$, we assume the surface facet to be non-illuminated. Facets that have a $\theta_i < 90^\circ$ but are shadowed by other parts of the nucleus are also considered to be non-illuminated and no self-illumination effect is considered. The code for this calculation has been developed in FORTRAN by Marschall et al. [2016].

2.2.3 Thermal model

In the simplest case of sublimation from the surface (depth $z = 0$), we use a thermal model to calculate the energy balance at each surface facet i of the nucleus, set the chemical composition of the gas, and the sublimation fronts at different depths. This is done using the surface energy balance equation

$$\frac{S_\odot(1-A)}{r_h^2} \cos(\theta_i) = \epsilon \sigma T_{0,i}^4 + L_g \left. \frac{dm_i}{dt} \right|_{z=0} + \kappa \left. \frac{dT_i}{dz} \right|_{z=0} \quad (2.3)$$

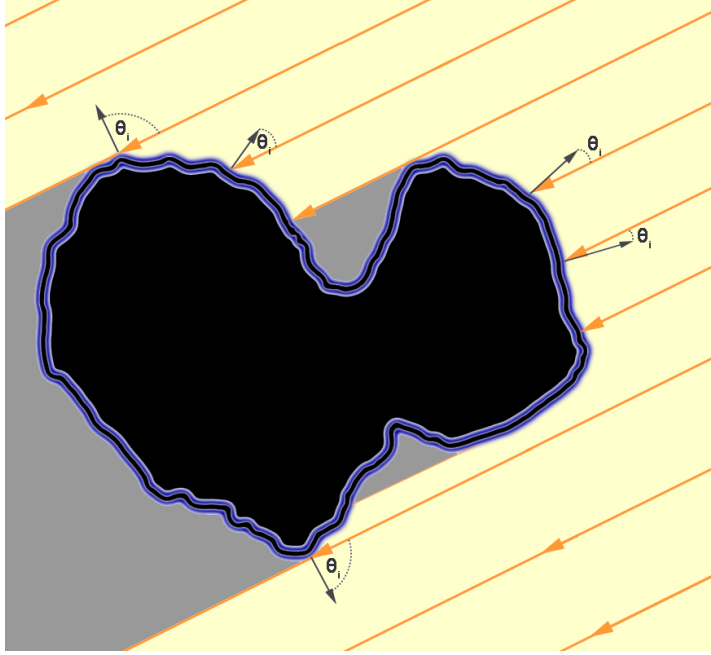


Figure 2.3: Sketch of the incidence solar angle θ_i . Orange arrows indicate the incidence solar radiation in the surface and the black arrows are the vectors normal to the surface at each particular point. Unilluminated areas around the comet are in gray.

The term to the left side of equation 2.3 is the input solar energy, where S_\odot is the solar constant at 1AU (1383 W/m^2), A is the directional-hemispheric albedo, r_h is the heliocentric distance and θ_i is the solar incidence angle. The first term on the right side is the thermal radiated emission from the surface, where the infrared emissivity ϵ is equal to 0.9, σ is the Stefan-Boltzmann constant and $T_{0,i}$ is the temperature at the surface. The second term is the loss of energy through sublimation of ice per unit time, where L_g is the latent heat of sublimation of the gas species ($L_{H_2O} = 2.84 \text{ MJ/kg}$ and $L_{CO_2} = 0.45 \text{ MJ/kg}$) and $dm_i/dt|_{z=0}$ is the mass loss rate per unit time per unit area at the surface. The last term is the effect of thermal conduction at the surface and influences the amount of heat transported to depth, where κ is the thermal conductivity and $dT_i/dz|_{z=0}$ is the temperature gradient with depth.

The degree to which a body stores or releases heat from its surface is quantified using the thermal inertia (Γ) in units of $J/(m^2 K \sqrt{s})$ (also referred as TIU)

$$\Gamma = \sqrt{\rho c \kappa} \quad (2.4)$$

where c is the specific heat and ρ is the bulk mass density. The effect of the last term in Equation 2.3 has been neglected for all studies presented in Chapter 3, in which we assume thermal inertia does not to play a huge role in the distribution of H_2O sources around the nucleus. However, it will become very important in Chapter 4 and Chapter 5, where I will study the effect of thermal inertia in the distribution of H_2O and CO_2 -ice sources for a spherical nucleus comet, and for

comet's 67P/CG complex shape model.

Under thermodynamic equilibrium and assuming the back-scattered condensing flux is very small, dm_i/dt for a molecule of mass m is calculated using the Hertz-Knudsen equation

$$\frac{dm_i}{dt} = \frac{P_s}{\sqrt{2\pi m k_B T_i}} \quad (2.5)$$

where P_s is the sublimation pressure, k_B is the Boltzmann constant and T_i the temperature at the sublimation front. Assuming a half-Maxwellian velocity distribution, Equation 2.5 can be written in terms of the number density n_g with units of molecules/m³ at the surface

$$\frac{dm_i}{dt} = \frac{1}{4} n_g m v_g \quad (2.6)$$

where $v_g = \sqrt{8k_B T/\pi m}$ is the speed of the gas.

For sub-surface sublimation, the heat balance at a given sublimation front of depth z_{H_2O} and z_{CO_2} is given by

$$-\kappa \frac{dT}{dz} \Big|_{z_{H_2O}^-} = -\kappa \frac{dT}{dz} \Big|_{z_{H_2O}^+} + L_{H_2O} \frac{dm_{H_2O}}{dt} \Big|_{z_{H_2O}} \quad (2.7a)$$

$$-\kappa \frac{dT}{dz} \Big|_{z_{CO_2}^-} = -\kappa \frac{dT}{dz} \Big|_{z_{CO_2}^+} + L_{CO_2} \frac{dm_{CO_2}}{dt} \Big|_{z_{CO_2}} \quad (2.7b)$$

where z^- and z^+ indicate the side before and after the correspondent sublimating interface for each gas species, respectively, for which the temperature gradient is calculated. At the surface the balance equation is given by

$$\frac{S_\odot(1-A)}{r_h^2} \cos(\theta_i) = c\sigma T_{0,i}^4 + \kappa \frac{dT_i}{dz} \Big|_{z=0} \quad (2.8)$$

In this work we assume κ , ρ and c to be constant across any internal boundaries. This is a major simplification over the 1D analysis seen in e.g. Huebner et al. [2006], where these variable are temperature dependent. Furthermore, heat transport by gas and the effect of increased subsurface gas pressure are ignored. This allows us to compute results for all surfaces of 67P/CG at the cost of simplification of a complex problem. Approaches addressing this issue have been studied by Marboeuf et al. [2012]; Marboeuf and Schmitt [2014] and used by Herny et al. [submitted for publication]. But it is important to point out here that these models are 1-D and remain somewhat unsatisfactory when applied to Rosetta data.

In the coupled case, both equations (2.7a and 2.7b) are used simultaneously to calculate the temperature gradient. In the decoupled case, the code is run separately for each species with only one of the equations being used at a time. This approach is a modified version of the "standard thermal model" for slow-rotators [Lebofsky and Spencer, 1989; Festou et al., 2004; Huebner et al., 2006]. It calculates the insolation condition at a certain heliocentric distance for one point on the surface after N_{rot} nucleus rotations on its axis. We have determined that our model converges for $N_{rot}=20$. Thereby, one can estimate the diurnal change in temperature and mass loss rate from a

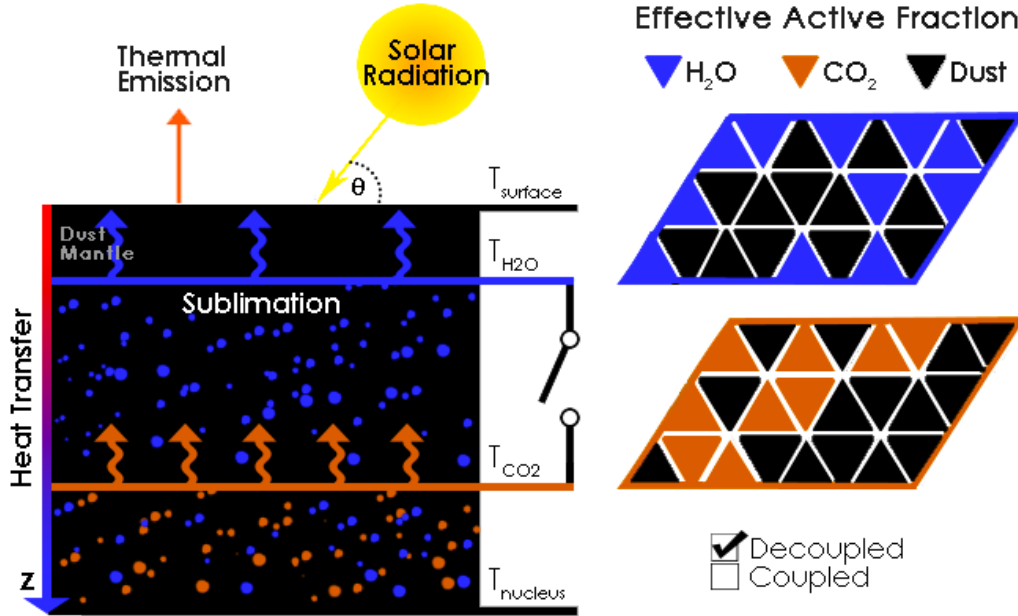


Figure 2.4: Sketch of the energy exchanges (heat sources and sinks) at the surface and sub-surface of a cometary nucleus. $T_{surface}$ is the temperature at the surface of the nucleus, T_{H_2O} and T_{CO_2} are the temperatures at the sublimation fronts for the respective type of ice, and $T_{nucleus}$ is the lower boundary temperature of the nucleus. The magnified boxes at the right represent the selected Effective Active Fractions used at the surface for each molecule. The coupling mode is represented as a switch in between the H_2O and CO_2 sublimation fronts.

sub-surface layer. This calculation is done for both molecules in decoupled (independent energy balance) and coupled (the two species influence each other) mode for which we define sublimation fronts at different depths as shown in Figure 2.4. The left panel of this Figure illustrates a possible distribution of H_2O , CO_2 and the non-volatile material within the nucleus, with the presence of a desiccated dust mantle at the surface. Sublimation fronts are shown at different depths (z_{H_2O} and z_{CO_2}) under the assumption that CO_2 is more depleted than H_2O close to the surface. The distinction between coupled and decoupled modes is very important, because the temperature distribution with depth can change significantly the sublimation rate dm_i/dt at the nucleus. Therefore, we need to compensate this effect by using an effective active fraction (EAF).

The sublimation rate is throttled by the presence of a desiccated surface layer, which reduces the energy input to the sub-surface sublimation front. It is important to note that we assume the desiccated layer does not provide resistance to the gas flow. The high porosity of the surface layers [Pätzold et al., 2016] provides some justification for small depths. The thermal skin depth

$$\delta = \sqrt{\frac{\kappa P}{\rho c \pi}} \quad (2.9)$$

where P is the rotation period of the nucleus. In most cases, δ is about 2cm, so that thermal

penetration is fairly limited in scale. If this resistance were to be incorporated, the gas production rate would probably not be dramatically altered, because the internal temperature would rise to compensate for the modified sublimation rate at the front. This should not make a qualitative difference to our results.

The lower boundary condition is set by fixing the internal temperature $T_{nucleus}$. Values of the ortho-to-para ratio suggest internal temperatures of between 30-50K [Bonev et al., 2007; Mumma and Charnley, 2011; Willacy et al., 2015; Shinnaka et al., 2016]. We have used $T_{nucleus} = 50\text{K}$, which sets a lower estimate for the heat transport within the nucleus.

2.2.4 Effective active fraction

A way to parametrize the complexity of the structure and composition within the cometary nuclei is to define an effective active fraction (EAF). This quantity is not only used to scale the total production rates coming from the comet, but also to define local inhomogeneities in its composition. The right side of Figure 2.4 is an interpretation of the EAF as a pattern of activity at the surface that is linked with the composition and activity of deeper layers of the nucleus. EAF is not implemented exactly as shown in the Figure 2.4, however, this illustration is used to display how each surface facet has an associated EAF for each species, which tell us what sides of the comet outgas more or less H_2O and CO_2 .

The sublimation rates of the species present at different depths are modulated by an EAF such that the global production rate is

$$Q_{gas} = \sum_i^{N_s} a_i \frac{dm_i}{dt} \cdot EAF_i \quad (2.10)$$

where a_i is the area per surface facet and N_s is the total number of facets. The sub-surface layer cannot be so deep that EAF exceeds 1, setting a natural limit on the depth of the sublimation front. In this way, the EAF can be interpreted either as the percentage of the surface area that is active or as the magnitude of the influence of sub-surface sublimation through a porous layer of relatively low thermal inertia [Skorov and Rickman, 1995; Skorov et al., 1999a, 2001, 2002b; Thomas, 2009].

2.3 Collision Model

The study of cometary atmospheres requires to describe the behaviour of a large number of gas molecules using a statistical approach. In highly diluted gases, the size of the molecules is much smaller than the distance between them. Therefore, it is possible to use some simplifications to calculate all possible interactions between them and estimate the average properties of the whole gas flow. In this Section, I shall give a small summary of the flow regimes in gas dynamics and the selection of Direct Simulation Monte Carlo to simulate cometary comae.

2.3.1 Overview of flow regimes in gas dynamics

In fluid dynamics, one classifies fluid regimes by using the so called *Knudsen number*

$$Kn = \frac{mfp}{L} \quad (2.11)$$

where mfp is the mean free path and L is the characteristic scale length of the flow. Depending on the selection of L , we talk of local or global Kn . If L is selected to be the mean size of the comet, for example, we are calculating a global Kn . However, if we take Δs to be the characteristic length of the system, then we have more detailed information of how Kn changes within the coma. Figure 2.5 shows the fluid classification according to the Kn value. The Knudsen number describes the level of rarefaction of a fluid. Gas flows with large densities have a very small Kn value, which typically go below 0.01. In this case, one can use a macroscopic model to describe the gas as a continuum. Euler (e.g. Knollenberg [1994]) or the Navier-Stokes equations (e.g. Crifo et al. [2002]) are a good choice for such flow regimes. However, when the density of the flow decreases, its rarefaction increases and therefore Kn becomes larger. In that case, the gas flow goes from the continuum to the slip-flow regime ($0.01 < Kn < 0.1$), and if the distance between gas particles becomes even larger, it goes farther to the transitional ($0.1 < Kn < 10$) and free-molecular flow regime ($Kn > 10$). Up to $Kn \sim 0.1$, Navier-Stokes is still considered to be valid. However, for even more rarefied gases one has to use microscopic models that study the inter-molecular interactions within the flow.

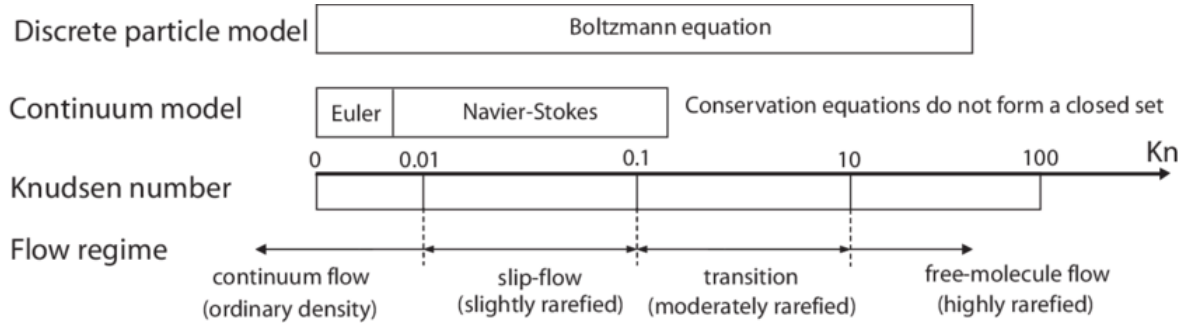


Figure 2.5: Flow regimes given the Knudsen number and the range in which mathematical models are valid. Credit: Yu [2004].

The Maxwell-Boltzmann distribution (M-BD) is the best mathematical description in the kinetic theory of gases for every flow regime. It recognizes the microscopic level of a gas, at the same time it provides information of the macroscopic properties of gas flow. The M-BD assumes a pure gas in thermal equilibrium and describes its evolution through a density function $F(\vec{x}, \vec{v}, \vec{t})$, such that for each every point at position x in the gas there are $F(x, v, t) dx dv$ particles moving with a velocity v . The Boltzmann equation can be written as a continuity equation

$$\partial_t F(x, v, t) + v \cdot \partial_x F(x, v, t) = Q(F, F) \quad (2.12)$$

where Q is a collision kernel [Caflisch, 1984; Masmoudi, 2007]. It is possible to find an analytical solution to this equation for a monoatomic gas with no internal degrees of freedom. However, when complexities arise, one has to deal with hyper-dimensional flow fields ($> 5D$) that has no easy solution. Therefore, numerical solutions of this equation are commonly used, which under certain assumptions are valid for the flow regime one wants to study. In this work, I use one of this practical tools that has been created in order to solve numerically the Boltzmann equation using probabilistic Monte Carlo simulations.

2.3.2 3D Direct Simulation Monte Carlo

In 1963, a new computational approach was developed by Professor Graeme Bird [Bird, 1963, 1994, 2005] in which the gases are simulated by studying their mechanical and chemical interactions. DSMC is a powerful method that allows us to use a molecular model to find a probabilistic solution to the Boltzmann equation for every flow regime from continuum to free molecular flow. The general idea was to simulate the motion of the particles in steps. In the first one, the code lets molecules (hereafter *simulated particles*) move freely into space. Then, collision partners are randomly selected. And finally, the code estimates how many collisions occurred after certain time step Δt . This process repeats multiple times until the amount of collisions stabilizes and one would be able to compute the average number density, temperature and speed of the flow. This method is very computationally demanding, but has been used for cometary studies in the past [Combi and Smyth, 1988a; Combi, 1988b; Crifo et al., 2002, 2003, 2005; Zakharov et al., 2009; Finklenburg and Thomas, 2014a; Finklenburg et al., 2014b; Liao et al., 2016, 2018; Marschall et al., 2016, 2019].

The DSMC method is applied to simulations of rarefied gases and solves the average properties of the gas flow around any type of 3D shape for given boundary conditions. In our study, this is particularly important as the gas field coming from the sublimation of ices at the surface of the nucleus encompasses different flow regimes. We use the ultra-fast Statistical PARTicle Simulation Package (ultraSPARTS), which is a C++ parallel DSMC code to simulate gas interactions in the coma developed by Professor Wu's group [Wu and Lian, 2003; Wu et al., 2004; Wu and Tseng, 2005]. Some of the computational simplifications and methods this code uses to reduce the computational time and improve the accuracy of the DSMC method are:

1. the statistical weighting is defined as

$$W = \frac{\text{number of real particles}}{\text{number of simulated molecules}} = \frac{N_{real}}{N_{sim}} \quad (2.13)$$

where $N_{sim} \ll N_{real}$ to make the sampling faster, but large enough ($N_{sim} \gg 1$) so it does not lead to a big statistical error in the computations. Therefore, one has to make sure that the N_{sim} per cell is between 20-30 for the results to be reliable and efficient.

2. an transient adaptive sub-cell scheme (TAS) that subdivides the cells into smaller segments depending on the number of collision partners at a local scale ($\Delta s \rightarrow \text{mfp}$). This approximation is chosen to make sure the code is not selecting collision pairs from the farther extremes of the cell.
3. a virtual mesh refinement method (VMR) in which the code re-arranges the mesh using an initial DSMC simulation [Su, 2013]. This means every model case needs two simulations.
4. a variable time-step scheme (VTS) to reduce the number of simulated particles necessary to get a small statistical uncertainty and the number of iterations towards steady state. The time step Δt has to be as small as possible to make the DSMC computations more accurate. In this way, gas particles move independently from each other and their collisions are decoupled over time intervals that are much smaller than their mean collision time (mct) [Wu et al., 2004]. In our case, we have selected an initial $\Delta t = 10^{-4}\text{s}$.
5. a dynamic load-balancing technique to distribute the calculations of parts of the simulation domain over different computer cores taking advantage of the unstructured mesh topology [Su, 2013].

An early version of this code has been used by Finklenburg and Thomas [2014a]; Finklenburg et al. [2014b] and Liao et al. [2016, 2018] to simulate gas dynamics from Tempel 1 and comet 67P/CG, respectively. An updated version of the code has been used by Marschall et al. [2019] and Gerig et al. [2020] to simulate gas and dust emissions from the nucleus of 67P/CG.

In the DSMC method the gas is represented by a state

$$X^n(t) = [\vec{r}_1, \vec{v}_1, \dots, \vec{r}_i, \vec{v}_i, \dots, \vec{r}_N, \vec{v}_N] \quad (2.14)$$

where n is the index of the time step, \vec{r}_i and \vec{v}_i are the time-dependent position and velocity of particle i , respectively, and $N = N_{sim}$. At every time step Δt (time loop), the equation of motion for a gas particle of mass m_i is given by

$$m_i \frac{d^2 \vec{v}_i}{dt^2} = \vec{F} \quad (2.15)$$

and the change from state $X^n \rightarrow X^{n+1}$ (or $X(t) \rightarrow X(t + \Delta t)$) is splitted in the following three stages [Bird, 1994; Volkov, 2011]:

1. **Collisionless motion** of simulated particles under the effect of external forces (F), pair interactions between particles, or interaction of particles with boundary surfaces, walls, etc. The solution of equation 2.15 is

$$\frac{d\vec{r}_i}{dt} = \vec{v}_i \quad (2.16a)$$

$$m_i \frac{d\vec{v}_i}{dt} = \vec{F} \quad (2.16b)$$

In case of free motion, the external force field is $F = 0$, such that the position in the new state is

$$r_i^* = r_i + v_i \Delta t \quad (2.17)$$

However, if $F \neq 0$, the code uses the Runge-Kutta method to solve numerically equation 2.15 such that

$$r_i = r_i + v_i \frac{\Delta t}{2} \quad (2.18a)$$

$$r_i^* = v_i + v_i \Delta t \quad (2.18b)$$

and

$$v_i = v_i + F(r_i) \frac{\Delta t}{2} \quad (2.19a)$$

$$v_i^* = v_i + F(r_i) \Delta t \quad (2.19b)$$

where v^* is the velocity in the new state X^* .

2. **Collision sampling.** In this stage, the code indexes gas particles according to which cell in the simulation domain they belong. At a time step, only collisions within the same cell are taken into account. Molecules are supposed to be homogeneously distributed inside each cell and collision partners are randomly selected. The probability of collision between particles i and j is

$$P_{ij} = \frac{\sigma_{ij} v_r \Delta t}{V_{cell}} \quad (2.20)$$

where $\sigma_{ij} = \sigma W$ is the collision cross-section of simulated molecules, $v_r = |v_j - v_i|$ is the relative velocity of particles i and j , and V_{cell} is the volume of the cell. For the calculation of particles after the collision, one has to take into account the conservation equations in the flow, such that the velocities of particles after collision are

$$v_i' = v_i + (\vec{v}_r \cdot \vec{n}) \vec{n} \quad (2.21a)$$

$$v_j' = v_j - (\vec{v}_r \cdot \vec{n}) \vec{n} \quad (2.21b)$$

where \vec{n} is the unity vector for a hard sphere (HS) shown in Figure 2.6, which in the code is generated using a random number generator. The HS model treats simulation particles as impenetrable spheres which do not overlap in space when colliding with each other. This however produces an isotropic scattering that is independent of the relative translational energy ($E_{Trans} = m_i v^2/2$) in the collision [Bird, 1994]. Therefore, we adopt the Variable Soft Sphere (VSS) model, which takes into account the distance d as a function of v_r (also used by the Variable Hard Sphere (VHS) model) plus the deflection angle

$$\chi = 2 \cos^{-1} \left(\frac{b}{d} \right)^{1/\alpha} \quad (2.22)$$

where b is the center of mass impact parameter and α is the viscosity coefficient for each chemical species.

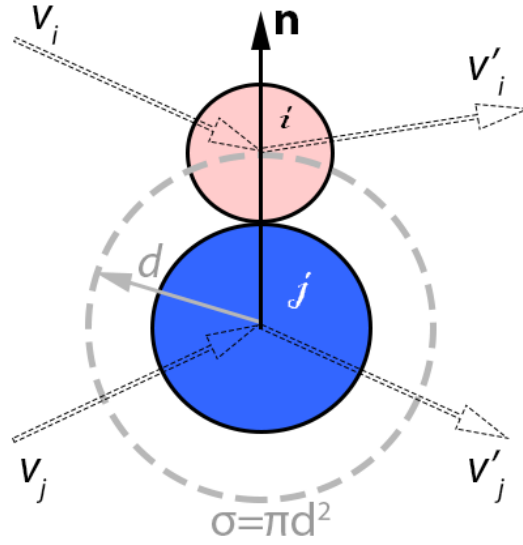


Figure 2.6: Collision between two simulation particles i and j assuming a hard sphere collision model. σ is the collision cross section and d is the distance between particles or the sum of the radii of each particle. Different colors are used to indicate a general case in which particles might or might not have the same chemical composition.

In order to simulate properly the non-equilibrium effects at the molecular level in a collisional flow, one needs to define the rate at which energy is exchanged between the translational and the rotational modes [Valentini et al., 2012]. This is a function of the average number of collisions per particle required to bring the system to equilibrium, also called rotational relaxation number, Z_{rot} . Typical values used for Z_{rot} are 1 [Crifo, 1989; Crifo et al., 2002; Liao et al., 2016] and 8 [Bird, 1994] for H_2O and CO_2 , respectively.

- 3. Implementations of boundary conditions.** In this stage, the code takes into account the interaction of the simulated particles with the boundaries and generates new particles in order to produce sublimation. The boundaries can be between different regions of the simulation domain or at an impermeable surface or wall where gas particles rebound using a Maxwell model of specular or diffusive scattering. In the second case, the reflected particles have a velocity distribution

$$f(v) = \frac{mn_g}{(2\pi k_B T)^{2/3}} \exp\left(-\frac{m(v-v_g)^2}{2k_B T}\right) \quad (2.23)$$

where m is the particle's mass, n_g is the number density, T is the gas temperature and v_g is the gas velocity.

This sequence of calculations is repeated multiple times until the flow reaches the steady state and the statistical uncertainty is small in the calculation.

2.4 Rosetta Instruments

Numerical models need to be compared to remote sensing data in order to corroborate the reliability of their results. Therefore, we have used data from three different instruments on board the Rosetta spacecraft: ROSINA, MIRO and VIRTIS-M. A small summary of their main characteristics is described in this section.

2.4.1 ROSINA

The objective of the Rosetta Orbiter Spectrometer for Ion and Neutral Analysis (ROSINA) was to study the composition of the gaseous part of the coma of comet 67P/CG. It consisted of three sensors:

- The comet pressure sensor (COPS) measured the local number densities of the neutral gas around comet 67P/CG with a maximum time resolution of 10 seconds [Tzou, 2017].
- The double focusing magnetic mass spectrometer (DFMS) measured the gas and ion relative abundances within the coma with a mass resolution greater than 3000 at 1% peak height [Balsiger et al., 2007]. DFMS measures masses sequentially, with typical time intervals for the same mass of around 50 minutes [Altwegg et al., 2017; Tzou, 2017].
- The reflectron time-of-flight (RTOF) which was used to increase the resolution of DFMS spectrometer by combining an extremely high mass resolution (> 500 at 1% peak height) with time resolution (< 10 kHz) at a single shot.

In the present work, only COPS and DFMS data will be used for our model comparison. The total abundance measured by COPS is a function of the sensitivity factors for different species normalized to molecular nitrogen N_2 [Gasc et al., 2017]. In this way, COPS number densities can be inferred from the DFMS values of the main volatile species in the coma as

$$n_{COPS} = \frac{n_{H_2O}}{0.893} + \frac{n_{CO_2}}{0.704} + \frac{n_{CO}}{0.952} + \frac{n_{O_2}}{0.990} \quad (2.24)$$

from which the background signal has been removed to obtain only the cometary signal for each measured species.

The analysis of the acquired ROSINA/DFMS data suggest that H_2O represents around 90% of the bulk composition, while CO_2 represents only about 5 - 8% [Rubin et al., 2019; Läuter et al., 2018; Combi et al., 2020; Hery et al., submitted for publication]. Therefore, we can scale COPS data to the H_2O abundance measured by DFMS at any given time and make a direct comparison with COPS data for cases with purely H_2O outgassing. DFMS data is used to estimate average number density mixing ratios shown in Figure 2.7 for certain time range and set the equivalent CO_2 global production rate Q_{CO_2} in our simulations.

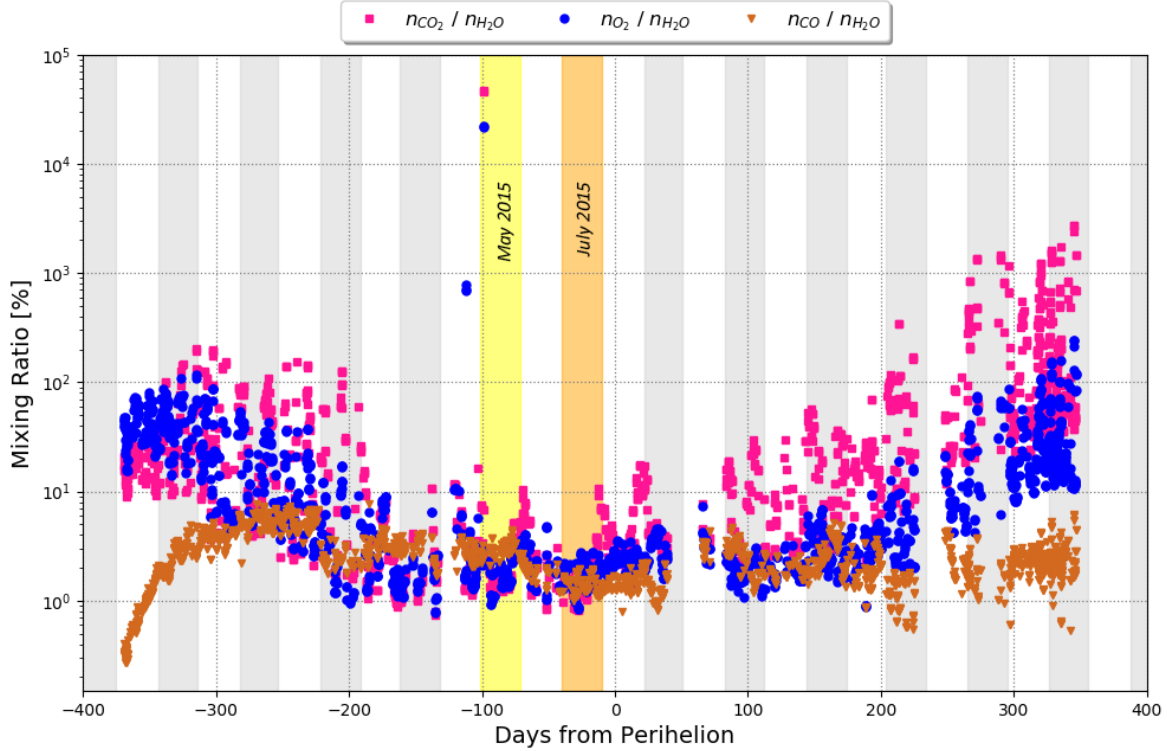


Figure 2.7: Percentage of the number density mixing ratios n_{CO_2}/n_{H_2O} (pink), n_{O_2}/n_{H_2O} (blue) and n_{CO}/n_{H_2O} (light brown) measured by ROSINA/DFMS for the whole mission. Only data with sub-solar longitudes equal to 0° , 90° , 180° and 270° are shown. The vertical area in yellow highlights data point in May 2015, while July 2015 is highlighted in orange. All other gray and white areas indicate each month from the beginning to the end of the mission.

2.4.2 MIRO

The Microwave Instrument for the Rosetta Orbiter (MIRO) worked at two center-band frequencies: 188 GHz (or 1.6mm) and 562 GHz (or 0.5 mm). The receiver in the first frequency provides band continuum data only, while the receiver in the second frequency provides both broad band continuum and high resolution spectroscopic data [ESA]. The instrument's field of view (FOV) is a circle centered around the boresight vector with an angular resolution of 23.8 arcmin and 7.5 arcmin for the mm receiver and sub-mm receiver, respectively [Gulkis et al., 2007].

MIRO could measure the abundances of CO, CH₃OH, NH₃ as well as the abundance of three, oxygen-related isotopologues of water, H₂¹⁶O, H₂¹⁷O and H₂¹⁸O [Gulkis et al., 2007]. It measured the photons emitted from the rotational transition (change in angular momentum) of each molecule species. MIRO aimed to retrieve information of the surface outgassing rates, subsurface temperatures and the kinematic velocity of these species along the FOV.

Figure 2.8 illustrates the observation geometry of MIRO's beam. *At limb* observations indicate that no part of the beam pattern intersects the nucleus, while *at nadir* observations indicate

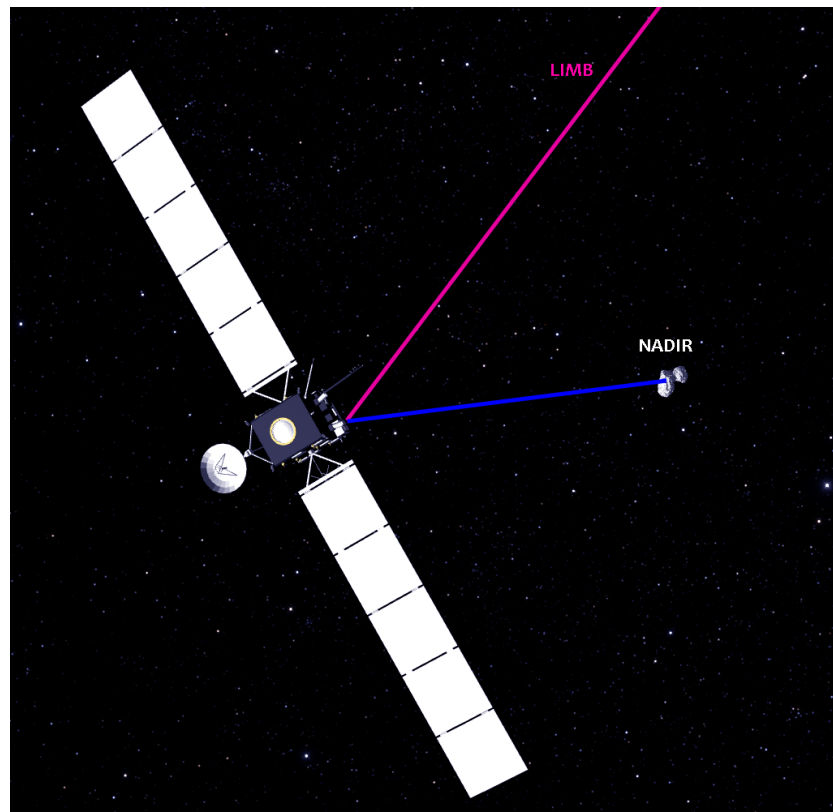


Figure 2.8: MIRO's field of view.

that no part of the beam is looking into empty space. We have only selected MIRO observations pointing at nadir to infer some of the thermophysical properties of the comet 67P/CG nucleus.

2.4.3 VIRTIS

The Visible and InfraRed Thermal Imaging Spectrometer (VIRTIS) was an instrument that used IR spectroscopy to study different gas emissions around the nucleus of comet 67P/CG from the UV to the infrared. Unlike MIRO, VIRTIS observed the vibrational transitions of the molecules, which are excited by solar light absorption. VIRTIS was a combination of two channels:

- **VIRTIS-M** - An imager spectrometer that worked between the 0.25 to 5 μm [Coradini et al., 2007]. It has a spectral resolution $\lambda/\Delta\lambda$ between 100 to 380 in the visible and between 70 to 360 in the infrared. VIRTIS-M has a rectangular FOV (hereafter name "cube") equal to 64 mrad (slit) x 64 mrad (scan).
- **VIRTIS-H** - A high resolution spectrometer that worked between the 2.03 to 5.03 μm . It has a spectral resolution $\lambda/\Delta\lambda$ between 1300 and 3000 and a FOV equal to 0.583 mrad x 1.749 mrad.

VIRTIS data have been used to show that the comet surface is very rich in organic material with no hydrated minerals [Capaccioni et al., 2015; Quirico et al., 2016]. Bockelée-Morvan et al. [2015] have used VIRTIS to produce H₂O and CO₂ maps of the inner coma of 67P/CG at 1.8–2.2 AU pre-perihelion, which shows a strong dichotomy between their emissions. Marschall et al. [2019] use DSMC results to produce synthetic H₂O column density maps that are directly compared to VIRTIS-M-IR data and from which localized H₂O emissions were observed. This work uses cubes from VIRTIS-M-IR, which scanned H₂O and CO₂ emissions in the proximity of the comet. These cubes were produced by David Kappel at DLR using a continuum subtraction and emission band integration procedure [Migliorini et al., 2016]. Additional pre-processing of the H₂O and CO₂ cubes included a median filter and subsequent binning of 2x2 pixels in order to increase the signal-to-noise ratio [Marschall et al., 2019]. Bright features in VIRTIS-M cubes can be used to track CO₂ sources in the nucleus and constrain our model parameters selection of local EAFs, which will be explained in Appendix B.

2.5 Model comparison approach

Depending on the type of data we want to analyse, different approaches to compare the model to the data need to be used. Therefore, in this section, I will summarize the techniques used to extract the information from our simulation domain and interpolate their results to compare them directly with *in situ* measurements of comet 67P/CG.

2.5.1 Extraction of local number densities from the model results

I have used the same approach described by Marschall et al. [2016, 2017, 2019] in order to get the modeled number densities at the spacecraft position for different viewing geometries and compare it with ROSINA measurements. In a first step, I use SPICE [Acton, 1996; Acton et al., 2017] to calculate the position of the spacecraft with respect to the comet-fixed frame for each of the ROSINA data points. In order to simulate the nucleus rotations at certain time, I need to run DSMC simulations for at least 4 sub-solar longitudes (ϕ_{\odot}). For ROSINA comparison, I have normally worked with ϕ_{\odot} equal to 0°, 90°, 180° and 270° in our nucleus coordinate system (section 2.2.1). In this way, I select the ROSINA data points that have the same sub-solar geometry as the ones I simulated, and estimate which is the closest cell in the simulation domain to the spacecraft position, as it is shown in Figure 2.9. From this cell, I extract the number density n_c and calculate the value of the number density at the spacecraft position as

$$n_g(r) = n_c \left(\frac{10 \text{ km}}{r_{sp}} \right)^2 \quad (2.25)$$

As illumination conditions at the nucleus change quickly with time, I needed to select a time range in which my model is valid. This range is selected between the 5 days before and

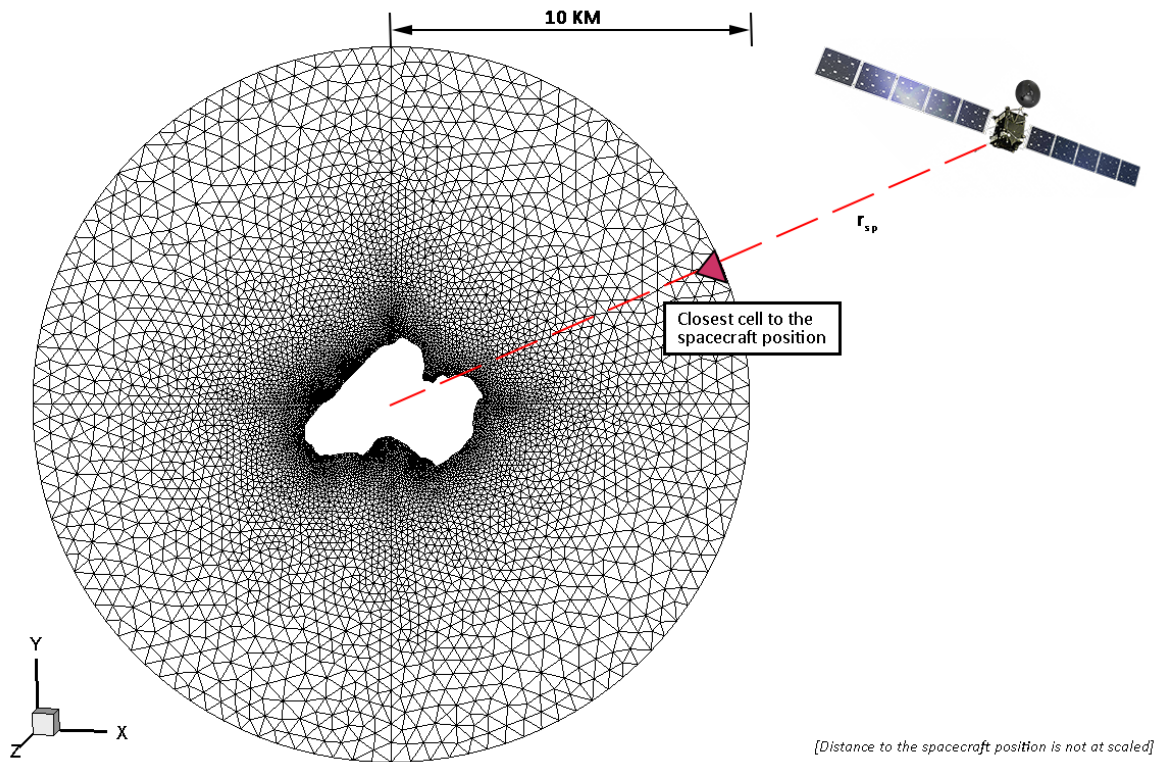


Figure 2.9: Sketch of the procedure to extract average gas properties from the closest cell inside our DSMC simulation domain to the spacecraft position r_{sp} .

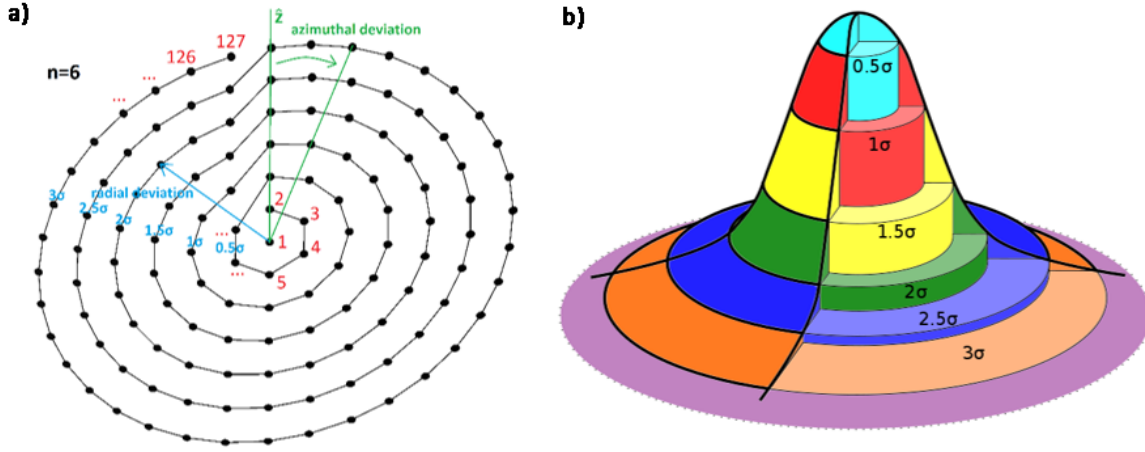
after the targeted date for the DSMC calculations, in which one can compare directly n_g with ROSINA/COPS and ROSINA/DFMS data.

2.5.2 Calculation of multi-beam profiles along the line of sight of MIRO

For MIRO Comparisons, the first thing to do is to select a set of measurements around the targeted time, in which MIRO observes different parts of the nucleus. For each of these times, I use SPICE kernels to calculate the spacecraft position r_{sp} and the boresight vector \vec{b} of MIRO's sub-mm channel in the comet-fixed frame. For MIRO comparisons I need to make sure that the illuminations conditions of the model and the measurements are the same. In this case, I need one DSMC simulation with the correspondent sub-solar point for each of the sampled times.

Once r_{sp} and \vec{b} are known, the second step is to extract the information of number density, velocity and temperature from the cells in the outer boundary of the simulation domain that (i) lay along the FOV and (ii) are the closest to the spacecraft position. Then, we perform a linear interpolation along MIRO's FOV which can extend up to a distance of 1000 km from the center of the comet [Marschall, 2017]. The approach is similar to the one described in Section 2.5.1, but in this case, it depends on MIRO's pointing geometry (Figure 2.8). When pointing at nadir, the

code collects all information starting from the spacecraft position in the direction of \vec{b} until it reaches a surface facet, in which case, the code stops collecting data along the FOV. However, when pointing at the limb, the code is never meeting a surface facet, and therefore, it continues to collect data until it reaches the limit of our extrapolation space at 1000 km. In the current work, we have only worked with MIRO observations pointing at nadir.



Credit: S.-B. Gerig

Figure 2.10: Definition of the multi-beam profiles inside MIRO's FOV. a) Illustrates the number of samples inside the beam. They are set by defining an initial number of points inside the inner circle $n = 6$, so that the total number of samples is 127. b) Visualization of the beam as a 2D Gaussian.

MIRO's circular beam has a central profile around \vec{b} from which one can extract the average gas properties of the flow. However, there are contributions from multiple profiles inside the beam that must be taken into account. Therefore, we have used a 2-D Gaussian function

$$G(x, y, \sigma) = \frac{1}{2\pi\sigma^2} \exp\left\{-\frac{x^2 + y^2}{2\sigma^2}\right\} \quad (2.26)$$

truncated to three standard deviations (σ) [Sathyamoorthy and Palanikumar, 2006] in order to model MIRO's beam. The standard deviation is given in terms of the full width at half maximum (FWHM)

$$\sigma = \frac{\text{FWHM}}{2\sqrt{2\log 2}} \quad (2.27)$$

This has been done by defining 6 circles with radial deviation that increase by 0.5σ from the central beam, as shown in Figure 2.10. Figure 2.10a illustrates the selection of all samples inside the beam from $1 < j < 127$. For the 0.5σ -circle, the number of samples is fixed to $j = 6$; it increase as $\Delta j = 6 \times k$ for larger radial deviations, where k is used to indicate the circle's index from 1 to 6. All 127 profiles have been interpolated in such a way that their values are calculated at the same spacecraft position as the central profile. A 3-D view of the beam as a 2D Gaussian distribution

is illustrated in Figure 2.10b, from which we can have an idea of how the contribution of each σ circle decreases with its distance from the central beam. Therefore, we need to calculate their weighted contribution (w_k) to get the average number density

$$\bar{n}_j = \sum_k n_{jk} \cdot w_k, \quad (2.28)$$

speed

$$\bar{v}_j = - \frac{\sum_k n_{jk} \cdot w_k \cdot v_{ij}}{\sum_k n_{jk} \cdot w_k}, \quad (2.29)$$

and temperature

$$\bar{T}_j = \frac{\sum_k n_{jk} \cdot w_k \cdot T_{ij}}{\sum_k n_{jk} \cdot w_k}, \quad (2.30)$$

along the FOV. These averaged beam profiles are used as input for the radial transfer calculation explained in Section 2.5.3. The first version of this code has been created by Raphael Marschall. And the updated calculation with multiple lines inside MIRO's beam has been developed by Selina-Barbara Gerig.

2.5.3 Radiative Transfer calculation

We are able to see objects thanks to their interaction with light. In the case of remote sensing data from MIRO, the same universal principle applies. In the current study, solar radiation is the only energy source. Other effects like electron impact excitation or exothermic chemical reactions are considered negligible in the inner most part of the coma [Thomas, in press]. When solar light interacts with comet 67P/CG, it can be absorbed or emitted by the gas in the coma. However, MIRO will only observe the emission from the rotational transition of molecules that are traveling in the direction of its detector. This is described by the radiative transfer equation

$$dI_\nu = -n_g \sigma_{ext} (I_\nu - J_\nu) ds = -\kappa_{ext} (I_\nu - J_\nu) ds \quad (2.31)$$

where dI_ν is the change of intensity (sometimes also called *radiance*) at a specific frequency ν along a distance ds ; $n_g \sigma_{ext}$ is the product of the gas number density with the extinction cross-section, which can be written as the extinction coefficient κ_{ext} (in units of molecules/m); and finally J_ν is the source function measured in the intensity units of $\text{W m}^{-2} \text{sr}^{-1} \text{Hz}^{-1}$ [Chamberlain, 1978]. J_ν includes complexities related to thermal emission from the gas along the beam [Heng, 2017] as well as non-thermal effects within the molecules. For a purely absorbing source, which in this case is assumed to be the comet nucleus, one neglects emission and scattering into the beam ($J_\nu=0$), such that the solution of equation 2.31 is the Lambert's exponential absorption law

$$I_\nu(s) = I_{\nu,0} e^{-\kappa_{ext} ds} \quad (2.32)$$

where $I_{\nu,0}$ is the the initial intensity in a frequency interval at the end of the line of sight. However, our source of emission includes scattering, therefore we need to include J_ν for a more

general approach. We consider the gas flux in the inner-coma to be in local thermal equilibrium (LTE), such that J_ν can be written in terms of the frequency-dependent Planck's function

$$J_\nu = B_\nu(T) \quad (2.33)$$

For polar molecules such as H_2O , one can measure absorption and emission lines in the sub-mm wavelength, which allow us to write $B_\nu(T)$ in terms of the Rayleigh-Jeans distribution such that

$$J_\nu = \frac{2\nu^2 k_B T}{c^2} \quad (2.34)$$

where c is the speed of light, k_B is the Boltzmann constant and T is the temperature of the source. For sub-mm lines the natural broadening is negligible, such that how broad these lines are will mainly depend on the density, temperature and velocity of the gas in the coma. Gas molecules moving at certain velocity along the FOV produce a Doppler-shift. Therefore, κ_{ext} can be written as a function of a shift in frequency

$$\kappa_{ext}(\nu) = \frac{S_s}{\Delta\nu_D \sqrt{\pi}} \exp\left\{-\frac{(\nu - \nu_0)^2}{(\Delta\nu_D)^2}\right\} \quad (2.35)$$

where S_s is the spectral line intensity, ν_0 is the frequency in the rest frame and $\Delta\nu_D$ is the Doppler width, which is the standard deviation of the Gaussian distribution used to describe the gas velocity along the FOV

$$\Delta\nu_D = \frac{\nu_0}{c} \sqrt{\frac{2k_B T}{m}} = \frac{\nu_0}{c} v_{th} \quad (2.36)$$

where v_{th} is the most probable speed of motion in the direction of the beam, also called thermal velocity. In this case, the Doppler width can be expressed in terms of MIRO's FWHM [Gulakis et al., 2007]

$$\Delta\nu_D = 7.15\nu_0 \sqrt{T/m} 10^{-7} \text{ Hz} \quad (2.37)$$

Therefore, one can find a solution for Eq. 2.31 (fully derived in Chamberlain [1978]), which has the following form

$$I(s) = I_0 e^{-\tau_\nu(s,0)} + \int_0^s J(s') e^{-\tau_\nu(s,s')} \kappa_{ext} ds' \quad (2.38)$$

in which the first term to the right refers to the background emissions and the *optical thickness* from a point s to s' along the FOV is

$$\tau_\nu(s, s') = \int_s^{s'} \kappa_{ext} ds \quad (2.39)$$

The study of the relative abundances of the isotopologues H_2^{16}O , H_2^{17}O and H_2^{18}O is more convenient when analysing MIRO measurements. Even though H_2^{16}O is optically thicker than the other two isotopologues, the present work will only study H_2^{16}O absorption lines as an initial step for the MIRO comparison. The analysis of H_2^{17}O and H_2^{18}O lines is reserved for future work. With this in mind, we use the previous approximations to calculate 1) the absorption spectra measured

by MIRO when looking at nadir, and 2) the radiance along the FOV of our DSMC results, which will be presented in Section 5.3.2.

Some pre-perihelion cases ($r_h \approx 1.31\text{AU}$) have been studied under conditions of non-LTE. This was done in collaboration with Ladislav Rezac and Paul Hartogh from the Max-Planck Institut for Solar System Research (MPS), whose code has been used in the past by Rezac, L. et al. [2019]; Marschall et al. [2019]; Zhao et al. [2019]. For these studies, however, no thermal inertia cases were used, which resulted in larger Doppler shifts in temperature as it will be presented in Section 3.3.2.

2.5.4 Column density integration for artificial IR-images

Comparison with VIRTIS-M cubes require the same approach explained in Section 2.5.2. In this case, however, we need to perform an integration along the FOV in order to obtain a 2-dimensional array similar to the FOV of VIRTIS-M. Our artificial IR-images are made of integrated column densities for H_2O and CO_2 gas along FOV which are calculated as

$$n_l = \sum_i n_g(x, y, z) \Delta l \quad (2.40)$$

where n_g is the gas number density for one single species at certain point in 3D space and Δl is the integration step such that $\sum_i \Delta l = D_c + 1000\text{km}$ [Marschall et al., 2016], with D_c being the distance from VIRTIS-M sensor to the center of the FOV, as it is shown in Figure 2.11. The code not only integrates points from the spacecraft to the comet's position, but it goes up to 1000 km behind the nucleus in order to integrate the contribution from the background gas.

Once this is done, we need to calculate the shadowing effect on the nightside of the nucleus. This is done by calculating the solar zenith angle (SZA) shown in Figure 2.12 for every cube geometry from which we estimate which facets inside the simulation domain are not directly illuminated by solar light. This is used to create a mask that is multiplied with the previous column density calculation, where non-illuminated facets are multiplied by zero and illuminated facets are multiplied by 1. This is very important since emission from the nucleus can only be observed when photons interact with the gas particles in the coma by absorption, emission, or reflection. Results from the current procedure will be presented in Section 5.3.3, where cases with multiple gas species in the coma have been simulated for times before the Spring equinox.

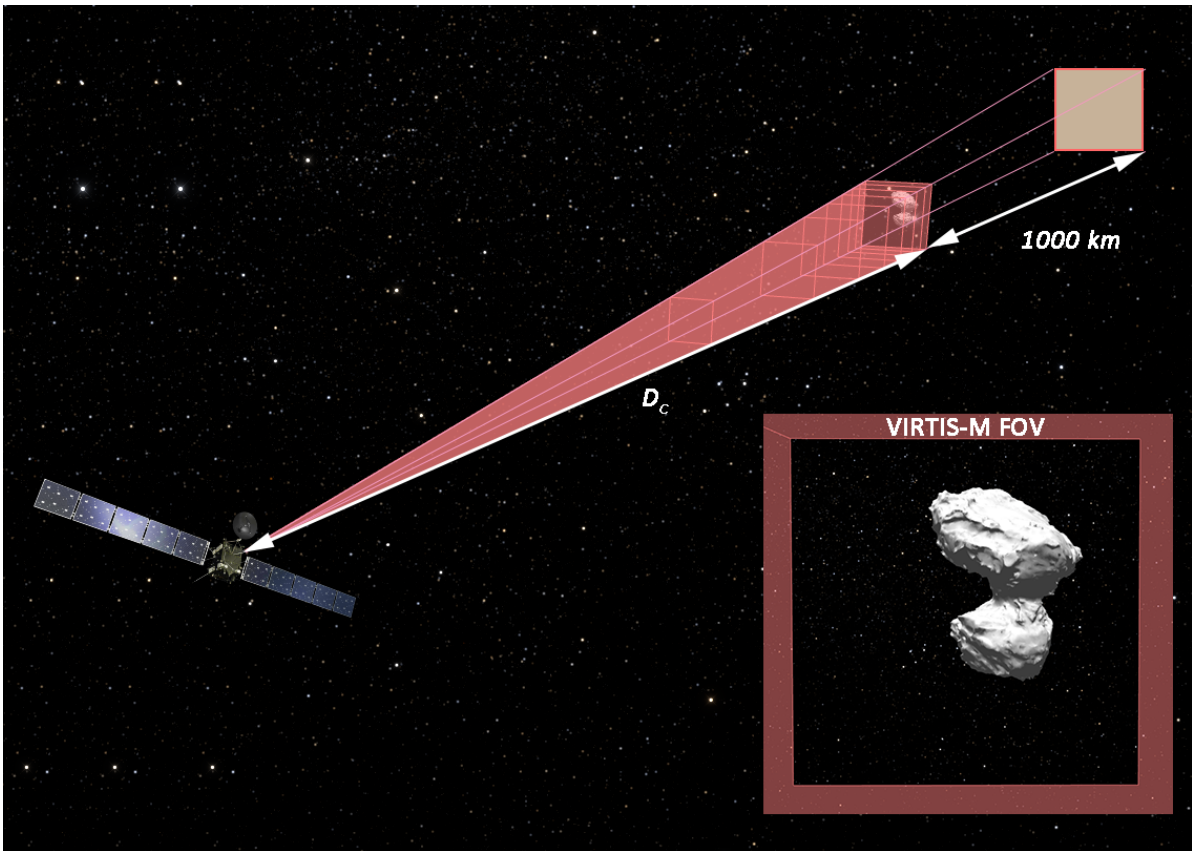


Figure 2.11: Viewing geometry of VIRTIS-M, indicating the parameters used for the column integration.

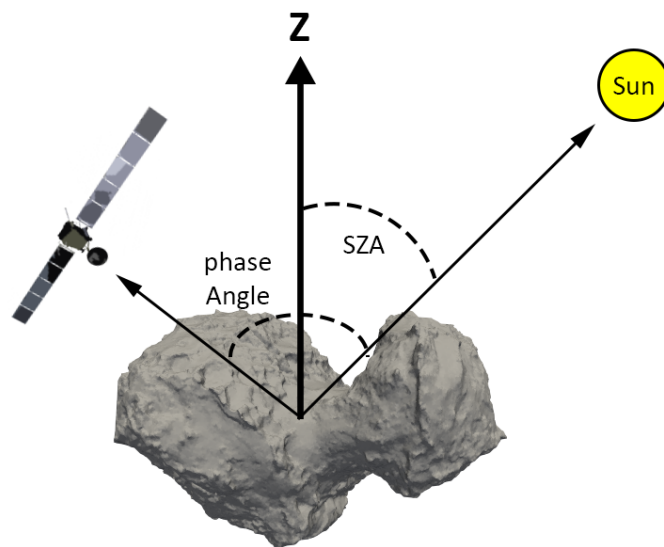


Figure 2.12: Solar Zenith Angle (SZA) and phase angle.

Basic studies on gas dynamics

The first step before studying the gas dynamics in cometary nuclei has to be as simple as possible. Therefore, the current chapter is structured as follows. The first part of the chapter contains studies related to gas sublimation from a spherical and homogeneously distributed source of ice. I will present simulation results for the outgassing of H₂O and CO₂ as single species and as gas mixtures. In the last section of this first part, I will present some studies regarding the generation of H₂O plumes with different EAFs, which have been used by Selina-Barbara Gerig to study the generation of dust jets in cometary nuclei.

In the second part of this chapter, I will apply similar studies to the complex shape model of comet 67P/CG for cases that neglect thermal inertia effects. Here, I will also use a homogeneous distribution of ice-sources at the nucleus, before exploring the possibility of inhomogeneous ice sources that could explain some of the measurements taken by ROSINA, MIRO and VIRTIS-M.

3.1 Spherical Nucleus

In a first step, I study the outgassing from a spherical nucleus with a 2 km radius, that has approximately the same $51.7 \pm 0.1 \text{ km}^2$ surface area that the comet's shape model [Preusker et al., 2017]. A spherical nucleus is used to eliminate the effects associated with the nucleus shape and possible differences created by topography. A homogeneous distribution of ice sources can have different outgassing distributions. At the beginning, we assume a uniform outgassing from a fully illuminated surface. Later, we include illumination differences that trigger some surface areas to be more active than others.

3.1.1 Uniform outgassing of H₂O and CO₂

I have set DSMC simulations for an uniform H₂O and CO₂ outgassing separately with three different global production rates Q_g : 1×10^{26} molecules/s, 1×10^{27} molecules/s and 1×10^{28} molecules/s.

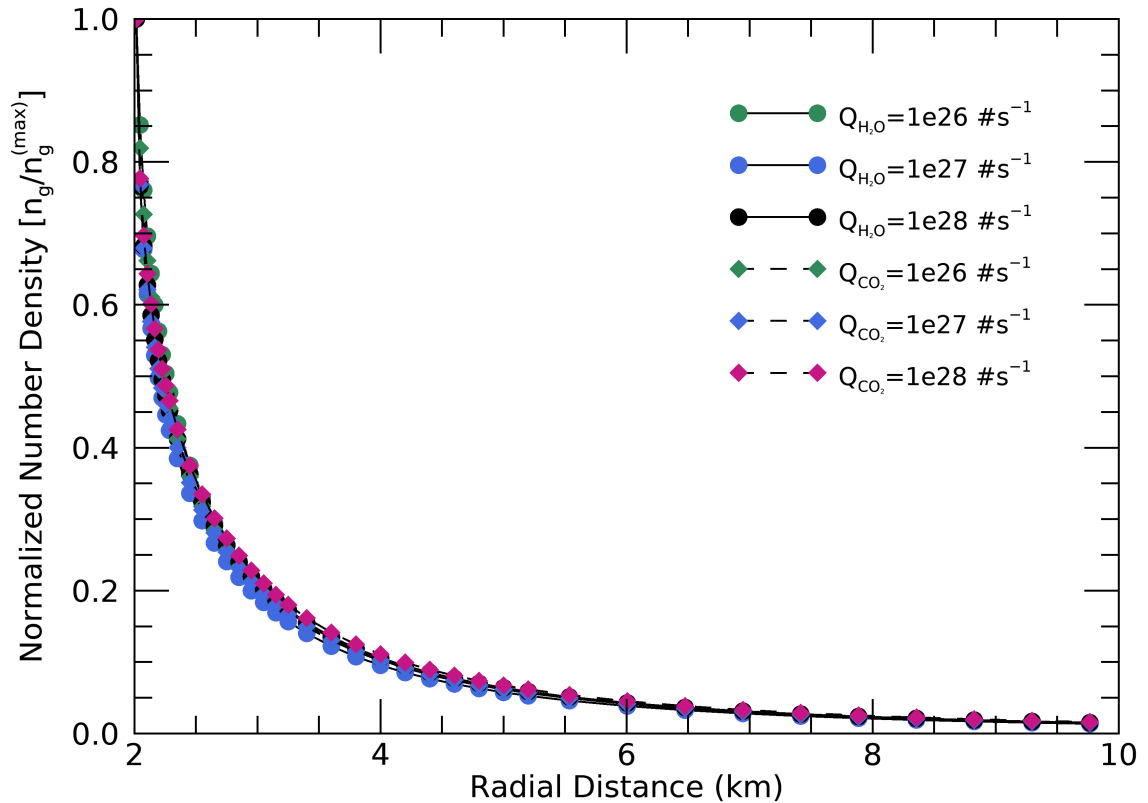


Figure 3.1: Change with distance from the nucleus of the normalized number density n_g to its maximum value $n_g^{(max)}$ for all the tested cases. The radial distance refers to the distance from the center of the nucleus, so 2km distance refers to the location of the surface.

In this manner, I can detect differences in the average properties of the flow given the amount and type of molecule used. Since I work with 3D DSMC simulations, I need to extract the change of the average number densities, velocities and temperatures of the flows with distance from the nucleus. Therefore, for these cases I have calculated their mean values within 40 shells with increasing radius from 2.015 to 9.765 km.

Figure 3.1 shows the change of the normalized number density ($n_g/n_g^{(max)}$) with distance for all the tested cases. From this figure one can see a very similar decrease of $n_g/n_g^{(max)}$ which resembles a $(10\text{km}/r)^2$ function independently of the molecule type used. There seems to be a very small effect that decreases the slope of the curve in the first 5 km for large production rates (1×10^{28} molecules/s) of CO_2 , but it does not seem to be significant enough.

In a cometary coma the pressure decreases with distance from the nucleus. The gas experiences an adiabatic expansion, because it needs to transform internal energy into work in order to move, which decreases quickly the gas temperature with distance. At the same time, the gas expanding outwards experiences an acceleration due to a pressure gradient between the inner

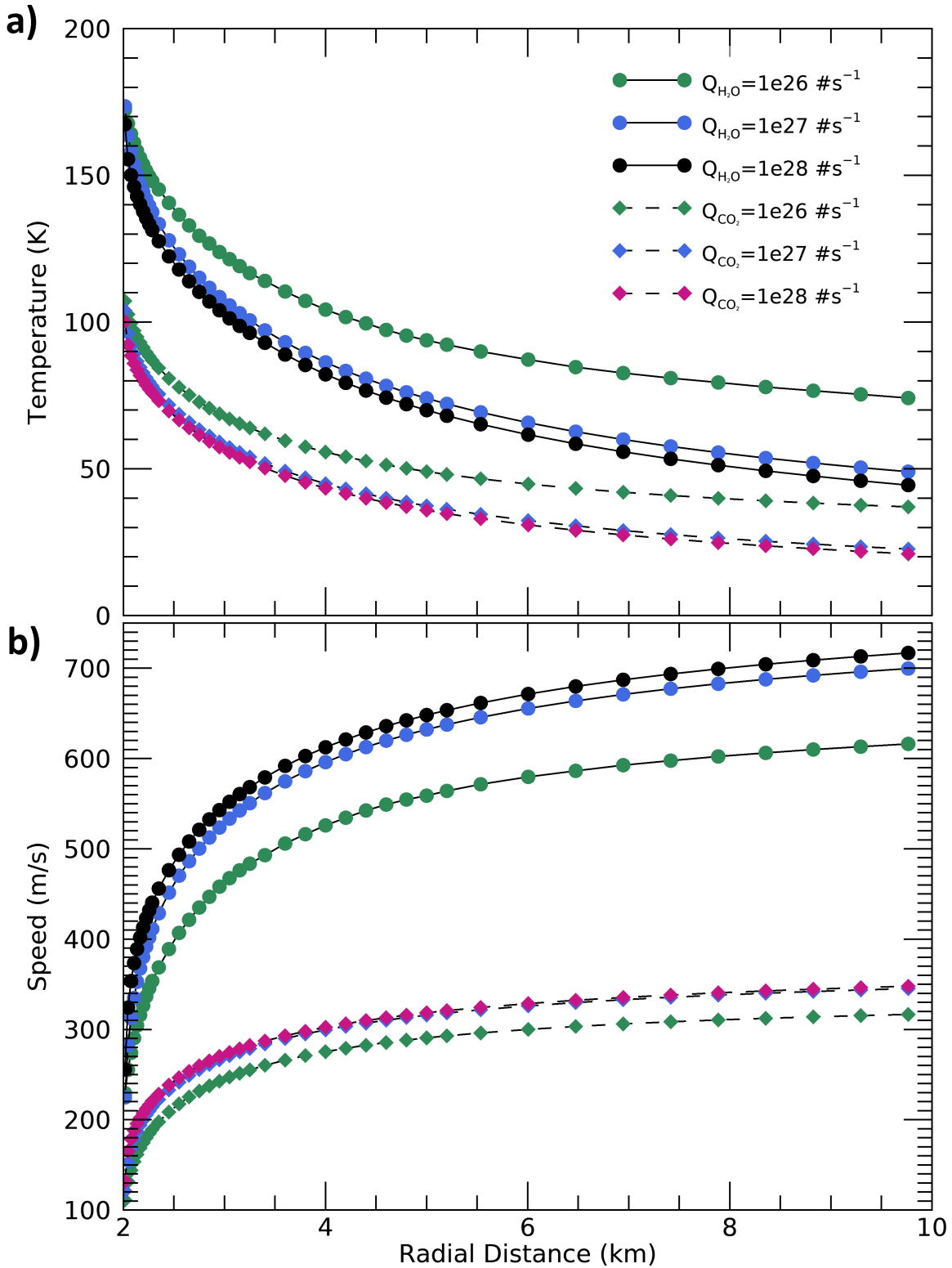


Figure 3.2: Average temperature (a) and speed (b) of the uniform emission cases. The radial distance refers to the distance from the center of the nucleus, so 2km distance refers to the location of the surface.

and the outer part of the coma and to inter-molecular collisions. This behaviour can be seen in Figure 3.2, which shows the model results of the temperature and speed of the flows at different distances from the nucleus. Figure 3.2a indicates large differences between the H₂O and CO₂ gases due mainly to the difference in their sublimation temperatures, which have been set to 200K and 130K, respectively. H₂O gas seems to have a steeper decrease in temperature with distance compared to CO₂ gas, specially for the two largest Q_g . This small difference in slope can be caused by the ability of CO₂ to retain more internal energy compared to H₂O, given that CO₂, being a linear molecules, has one rotational degree of freedom less than H₂O. We can also notice in Figure 3.2a that the lowest Q_g for both molecules has the smallest relative decrease in temperature with distance. In this case, it is connected to the amount of collisions in the flow. A low Q_g means a lower gas density and, therefore, the energy transfer between molecules is less effective, which also make the gas flow in this case slower, as can be seen in Figure 3.2b. Intermediate and large production rates are significantly better at transforming the energy between the translational and the rotational states. In the case of the speed, we see that H₂O gas can reach speeds of approximately 610m/s and 720m/s, for the largest and lowest Q_g , respectively. While CO₂ has maximum speed values of approximately 350m/s and 315m/s also for the lowest and largest Q_g , respectively. The fact that the difference between the intermediate to the larger Q_g is smaller than the difference between the smallest to the intermediate Q_g for both molecules could indicate that there is a limited amount of energy that can be transferred through collisions alone in order to produce larger accelerations in the flow at large distances.

One can also calculate the ratio between the rotational to the translational temperature of the flow (T_{rot}/T_{trans}) in order to get the indicator of non-equilibrium shown in Figure 3.3. Cases in LTE should have a $T_{rot}/T_{trans} \approx 1$, while a larger ratio indicates that there are not enough collisions to transform energy from the rotational to the translational state. This is the case of low production rates of H₂O and CO₂, where CO₂ seems to transfer energy less effectively than H₂O. For larger production rates the T_{rot}/T_{trans} tends to 1 and the difference between H₂O and CO₂ becomes small.

An uniform outgassing is clearly not a realistic scenario because it would require the whole surface of the sphere to be equally illuminated, which in the case of comets does not seem to be plausible. However, uniform outgassing has given us a fundamental idea of the adiabatic expansion of gas in cometary comae and the behaviour of the flow depending the type of molecule and the simulated global production rate used.

3.1.2 Insolation-Driven Outgassing and Cometary Plumes

A second level of complexity that includes the illumination geometry on the nucleus needs to be applied to study more realistic cases. Therefore, in the current section, I study a so called "purely insolation-driven" case in which a homogeneous H₂O-ice composition is set by using a constant EAF all over the surface, but setting a sub-solar geometry such that solar light meets every

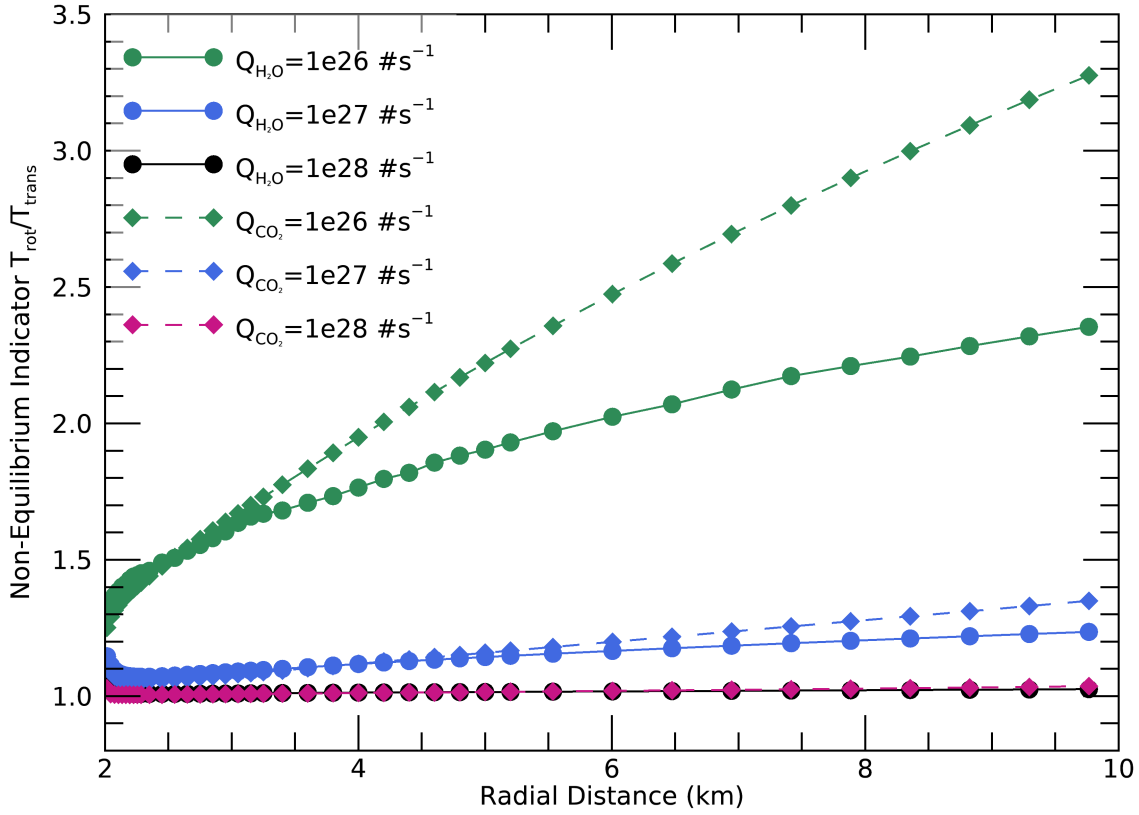


Figure 3.3: Ratio between the rotational temperature T_{rot} and the translational temperature T_{trans} . The radial distance refers to the distance from the center of the nucleus, so 2km distance refers to the location of the surface.

surface facet with a different incidence angle θ_i . This changes the temperature and production rate at the surface, which strong respond to insolation, and defines the dayside outgassing of the comet.

Case	EAF _{JET} (%)	Q_{TOT} (kg/s)	Q_{JET} (kg/s)	Surface type
1x	1	27.94	0.04	100% diffuse reflection
10x	10	28.26	0.36	100% diffuse reflection
100x	100	31.54	3.64	100% diffuse reflection

Table 3.1: Purely insolation-driven cases with cometary plumes.

Additional to this, I have performed a set of cases in which I study the effect of focused outgassing by a H₂O plume with different production rates, which are listed in Table 3.1. The outgassing source is again an spherical nucleus above which a plume with an area of 1.5×10^4 m² and a solid angle of $\Omega_{jet} = 3.83 \times 10^{-3}$ sr has been defined. The outgassing is purely driven by illumination, such that the the energy balance of equation 2.3 is used, but we neglect the thermal

conductivity term. The upper row of Figure 3.4 shows the distribution of ice sources for all tested cases. EAF is equal to 1% all over the surface, except in the plume, where I vary the EAF in order to set larger local production rates. The plume has been located at the sub-solar point in the +z direction and its EAF has been increase by one order or magnitude from case **1x** to **100x**. The bottom row of Figure 3.4 also shows the ice temperature on the surface of the sphere. There one can see that the temperature is maximum 200K at the sub-solar point, it drops very quickly close to the terminator, and it is set equal to 100K on the nightside of the sphere. Since these cases are simulating H₂O outgassing, we do not expect to get any activity from the nightside.

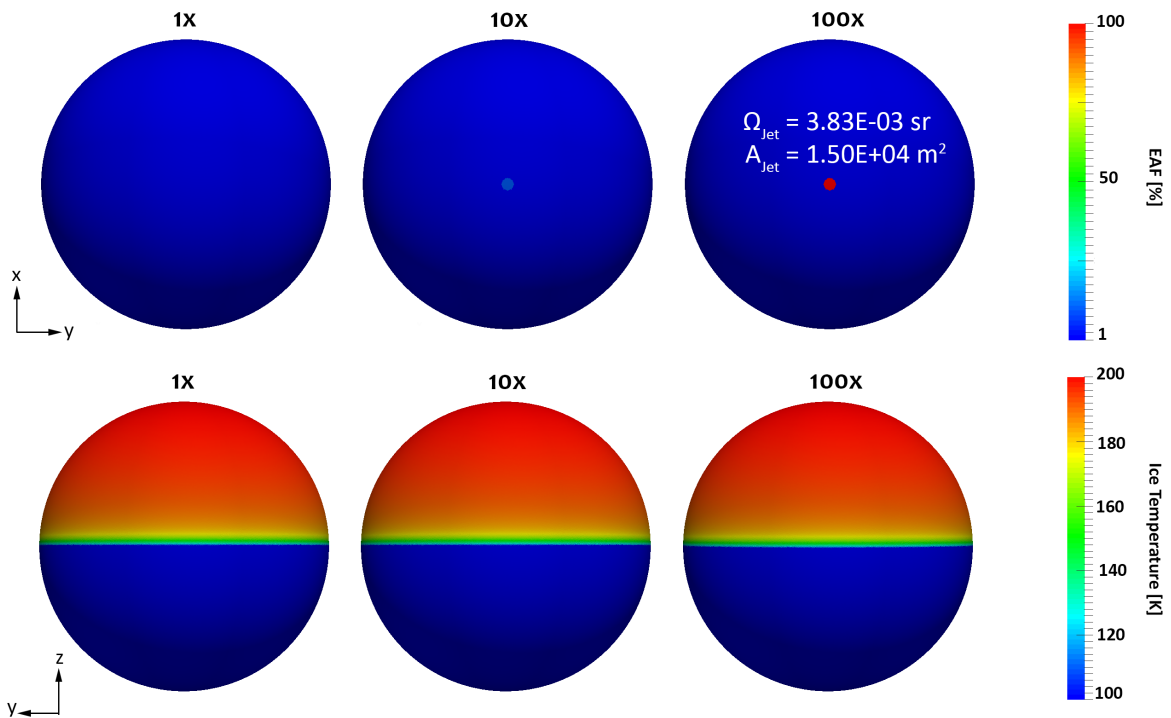


Figure 3.4: Boundary Conditions for a jet with different outgassing strengths. The upper row shows the EAF, while the lower panel shows the ice temperature at the surface.

DSMC results of these cases are shown in Figure 3.5, where we get information of the number density, temperature, speed and T_{rot}/T_{trans} of the gas flow on the yz-plane. Row (a) of Figure 3.5 is case 1x, (b) is case 10x and (c) is case 100x. In terms of number density, we see that the purely insolation-driven case 1x has its maximum density in the +z direction, where the sub-solar point has been set. As expected, the number density decreases with the distance from the nucleus and as one gets closer to the nightside, it becomes very small compared to the dayside. By including a plume 10 times stronger than the surrounding environment, we can see that the flow behaviour is changed significantly above the plume and relatively close to the nucleus up to a distance of ~ 6 km. At larger distances from the nucleus we cannot distinguish any differences in this figure. The difference becomes greater when increasing the strength of the plume to 100. The number

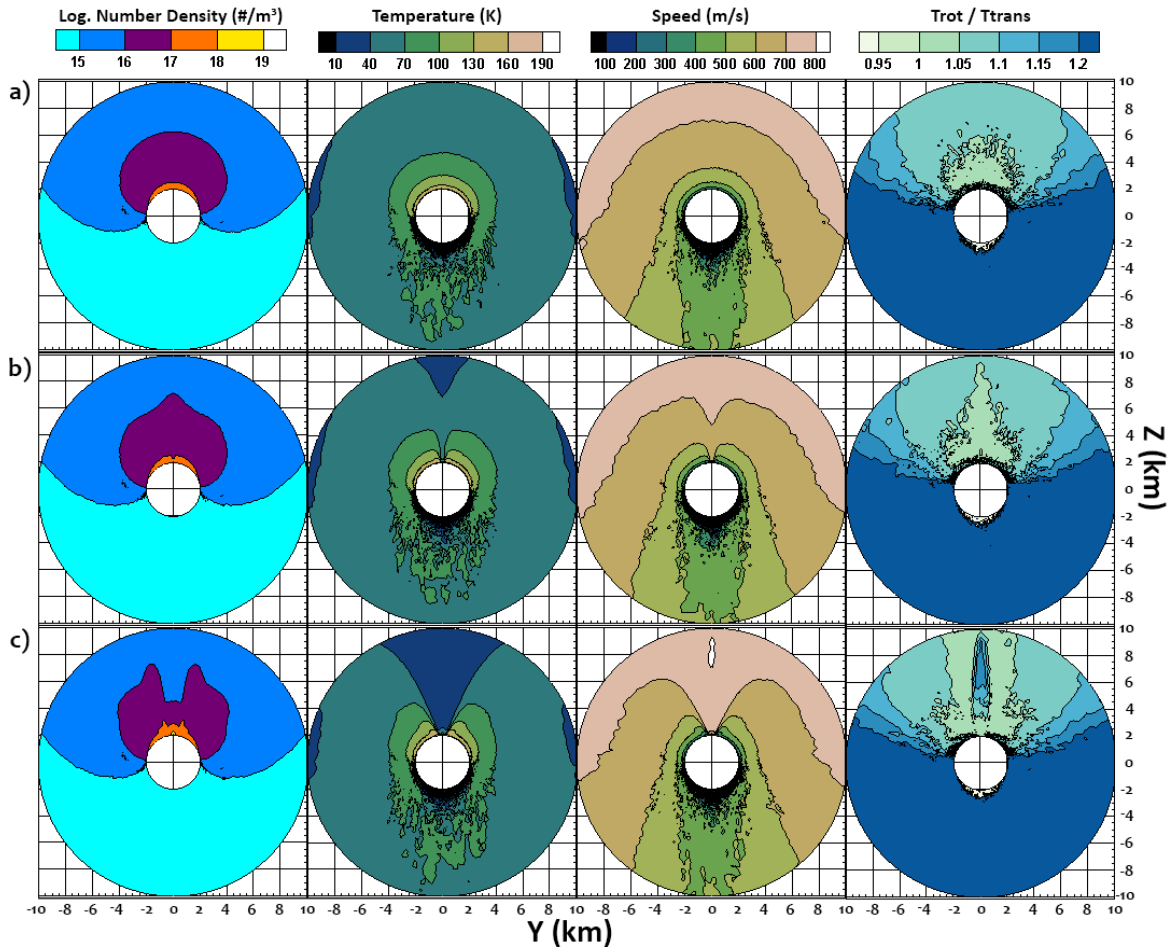


Figure 3.5: Slice of the DSMC results on the yz -plane from the center of the nucleus to the border of the simulation domain for the H₂O plumes cases (listed in Table 3.1) with different EAFs at a 3.8×10^{-3} sr source. The plume is located at $(y,z)=(0,2\text{km})$ in all panels. a) Case 1x with a homogeneous EAF everywhere, b) case 10x and c) case 100x. From left to right: the first column shows the logarithmic number density, the second column shows results of the gas temperature, the third column shows the speed of the flow and the last column on the right shows the parameter of thermal equilibrium T_{rot}/T_{trans} .

density seems to decrease even faster above the plume, creating a density gap at around 4km from the center of the nucleus. For a quantitative comparison we need to extract the information along the $+z$ direction shown in Figure 3.6. The upper panel to the left of Figure 3.6 indicates that a steeper decrease in the number density for the 100x case, which reaches values significantly lower at 10km from the center of the nucleus compared to the other two models. Cases 10x has only a significantly steeper decrease in number density very close to the nucleus compared to case 1x. However, within the first km from the nucleus surface, case 10x has the same decrease in number density with a slightly larger abundance caused by the contribution of the plume to

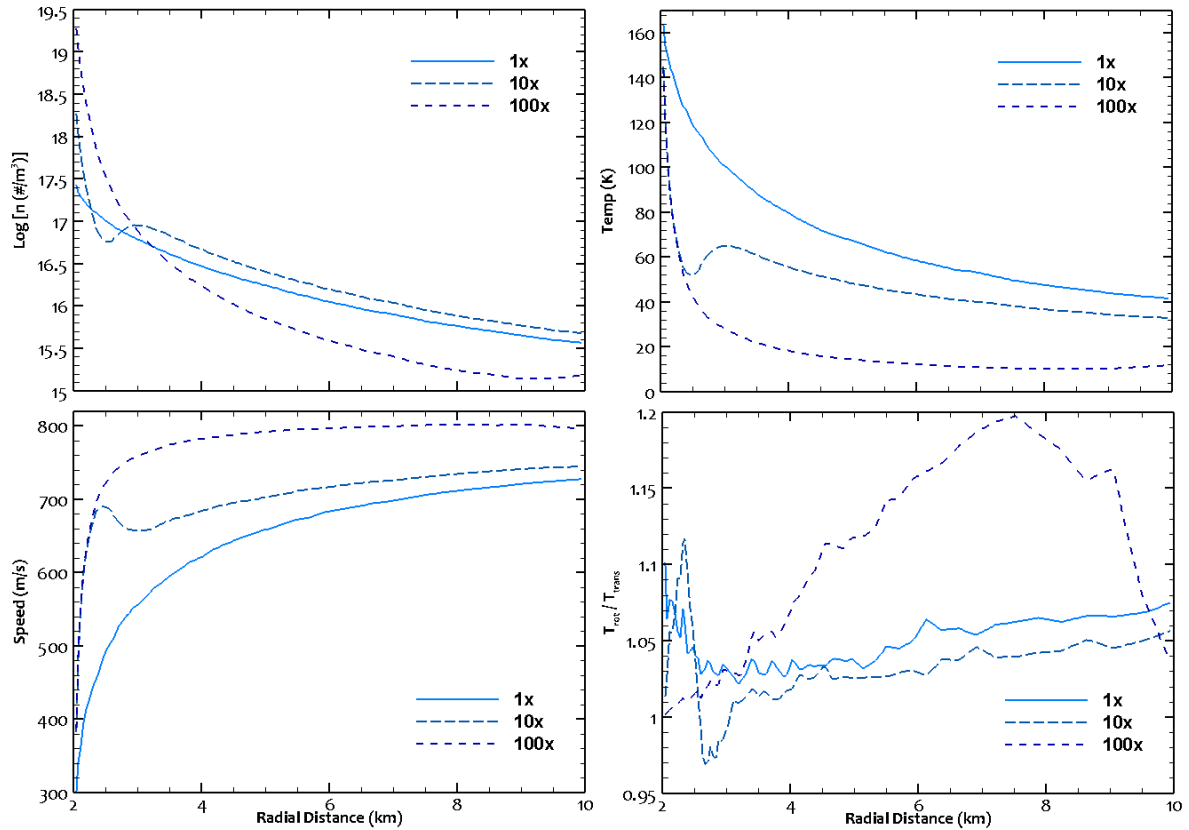


Figure 3.6: Extracted DSMC results along the +z direction for all cases listed in Table 3.1. The radial distance refers to the distance from the center of the nucleus, so 2km distance refers to the location of the surface.

the total production rate.

In terms of temperature, Figures 3.5 and 3.6 suggest a strong change in the flow for cases 10x and 100x caused by the increasing activity of the plume. Larger densities from the plumes mean more collisions and a larger pressure gradient between it and its surroundings. This decreases faster the temperature of the flow coming from the plume, because the gas needs to exert more work in order to expand into space. This adiabatic cooling also explains the change in the flow speed, given that the vapour pressure inside the plume significantly decreases and the gas is able to move faster, reaching a speed of approximately 800 m/s in the first 2 km from the surface for case 100x. Case 10x has the same steep decrease in temperature observed in the number density, which causes its speed to increase up to 700 m/s very close to the surface. However, as the gas moves away from the nucleus its speed stabilizes to a slightly larger speed than the purely insolation-driven case 1x.

When looking at the non-thermal equilibrium factor T_{rot}/T_{trans} in Figures 3.5 and 3.6, we can observe that the dayside has a T_{rot}/T_{trans} value closer to 1, given the larger number of inter-molecular collisions that facilitate the energy exchange within the flow. For the region above

the plume, cases 1x and 10x do not seem to have significantly large differences except in the first km from the surface. Case 100x however forms kind of a T_{rot}/T_{trans} bubble which is probably formed by a shock front in the vicinity of the plume due to the strong difference in pressure. However, these differences can only be seen in a T_{rot}/T_{trans} range very close to 1, which indicates that for all the tested cases the flow on the dayside can be assume to be in LTE.

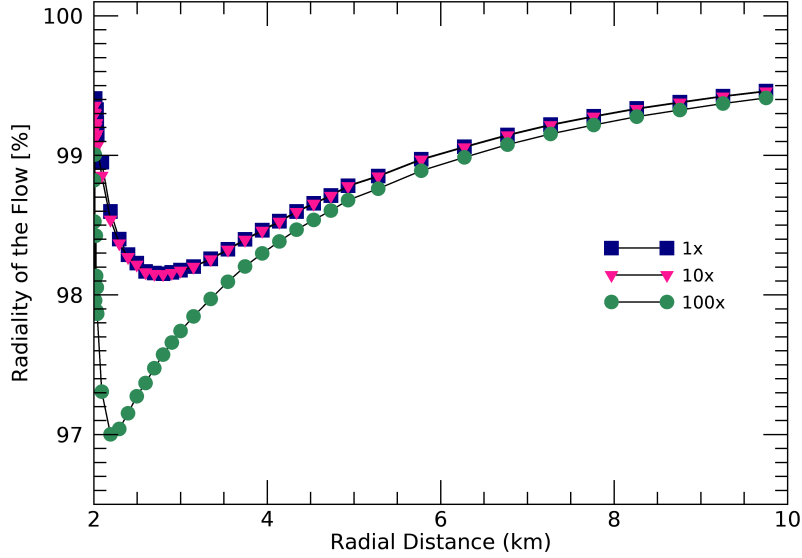


Figure 3.7: Radiality of the flow field for the purely insolation-driven or 1x case (blue squares), 10x case (pink triangles) and 100x case (green circles). The radial distance refers to the distance from the center of the nucleus, so 2km distance refers to the location of the surface.

Finally, I have calculated the radiality (ξ) of the flow as

$$\xi = 100\% \cdot \frac{\vec{x} \cdot \vec{v}_x + \vec{y} \cdot \vec{v}_y + \vec{z} \cdot \vec{v}_z}{|\vec{v}| \cdot r} \quad (3.1)$$

where \vec{x} , \vec{y} and \vec{z} are the position coordinates, \vec{v}_x , \vec{v}_y , \vec{v}_z are the velocity components and r is the radial distance from the nucleus. Directly above the plume (along the +z direction) I have determined the flow to reach a radiality equal to 100% within the first km from the surface for all cases. Therefore, in Figure 3.7 I show the average radiality of the whole flow instead, calculated with the shell approach used for the uniform cases. In this case we notice that in terms of radiality, a plume 10 time stronger than its surroundings does not affect significantly the average movement of the whole flow, however, a plume 100 times stronger than its surrounding can decrease the average radiality of the flow by a little bit more than 1%, due to the lateral expansion it creates in regions close to the plume. This effect is only observed in the first 2 km from the surface. At larger distances from the nucleus the radiality of the whole flow tend to 100%.

These results can be compared to the first models of axi-symmetric cometary outflow from a sphere made by Kitamura [1987]. The calculations given here serve as a baseline for comparison when introducing increased complexity into the calculation.

3.2 Complex Shape Nucleus

We now go a step farther and study the outgassing for the actual shape of comet 67P/CG. In this section, I present first cases with a homogeneous distribution of H₂O-ice sources with a uniform and insolation-driven outgassing. Then, I explore possible regional inhomogeneities in ice composition with insolation-driven outgassing cases in an attempt to fit Rosetta data. The selected time for these studies is July 10 2015, since for this date the southern hemisphere of the nucleus is fully illuminated in one rotation, given that the sub-solar latitude is approximately -30°. Using this date also extends the work of Marschall et al. [2016], which focused on November 2015. The idea is to determine if the southern hemisphere also has regions with more activity than others, as it is the case of the northern hemisphere and the Hapi region. This is important because model cases presented by Marschall et al. [2016, 2019] do not always fit perfectly ROSINA/COPS data.

3.2.1 Homogeneous ice distribution on comet 67P/CG

3.2.1.1 Uniform outgassing

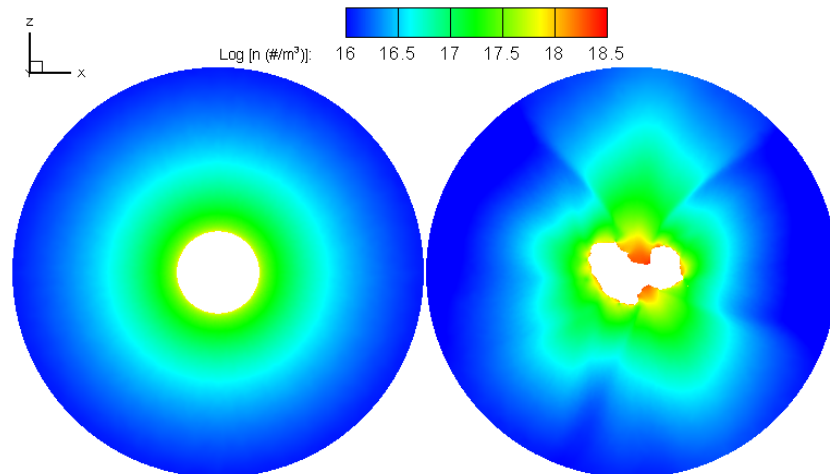


Figure 3.8: Slice in the xz -plane of the 3D DSMC results of number density for the uniform outgassing of a sphere and comet 67P/CG. Both cases have a global water production rate equal to 300 kg/s.

Similar to the cases shown in the previous section, I have set a case with a comet with a diffusely reflecting surface that is uniformly outgassing with a global production rate equal to

$Q_g = 300$ kg/s and a rotational relaxation collision number $Z_{rot} = 1$. This case can be directly compared to the uniform $Q_{H_2O} = 1 \times 10^{28}$ molecules/s case of section 3.1.1. The EAF in both cases is homogeneous and the inlet temperature is set to 200K everywhere. Figure 3.8 is a slice in the xz-plane of the 3D DSMC results of number density for the uniform outgassing of a sphere and comet 67P/CG. We can clearly see the effect of the shape in the distribution of number densities around the nucleus. For the spherical nucleus case, the number density decreases uniformly in every direction (Figure 3.1), while the complex shape of comet 67P/CG produces inhomogeneities in the distribution of the gas, which are stronger close to the nucleus, but still can be detected at large distances from it.

I have also tested a case with $Z_{rot} = 8$, but, similarly to Liao et al. [2016] results for low production rates, Z_{rot} does not seem to have a significant effect on the macroscopic properties of the gas flow for large production rates. Figure 3.9 shows the DSMC results of number density, speed, temperature and $\Delta s/mfp$ for both Z_{rot} values, and we can see no significant change in any of this parameters. Therefore, I have selected a $Z_{rot} = 1$ for all DSMC simulations shown in this work.

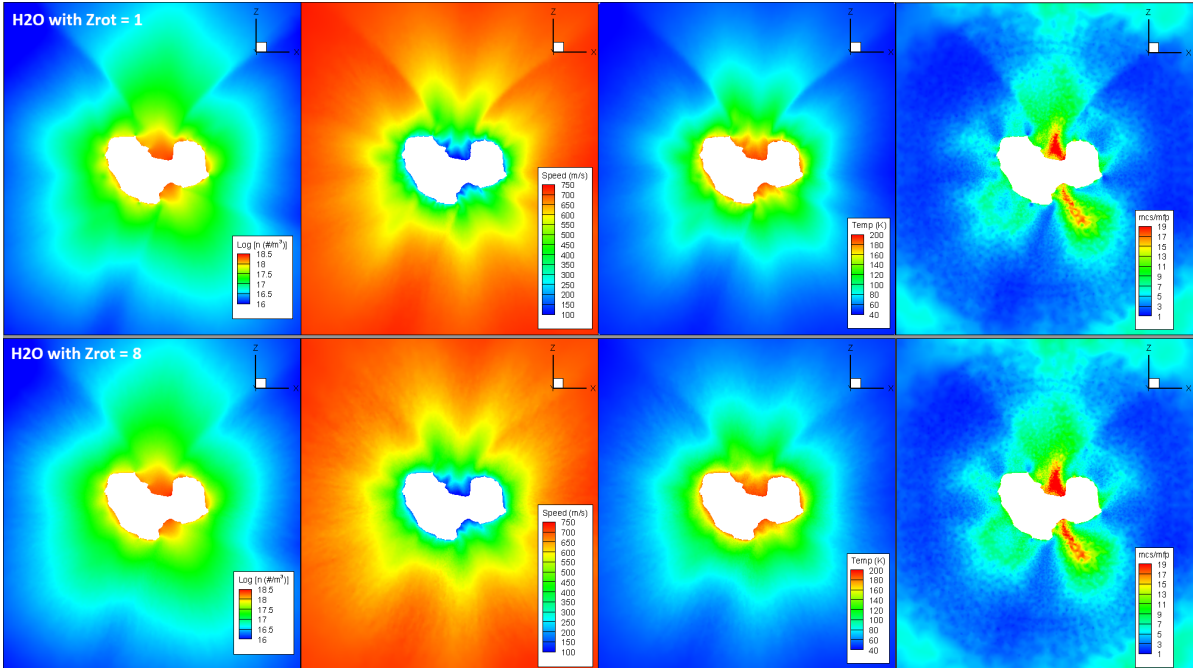


Figure 3.9: DSMC results for the uniform outgassing from the complex shape of comet 67P/CG. the global production rate is both cases is $Q_g = 300$ kg/s. The rotational relaxation collision number Z_{rot} is changed to test possible differences in the flow properties. From left to right number density, speed, temperature and mcs/mfp ratio.

An uniform outgassing case has been initially used to test the quality factor $\Delta s/mfp$ of the simulation mesh (last column in Figure 3.9), which seems to get closer to 20 only very close to the neck region. However, the uniform outgassing case has proven very useful when studying the

distribution of activity coming from a complex shape nucleus as is the case for comet 67P/CG, as it will be presented in the following section.

3.2.1.2 Insolation-driven outgassing

Once again, the second step in complexity is given when setting different illumination conditions on a diffusely reflecting surface. This triggers outgassing differences depending on the geometry of the observation. Figure 3.10 shows an example of the boundary conditions set at the surface of comet 67P/CG for a rotational step equal to 30° in longitude. As $EAF=10$ everywhere, the differences in the outgassing will be produced mainly by the illumination geometry selected and the shape of the nucleus itself. Therefore, the middle panel of Figure 3.10 shows differences in the surface temperature, which cause differences in the production rates per unit area shown in the right panel of the same figure.

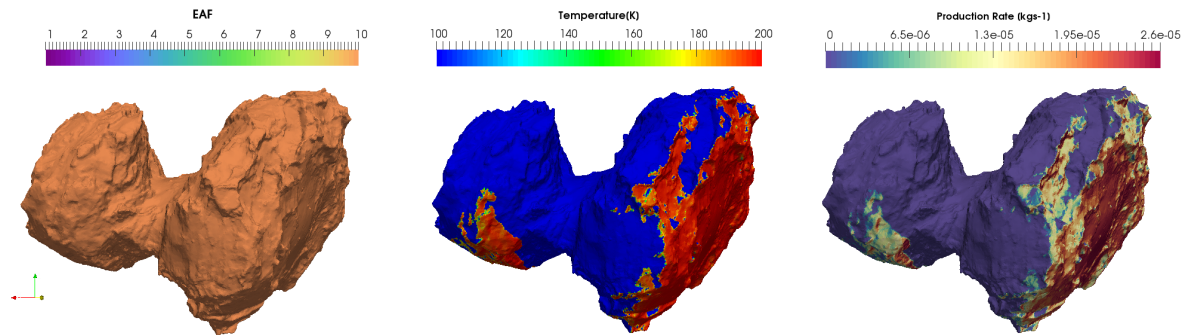


Figure 3.10: Boundary conditions for the purely insolation-driven H_2O outgassing from a nucleus with a homogeneous ice composition. The left panel shows the homogeneous distribution of EAF, which is set to 10 everywhere. The middle panel is the inlet temperature and the panel to the right is the gas production rate set at the surface. In this case, the sub-solar longitude is at 30° , such that the maximum temperatures and production rates are in Imhotep and its surrounding areas.

As mention in Chapter 2, we need at least 4 rotational steps to compare our simulation results with ROSINA data. Therefore, I have run four simulations at my standard sub-solar longitudes which are separately by 90° . The purely insolation-driven case and the uniform outgassing case are compared with ROSINA/COPS data in Figure 3.11 for the time between July 5 to July 15, 2015. There we see that the uniform outgassing case fits properly the magnitude of the daily variations measured by ROSINA/COPS, however it does not match their trend. On the other hand, the purely insolation driven case fits much better the daily variations, however it overestimates the magnitude of such variations with time. I infer this to be an indication of either *(i)* possible extended ice sources from dust particles above the nightside, *(ii)* an inhomogeneous composition of the nucleus or *(iii)* the lack of nightside activity included in the model. The first hypothesis has been observed in several comets [Eberhardt, 1999; Harris et al., 1997; Cottin and Fray, 1970],

and the Alice far-ultraviolet imaging spectrograph onboard Rosetta has detected OI $\lambda 1304$ and Ly- β emissions (related to H₂O photodissociation) close to perihelion from resonance scattering on the anti-sunward side of the nucleus from the extended coma [Feldman et al., 2017]. However, this hypothesis cannot be tested with our DSMC code and given that the contribution of dirty icy aggregates has been inferred to be very small in comet 9P/Tempel 1 [Gicquel et al., 2012], which has production rates in the same order of magnitude than comet 67P/CG on July 2015, we assume their contribution to be also very small for comet 67P/CG. The absence significant deviations from $1/r$ seen in OSIRIS images [Gerig et al., 2018] also argues against sublimation of grains. For the second hypothesis, I have tested different H₂O EAF distributions, which will be presented in Section 3.2.2. A single attempt to include CO₂ inhomogeneities is mentioned in Chapter 5, but this is a very preliminary result that needs further investigation. For the third hypothesis, I needed to include the effects of thermal conductivity and sub-surface sublimation on the H₂O and CO₂ outgassing, which will be presented in chapters 4 and 5.

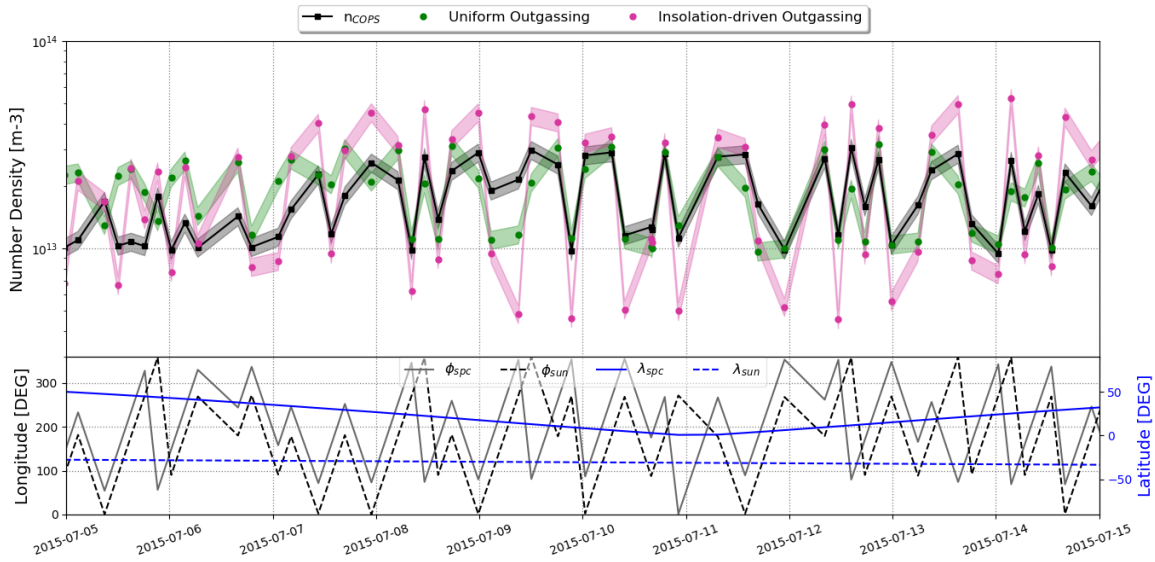


Figure 3.11: First model comparison with ROSINA/COPS data (black squares) for the time between July 5 and July 15 2015. Upper panel: The purely insolation driven case is shown with pink circles, while the uniform outgassing case is shown with green circles. The solid line connecting data points is used to improve the visual comparison, it is not real data. Thick lines indicate an uncertainty of 10% in the measured and modelled number densities. Lower panel: Sub-spacecraft (spc) and sub-solar (sun) coordinates for each data point. The left axis refers to the longitude label ϕ and the right axis refers to the latitude label λ .

3.2.2 Inhomogeneous ice distribution on comet 67P/CG

A purely insolation-driven model of H₂O outgassing does not seem to explain the magnitude of the daily variations measured by ROSINA. Therefore, different model cases were tested changing

the strength of the activity for certain regions in an attempt to fit better ROSINA/COPS data. These regions were selected based on observation geometry assumptions and the illumination conditions for that time, which would make them good candidates for inhomogeneous ice sources at the nucleus. I therefore have set a base EAF=10% for the whole nucleus, and vary the EAF for single regions to tests their contribution to the flow. I have changed the EAF of 10 regions in total (two times for Imhotep) and compare their model results with ROSINA/COPS.

A similar approach has been used by Marschall et al. [2016, 2017, 2019] in order to fit ROSINA/COPS data for the spring equinox. Their inhomogeneous case has strong sources localized in the Hapi region with an EAF equal to 30%, and a very depleted area everywhere else except in the southern hemispheric regions. Therefore, I have also tested a case with a similar inhomogeneous distribution of H₂O-ice, but scaled to the measured production rates on July 2015 (see Figure 3.12) by ROSINA/COPS.

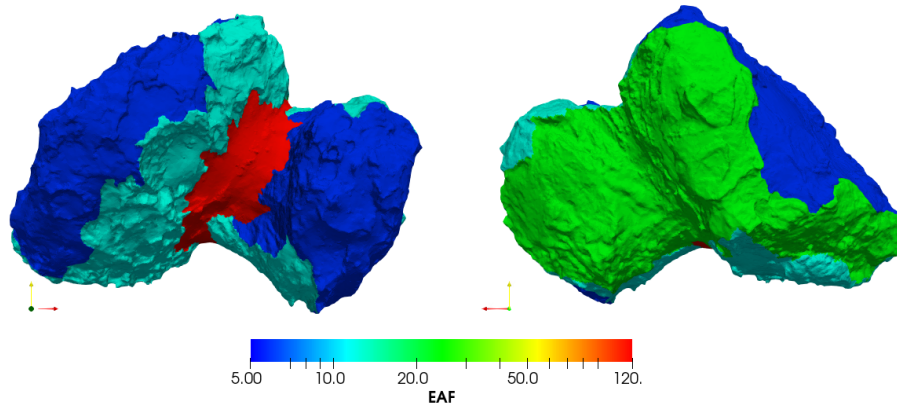


Figure 3.12: Distribution of the H₂O activity in 67P/CG given the EAF defined by Marschall et al. [2019] for the spring equinox time, but scaled to the production rates of July 2015. The colorbar is in a logarithmic scale to emphasize EAF differences.

Figure 3.13 shows the model comparison with ROSINA/COPS for the best 6 out of 13 cases I tested for July 2015. Except from the inhomogeneous case and the Bes regional test, all other cases seem to have the same variation as the purely insolation-driven case (here labeled as "homogeneous") and strong diurnal variations did not seem to disappear will all tested regional models. Compared to the purely insolation-driven case, the inhomogeneous systematically over-estimates the number densities in observations geometries close to $\phi_{spc} = 250^\circ$, when the sub-solar point is above the Wosret region ($\phi_{sun} = 180^\circ$ and $\lambda_{sun} = -30^\circ$). On the other hand, the case with strong ice sources in Bes over-estimates number densities for observation geometries close to $\phi_{spc} = 90^\circ$, when the sub-solar point is above the Imhotep region ($\phi_{sun} = 0^\circ$ and $\lambda_{sun} = -30^\circ$). Cases with strong sources in Khonsu and Apis seem to improve the fit, specially in cases where the number densities are under-estimated.

In order to get a quantitative comparison of all tested models, we need to use a statistical

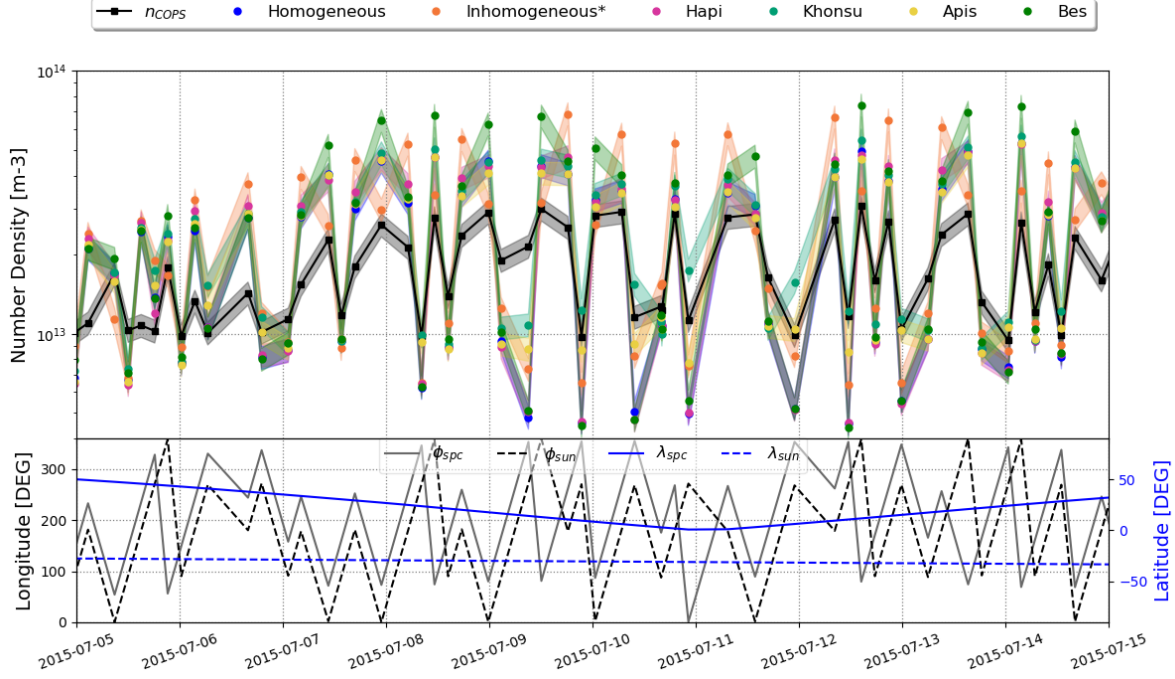


Figure 3.13: Upper panel: Comparison of DSMC results with local measurements of number density taken by ROSINA/COPS between July 5 to July 15, 2015. The solid line connecting data points is used to improve the visual comparison, it is not real data. Thick lines indicate an uncertainty of 10% in the measured and modelled number densities. Lower panel: Sub-spacecraft (spc) and sub-solar (sun) coordinates for each data point. The left axis refers to the longitude label ϕ and the right axis refers to the latitude label λ .

approach. I have therefore calculated the root mean square logarithmic error (RMSLE)

$$RMSLE = \sqrt{\frac{1}{N_P} \sum_i^{N_P} [\log(n_{COPS,i}) - \log(n_{g,i})]^2} \quad (3.2)$$

and the Pearson correlation coefficient (PCC)

$$PCC = \frac{\sum_i^{N_P} (n_{COPS,i} - \bar{n}_{COPS,i}) * (n_{g,i} - \bar{n}_{g,i})}{\sqrt{\sum_i^{N_P} (n_{COPS,i} - \bar{n}_{COPS,i})^2 \sum_i^{N_P} (n_{g,i} - \bar{n}_{g,i})^2}} \quad (3.3)$$

to compare all model cases. N_P is the number of data points used for the calculation and \bar{n} is the mean value of the number densities in the selected data set. The RMSLE is used because it does not penalize huge differences in the predicted (n_g) and true values (n_{COPS}) when both numbers are huge numbers, which is the case for the number density values we are comparing. A RMSLE closer to 0 indicates a smaller relative error and, therefore, a better fit. On the other hand, the PCC measures the linear correlation between n_{COPS} and the model number density n_g for the N_P points of data from 2015-07-05 to 2015-07-15. PCC values closer to +1 have a positive correlation, PCC values equal to 0 have no correlation and PCC values equal to -1 have

a negative correlation. This calculation is done using all data points shown in Figure 3.13 and it is shown in Figure 3.14. For the current set of model cases, the RMSLE indicates that cases with strong sources (EAF=100%) in Apis and Khonsu have the smallest relative error (19% and 20%, respectively) compared to the data. These two are closely followed by the homogeneous EAF case, the low EAF case set in Imhotep and the moderate EAF case in the Anubis region, all with a RMSLE=23%. On the other hand, the PCC coefficient indicates the case with strong sources in the Bes region correlates better the data, with a PCC=0.86. However, many other model cases have very close PCC values (Homogeneous EAF and Khonsu have a PCC=0.86; Anubis and Khepry have a PCC=0.85; Hapi and Apis have a PCC=0.84; etc.). This is certainly not a large difference between model cases, such that we can not unequivocally select a model by studying ROSINA/COPS measurements only. We can however dismiss strong H₂O sources in Imhotep, Bastet and Atum, since these three model cases have very large relative errors and a poor correlation with the data. The case with depleted sources (EAF=1%) in Imhotep has a significantly poorer correlation with respect to the data, however the relative error is the same as the purely insolation-driven case. In this case, one needs to evaluate what aspect of the data is more important to fit: the absolute number density values or the variability of the data. An ideal case would fit both aspects of the data, however we give prevalence to models that have a smaller RMSLE over models that have a larger PCC value. Therefore, we do not dismiss the possibility of Imhotep being very depleted in H₂O even if the dispersion of the number densities given by the model is greater. A categorical answer requires to study measurements taken by other instruments onboard Rosetta.

3.3 Model comparison with MIRO

We have selected a set of times listed in Table A.1 in order to compare some of a model cases with MIRO measurements. In this section however, I will only mention results for the 2015-07-10T01:32:39 observations, because it is the only measurement that has a comparison with the two thermal inputs I introduce in this section. All other observations and their respective model comparison with MIRO spectra (under non-LTE conditions) will be in Appendix A.

For this time, I have extracted the information of number density, Doppler velocity and temperature along the FOV and plotted it against the distance from the nucleus as shown in Figure 3.15. T_{Front} makes reference to the purely insolation-driven case shown in the previous section using as input the temperature of the sublimation front calculated with a thermal inertia equal to 0 TIU. On the other hand, $T_{Front} + 100K \cdot \text{Cos}(\theta_i)$ makes reference to an artificial model in which we increase the temperature at which gas particles leave the nucleus as a cosine function of the incidence solar angle θ_i . The additional temperature ($+100K \cdot \text{Cos}\theta_i$) is introduced as a solution of the heat transfer to the gas from the dust mantle [Christou et al., 2018]. Both thermal inputs are shown in Figure 3.16 from which it is easier to compare the difference in temperatures set for

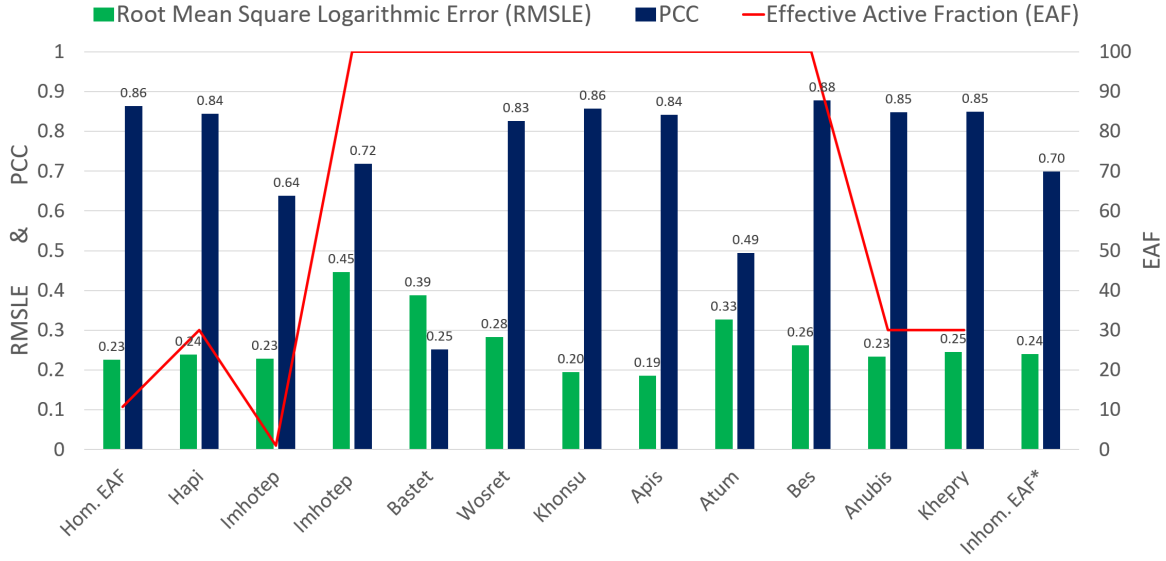


Figure 3.14: Estimation of the goodness of the DSMC models with homogeneous, inhomogeneous and regional sources compared to ROSINA/COPS measurements for the time between the 2015-07-05 to 2015-07-15 using two methods: the RMSLE in green and the PCC in blue. The red line indicates the EAF used in the test for each regional source. Since the inhomogeneous case has a large set of EAF values, we have not included this in the plot.

each model case, especially in the region pointed by MIRO’s FOV (black box) at this particular time. This figure only illustrates differences between the two models, from which is clear that an increment of $100K \cdot \cos(\theta_i)$ at the surface can produce larger Doppler velocities at the spacecraft position for that time, as a result of a steeper decrease in temperature with altitude. In order to see how well both tests have performed, I have compared them with MIRO spectra assuming that the H_2O gas is in LTE and non-LTE.

3.3.1 LTE condition

Figure 3.17 shows the T_{Front} and $T_{Front} + 100K \cdot \cos(\theta_i)$ cases with homogeneous distribution of ice sources compared to the $H_2^{16}O$ band obtained by MIRO on 2015-07-10T01-32-39. At this time, the phase angle is equal to 89.6109° and MIRO’s FOV is pointing to the Aten/Khepry region, while the sub-solar point is located above the Imhotep region. Using a Gaussian fit on MIRO $H_2^{16}O$ band indicates a central velocity $v_c = -0.6482$ km/s along the FOV, with a standard deviation $\sigma = 0.56$ and a background temperature $T_{back} = 185.51K$. For the model comparison, we used $T_{back} = 200K$, therefore both models shown a larger amplitude in the absorption band. The purely insolation-driven case using T_{front} as input does not seem to fit well MIRO spectra, it has been determined to have a $v_c = -0.4859$ km/s which is approximately 0.162 km/s slower than the measurements. However, the case with $T_{Front} + 100K \cdot \cos(\theta_i)$ as input, seems to improve the fit to MIRO, with a difference in central velocity of only 10m/s. Although a warmer thermal

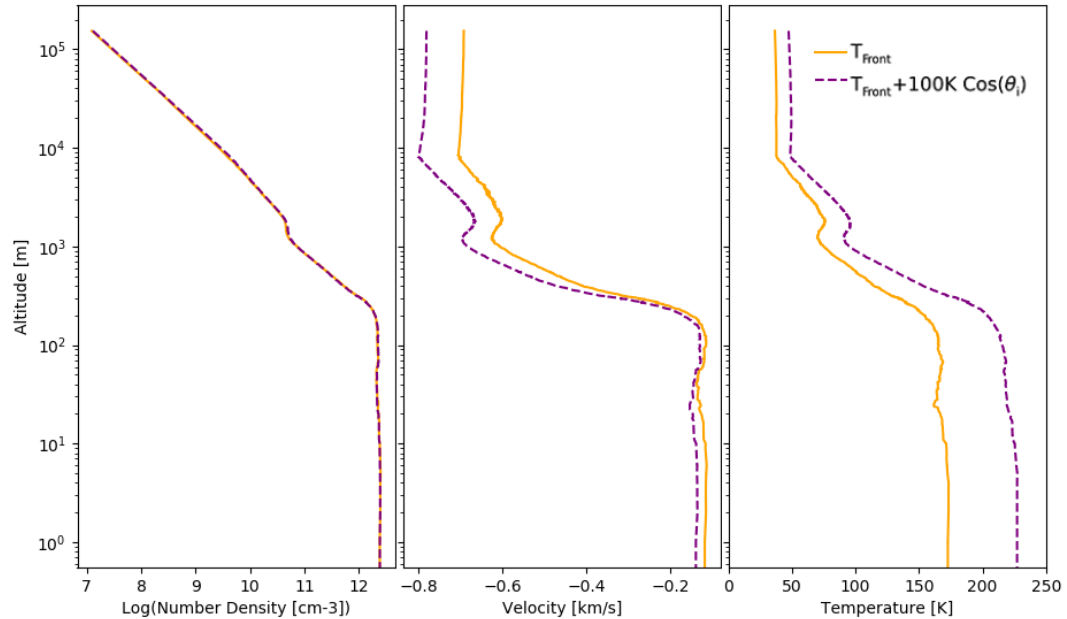


Figure 3.15: Vertical profile of number density (left panel), Doppler velocity (middle panel) and temperature (right panel) for the purely insolation-driven case along MIRO's FOV on 2015-07-10T01-32-39 using two different thermal inputs: T_{Front} (solid orange line) and $T_{Front} + 100K \cdot \text{Cos}(\theta_i)$ (dashed purple line).

input at the surface slightly under-estimates the depth of the absorption band, it fits almost perfectly the central velocity and the width of the band, which indicates the $T_{Front} + 100K \cdot \text{Cos}(\theta_i)$ case accurately describes the flow velocities along MIRO's FOV, only slightly over-estimating the bulk temperature by approximately 10-15K. It is also important to notice that this model case generates a "red emission wing" at approximately +0.8 km/s. This feature is not sharply observed in the data for this particular time, it however has been observed in all spring equinox H_2^{16}O absorption bands studied by Marschall et al. [2019]. The gas being warmer than the background could be the result of a thin dust mantle heating up the gas on its way out and/or originate from strongly illuminated neighboring areas and not necessarily from the surface pointed by the beam [Marschall et al., 2019]. It is probably a combination of both, but from this particular example it is difficult to determine what factor is more important, because our $T_{Front} + 100K \cdot \text{Cos}(\theta_i)$ case does not only increases the temperature all over the illuminated areas of the nucleus, but it enhances the temperature gradient at the surface as θ_i increases.

3.3.2 Non-LTE condition

In order to compare DSMC results with MIRO measurements, Marschall et al. [2019] have assumed the gas field to be in non-LTE and used an iterative inversion approach to fit MIRO spectra for the spring equinox. Therefore, we use the same approach to test how well the

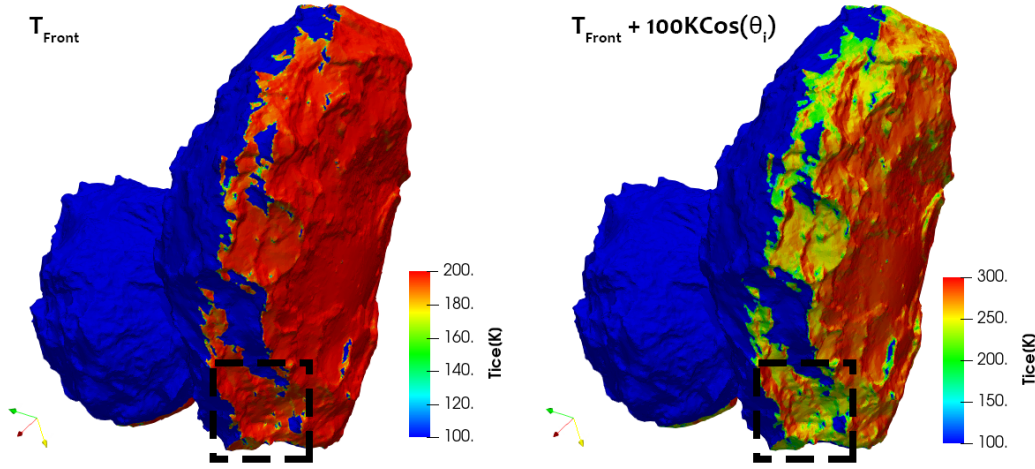


Figure 3.16: Comparison of the two thermal inputs at the surface boundary: T_{Front} and $T_{Front}+100K \cdot \cos(\theta_i)$. They are scaled to their maximum values which are 200K and 300K, respectively. The surface area pointed by MIRO's beam on 2015-07-10T01:32:39 is highlighted by the black boxes.

purely-insolation driven model with the T_{Front} and $T_{Front} + 100K \cdot \cos(\theta_i)$ temperatures performs compared to MIRO data.

Comparison with multiple data sets shown in Appendix A indicate that a homogeneous distribution of H₂O-ice sources outgassing at a temperature T_{Front} do not adjust the measurements at all. All observation geometries showed the same problems in order to fit MIRO data properly. This sets two possible scenarios: 1) the comet has an inhomogeneous composition which is not included in by the model or 2) the model underestimates the effects of the dust mantle on the gas. The two scenarios are not mutually exclusive. Therefore, we have tested the second scenario using the non-LTE condition as well. This comparison is shown in Figures 3.18 and 3.20 for the T_{Front} and $T_{Front}+100K \cdot \cos(\theta_i)$ cases, respectively. T_A in the y-axis of the upper panel indicates the brightness or antenna temperature, while the x-axis indicates the Doppler velocity. The bottom panel shows the variation of the temperature difference between MIRO measurements and the adjusted spectrum after iteration. We can clearly see that the calculated spectra for the DSMC simulations after first iteration does not adjust in either of the cases to MIRO spectra. The non-LTE code calculates a spectrum that fits better to the observations within 2σ measurement errors and it estimates slight differences in the vertical profiles shown in Figures 3.19 and 3.21. These vertical profiles indicate that the T_{Front} case requires a slightly larger production rate, such that the gas field is approximately 25K warmer and 350 m/s faster along the FOV. On the other hand, the $T_{Front}+100K \cdot \cos(\theta_i)$ case would require slightly lower production rates with a minimal increase in the average temperature of the gas ($\sim 10K$ close to the surface), but significantly larger velocities along MIRO's FOV.

The LTE and non-LTE conditions give us different interpretations of the same model cases

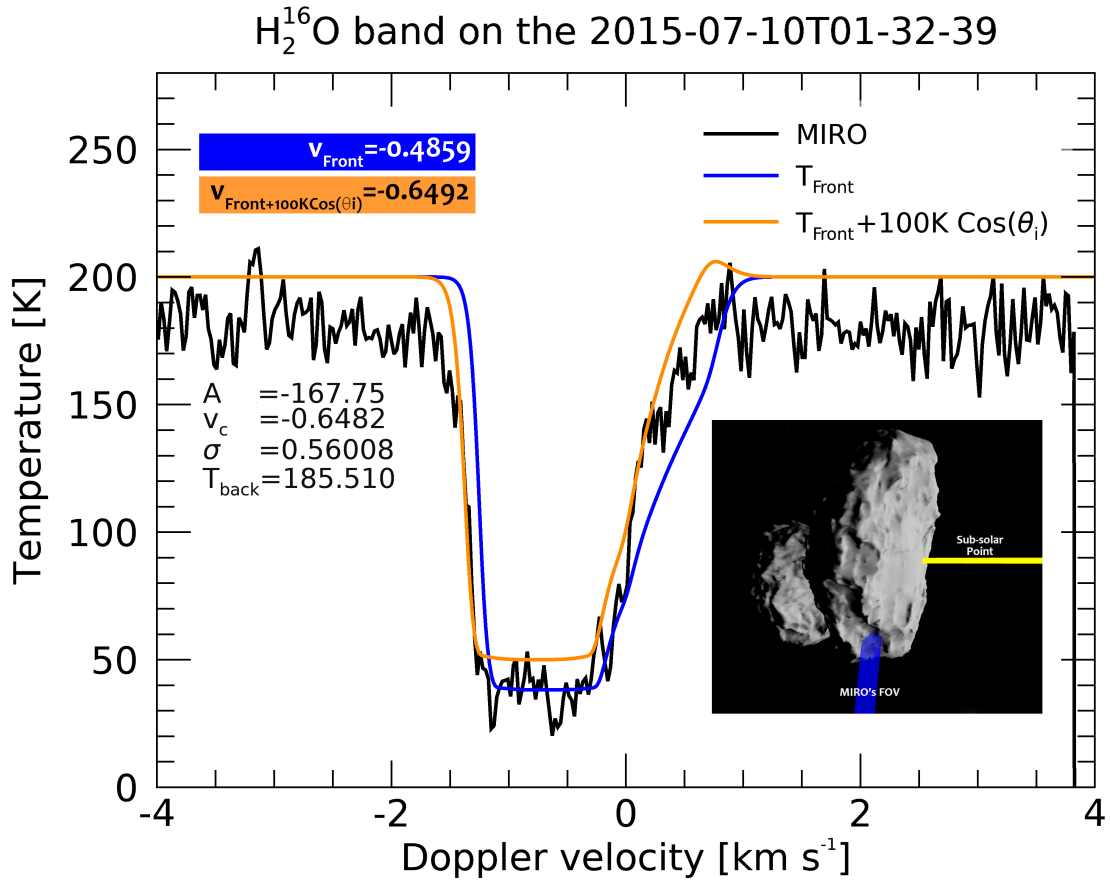


Figure 3.17: Purely insolation-driven case using two different thermal inputs compared to the MIRO H_2^{16}O band obtained on 2015-07-10T01-32-39 and assuming a flow filled in LTE. The background temperature T_{back} was set to 200K for both models. Text in black gives the information of height A , the central velocity v_c , the standard deviation σ and the background temperature T_{back} of a Gaussian fit to the MIRO absorption band. The colored velocities on the top left are the estimated central velocities of each model by using a Gaussian fit. On the bottom right there is an image of the pointing location of MIRO's FOV on the nucleus (blue path) and the sub-solar point (yellow path).

that seem to contradict each other. Especially intriguing are the differences between the gas velocities for both model cases. The assumption of the gas being under LTE suggest that by increasing the temperature at the illuminated surface, the model adjusts better to the central velocity of the measured spectra. Conversely, the analysis with a non-LTE condition indicates the same model under-estimates to a large degree the average velocity of the flow, especially at distances from the nucleus below 100 m. However, we need to take into account that non-LTE inversions require certain assumptions that depend in some measure on the model it is applied to. The adjusted spectra they suggest are not unique solutions, so it is possible that the non-LTE

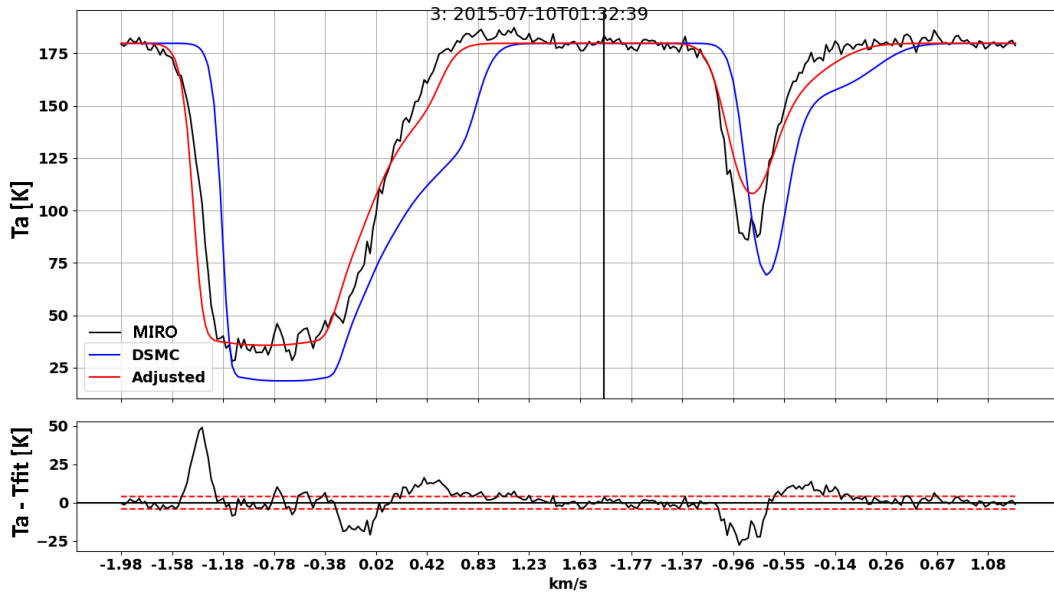


Figure 3.18: Upper panel: Purely insolation-driven case using the T_{Front} as input temperature (in blue) compared to the MIRO $H_2^{16}O$ (left) and $H_2^{18}O$ (right) bands (in black) obtained on 2015-07-10T01:32:39 and assuming a flow field in non-LTE. The best fit within 2σ of random measurement error is shown in red. Bottom panel: residual between the measurement and the best fit.

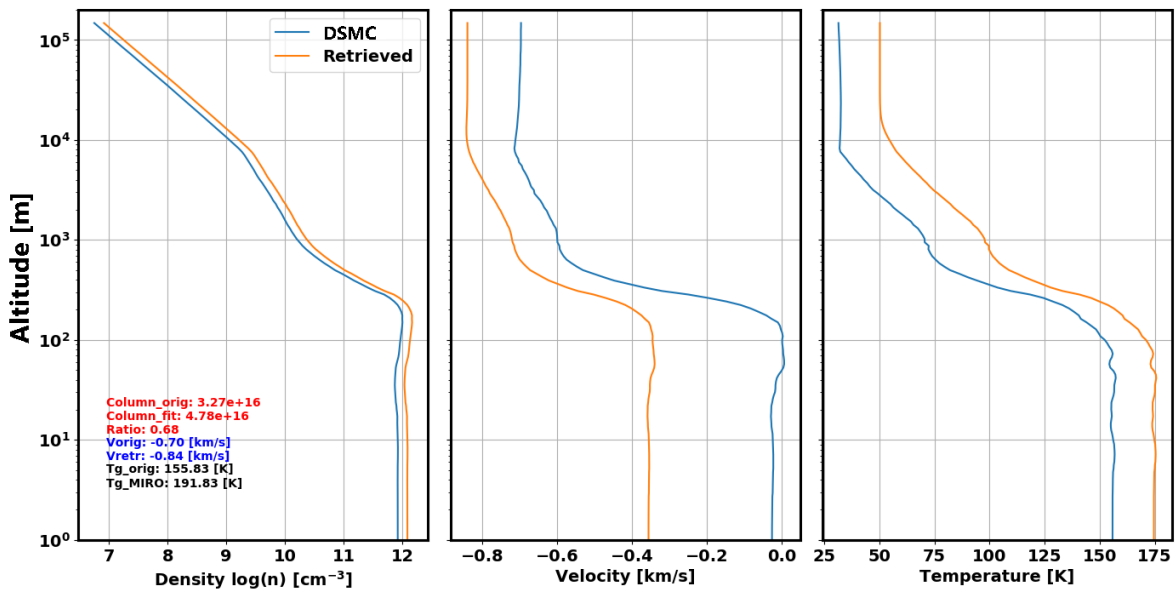


Figure 3.19: Vertical profiles of number density (left panel), Doppler velocity (middle panel) and temperature (right panel) along MIRO's FOV calculated for the DSMC model T_{Front} (blue) and the adjusted fit to MIRO after iteration (orange).

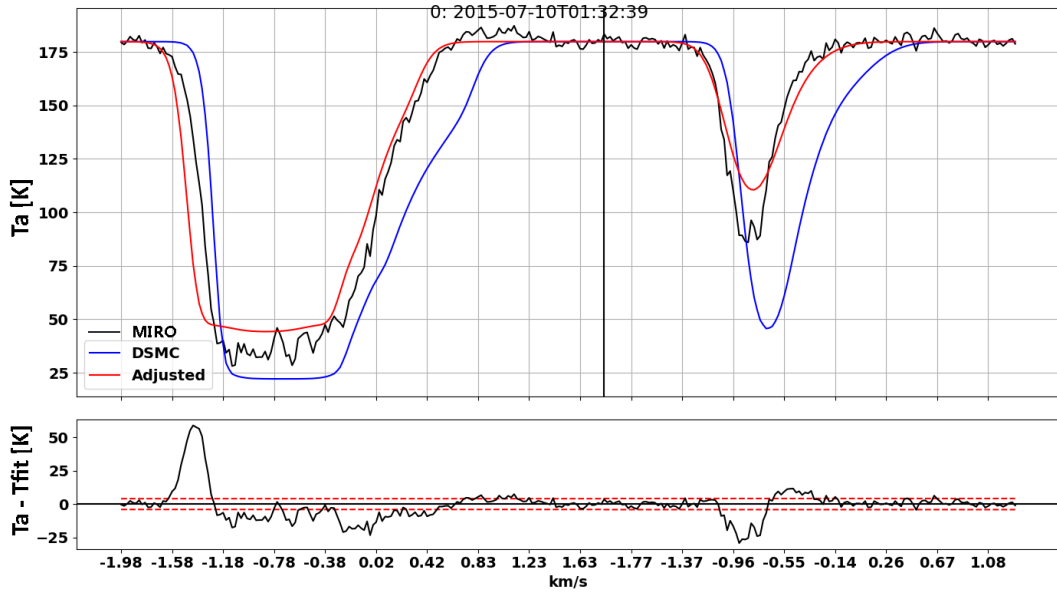


Figure 3.20: Upper panel: Purely insolation-driven case using the $T_{Front}+100K \cdot \cos(\theta_i)$ as input temperature (in blue) compared to the MIRO $H_2^{16}O$ (left) and $H_2^{18}O$ (right) bands (in black) obtained on 2015-07-10T01:32:39 and assuming a flow field in non-LTE. The best fit within 2σ of random measurement error is shown in red. Bottom panel: residual between the measurement and the best fit.

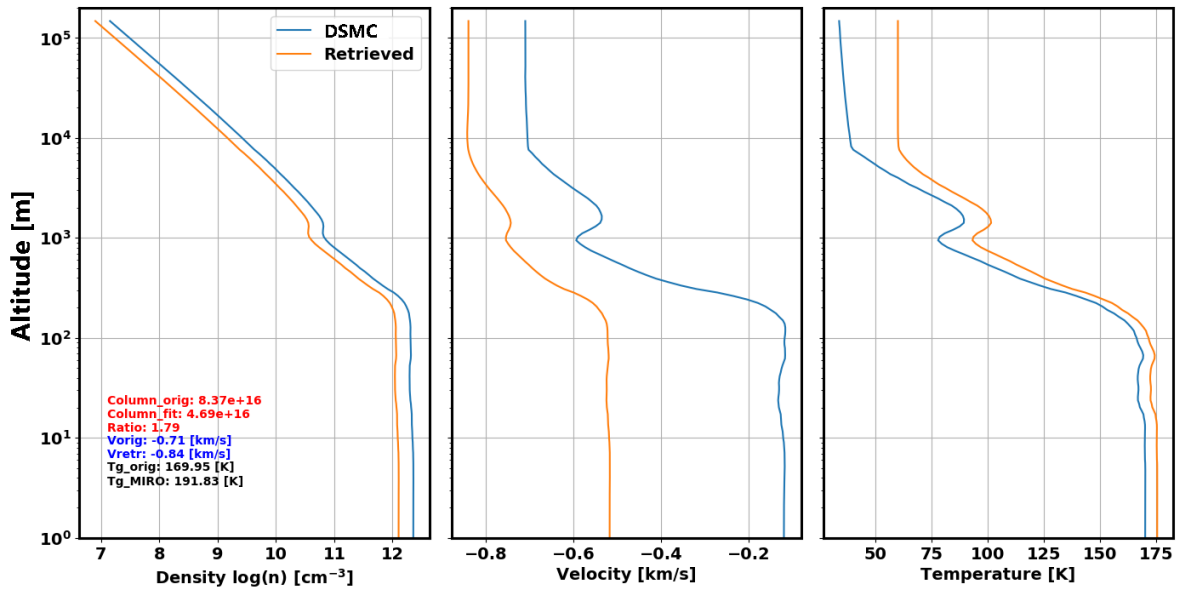


Figure 3.21: Vertical profiles of number density (left panel), Doppler velocity (middle panel) and temperature (right panel) along MIRO's FOV calculated for the DSMC model $T_{Front}+100K \cdot \cos(\theta_i)$ (blue) and the adjusted fit to MIRO after iteration (orange).

solutions for this particular time are not unambiguously explicit to discard the conclusions given by the model comparison using a LTE condition. A categorical conclusion requires comparison with more data sets. Unfortunately for this time, there are no VIRTIS-M IR images available that can help us to constrain our models. We have therefore, chosen to include thermal conductivity in our calculation, for a time range that has been well studied before, the spring equinox. This phenomenon must have influence on the flow field and could provide a possible solution to the problem. The effect of thermal conductivity on the distribution of H₂O and CO₂ sources at the surface will be presented for a spherical nucleus comet (Chapter 4) and for the complex shape of comet 67P/CG (Chapter 5).

The effect of thermal conductivity on the outgassing and local gas dynamics from cometary nuclei

Manuscript submitted for publication to *Astronomy and Astrophysics* on November 1st, 2020.
Currently under revision.

O. Pinzón-Rodríguez¹, R. Marschall², S.-B. Gerig¹, C. Herny¹, J.S. Wu³, and N. Thomas¹

¹ Physikalisches Institut, University of Bern, Switzerland Sidlerstrasse 5, CH-3012 Bern, Switzerland

² Southwest Research Institute, Boulder Office, 1050 Walnut St Suite 300, Boulder, CO 80302, USA

³ Department of Mechanical Engineering, National Chiao Tung University, Hsinchu, Taiwan

NOTE: Part of the introduction and methods have been taken out and included in Chapters 1 and 2 to avoid repetition.

Abstract

Aims The aim of this work is to investigate the parameters influencing the generation of the inner comae of comets and model the gas activity distribution around their nuclei. Herein the influence of thermal inertia combined with sub-surface sources on insolation-driven sublimation and the resulting gas flow field is investigated using both H₂O and CO₂ as driving volatiles. We apply this study to a spherical nucleus comet only, but we adopt some of the rotational and surface properties of the target of the Rosetta mission, comet 67P/Churyumov-Gerasimenko (67P/CG).

Methods We use a simplified model of heat transport through the surface layer to establish sublimation rates from a H₂O- and CO₂-ice subsurface into vacuum. The 3D Direct Simulation Monte Carlo method is then used to model the coma as a sublimation-driven flow. The free parameters of the model are used to test the range of effects arising from thermal inertia and the depth of the source on the gas outflow.

Results Thermal inertia and the depth of the sublimation front can have a strong effect on the emission distribution of the flow at the surface. In models with a thermal inertia up to 80 TIU, the H₂O distribution can be rotated about the rotation axis by about 20° relative to models with no thermal lag. For CO₂, the maximum activity can be shifted towards the sunset terminator with activity going far into the nightside. The presence of a small amount of CO₂ can reduce the presence of H₂O by at least an order of magnitude on the nightside by blocking H₂O flow. CO₂ can also decrease the speed of the mixed flow in the same region up to 200 m/s, compared to cases with no CO₂ activity.

Conclusions H₂O is the dominant species on the dayside in all cases, while CO₂ is clearly the main driver for activity on the nightside in cases with sublimation fronts at large depths and a relatively low thermal inertia of 40 TIU. This would be consistent with previously reported observations of gas density and dust column density above the nightside hemisphere of the nucleus of 67P/CG. Strong variations in the local CO₂/H₂O density ratio between the day- and nightside are clearly evident. The gas dynamics flow fields show evidence of thermal inertia effects and species interactions. The results cannot be approximated by free-radial outflow of insolation-driven sublimation products.

4.1 Introduction

In the current chapter, we shall study the gas emission distribution from a spherical nucleus source and combine this with gas dynamics simulations to investigate the effects on the coma distributions of H₂O and CO₂. We have therefore construct a simple model to replicate cometary outgassing and perform a parameter study of the most important physical properties that influence the energy exchange at the sub-surface. The starting point of this work is a thermal model that neglects thermal inertia. This has been used before to replicate fairly accurately the H₂O outgassing from 67P/CG [Marschall et al., 2016, 2017, 2019]. However, this is probably not applicable to CO₂ emissions. In order to include CO₂ activity into the problem, we need to take into account the effect of thermal conductivity and the transport of heat to deeper layers of the nucleus (see Section 2.2.3). Thus, we have included different values of thermal inertia and have simulated sublimation fronts at different depths for the H₂O and CO₂ molecules.

It is important to clarify that the current work does not intend to actually fit Rosetta data, but only to understand the processes triggering nightside activity which will be used in future studies to investigate extensively mixed gas emissions from the real comet's shape and compare them to observations. In the following sections, we shall detail the model assumptions (Section 4.2) and provide a description of the selected cases (Section 4.3) to model cometary activity. In Section 4.4, we present the main findings of this work and discuss their relevance for the comparison of numerical modelling methods with multi-instrument data. Finally, in Section 4.6 we shall enumerate the conclusions of our work.

4.2 Model assumptions

In order to model gas activity in the inner coma, we have chosen a case in which we assume the nucleus is a sphere with a 2 km radius. Although the considered spherical shape is highly simplified compared to the complex shape of e.g. 67P/CG's nucleus, this approach reveals the physical interaction of the different volatile species mixed within the flow, while avoiding the additional effects of irregular geometry. We have selected the outer limit of our simulation domain to be at 10km from the centre of the nucleus, as beyond this distance collisions no longer play a large role and the gas flow can be assumed to be close to radial [Marschall et al., 2016; Zakharov et al., 2018].

We also neglect gravity. This is based on the fact that the gravity field of comet 67P/CG is very weak ($\sim 10^{-4}$ m s⁻² at the surface) and the speed at which gas particles leave the surface is much higher than the average escape velocity of 0.81 m/s [Thomas et al., 2015b]. Under the given illumination conditions most of the gas particles are ejected from the surface at speeds above 100 m/s. We estimate that with constant speed, gas particles reach the edge of the simulation domain in less than 2 minutes. This is only 0.27% of the rotation period of comet 67P/CG [Keller et al., 2015], which means we can in principle neglect the influence of the nucleus rotation in the coma

Parameter	Symbol	Value
Solar irradiance at 1AU	S	1368 W/m ²
Directional hemispheric albedo	A	4%
Heliocentric distance	r_h	1.67 AU
IR emissivity	ϵ	0.9
Stefan-Boltzmann constant	σ	5.67×10^{-8} J/(m ² K ⁴ s)
Boltzmann constant	k_B	1.38065×10^{-23} J K ⁻¹
Lower boundary temperature	$T_{nucleus}$	50K
H ₂ O Latent heat	$L_{(H_2O)}$	2.84 MJ/kg
CO ₂ Latent heat	$L_{(CO_2)}$	0.45 MJ/kg
Rotation period	P	12.406 h
Number of depths	N_z	200
Number of rotations	N_{rot}	20

Table 4.1: Physical parameters used in the model.

and use steady state DSMC solutions for the flow. However, the nucleus rotation is taken into account in the thermal model used to compute the surface boundary conditions as explained in Section 2.2.3.

We assume that the activity is mainly driven by H₂O and in a smaller percentage by CO₂, as these molecules have been determined as two of the main volatile species of 67P/CG coma [Le Roy et al., 2015; Combi et al., 2020]. We use mixing ratios CO₂/H₂O in terms of mass loss of about 7% and 14%. We have selected these values based on the mean estimates of the gas density above the nightside needed to fit ROSINA data [Bieler et al., 2015b]. The day to nightside brightness ratio of the dust coma also indicates nightside outgassing [Gerig et al., 2020].

Other authors [Skorov and Rickman, 1995; Skorov et al., 1999a, 2001, 2002a,b, 2011; Davids-son and Skorov, 2004] have produced mathematical models of the surface layer to account for the effect of finite porosity on the gas flow from a sub-surface sublimation front. These models are, however, 1D and our aim is to provide for the first time 3D solutions for the gas flow and ultimately for complex shapes. This additional complexity prevents more sophisticated numerical solutions. We have ignored the influence of heating of gas through collision with a hotter dust mantle, e.g. Christou et al. [2018], in the present model, considering that these additional effects probably only result in relatively small changes in the position of the sublimation front due to the exponential change in sublimation rate with temperature. However, we have set a test with larger surface temperatures as an approximation for such physical processes.

4.3 Boundary Conditions

In this section we describe the selection of models with different boundary conditions (listed in table 4.2) based on previous estimates of the thermal inertia of comet 67P/CG. The listed free parameters have been varied to, first, show the effect of thermal inertia in the model and, second,

Case	Γ ($J/(m^2K\sqrt{s})$)	κ ($W/(mK)$)	ρc ($J/(m^3K)$)	δ (cm)	α (m^2/s)	z_{H_2O} (cm)	z_{CO_2} (cm)	$\frac{Q_{CO_2}}{Q_{H_2O}}$	$\frac{H_2O}{EAF}$	$\frac{CO_2}{EAF}$
A0	0	0	3.0 %	...
B0	40	1×10^{-2}	1.6×10^5	2.98	6.25×10^{-8}	1.40	20.0 %	...
B1		1×10^{-2}	1.6×10^5	2.98	6.25×10^{-8}	1.40	1.40	6.8 %	20.0 %	0.1 %
B2		1×10^{-2}	1.6×10^5	2.98	6.25×10^{-8}	1.40	5.62	6.8 %	20.0 %	0.3 %
B2 ^(C)		1×10^{-2}	1.6×10^5	2.98	6.25×10^{-8}	1.40	5.62	6.8 %	31.1 %	0.4 %
B3		1×10^{-2}	1.6×10^5	2.98	6.25×10^{-8}	1.40	5.62	13.8 %	20.0 %	0.6 %
B4		6×10^{-3}	2.66×10^5	1.79	2.25×10^{-8}	1.40	5.62	6.8 %	41.6 %	0.7 %
C1	80	4×10^{-2}	1.6×10^5	5.96	2.5×10^{-7}	1.40	5.62	6.8 %	6.8 %	0.1 %
C2		4×10^{-2}	1.6×10^5	5.96	2.5×10^{-7}	2.81	11.24	6.8 %	12.6 %	0.15 %

Table 4.2: List of tested parameters for model calculations. All cases lead to a production rate of 50 kg/s for H₂O.

show the influence of including a small amount of CO₂ in the gas flow field. All cases listed in table 4.2, except case B2^(C), are set using the decoupled mode of the thermal model in which the thermal properties of each front are independent from the other sublimation front. This is justified by the fact that the EAFs are generally small compared to the total area so that the H₂O sublimation front can be independent of the CO₂ front. Case B2^(C) uses a coupled mode to account for the effect of including CO₂ on H₂O sublimation and vice versa. In this case, the sublimation of both species influences the temperature gradients in the system and thus the production rates of each species. We find, predictably, that the *EAF* for both species has to be slightly larger in order to compensate the different energy distribution between the two sublimation fronts compared to the decoupled mode. The H₂O production rate is set to $Q_{H_2O} = 50$ kg/s, which is a mean estimate of the global production rate measured by ROSINA for comet 67P/CG during its spring equinox at 1.67AU.

We first have neglected the thermal conductivity term and studied a case in which the thermal inertia is set to zero (case A0). It is used as a standard case to compare with results of cases with different thermal inertia values. In the case where the thermal inertia is zero, the model requires the absence of a dust mantle on the top of the sublimation front of H₂O, which leads to a very low *EAF* compared to the other cases where a dust mantle is introduced. The *EAF* to match the required production rate depends not only on the depth of the sublimation front, but also on the thermal conductivity of the nucleus as indicated by cases B2 and C1 in Table 4.2. The thermal skin depth of Equation 2.9 can be re-written in term of the thermal diffusivity (α) through the equation

$$\delta = \sqrt{\alpha \frac{P}{\pi}} \quad (4.1)$$

where α measures the rate of transfer of heat from the surface to the interior of the nucleus.

Sublimation fronts at different depth have been selected for H₂O and CO₂ molecules with the assumption that CO₂ has to be more depleted close to the surface because of its lower free sublimation temperature. The chosen values are of course not unique, but are intended to

investigate the range of possibilities.

We have used the temperature at the sublimation front of each molecule (T_{H_2O} and T_{CO_2}) as the boundary condition for our DSMC simulations, so that these are the temperatures at which the sublimating flow escapes from the (sub)surface into vacuum. However, the dust mantle on top of the fronts is not transparent to gas emissions and there should be some heat exchange between the dust-matrix and the gas particles which would be responsible for higher temperatures of the gas leaving the nucleus [Christou et al., 2018] and ultimately results in higher terminal velocities for the flow. Consequently, we have also used the surface temperature as a boundary condition for a variation of case B2 and studied how it changes the average characteristics of the gas flow.

4.4 Results

In the first part of this section, we discuss the outcome of the thermal model to study the daily evolution of the temperatures at the sublimation front and at the surface for all the cases listed in Table 4.2. In the second part, we use the slices through the DSMC domain along the equatorial plane to study the role of thermal inertia in modifying surface source distributions and the effect of CO_2 activity in the flow dynamics.

4.4.1 Diurnal evolution of temperatures at the surface

An overview of the variation of temperatures over one comet rotation is shown in Fig. 4.1. In this Fig., the sunrise terminator and sunset terminator are at 0h and 6.2h, respectively. Figure 4.1a illustrates the daily evolution of the surface temperature, the modulation of which is similar on the dayside for all cases, with its maximum shortly after midday. Case A0 has no dust mantle at the top of the sublimation front, therefore its maximum temperature is below 200K and its maximum is at midday. Cases with dust mantles and low thermal inertia values (40TIU) conduct heat less well and, therefore, the amplitude of their diurnal temperature curves is larger. This means that their surface layers heat very quickly when illuminated, but also cool faster when solar radiation decreases. On the other hand, cases with larger thermal inertia values (C1 and C2) have lower surface temperatures on the dayside.

The evolution of the temperature at the sublimation front of H_2O is shown in Fig. 4.1b. The maximum temperature is always on the dayside. After the sunset terminator the temperature decreases slowly with time, except for the coupled case B2^(C), in which the temperature at the H_2O -front decreases much faster due to the presence of the CO_2 outgassing at deeper layers of the nucleus. The case with a larger ρc value (B4) has the smallest range of H_2O temperatures during day, because the thermal diffusivity α is smaller in this case in comparison to case B2, which has the same thermal inertia value and depth for both sublimation fronts. Therefore, the lower α is, the slower is the rate of transfer of heat within the material. Case C2 also has a small H_2O temperature difference between dayside and nightside, but in this case it is caused by the

combination of a larger thermal inertia value and sublimation fronts two times deeper. We see in these models expected trends. Temperatures at an H₂O sublimation front close to the surface (within 1 thermal skin depth δ) suggest dayside sublimation of H₂O with only a small phase shift towards the terminator. In the higher thermal inertia case with larger front depth, the phase shift is larger.

Finally, the temperature evolution of CO₂ is shown in Fig 4.1c. It shows that CO₂ activity is coming exclusively from the dayside if the sublimation front is very close to the surface (B1) for a low thermal inertia value (40TIU). Once we increase the depth of the sublimation front from 1cm to 5cm and double the thermal inertia value (C1), the CO₂-ice also has its maximum activity on the dayside, but it is shifted about 40 minutes towards sunset compared to case B1. For all other cases, the heat wave is maximum around sunset, triggering higher temperatures and fairly large production rates on the nightside. The evolution of these cases, except B4, follow the same trend, however, a nucleus with higher thermal inertia increases the thermal energy at the front, which translates into larger temperatures for case C2. We can therefore say that the temperature at a sublimation front of CO₂ well below its surface maximizes close to the sunset terminator or even beyond for thermal inertia values expected at 67P/C-G.

4.4.2 DSMC calculation

4.4.2.1 Gas flow fields

The DSMC results presented in Fig. 4.2 are slices through the 3D simulation domain on the xy-plane for the number densities for all tested cases. The view is from above the north pole of the nucleus. The comet's rotation is anti-clockwise and the sub-solar point is located at (-2km, 0, 0) in the comet's fixed frame. We have defined this to be the 0° longitude, with all other longitudes being indicated in the upper left panel of the Fig.. A sub-solar point of 0° is equivalent to midday at approximately 3.1h (in Fig. 4.1), while 90° and 270° longitude correspond to the sunset terminator (~6.2h) and the sunrise terminator (0h), respectively. The difference between day and nightside in terms of number densities on the nucleus is in agreement with the boundary conditions for temperature shown in Fig. 4.1. However, the distribution of the flow field around the nucleus changes as a consequence of inter-molecular interactions within the mixture of gases.

By comparing the number densities in Fig. 4.2, we can see the changes in the gas distribution away from the sub-solar point and therefore the effect of the thermal inertia on the sublimation of H₂O-ice and CO₂-ice. In order to quantify such changes, we have also extracted the number density along the circle at the edge of the simulation domain (highlighted in blue in Fig. 4.2) in steps of 10° on the xy-plane of the DSMC results to obtain its daily variation as shown in Fig. 4.3. We notice, for example, that compared to the reference case (A0), the single-species case (B0) with a thermal inertia of 40TIU shows a very similar outgassing pattern, but has a shift by about 20° in longitude with respect to the sub-solar point. This is also true for all multi-species cases

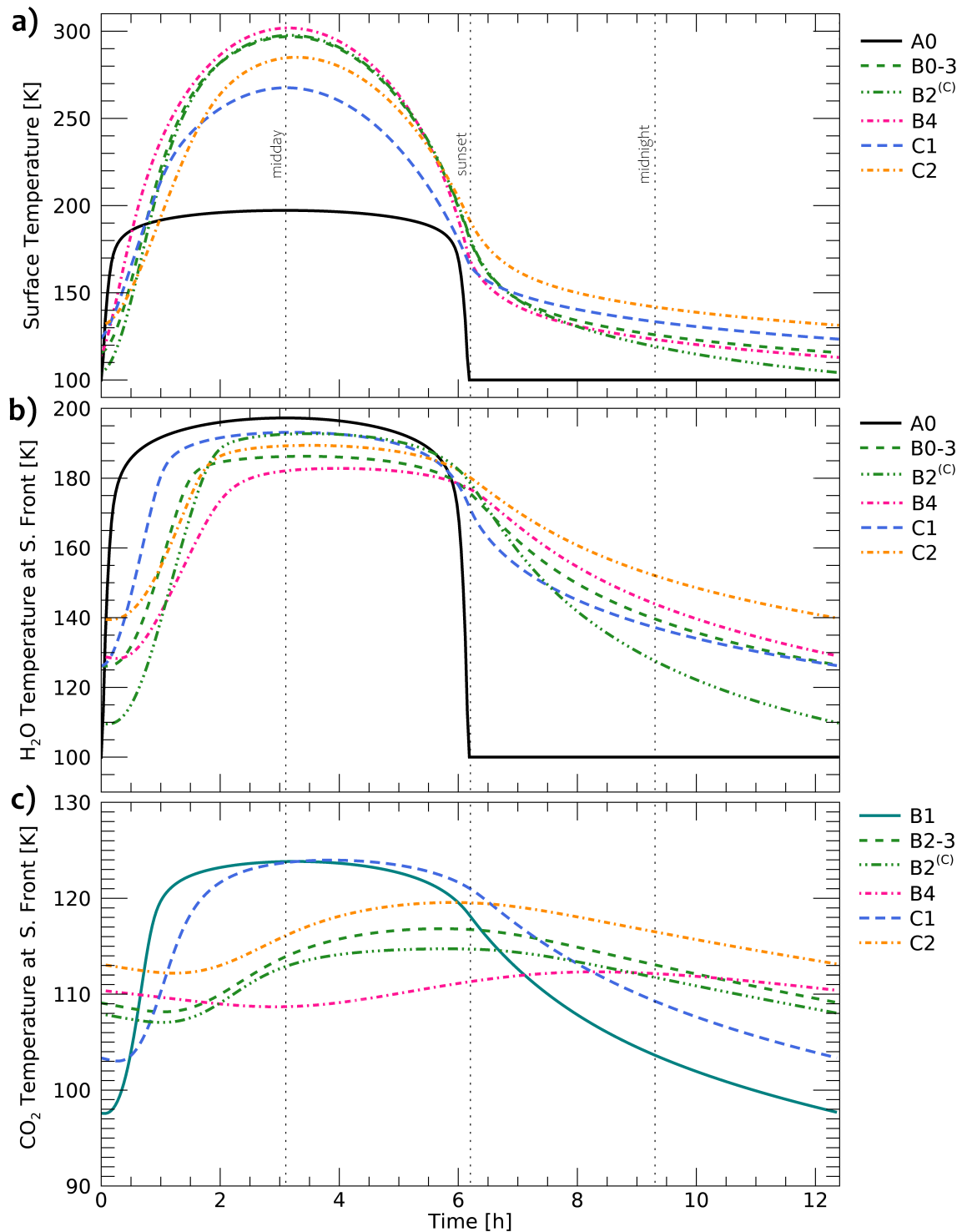


Figure 4.1: Diurnal change of the temperature at the surface (a), at the sublimation front of H₂O-ice (b) and at the sublimation front of CO₂-ice (c). The parameters of the different models are presented in Table 4.2. The dotted vertical lines indicate midday, the sunset terminator and the midnight.

with non-zero thermal lag, which have a similar shift in the direction of maximum emission of H₂O outgassing.

In terms of CO₂ number densities, however, the distribution of activity is very heterogeneous and can influence the number of H₂O particles transported towards the nightside of the comet. Cases B1 and C1, for example, show that if CO₂ outgassing is predominantly from the dayside, then H₂O can be easily transported towards the nightside and the abundances measured above the anti-solar point of the nucleus could be equal to or higher for H₂O than for CO₂ compared to the other multi-species cases. However, if the sublimation front of CO₂ is set at deeper layers for the same thermal inertia value (cases B2-4), the maximum activity of CO₂ is shifted beyond the sunset terminator and the H₂O number densities can decrease by at least one order of magnitude in the region above the anti-solar point. If one increases the production rate mixing ratio Q_{CO_2}/Q_{H_2O} by a factor of 2 (case B3), one gets a larger region on the nightside in which H₂O is effectively "blocked" compared to case B2. However, in terminator orbits similar to those frequently used by the Rosetta spacecraft at 67P/CG these differences would not have been detectable.

In the panel on the bottom left of Fig. 4.2, we can compare the effect of doubling the depth of the sublimation fronts for the high thermal inertia cases. For H₂O the effect is minimal on the dayside, however, on the nightside the lower number density values are linked to the maximum abundance of CO₂ in this region. In other words, we obtain a stronger shift in the maximum CO₂ outgassing for fronts at deeper layers, which influence the distribution abundance of H₂O on the nightside of the comet. This is intuitively correct based on our understanding of how thermal inertia and the depth of the sublimation front influences the surface production.

4.4.2.2 Diurnal evolution of mixing ratios

Number densities in Fig. 4.3 can be used to define a CO₂ to H₂O number density mixing ratio (CO₂/H₂O) as illustrated in Fig. 4.4 for all multi-species cases used herein. The maximum mixing ratio is close to local midnight in all cases. Case B1 only shows a weak variability with local time as one goes around the nucleus. But even here the maximum mixing ratio is on the nightside.

Cases with same boundary conditions, but set in different coupling modes (B2 and B2^(C)) have the same evolution trend. However, the overall mixing ratio is smaller for the coupled case than for the decoupled case. Using the Fourier's law of thermal conduction in its one-dimensional form, we can calculate the heat flux density (q_z) at each sublimation front

$$q_z = -\kappa \frac{dT}{dz} \quad (4.2)$$

and estimate the heat distribution between the two layers for both coupling modes. Figure 4.5 shows the diurnal evolution of q_z at the H₂O and CO₂ sublimation fronts for cases B2 and B2^(C), from which we can notice how the presence of CO₂-ice at deeper layers decreases the heat flow at the H₂O sublimation front around midday, and therefore, the energy budget for H₂O sublimation.

CHAPTER 4. THE EFFECT OF THERMAL CONDUCTIVITY ON THE OUTGASSING AND LOCAL GAS DYNAMICS FROM COMETARY NUCLEI

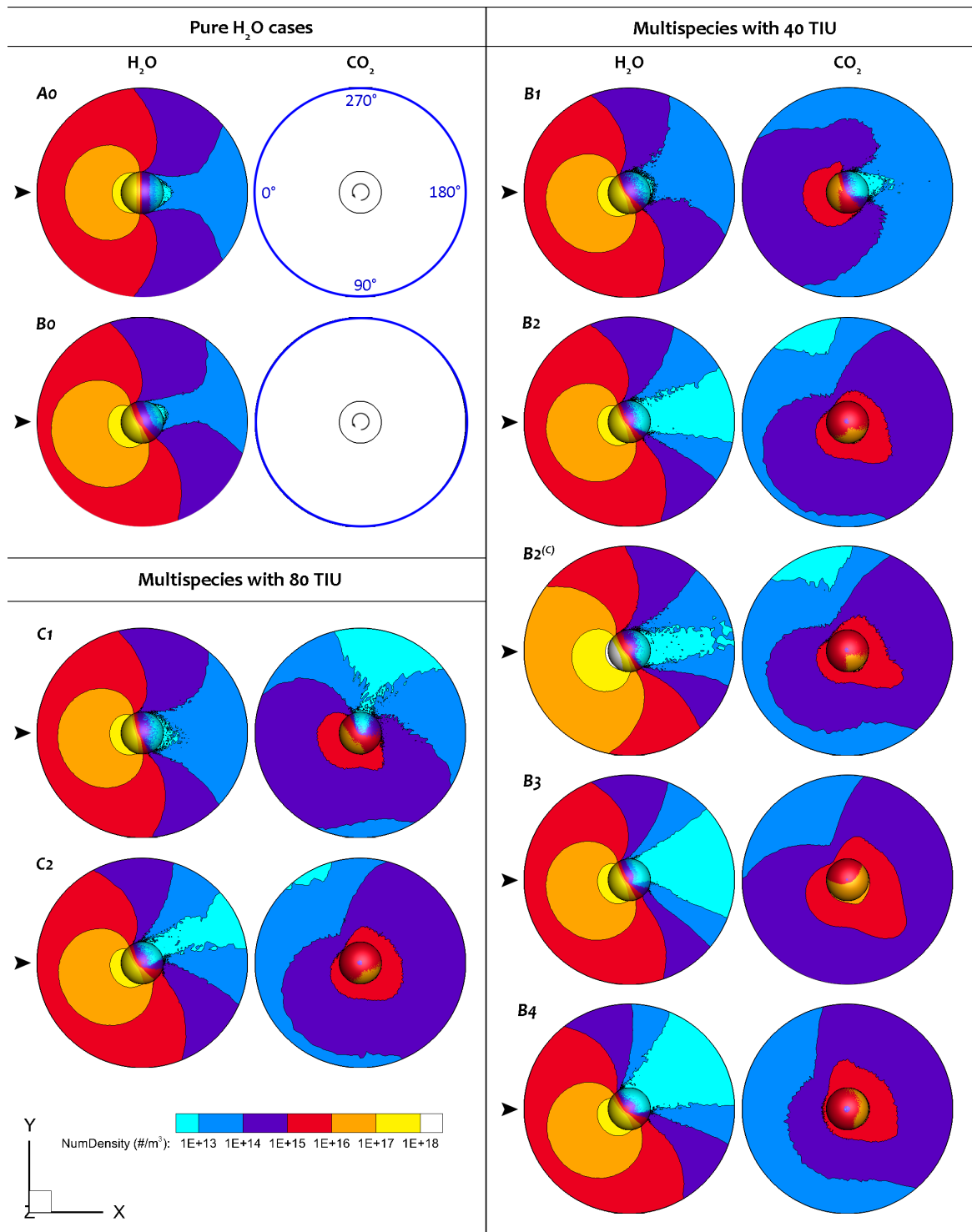


Figure 4.2: Slice of the 3D simulation domain on the xy-plane, with information of number density within the flow for all cases listed in Table 4.2. The arrows on the left side of each slide indicate the position of the sub-solar point at (-2km,0,0), which is also labeled as the 0° longitude in the upper left panel.

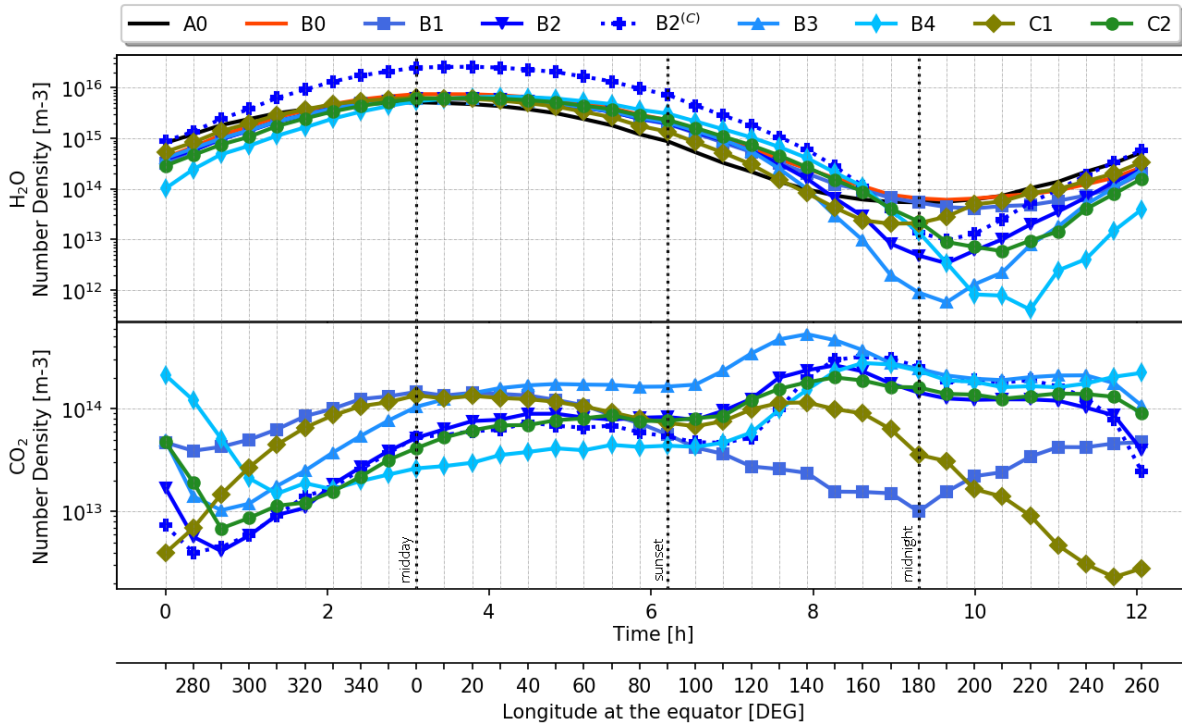


Figure 4.3: Temporal and longitudinal variation in the H_2O and CO_2 number densities obtained with DSMC calculations at 8km from the surface. The dotted dark vertical lines indicate the location of the midday, the terminator with the sunset at 90° and the midnight.

On the nightside, the heat flux is moving in the $-\vec{z}$ direction, as the surface layer gets colder faster compared to the subsurface layers of the nucleus. Similar to what happens around midday, the difference in heat flux between the decoupled and the coupled mode for the H_2O sublimation front increases about 1h after sunset.

By increasing the thermal inertia value from 40TIU to 80TIU, we see that for the same front depths (C1 compared to B2), the amplitude of the mixing ratio variation is smaller and occurs earlier, because the CO_2 outgassing has a slightly higher production rate on the dayside of the comet. However, if one also doubles the depth of the sublimation front for both molecules, the maximum mixing ratio is after midnight due to the strong delay in the thermal wave reaching deeper layers.

4.4.2.3 Diurnal evolution of gas temperatures and velocities in the coma

Figure 4.6 shows a polar view of the gas temperature (upper row) and speed (bottom row) flow field, with all data points $(\vec{x}, \vec{y}, 0)$ in the simulation domain for cases A0, B0 and B2. A simple comparison of cases A0 and B0 shows that including thermal inertia in the model also affects the temperature and velocity distributions of H_2O about the nucleus. Similar to results in Fig. 4.2, in terms of temperature, H_2O responds strongly to illumination, but there is a small shift in

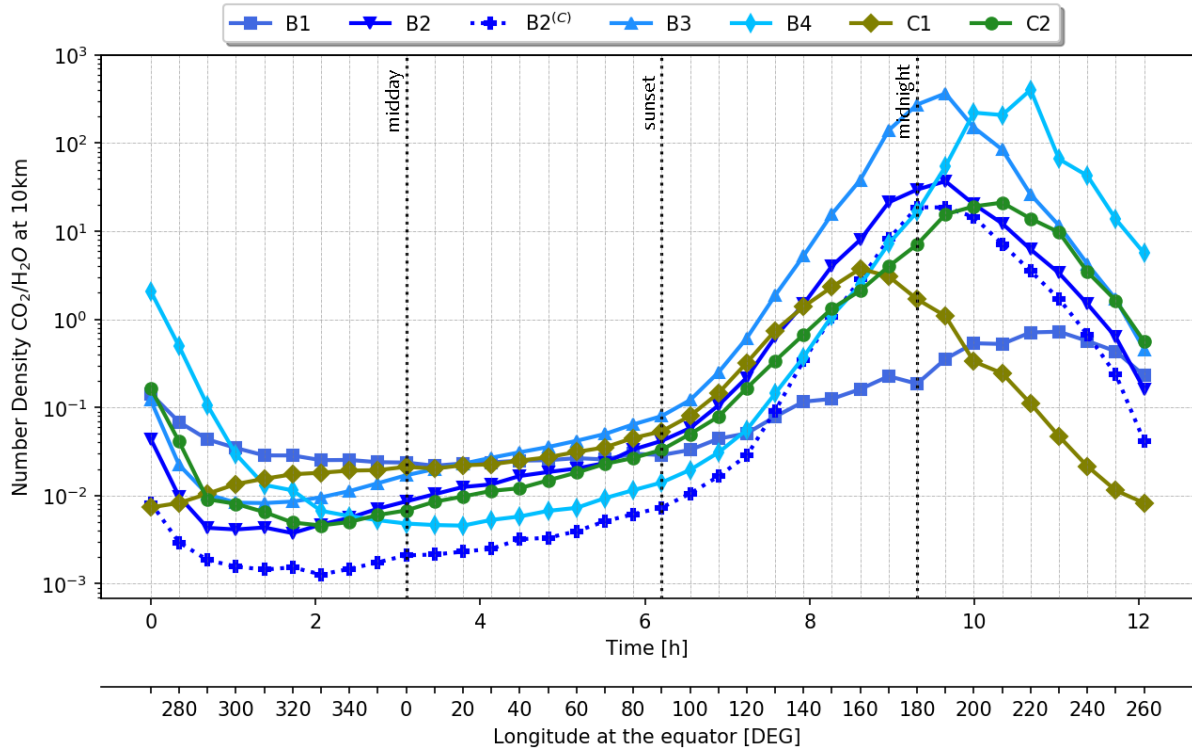


Figure 4.4: Variation in the CO_2 to H_2O number density mixing ratio obtained with DSMC calculations at 8km from the surface with longitude at the equator for all cases with multi-species gas sources. The dotted dark vertical lines indicate the location of the midday, the terminator with the sunset at 90° and the midnight.

the same direction of the nucleus' rotation when including thermal inertia. This can result in different temperatures very close to the nucleus when taking measurements in terminator orbits.

In terms of flow velocities, we see that when CO_2 interacts with H_2O (case B2), the velocities decrease quickly (by approximately 200 m/s) close to the 130° and 260° longitude positions. Results for both molecules show a very similar behaviour towards the dayside, which is an indication of the strong effect of H_2O increasing the nominal speed of CO_2 in this region through drag. On the nightside however, the flow speed of H_2O seems to be lower than for CO_2 presumably arising from lateral flow and low collision frequencies.

We can also extract information on the average temperature and speed of the whole flow at the edge of the simulation domain, as has been done before for the number densities. Figure 4.7 illustrates both variables at 8km from the surface of the nucleus as a function of longitude (equivalent to local time). Cases where most of the flow is focused towards the dayside of the comet (A0, B0, B1 and C1), have maximum gas temperatures around midnight. This can be explained by the fact that in these cases, H_2O gas can be transported more easily to the nightside compared to the cases with a larger CO_2 presence. Therefore, in those regions the temperature that dominates is the temperature of the H_2O gas flow. All other cases have lower gas temperatures, which is

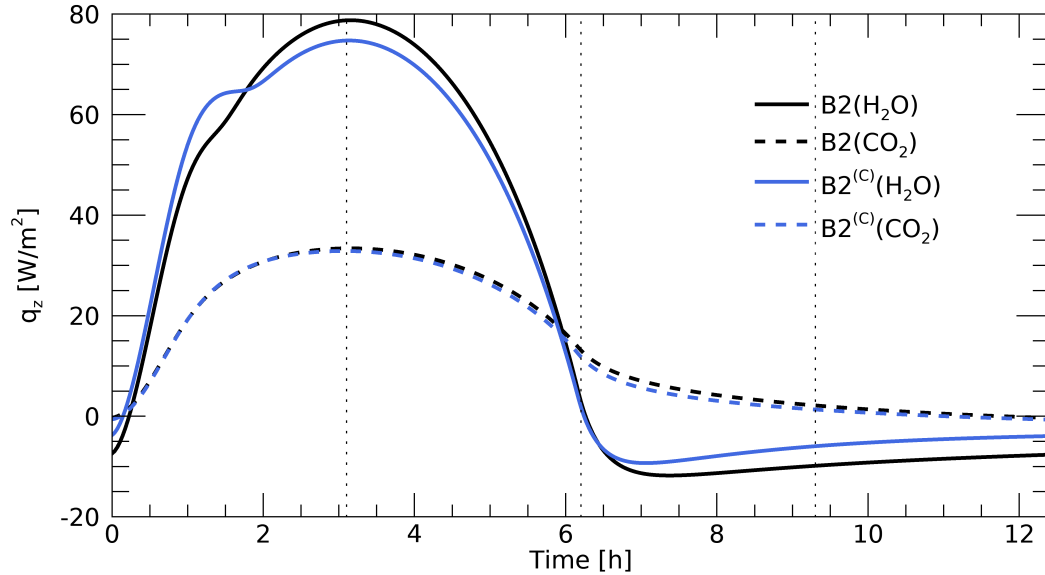


Figure 4.5: Diurnal variation of the heat flux density at the H₂O and CO₂ sublimation fronts for the decoupled case B2 and the coupled case B2^(C).

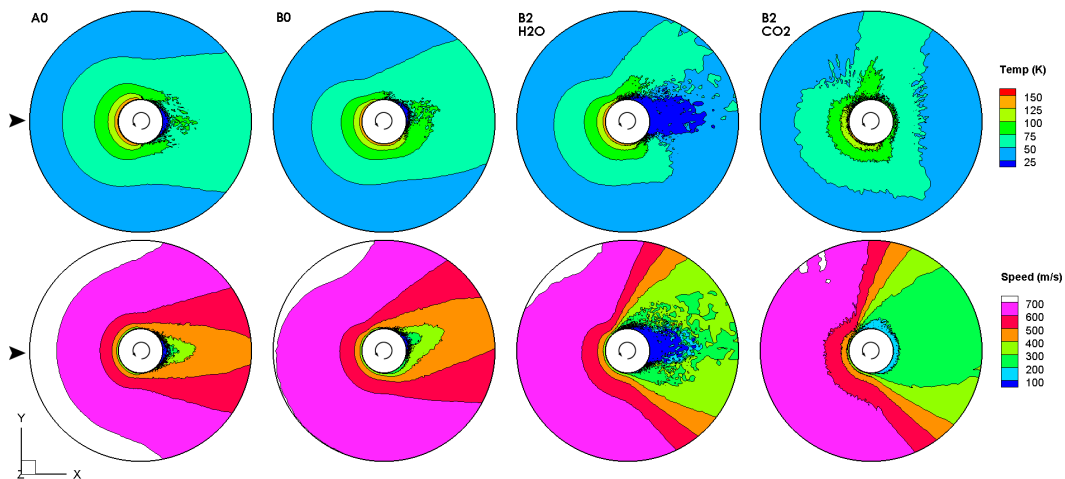


Figure 4.6: Slice of the 3D simulation domain on the xy -plane, with information of temperature (upper row) and speed (bottom row) within the flow for model A0, B0 and model B2. The arrows on the left side indicate the position of the sub-solar point. By looking above the northern hemisphere of the nucleus, we can appreciate how the temperature and speed of the H₂O flow is slightly shifted from the sub-solar point once thermal inertia is included in our model and how the presence of CO₂ affects the behavior of the H₂O gas field towards the nightside.

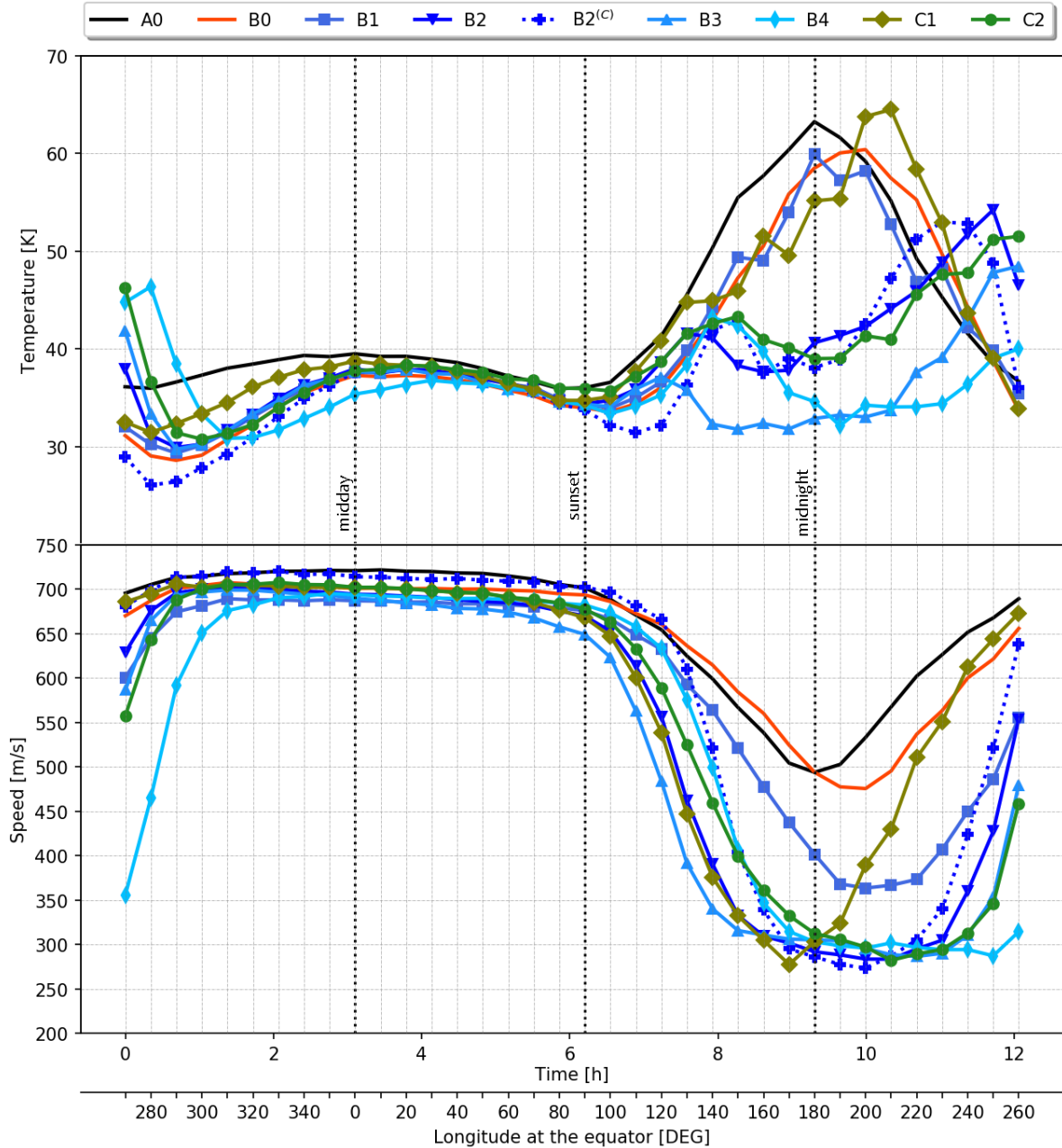


Figure 4.7: Averaged temperature and velocity of the gas mixture obtained with DSMC calculations at 8km from the surface on the xy-plane (Fig. 4.6) as a function of the longitude for each of the cases (Table 4.2). Data with circles illustrate the results from simulations for which only one gas molecule was outgassing from the nucleus. Data with diamonds are models in which a mixture of H_2O and CO_2 was used. The vertical dashed lines represent the location of the terminator with the sunset at 90° and the sunrise at 270° .

linked to larger abundances of CO_2 at midnight (see Fig. 4.4). Similar to the effect we see in the mixing ratios, comparing cases B2 and B3 shows that the increase of a small amount of CO_2 can also decrease the temperature of the flow by about 10K on the nightside. This is also caused by a smaller abundance of H_2O gas in this region for case B3. The difference between cases in decoupled and coupled mode (B2 and B2^(C)) is minimal in terms of temperature differences. We can also see these two cases have a very similar trend to case C2, showing that there are multiple combinations of model parameters than can lead to similar temperature results. Hence, it is difficult to establish unambiguously the physical properties of the nucleus from these quantities. The case with a larger ρc value (B4) has a smaller variation of temperature with time at 8km from the surface compared to case B2, which has the same thermal inertia value and front depths. The difference is minimal on the illuminated areas of the comet, however, bigger differences arise as one gets closer to the sunrise terminator, because the initial temperatures at the CO_2 sublimation front have a larger delay with longitude.

In panel on the bottom of Fig. 4.7 we see the variation of the speed of the mixed flow at 8km from the surface in one comet rotation. On the dayside all cases have very similar speeds. In contrast, on the nightside, most multi-species cases have fluxes with speeds between 100-200 m/s slower than the single-species cases due to the higher abundance of CO_2 , which has a molecular mass more than two times bigger than H_2O . For case B1, the speed of the flow on the nightside does not decrease as much, because H_2O molecules can travel more easily to this region. For case C1, the range in which the flow speed is small is much thinner than the other cases, which can be understood by the distribution of CO_2 molecules around the nucleus that is shown in Fig. 4.2 for this case. Once again, a delay of between 20-30° is observed for case B4 when looking at the speed of the flow.

4.4.2.4 Artificial heat transfer from the dust mantle to the gas

As mentioned in Sect. 4.3, one extra case has been tested (with $T_{surface}$ as the initial temperature at which gas particles leave the surface) in order to include the heat exchange between the dust mantle and the gas particles released after sublimation. This was compared to case B2. Vertical profiles of number density, Doppler velocity and temperature above the sub-solar point for these cases are shown in Fig. 4.8. In terms of number density, a larger thermal input does not make any difference for each molecule. However, the change in velocity is approximately +60m/s for H_2O gas. For CO_2 gas the change is +90m/s close to the nucleus and 60m/s at 8km from the surface. Assuming that the heat exchange between the dust mantle and the released gas molecules is 100% efficient, we can also determine from these cases that the H_2O gas flow can be about 100K warmer at 8km from the surface when looking exactly above the sub-solar point. For CO_2 however, a larger thermal input shows a difference of -10K at large altitudes.

In terminator orbits such differences are difficult to detect for the same model parameters. In Fig. 4.9, we have plotted the average number density, Doppler velocity and temperature for

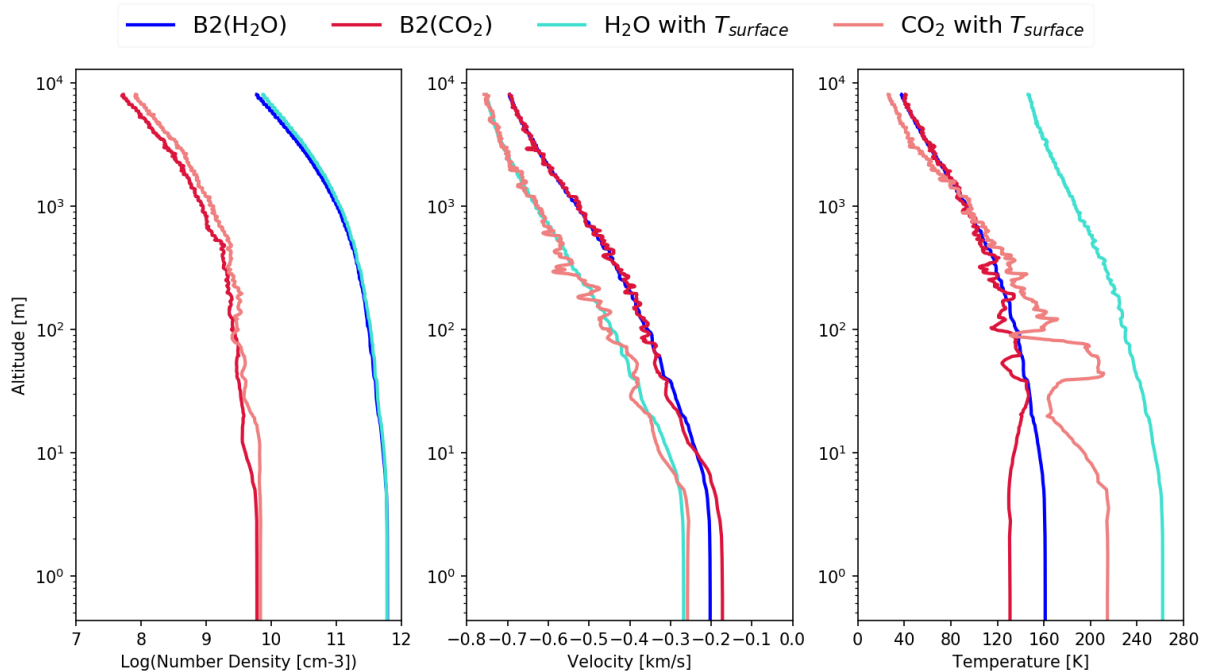


Figure 4.8: Vertical profiles of number density, Doppler velocity and temperature with altitude at the 0° phase angle for each gas molecule. Case B2 was tested with two different boundary temperatures at the surface: the temperature at the sublimation front and the temperature at the surface, which is about 100K greater than the other at the sub-solar point.

the mixed flow at 90° and 270° longitude. Similar to Fig. 4.8, we see no change in terms of number densities for the same viewing geometry and different thermal inputs. When looking at flow velocities, we can see slightly bigger differences far from the nucleus. However, these are less than 30 m/s and 50 m/s for the sunset terminator and sunrise terminator, respectively. Finally, our results suggest that in terminator orbits, small changes in the surface temperature can generate significant differences at 8km from it. At the sunset terminator a temperature difference of approximately 10K, can increase to about 70K at large altitudes. While for the sunrise terminator, the same difference at the surface, can produce temperature differences in the coma up to 90K at 8km from the surface.

4.5 Discussion

We have found that thermal inertia produces moderate changes to the distribution of H_2O emissions. However, CO_2 is more volatile and its surface emission distribution can be substantially changed by the assumed properties of the surface layer. For cases with sublimation fronts at large depths or relatively low thermal inertia values (40TIU), CO_2 activity was mainly focused on the nightside of the comet, which is in agreement with the proposal of Bockelée-Morvan et al. [2015] and the evidence for nightside dust emission found by Gerig et al. [2020] findings. I note

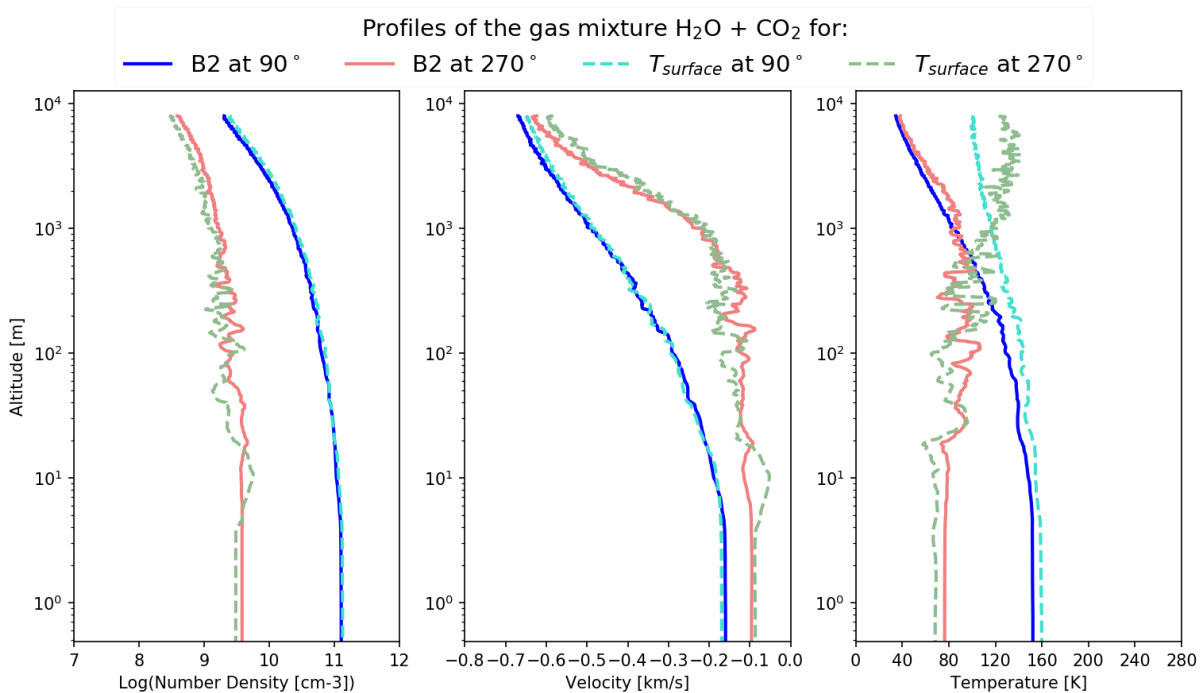


Figure 4.9: Vertical profiles of number density, Doppler velocity and temperature with altitude at terminator orbits for the gas mixture.

that several authors have assumed some level of outgassing from the nightside but this is the first work that provides a physical model of nightside outgassing and analyses the consequences. Therefore, the choice of different model parameters can impact the interpretation of remote sensing and in situ measurements significantly.

Several authors have used different approaches to accurately reproduce local measurements of number density within the coma of comet 67P/CG taken by ROSINA. However, when studying multiple data sets from other instruments on board the Rosetta spacecraft, Marschall et al. [2019] found a discrepancy between the model results and the measurements of temperature and speed along the MIRO line of sight. Given that many of the Rosetta orbits were on the terminator plane, our results show that including thermal lag can produce slight differences in the distribution of the gas sources at the surface, which can be detectable at large distances from the nucleus when looking above the terminator. However, a similar analysis needs to be done for the complex shape of comet 67P/CG [Preusker et al., 2017], in which in situ ROSINA/DFMS and MIRO measurements of number densities, temperatures and speeds along the viewing geometry are used to constrain the activity distribution at the nucleus. This can also be used to reproduce patterns of dust activity triggered by the gas as it is observed in OSIRIS images.

Given the large complexity of the nucleus structure and composition, the use of a 1D thermal model for the energy transport within the nucleus only give us a rough estimate of the distribution of ice sources close to the surface. Energy losses due to lateral expansion or re-condensation

would also play a role in gas diffusion through the dust matrix. However, compared to the radial diffusion of the flow, we assume their contribution to be very small. The cases in the current paper are possibly extreme scenarios of the real conditions in cometary nuclei. However, their results help us to constraint the thermophysical properties used when modelling a single- and multi-species cometary coma.

4.6 Conclusions

We have built a model to simulate cometary outgassing and study in detail the influence of CO₂ - H₂O mixtures on the distribution of gas activity around a spherical comet nucleus. We use a simplified thermal model to provide input to a DSMC code to study the properties of the gas flow under several conditions. We have seen the strong effect of thermal inertia on the distribution of the gas sources at the surface. This is especially important for contributions to nightside activity. The interaction between H₂O and CO₂ plays a significant role in the overall flow dynamics. We enumerate the main findings of our study in the following points:

1. Sublimation fronts for H₂O and CO₂ at 1cm depth and 40 TIU result in most of the activity being focused towards the illuminated regions of the comet. In order to produce substantial nightside activity, CO₂-ice needs to be deeper to produce a delay in the outgassing pattern towards sunset. CO₂ fronts at 5cm and 10cm depth with thermal inertia values of 40 TIU and 80TIU, respectively, produce their maximum activity shortly after sunset, which leads to strong emission from the non-illuminated regions of the comet.
2. A comparison between purely insolation driven models with 0 TIU, 40 TIU and 80 TIU shows us that by increasing the thermal inertia values one can shift the distribution of H₂O emission towards the evening terminator by about 20° in longitude from the sub-solar point. This results in considerable differences in number densities at positions far from the sub-solar point when compared to purely insolation driven models [Bieler et al., 2015b; Marschall et al., 2019]. In terms of the temperature and speed of the H₂O flux, no large changes are detectable. For CO₂-ice, cases with different thermal inertia values and sublimation fronts can display very different outgassing distributions. These can have their maxima beyond the terminator and, thus, make CO₂-ice the main source of nightside activity (as proposed by Bockelée-Morvan et al. [2015] to explain VIRTIS observations of CO₂ and by Gerig et al. [2020] to explain dust observations made using OSIRIS).
3. Number density mixing ratios at 8km from the surface of the nucleus show that H₂O is the most abundant species on the illuminated side of the comet as expected. There is also a strong effect of CO₂ activity on the distribution of the H₂O flow field on the nightside, which can decrease the amount of H₂O molecules per cubic meter by at least one order of

magnitude compared to a pure H₂O case. This arises from CO₂ limiting lateral expansion of the H₂O.

4. On average, CO₂ gas decreases the flow velocities on the nightside of the comet. In the cases we studied, velocities were between 100-200 m/s slower than the cases without CO₂ activity. This is connected to the larger abundance in this region of CO₂. However, on the dayside, CO₂ has no significant effect on the temperature and speed of the flow.
5. Models with different energy inputs for the gas release from the surface, only show significant differences at > 8km from the surface when looking above the sub-solar point. Assuming that the dust mantle on top of the sublimation front can heat the gas by 100K as it leaves the nucleus, one can measure flow speeds 60-90 m/s faster and temperatures of H₂O gas around 100K larger at 8km from the surface. However, in terminator orbits, differences can only be seen in terms of the flow temperature, which can be between 70-90K warmer. For an ideal adiabatic expansion of the gas, these differences could be detected at larger distances from the nucleus.

In summary, the CO₂ emission distribution may be markedly different from H₂O and can also influence the H₂O gas distribution pattern. For non-zero thermal inertia and sublimation from depth, nightside gas emission will be non-negligible and is a potential source of dust above the nightside hemisphere of 67P/CG [Gerig et al., 2020].

Acknowledgements

This work has been carried out within the framework of the National Centre of Competence in Research PlanetS supported by the Swiss National Science Foundation. The authors acknowledge the financial support of the SNSF.

Raphael Marschall acknowledges the support from the Swiss National Science Foundation grant P2BEP2 184482."

3D modelling of the H₂O and CO₂ outgassing from comet 67P/CG

Constraining the nucleus composition of the comet using ROSINA,
MIRO and VIRTIS-M data for the Spring Equinox

Manuscript in preparation.

O. Pinzón-Rodríguez¹, S.-B. Gerig¹, R. Marschall², L. Rezac³, D. Kappel⁴, M. Rubin¹,
J. S. Wu⁵, and N. Thomas¹

¹ Physikalisches Institut, University of Bern, Switzerland Sidlerstrasse 5, CH-3012 Bern, Switzerland

² Southwest Research Institute, Boulder Office, 1050 Walnut St Suite 300, Boulder, CO 80302, USA

³ Max-Planck-Institut für Sonnensystemforschung, Justus-von-Liebig-Weg, 3, 37077 Göttingen, Germany

⁴ Deutsches Zentrum für Luft- und Raumfahrt (DLR), Institut für Planetenforschung, Rutherfordstrasse 2, Berlin 12489,
Germany

⁵ Department of Mechanical Engineering, National Chiao Tung University, Hsinchu, Taiwan

NOTE: The methods section has been taken out and included in Chapter 2 to avoid repetition.

Abstract

The purpose of this work is to link the activity distribution observed in the coma of comet 67P/CG with the composition and activity at the nucleus for the spring equinox. By this date, the comet is at a distance from to the sun of 1.67AU and its southern hemisphere starts to receive solar radiation after a long winter season.

We use a thermal model that includes an energy source due to solar radiation and energy sinks due to thermal emission from the surface, ice sublimation and thermal conduction. We use a dust mantle of 5mm thickness $40J/(m^2K\sqrt{s})$ and compare our results with a model that neglects thermal conductivity for superficial H₂O outgassing. Distributions of H₂O and CO₂ ices at different depths of the nucleus are set and tested using a 3D Direct simulation Monte Carlo method to model the coma. Our model results are compare with data from ROSINA, MIRO and VIRTIS-M onboard the Rosetta mission. Our work is therefore complementary to similar studies carried out for the November 2014 and May 2015 (equinox) periods [Marschall et al., 2016, 2019].

We have found that a thin dust mantle has a small effect in the temperature at the H₂O sublimation front, such that the difference in number densities within the flow fields are so small that ROSINA measurements are not able to detect. It however could have a strong effect on the expansion velocity of the gas in the extreme case the energy transfer is 100% efficient. Regional inhomogeneities in the H₂O content are confirmed, but the difference between them is probably smaller than previously determined. Even though many of the CO₂ IR emission features are reproduced by the model, the daily variation of CO₂/H₂O measured by ROSINA/DFMS seem to be very challenging to fit.

Thermal conduction plays a significant role in the sublimation of H₂O and CO₂ at different depths of comet 67P/CG's nucleus, specially in the most superficial layer, where a small difference in the energy budget can accelerate the average velocity of the gas by around 175 m/s close to the surface.

5.1 Introduction

The Rosetta mission studied comet 67P/CG and retrieved valuable information of the composition, structure and dynamics of its coma and surface. Continuum and spectral measurements of MIRO have been used to retrieve H₂O column densities and peak velocities around the nucleus [Biver et al., 2015; Gulkis et al., 2015]. Many studies have used numerical models to describe the outgassing of comet 67P/CG at different scales. Bieler et al. [2015a] used DSMC, a hydrodynamic code, and a purely geometric calculation to model the gas coma of comet 67P/CG to reproduce some of the number density results measured by ROSINA/COPS for the period between early August 2014 and January 1st 2015, when the comet was weakly outgassing. Multi-species outgassing has been studied by Fougere et al. [2016a,b]. H₂O and CO₂ sources were found to be not uniformly distributed over the surface of the nucleus, and differ significantly from one another. Fougere et al. [2016a] used a numerical inversion and DSMC calculations to model the comet outgassing, which is described by spherical harmonics. Their model is constrained by ROSINA/DFMS data, from which they obtain strong sources of H₂O on the *Hapi* region and CO₂ sources on the southern hemisphere of the comet. Their results reproduce ROSINA and VIRTIS observations for the time between August 4th 2014 and June 2nd 2015. ROSINA data up to February 2016, was later studied by Fougere et al. [2016b], who studied seasonal variations of the four major volatile species in the coma (e.g. Hässig et al. [2015]) using a numerical data inversion together with DSMC simulations. A parameter study of the inner gas coma of 67P/CG was done by Liao et al. [2016], who used DSMC simulations to investigate to which extend do model parameters influence the flow and gas temperature fields. Liao et al. found that thermal inertia and the rotational relaxation collision parameter have an insignificant effect at low H₂O production rates. In their 2018 paper, Liao et al. studied the re-condensation of H₂O ice at the surface of the comet due to gas coma deposition. They found gas deposition of several microns was more likely to be located in unilluminated areas of the dayside than on the nightside, due to the small amount of H₂O gas present at the nightside. Marschall et al. [2016, 2017] modelled the H₂O gas and dust emissions to reproduce ROSINA/COPS measurements and OSIRIS observations from August to September 2014. They also found inhomogeneous emissions of H₂O, with very strong sources coming from the neck of the comet, which together with outgassing from cliff areas produced a statistically better fit to ROSINA/COPS data compared to an purely insolation model with homogeneous ice sources everywhere (homogeneous EAF). A similar study was performed for the spring equinox in May 2015, in which Marschall et al. [2019] used data from ROSINA, MIRO, OSIRIS and VIRTIS-M to constrain their DSMC models of the coma. Their work includes inversions of MIRO data using a 1D radiative transfer code accounting for non-local thermodynamic equilibrium (non-LTE) effects, from which they determine that a purely-insolation driven model alone does not provide a good fit to the data. Imhotep and Hatmehit regions are observed to be very depleted in H₂O and dust emissions and they construct an inhomogeneous model that provides a better fit to the data. The RZC model by Zakharov et al. [2018] used DSMC, Eulerian/Navier-Stokes

equations and an iterative procedure to adjust the model parameters to reproduce the overall features of ROSINA/COPS and ROSINA/DFMS measurements in the period between August 1 and November 30, 2014. For H₂O, they use a classical sunlit ice energy budget equation and assume a small fraction of ice to be exposed. For CO₂, they assume sources to be distributed according to a cosine function $F = a + b \cos(z_{\odot}, 0)$, where a and b are free parameters and $z_{\odot} = \text{SZA}$. Zakharov et al. found illumination conditions to be the main driver for activity, however, they infer an inhomogeneous model that fits ROSINA data better. An inverse coma model has been used to fit ROSINA/DFMS data in 14 day intervals and construct the overall temporal evolution of the major volatile species in the coma during the entire comet mission [Läuter et al., 2018]. Läuter et al. [2020] extended this study to 14 gas species from comet 67P/CG using the same inverse modelling approach.

In general, all studies find that the outgassing pattern was observed to be periodical due to the combination of the nucleus rotation and shape, at the same time that the largest H₂O column densities were determined to originate from the *Hapi* region at the northern hemisphere of the comet. However, as the comet approaches perihelion, it was observed that the maximum outgassing originates from the southern hemisphere with a peak production rate of 0.8×10^{28} molecules per second, which is 2.5 times lower than what ROSINA data suggest for the same time [Biver et al., 2019]. Regarding CO₂ emissions, they seem to be mainly located in southern areas, specially after perihelion, where the sublimation fronts are expected to get closer to the surface due to a strong erosion.

In the current chapter, we shall study the gas emissions from the complex shape nucleus of comet 67P/CG for the time around the spring equinox. We do a similar analysis to the one presented in Chapter 4, in which thermal inertia is included in the thermal model to calculate the distribution of ice sources at the surface. This time however, we study the effect of a thin dust mantle at the top of the sublimation front of H₂O in the temperature of the gas as it is being released from the nucleus. We also include CO₂ outgassing from deeper layers of the nucleus assuming a constant thermal inertia of 40 thermal inertia units (TIU). The model results are compared with data from ROSINA, MIRO and VIRTIS-M using the methods described in Section 2.5.

5.2 Model assumptions and boundary conditions

For the studies in the current chapter, we use the low-resolution mesh for the comet nucleus (see Section 2.1). The selection of the low-res mesh is based on: i) reduction of the computational time of the thermal model at each of the 40'000 facets and ii) to reduce the computational time of the DSMC calculations given the low production rates at equinox without compromising the accuracy of the results. Similarly to the spherical nucleus case, we define the outer limit at 10 km and neglect gravity effects on the gas. All nucleus surface facets are set to be reflective, such that

simulation particles that scatter back to the surface do not stick to it and are reflected diffusely. At the outer surface of our simulation domain, facets are set to a vacuum boundary condition.

The selection of model parameters is shown in Table 5.1. We have selected three single-species cases for H₂O outgassing. Cases M1 and M2 are the same insolation-driven cases with homogeneous and inhomogeneous distribution of H₂O ice sources (EAFs), respectively, studied in Marschall et al. [2019]. Case M3 has been introduced to study the effect of a 5mm thickness dust mantle at the top of the H₂O sublimation front with a thermal inertia of 40TIU and a homogeneous distribution of ice at the sub-surface. Case M4 is introduced to study the effect of a CO₂ sublimation front at deeper layers of the nucleus for the same configuration as model M3. Case M4 has been computed in coupled mode (using equations 2.7a and 2.7b). Cases M5 and M6 are computed in decoupled mode, in which we include a CO₂ layer at 50mm from the surface. Finally, Case M7 was set to study the change in CO₂ emissions, if we assume shallower depths for its sublimation front. All cases that include CO₂ outgassing assume a homogeneous distribution of CO₂-ice in the nucleus, while the inhomogeneous cases in Table 5.1 refer only to H₂O-ice.

Given that ROSINA measurements suggest the number density mixing ratios (n_{CO_2}/n_{H_2O}) to be around 1.17% at equinox, we have chosen activity to be mostly driven by H₂O outgassing and we include a small percentage of CO₂ coming from deeper layers of the surface in 4 from 7 cases. The mixing ratio in our simulations also varies with time, although the composition of the nucleus is homogeneous in 3 of the multi-species cases. A thermal conductivity of $6 \times 10^{-3} \text{ Wm}^{-1}\text{K}^{-1}$ and a ρc equal to $2.66 \times 10^6 \text{ Jm}^3\text{K}$ have been selected for the thermal inertia calculation. These values have been chosen after the estimations of a bulk density of 532 kg m^{-3} for comet 67P/CG by Jorda et al. [2016] and the estimation of heat capacity equal to $500 \text{ Jkg}^{-1}\text{K}^{-1}$ for lunar-like materials by Robie et al. [1970].

Case No.	Γ [TIU]	$\kappa \times 10^{-3}$ [W/(mK)]	δ [mm]	$\alpha \times 10^{-8}$ [m ² /s]	z_{H_2O} [mm]	z_{CO_2} [mm]	EAF H ₂ O	EAF CO ₂	H ₂ O-ice Distribution	Decoupling mode
M1	0	0	0	0	0	...	4.7%	...	Homogeneous	D
M2					0	Inhomogeneous*	D
M3	40	6	17.9	2.3	5	...	19.3%	...	Homogeneous	D
M4					5	50	10.5%	4.7%	Homogeneous	C
M5					0	50	4.0%	1.4E-04%	Homogeneous	D
M6					0	50	...	1.1E-04%	Inhomogeneous*	D
M7					0	30	4.0%	3.8E-05%	Homogeneous	D

Table 5.1: List of tested parameters for model calculations. * Inhomogeneous cases are selected after Marschall et al. [2019] inhomogeneous EAF case for H₂O (Fig.6). The last column indicates if the sublimation production rate was calculated in decoupled (D) or coupled (C) mode.

5.3 Results and Discussion

ROSINA, MIRO and VIRTIS-M retrieve complementary information of the gas coma of comet 67/CG. In the following section I use the methods described in Chapter 2 in order to compare the

DSMC results with in situ data.

5.3.1 Comparison with ROSINA

We have compared our model results with local measurements of number density from the ROSINA's Cometary Pressure Sensor (COPS) scaled to the production rate for H₂O measured by the Double Focusing Mass Spectrometer (DFMS). We use the method described in Section 2.5.1 in order to derive number densities at the position of the spacecraft using DSMC simulations at 4 rotational steps: 0°, 90°, 180° and 270° sub-solar longitude (ϕ_{sun}). The upper panel of Figure 5.1 shows the daily variation of the number density measured by COPS and the one produced by our model cases. Similar to cases M2 and M6, cases M5 and M7 exhibits the same variation of number density with time, therefore we have not included case M7 in the figure. The bottom panel shows the sub-spacecraft (ϕ_{spc} and λ_{spc}) and sub-solar (ϕ_{sun} and λ_{sun}) coordinates of each data point. The model comparison is done between May 5 to May 15 2015, when the spacecraft was between 120-180 km from the comet nucleus. Our results in Figure 5.1 suggest that compared to the purely insolation driven case (M1), all cases with an homogeneous ice distribution have a very similar behaviour around the spring equinox time. They all reproduce the daily variations, however they significantly overestimate the measured daily variations that arise from the nucleus rotation. Cases with an inhomogeneous H₂O-ice distribution only seems to fit better the data when the spacecraft is above the southern latitudes of the nucleus. Once the spacecraft approaches the equator and goes farther into northern latitudes, cases M2 and M6 do not reproduce the measured number densities. From Figure 5.1 we can infer that 1) purely insolation-driven outgassing is not sufficient to explain the ROSINA/COPS measurements on May 2015; 2) a 5mm dust mantle does not make a significant difference in the outgassing of H₂O at large distances; 3) the inhomogeneity at northern latitudes is probably too sharp and ignores the contribution from certain areas in the global outgassing; and 4) the presence of a small amount of CO₂ does not improve the magnitude fit.

We quantify the goodness of our model cases using the same approach used in Chapter 3 for comparison with ROSINA/COPS. We have therefore calculated the RMSLE (Eq. 3.2) and PCC (Eq. 3.3) for each case shown in Figure 5.2. The RMSLE fundamentally indicates the relative error of each model (n_g) with respect to the expected value (n_{COPS}). On the other hand, the PCC indicates the statistical relationship between n_g and n_{COPS} , where PCC values closer to 1 indicate a strong positive correlation. The RMSLE indicates that cases M1, M5 and M3 are the best fit to ROSINA/COPS with relative error of 19%, 20% and 21%, respectively. While the PCC indicates that the model cases M1 and M5 correlate equally well ROSINA/COPS data with a PCC value of 0.83. Although cases M2 and M6 take into account H₂O inhomogeneities that adjusted well to VIRTIS-M and OSIRIS observations in the past [Marshall et al., 2019], comparison with ROSINA/COPS data seems to discard them. Given that both cases significantly underestimate the number densities when $\lambda_{spc} \geq 0$, it is possible that a factor of 10 difference between the Hapi

region and its surrounding area is too large.

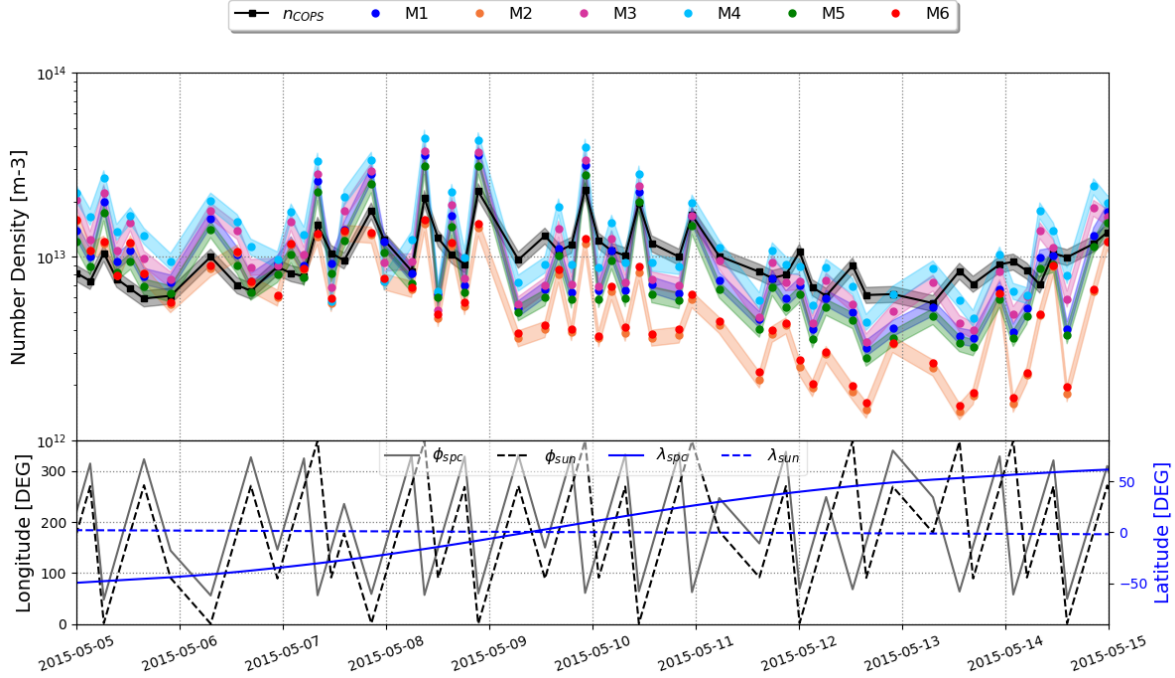


Figure 5.1: Upper panel: Comparison of DSMC results with local measurements of number density taken by ROSINA/COPS between May 5 to May 15, 2015. The solid line connecting data points is used to improve the visual comparison, it is not real data. The thickness of each line indicates an uncertainty of 10% for each data point and a maximum uncertainty of 10% for each point in the simulation results. Lower panel: Sub-spacecraft (spc) and sub-solar (sun) coordinates for each data point. The left axis refers to the longitude label ϕ and the right axis refers to the latitude label λ .

Figure 5.3 shows the number densities measurements for H_2O and CO_2 gas provided by ROSINA/DFMS for May 2015. It seems that, at least at the daily scale, CO_2 has very similar daily variation compared to H_2O , which is a bit more than 1 order of magnitude larger. Two consecutive data point on May 3 (04:38:12 and 04:39:18) indicate a strong emission of CO_2 , while the H_2O abundance decreases in almost three orders of magnitude from its mean emission. For this exact date, there are no OSIRIS images available that could indicate a strong outburst coming from the surface. Only one VIRTIS-M cube is available on this date a few hours later (see Figure 5.11), however from this, it is also difficult to infer any possible anomalous outgassing from the nucleus. Therefore, we cannot discard a sudden outburst of CO_2 activity detected by ROSINA/DFMS or a possible outlier in the data. In the first case, our simulations can certainly not predict such a behaviour, specially when assuming a homogeneous composition of CO_2 -ice in the nucleus. Therefore, we have chosen to ignore these data points in the following analysis.

We use these gas abundances to compute $n_{\text{CO}_2}/n_{\text{H}_2\text{O}}$ and compare with our model cases. Figure 5.4 shows the $n_{\text{CO}_2}/n_{\text{H}_2\text{O}}$ for all multi-species cases listed in Table 5.1 using the same 4 rotational

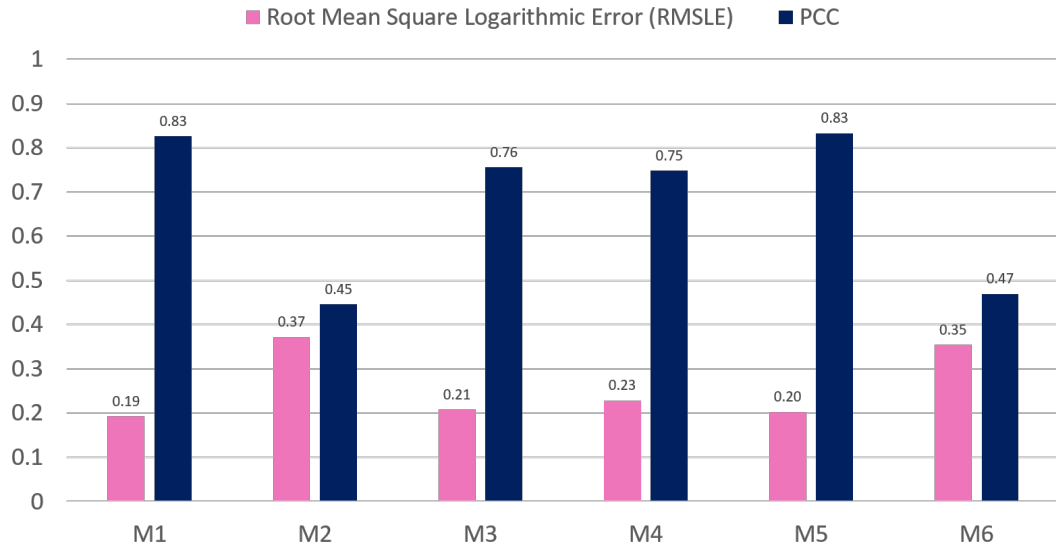


Figure 5.2: Estimation of the goodness of the DSMC models listed in Table 5.1 compared to ROSINA/COPS measurements using two methods: the RMSLE in pink, and the PCC in blue.

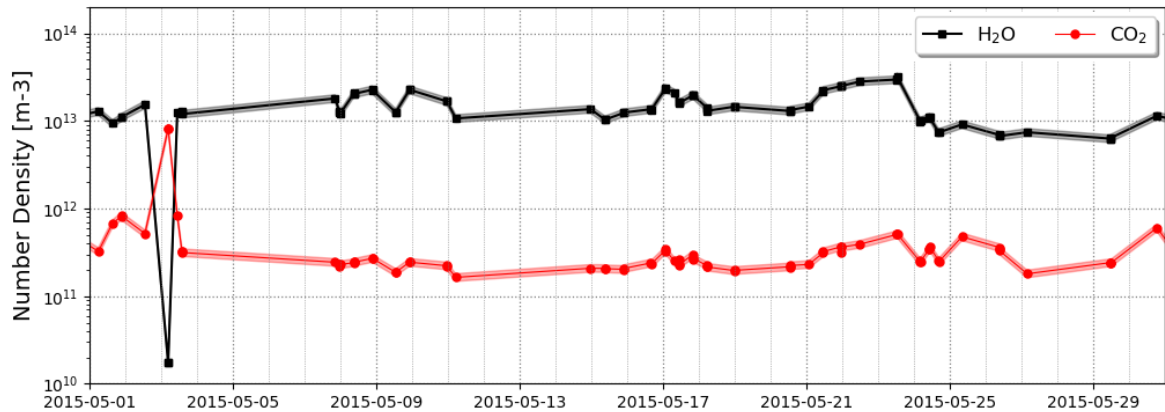


Figure 5.3: ROSINA/DFMS number density measurements for H₂O (black squares) and CO₂ (red dots) gas between May 1 to May 31, 2015. Only data points at 4 rotational steps are shown: 0°, 90°, 180° and 270° sub-solar longitude. The solid line connecting data points is used to improve the visual comparison, it is not real data. The thickness of each line indicates an uncertainty of 10% for each measurement.

steps used with ROSINA/COPS. Given that there are less data points from ROSINA/DFMS, we have chosen a larger time range to make the model comparison between May 1 to May 31 2015. From all cases, case M4 seems to be the one closer to the data, but with a slightly stronger daily variation. In general, all cases adjust the order of magnitude of the mixing ratio in most data points. However, they seem to have an inverse correlation with respect to the data. Therefore, we have also calculated the RMSLE and PCC for the mixing ratio comparison shown in Figure 5.5.

There, we corroborate M4 seems to be the one that better fits data as it has the smallest RMSLE; however, with a PCC close to zero, it does not seem to be correlated to the trend of the data much better than the other model cases. Even though with the current model approach and cases selection we can reproduce relatively well ROSINA/COPS measurements, it is very challenging to adequately reproduce the exact same mixing ratio trend obtained from ROSINA/DFMS data. It is possible that CO₂-ice sources are not homogeneously distributed in the nucleus as we assume in the current model cases. This would require to increase the number of free parameters in the model, which does not necessarily guaranty a better fit to DFMS data.

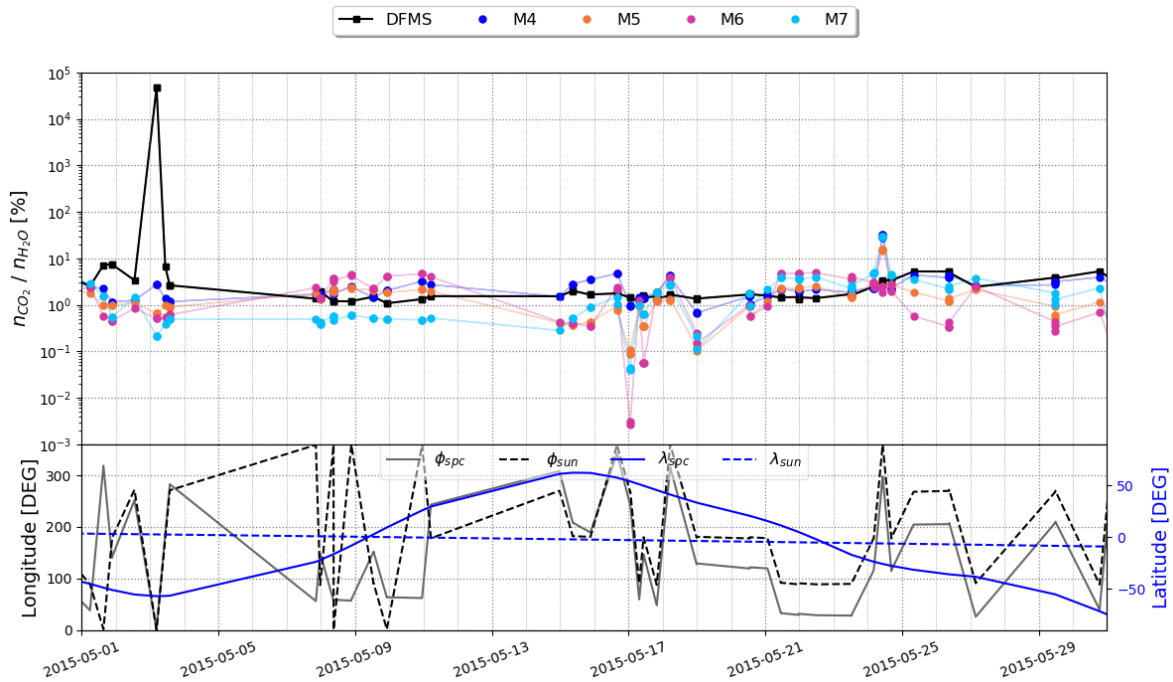


Figure 5.4: Upper panel: Mixing ratios $n_{\text{CO}_2}/n_{\text{H}_2\text{O}}$ compared to DFMS data for May 2015. The solid line connecting data points is used to improve the visual comparison, it is not real data. Lower panel: Sub-spacecraft (spc) and sub-solar (sun) coordinates for each data point. The left axis refers to the longitude label ϕ and the right axis refers to the latitude label λ .

At an early stage of this work, we used a set of VIRTIS-M cubes to track possible strong CO₂ sources (see Appendix B) and tested what we thought to be the most likely scenario: an insolation-driven H₂O outgassing with strong H₂O-ice sources at Hapi, plus an uniform CO₂ outgassing with strong CO₂-ice sources at Khonsu and Wosret. The comparison of the model case with ROSINA/COPS data is shown in Figure 5.6, where we identify a strong variability in number density similar to the cases listed in Table 5.1. Therefore, this particular case does not seem to improve the fit with ROSINA/COPS data. As it has been determined from previous model comparison with ROSINA/COPS measurements, such inhomogeneities are hard to spot even for H₂O using ROSINA data only. An appropriate study of CO₂ outgassing from the nucleus

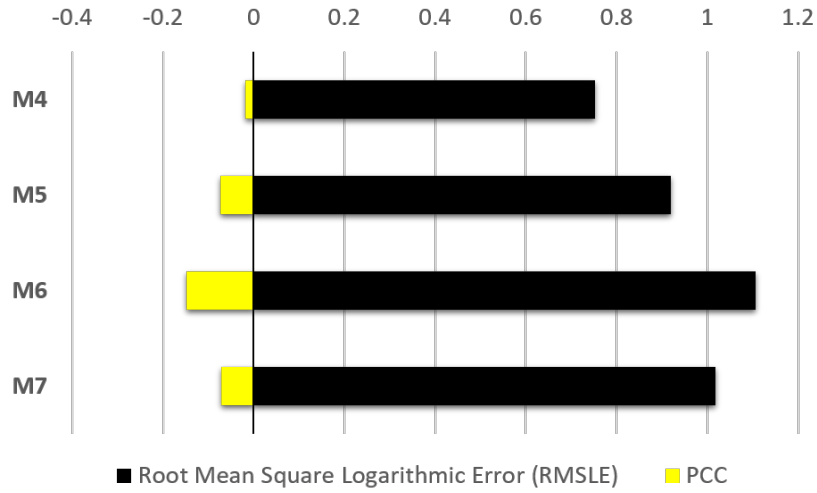


Figure 5.5: Estimation of goodness for the mixing ratios of all multi-species cases between May 1 to May 31, 2015.

would require multi-instrument data comparisons as well, that can give us more information about the spatial distribution of ejections around the nucleus.

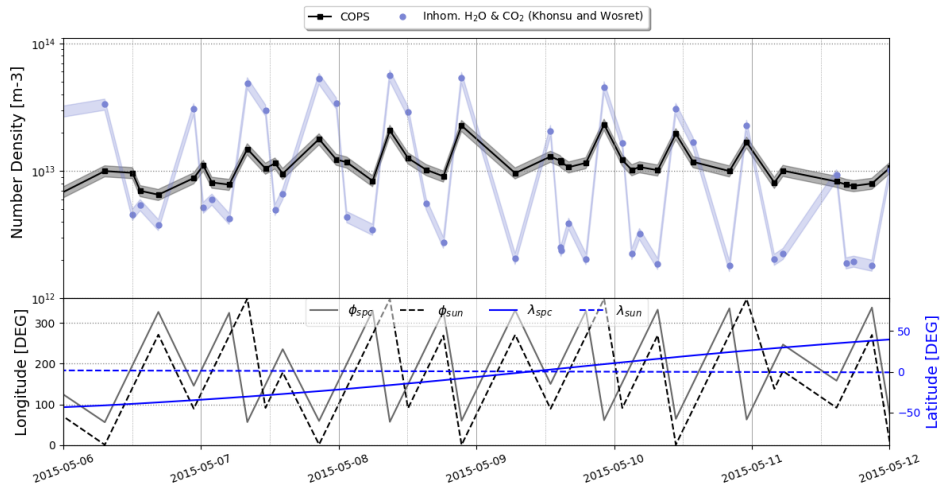


Figure 5.6: Upper panel: Comparison of DSMC results for a case including inhomogeneous H₂O- and CO₂-ice sources (blue circles) with local measurements of number density taken by ROSINA/COPS (black squares) between May 6 to May 12, 2015. The thickness of each line indicates an uncertainty of 10% for each data point and a maximum uncertainty of 10% for each point in the simulation results. Lower panel: Sub-spacecraft (spc) and sub-solar (sun) coordinates for each data point. The left axis refers to the longitude label ϕ and the right axis refers to the latitude label λ .

5.3.2 Comparison with MIRO

Following the same approach of Chapter 3, we compared our model results with data assuming a gas flow field in LTE. In the present section, we focus on nadir absorption lines of H_2^{16}O and have used calibrated MIRO data with a processing level ≥ 3 . The dates used for comparison are listed in Table 5.2. They have been selected so that MIRO's FOV is pointing to different locations around the nucleus. In this way, we can spot possible differences between regional emissions from the nucleus.

date	T_{back} [K]	ϕ_{sun} [DEG]	Obs. Region
2015-05-04T18:00:00	200	2	Imhotep
2015-05-10T06:00:00	160	224	Hapi/Anuket
2015-05-10T10:30:00	190	354	Imhotep/Ash
2015-05-10T13:30:00	150	81	Babi/Aker
2015-05-10T14:00:00	170	95	Aker/Hapi
2015-05-10T15:30:00	190	139	Hatmehit

Table 5.2: Selected dates for MIRO comparison. T_{back} is the background temperature used for the radiative transfer calculation, ϕ_{sun} is the sub-solar longitude and the last column indicates the region to which MIRO's beam is pointing.

In order to get an estimate of the central velocities (v_C) of MIRO data and our model cases, we have used the Gaussian function

$$f(v) = A \exp\left(\frac{-(v - v_C)^2}{2\sigma^2}\right) + T_{back} \quad (5.1)$$

where A and σ are the depth and the width of the absorption line, respectively, and T_{back} is the background (or nucleus) temperature. Even though a Gaussian fit does not fit perfectly all data features, it is important because it give us additional information to detect small relative shifts in the absorption bands produced by our model cases.

5.3.2.1 Gas flow field in LTE

Similar to the spherical nucleus comet studied in Section 4.4.2.4, we have run an extreme case for comet 67P/CG in which we assume a 5mm dust mantle transfers all its energy to the gas as it is being released from the nucleus. We have compared the absorption lines produced by the homogeneous H_2O models M1 and M3 with two different thermal inputs at the surface boundary: the temperature at the H_2O sublimation front (T_{Front}) and the temperature at the surface (T_{Surf}). For M1 (0mm), T_{Front} and T_{Surf} are the same. However, for case M3 (5mm) $T_{Surf} \geq T_{Front}$ on the illuminated side of the comet. Thus, we have set one simulation for each thermal input for case M3.

Figure 5.7 shows the model comparison for two different times where MIRO's beam is looking above the Imhotep region (a) and the Hapi/Anuket regions (b). In both cases, we notice there is

not significant difference in adding a 5mm dust mantle if we take T_{Front} as input temperature for our DSMC simulations. Figure 5.7a indicates a relative Doppler shift in the gas expansion velocity with respect to MIRO spectra of about 200.9 m/s and 222.9 m/s for the cases without and with a dust mantle, respectively, and a T_{Front} input. However, if we take into account the extreme case in which the gas heats up to a T_{Surf} temperature before leaving the nucleus, we obtain a relative difference in velocity of 44.0 m/s. For the observation geometry of Figure 5.7b, the Doppler shift is about 235.6 m/s and 272.0 m/s for the cases without and with a dust mantle, respectively, and a T_{Front} input, while for the T_{Surf} case the magnitude of the shift is only 43.9 m/s. In this geometry the T_{Surf} case even reproduces the so called "red emission wing" observed in all the H₂¹⁶O bands studied by [Marschall et al., 2019]. Even though the root mean square sensitivity in a 30 s integration time is ~ 2 K for the H₂¹⁵O absorption band [Gulkis et al., 2007], the measured spectra does not seem to have a similar emission wing. It is possibly related to the random noise of the data, for which one would need to average the measurements into a 10-20 min time interval. This has not been in the current work, but it is something to take into account for future work. Moreover, results indicate that for these geometries the model with T_{Surf} as input condition at the surface boundary reproduces relatively well the H₂¹⁶O band measured by MIRO, under-estimating only by a small amount the depth of the absorption which is possibly linked to slightly larger number densities.

Comparison with measurements at different times however seem to contradict the previous statement. Figure 5.8 shows the modelled spectral line of the water isotopologue H₂¹⁶O compared to MIRO measurements at different times. For this times, we only show a comparison between model cases with a 5mm dust mantle (M3) that use T_{Front} and T_{Surf} as thermal input. In this figure, both model cases underestimate the peak intensity and the width of the H₂¹⁶O absorption band of observations (a), (c) and (d). The width of the band contains information on the radial profiles of the gas velocity and temperature [Gulkis et al., 2015]. The T_{Surf} case only seem to fit better the gas expansion velocity of the absorption compared to the T_{Front} case. Given that it is required a column density of 8.1×10^{16} molecules/m² to produce a H₂¹⁶O line strength of 2K assuming a gas temperature of 300K [Gulkis et al., 2007], Figures (a), (c) and (d) indicate that our model case M3 with T_{Surf} as thermal input is under-estimating the gas column densities along the FOV by approximately 1.98×10^{18} molecules/m², 1.72×10^{18} molecules/m² and 1.45×10^{18} molecules/m² for observations (a), (c) and (d), respectively, while for observation (b) the column density should be increased of around 6.83×10^{17} molecules/m².

Although the OSIRIS camera observed some bright patches at the surface of the Imhotep region [Pommerol et al., 2015; Deshapriya et al., 2018] and there was evidence of strong activity coming from it at the early stages of the mission [Auger et al., 2015; Keller et al., 2015], other studies suggest it to be very depleted in H₂O sources compared to other regions [Marschall et al., 2019]. Our model comparison in Figures 5.7a and 5.8a indicates that a purely insolation-driven case with T_{surf} as input underestimates the production rates along the FOV in both geometries.

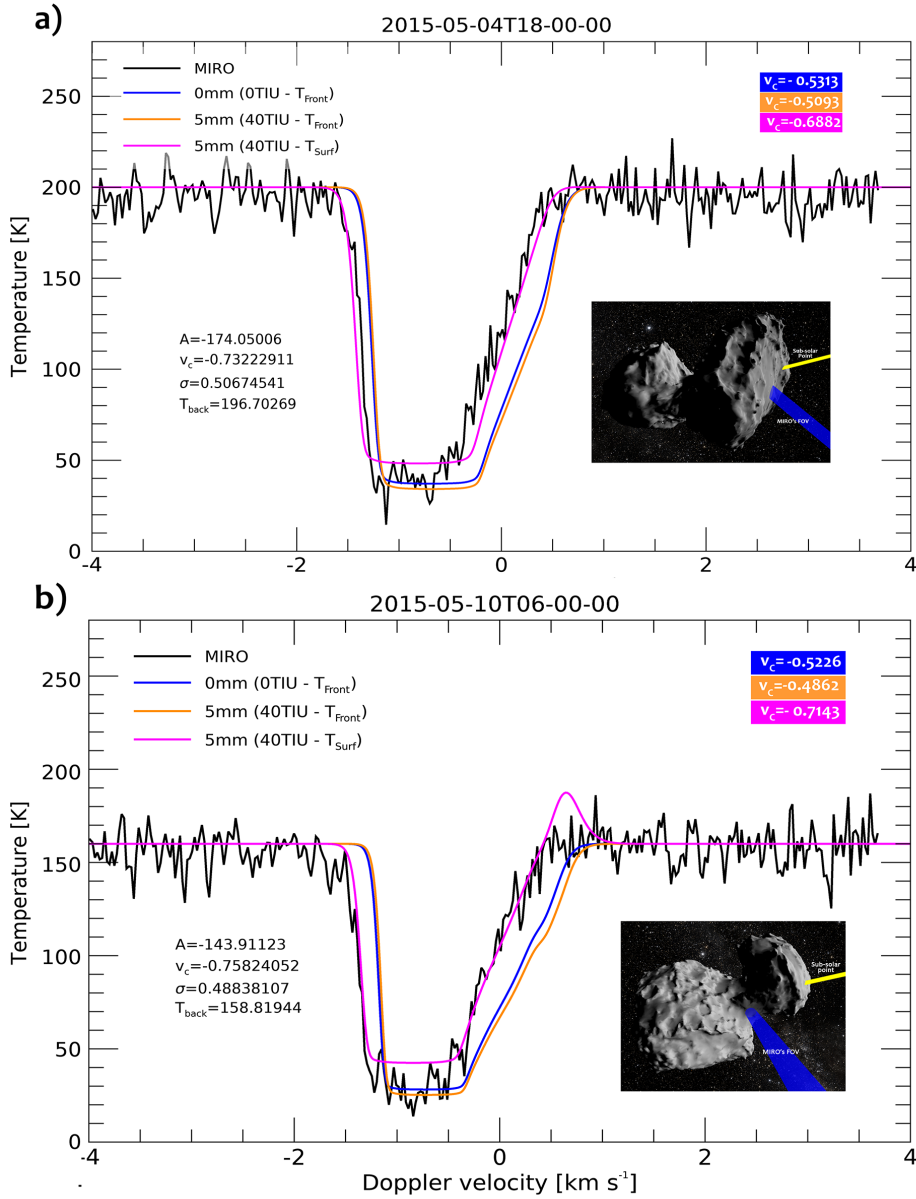


Figure 5.7: Comparison with MIRO absorption spectra (in black) for two different dates of case M1 (in blue) and case M3 with two thermal input parameters: the temperature at the H_2O sublimation front T_{Front} (in orange) and the temperature at the surface T_{Surf} (in magenta). Text in black gives information of the height A , the central velocity v_c , the standard deviation σ and the background temperature T_{back} of a Gaussian fit to MIRO's H_2^{16}O absorption band. Colored boxes on the top right of a) and b) give the central velocities estimated for each model case using a Gaussian fit. On the bottom right of a) and b) there is an image of the pointing location of MIRO's FOV (blue path) and the sub-solar point (yellow path).

The difference in intensity is very small in Figures 5.7a and very large in Figures 5.8a even when both beams are pointing at Imhotep. However, on 2015-05-04T18:00:00 the spacecraft is

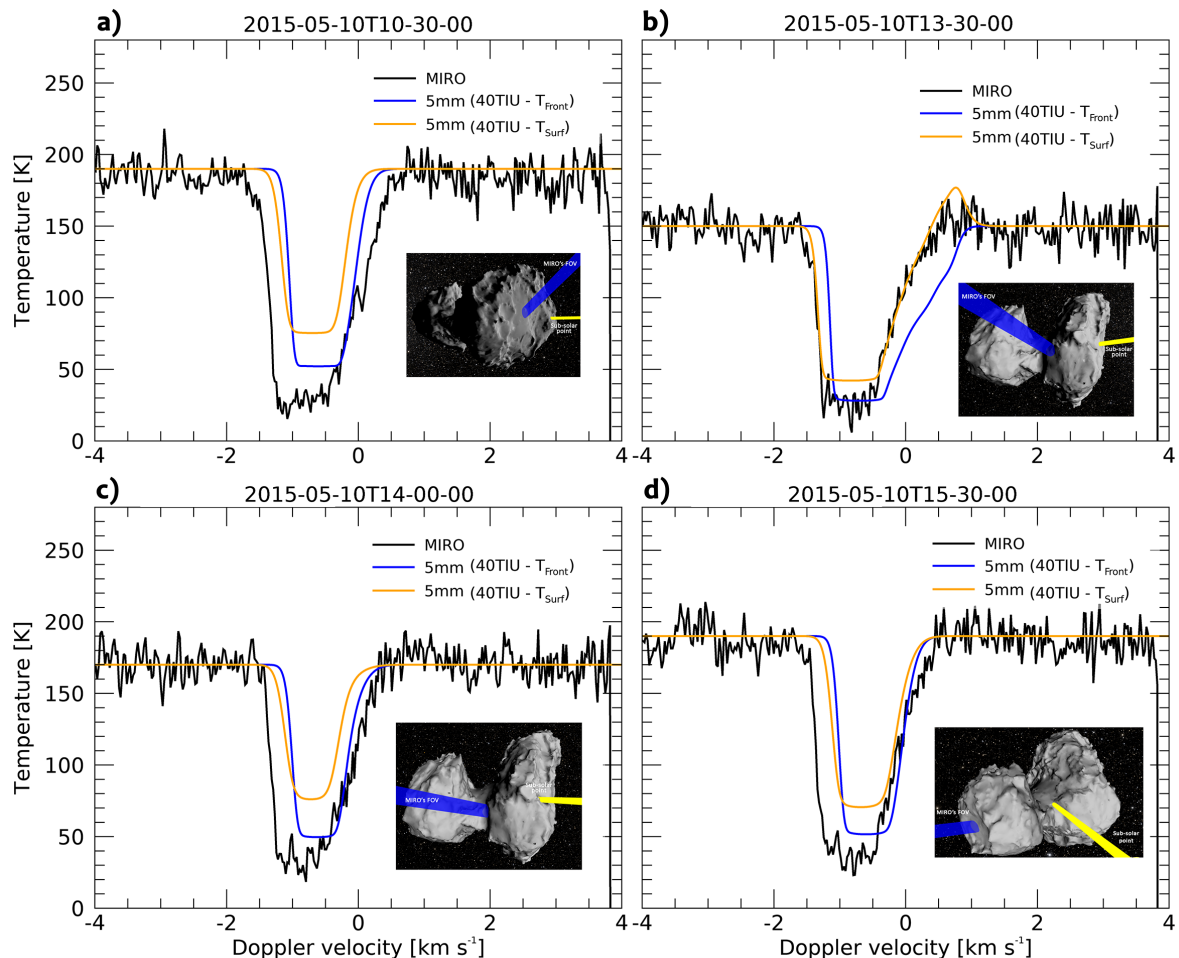


Figure 5.8: MIRO comparison of model M3 with two different thermal input parameters: the temperature at the H₂O sublimation front T_{Front} and the temperature at the surface T_{Surf} .

above the southern hemisphere ($\lambda_{spc} = -51^\circ$), while on 2015-05-10T10:30:00 the spacecraft is above northern latitudes ($\lambda_{spc} = +18^\circ$). This confirms our comparison with ROSINA/COPS data in Section 5.3.1, which suggest that the activity from northern latitudes is not well constrained by our models.

Comparison of Figures 5.8**b** and 5.8**c** also sets an interesting case to study. The measurements were acquired only 30 minutes apart from each other and the observation geometry in both cases is very similar. However, our models fit much better in **b** than in **c**. From the viewing geometry images, we can infer that when MIRO's beam gets closer to shadowed areas and to the smaller lobe of the nucleus, our models underestimate the production rates significantly. In terms of column densities, our model produces average column densities in the order of 4.5×10^{20} molecules/m² for both thermal inputs in the observation geometry **b** and 3.5×10^{18} molecules/m² for both thermal inputs in the observation geometry **c**. Therefore, it is possible that regions on the smaller lobe of

the comet are more active than expected.

Finally, M3 model for the observation above the Hatmehit region on the smaller lobe of the comet shown in Figure 5.8d also gives a worse fit to the spectra. Both thermal inputs underestimate the intensity and width of the band, which seems to contradict evidence of it being very depleted in H₂O-ice sources [Marschall et al., 2019], unless the contribution to the gas production rate comes from one of the regions close to the observation geometry.

5.3.3 Comparison with VIRTIS-M

The current section presents the comparison of the simulations results of the multi-species case M4 with VIRTIS-M IR images. For this, we need to calculate the column densities n_l along VIRTIS-M FOV and generate artificial IR images as it has been explained in Section 2.5.4. All selected cubes for comparison are listed in Table 5.3. They were acquired for times before the selected one for our DSMC simulations (May 10, 2015). However, we want to test if the model can still reproduce the same emissions observed by VIRTIS-M with a difference in sub-solar latitude of maximum 10°.

Cube ID	Date	ϕ_{sun} [DEG]	λ_{sun} [DEG]	SZA [DEG]
A	2015-04-11T13:18:06	91	10.2	79.8
B	2015-04-12T07:52:58	266	9.9	80.1
E	2015-05-01T00:59:43	325	3.6	86.4
F	2015-05-01T04:00:42	54	3.5	86.5
G	2015-05-03T13:05:43	256	2.6	87.4

Table 5.3: Selected dates for model comparison with VIRTIS-M IR images. T_{back} is the background temperature used for the radiative transfer calculation, ϕ_{sun} and λ_{sun} are the sub-solar longitude and latitude, respectively, and the last column indicates the region to which MIRO’s beam is pointing.

5.3.3.1 Homogeneous ice sources

Figures 5.10, 5.11 and 5.9 show the comparison of insolation-driven emissions of H₂O and CO₂ assuming a homogeneous composition of the nucleus (bottom row) with VIRTIS-M IR images (upper row). The surface radiance measured by VIRTIS-M is shown at the top-left-side of each Figure. An image of the illumination geometry is included in the bottom-left-side, where the yellow arrow indicates the position of the Sun. The H₂O (middle) and CO₂ (right) cubes allow us to make a comparison between the measured (top) and the modelled (bottom) column densities. Some numerated dashed boxed on the CO₂ emissions have been added for visual comparison.

A purely insolation-driven outgassing adjust relatively well the distribution of column densities measured for H₂O on the dayside of the nucleus shown in Figure 5.10. However, the artificial H₂O images in Figures 5.11 and 5.9 lack to reproduce the focused emissions observed

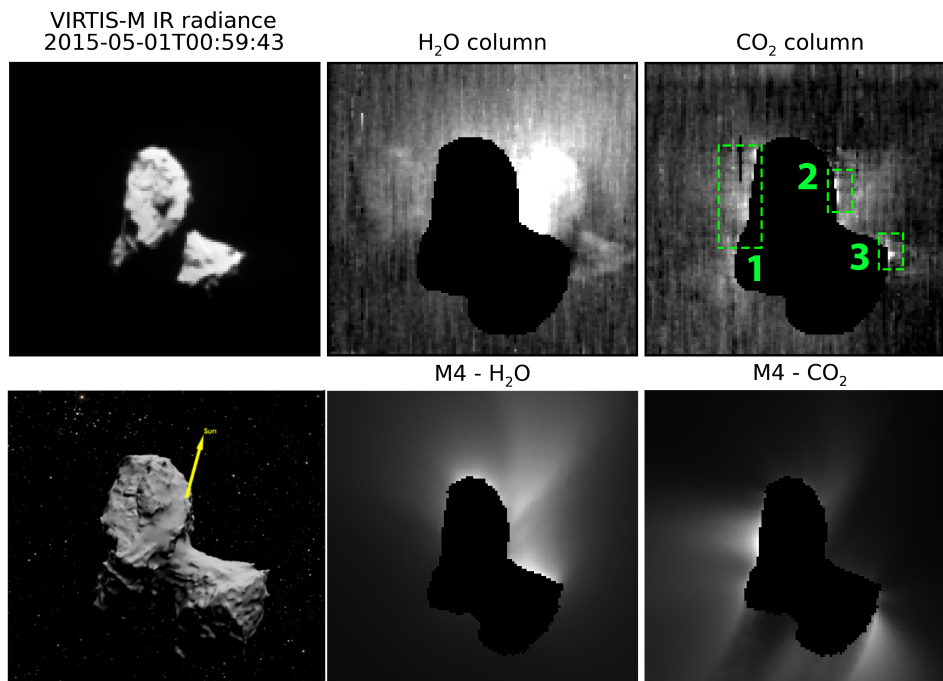


Figure 5.9: Model M4 compared to VIRTIS-M cube E in Table 5.3.

by VIRTIS-M on the neck, which is fully visible and illuminated in these cubes. For CO₂, on the other hand, the same model case (M4) only reproduces certain features close to the surface. Cube E in Figure 5.9 shows that our artificial IR image displays strong CO₂ emissions close to Imhotep and a milder one close to Seth, which are very similar to features 1 and 2, respectively, observed in the real data. The intense CO₂ column densities close to the Hatmehit region on the smaller lobe of the comet were very mildly observed by VIRTIS-M (feature 3). There seems to be some CO₂ outgassing in this side of the comet, but the emissions are not strong enough to produce large intensities. Cube F in Figure 5.10 shows that model M4 reproduces similar CO₂ emissions to the measured one labeled as 1, but overestimates the emissions of feature 2, which are not that strongly observed away from the nucleus.

Finally, the artificial CO₂ image in Figure 5.11 (Cube G) does not reproduce the strong column densities detected right above the neck (feature 3), in what seems to be the Anuket/Hathor region. But it produces large emissions close to the location of feature 1. The emission feature 2 also seems to be reproduced by the model, but a visual comparison in this case is difficult. The strong emission produced by the model in the bottom area of feature 2 is not observed in the real data. Unfortunately, the quality of the measurement for this CO₂ cube is poor as can be inferred by the dark horizontal shadow in the data, which covers an important part of the cube.

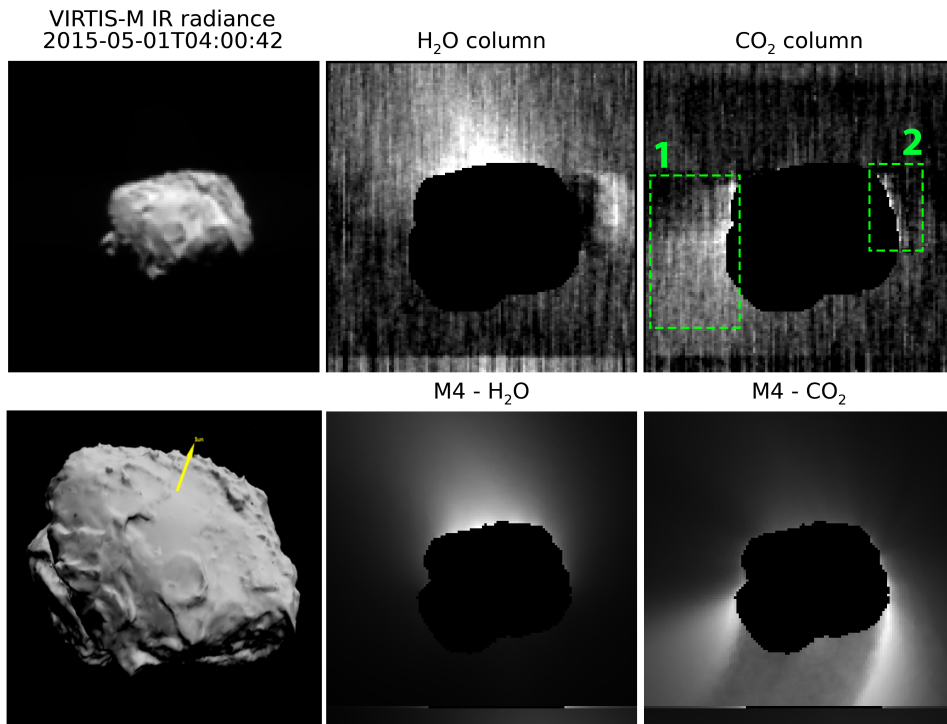


Figure 5.10: Model M4 compared to VIRTIS-M cube F in Table 5.3

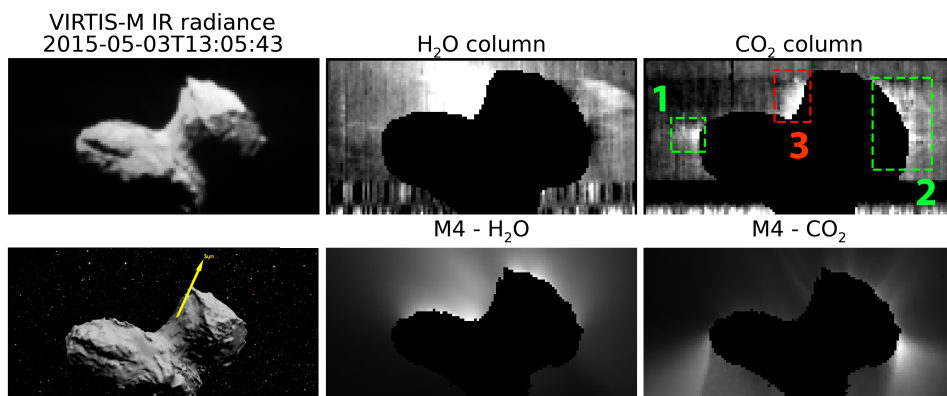


Figure 5.11: Model M4 compared to VIRTIS-M cube G in Table 5.3

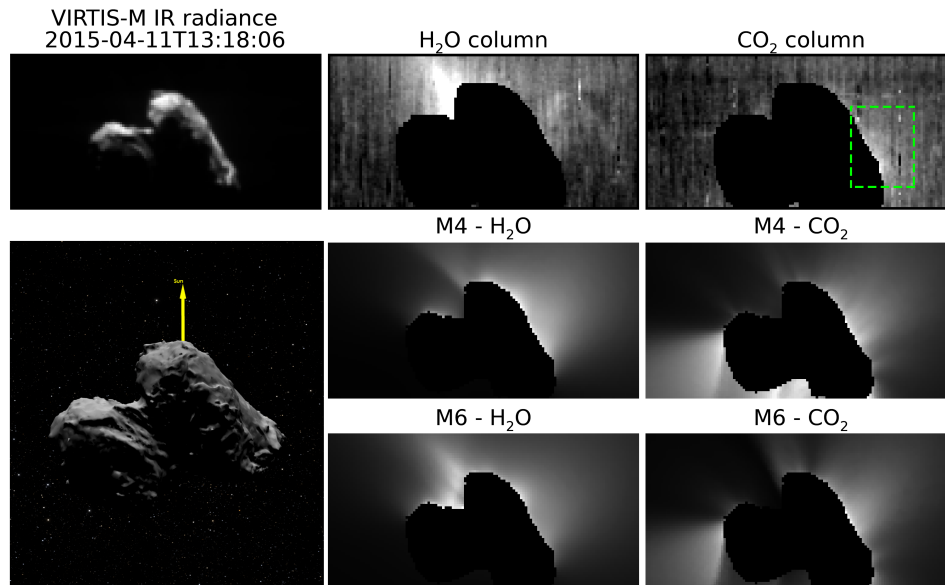


Figure 5.12: Models M4 and M6 compared to VIRTIS-M cube A in Table 5.3.

5.3.3.2 Inhomogeneous H₂O sources

We have also produced artificial IR-images for two extra cubes using a homogeneous and inhomogeneous H₂O distribution of sources with a small percentage of insolation-driven CO₂ outgassing (Cases M4 and M6, respectively). Figures 5.12 and 5.13 show that both model cases reproduce very similar results for the H₂O outgassing to the calculated ones by Marschall et al. [2019]. This seems to confirm their results of the Hapi region, on the neck of the comet, being very active in this period of time. We can also see that different surface distributions of H₂O-ice sources does not change significantly the distribution of the CO₂ emissions around the nucleus. A small decrease in the average brightness is observed, but a clear conclusion regarding this matter will only be possible by means of quantitative tools that help us determine the real differences, which are part of the future work of this project.

The observed CO₂ emissions in Figure 5.12 are very similar in the M4 and M6 cases. We only see a small difference in the CO₂ emissions of case M6 close to the neck of the comet, which is possibly an effect of the strong H₂O emissions on the Hapi region that decrease the number of gas particles in that area. Including thermal inertia of 40TIU into the model produces strong CO₂ emissions close to Imhotep that correlate to some extent VIRTIS's observations. However, it produces emissions from the smaller lobe (local sunrise) that are not observed by VIRTIS. The same model comparison is done for a cube with the illumination conditions in the opposite side of the nucleus shown in Figure 5.13. Both models (M4 and M6) reproduce the CO₂ emissions observed on the smaller lobe of the comet (green box), but reproduce emissions from the bigger lobe (local sunrise) that are not observed at all in the data.

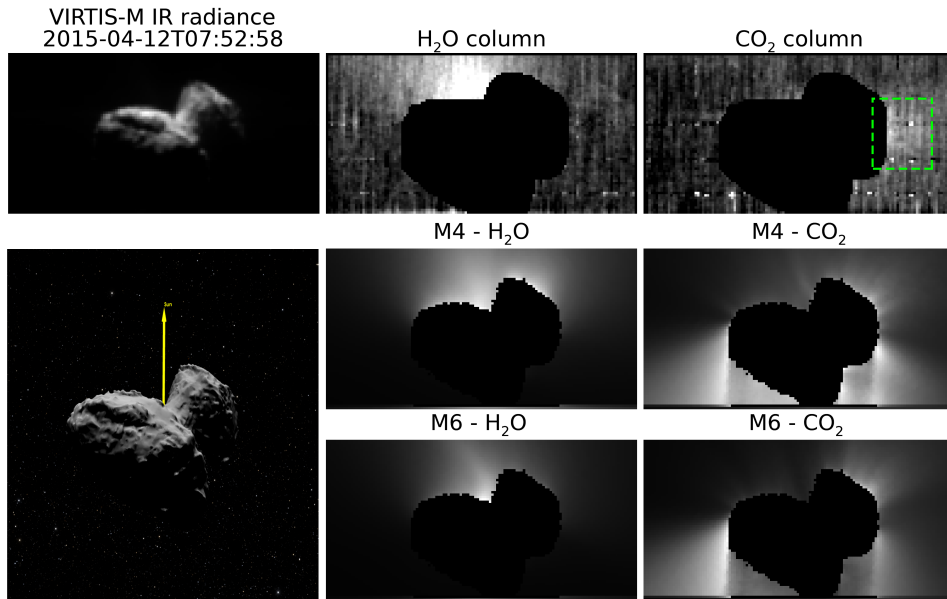


Figure 5.13: Models M4 and M6 compared to VIRTIS-M cube B in Table 5.3.

The fact that our models reproduce strong emissions in regions close to local sunrise is very intriguing, because it could mean that: *i* CO₂-ice is closer than 5cm to the surface for dust mantle with a thermal inertia of 40TIU or *ii* thermal inertia from the nucleus has to be larger than 40TIU in order to reach faster deeper layers of the nucleus. Even though models have suggested depths of about 1m for CO₂-ice for comet Halley [Fanale and Salvail, 1987], this one is much more active than comet 67P/CG. Bright patches of CO₂-ice have been found at the surface of comet 67P/CG [Filacchione et al., 2016]. Therefore, the first hypothesis cannot be discarded. The second hypothesis is connected to previous studies we have done (Chapter 4) for a spherical nucleus comet, that suggested an increase in thermal inertia can shift CO₂ emissions closer to the sunset, which could improve the comparison with VIRTIS-M data and other data sets. But, we cannot anticipate to any conclusion regarding thermal inertia values without making some tests that confirms our previous hypothesis.

5.4 Conclusion

Comparison with ROSINA data works as a first approach to study the abundance of gas mixtures in the coma of comet 67P/CG. However, there are strong limitations regarding the amount of information one can extract regarding the distribution of ice sources at the nucleus. There is strong evidence suggesting the neck of the comet being very active in H₂O emissions [Fougere et al., 2016a,b; Marschall et al., 2016, 2019], however comparison with ROSINA/COPS data seem to be worse when adding strong sources on the northern hemisphere of the comet. Comparison

with ROSINA/COPS alone can lead us to wrong conclusions, because statistically speaking, the inhomogeneous models were the ones that performed worse compared to the data. They had relative error of around 36%, compared to the case with homogeneous H₂O sources that had a relative error of 19% and a much larger correlation factor to the data. However, we think that the bad performance of both inhomogeneous cases (M2 and M6) compared to ROSINA/COPS is an indication that even if there are regional differences in the H₂O-ice content at the northern hemisphere of the nucleus, this does not have to be as strong as it has been defined in Marschall et al. [2019].

Model comparison with MIRO H₂¹⁶O spectral band gives an interesting insight to the models results that complement well with the findings after ROSINA comparison. Both instruments suggest a slightly larger activity when looking above the northern hemisphere of the nucleus. Comparison with MIRO spectra pointing to Imhotep, indicates that the purely insolation driven case adjust well the data when the spacecraft is above the southern hemisphere, which at the time was only partially illuminated. Model results for observations made directly above the neck of the comet also adjust better the data, except for one case that suggests larger contributions to the gas from the smaller lobe of the nucleus.

On the other hand, given that the relative abundance of CO₂ to the total flow is of approximately 7% [Rubin et al., 2019; Läuter et al., 2018; Combi et al., 2020; Herny et al., submitted for publication], we suspect CO₂ emissions could be strongly affected by H₂O emissions, which makes even more difficult to analyse CO₂/H₂O mixing ratios from ROSINA/DFMS data. At the moment we can only attain to fit average value of CO₂/H₂O. Our results of daily number density variations need to be compared to previous studies of the general temporal evolution of the abundances done by Läuter et al. [2018, 2020]. VIRTIS-M IR images indicate that H₂O outgassing affects the distribution of CO₂ outgassing around the nucleus depending on location and the strength of the illumination conditions. The neck and surface areas that are strongly illuminated (have a larger energy budget) dominate in H₂O emissions. On the other hand, areas that are mildly illuminated will have much less H₂O outgassing, allowing CO₂ to expand easier from the nucleus. Moreover, modelled inhomogeneities of H₂O-ice sources did not show any significant effect in the visual comparison of the CO₂ emissions compared to the homogeneous H₂O-ice sources. Contrariwise, it is unknown to which extend do CO₂ plays a role when analyzing MIRO absorption spectra of H₂¹⁶O. This requires a radiative transfer calculation for the H₂O gas fields in multi-species cases, which is work in progress.

The current state of our model takes into account the main aspects that are known trigger activity in comets. However, they seem to lack in the explanation of phenomena on the nightside regions. An attempt to include CO₂ emissions from the nightside using a thermal inertia of 40TIU reproduces most of the features observed on VIRTIS-M cubes between May-1 and May 3, 2015. However, as the illumination conditions change very fast in small time ranges, they do not reproduce results from previous dates, when the difference in latitude is larger than 5°. This

requires further investigations in which we include the effect of larger thermal inertia values and variations in the depth of the CO₂ sublimation layer.

Summary and conclusions

In the current work, I have studied the emission processes and the dynamics in cometary coma in order to understand remote sensing measurements of comet 67P/Churyumov-Gerasimenko (67P/CG) taken by the Rosetta mission. The 3D Direct Simulation Monte Carlo (DSMC) method has been selected to model the dynamics of the highly rarified inner-coma of the comet, which is produced by the sublimation of ices in the nucleus.

In the first stage, I have presented a comprehensive study of the outgassing patterns of the molecular species that have been determined to be more abundant in cometary comae: H₂O and CO₂. The change in number density, temperature and velocity of each type of gas with distance from the nucleus has been shown to be dependent on the production rates studied. The effect of local H₂O plumes on the average behaviour of the whole flow of a comet, and the detectability of such events at large distances has also been explored. I have shown the effect of the nucleus shape on the distribution of the gas around it, and how it gives us hints for the actual distribution of the gas in comet 67P/CG.

Insolation driven models for two time-ranges of the comet's orbit have been studied: the spring equinox (May 10, 2015) and a time-point one month before perihelion (July 10, 2015). For the first selected time, I have performed a study of the influence of thermal conductivity for *i*) a spherical nucleus comet with same orbit parameters as comet 67P/CG, and *ii*) a study with the complex shape of the nucleus in which we include for the first time insolation-driven CO₂ outgassing. In both studies, I have used an updated version of our thermal model. It calculates the gradient of the temperature with depth and the diurnal variations of temperature at the surface and the sub-surface layers, which vary depending on: *i*) the type of molecule used, *ii*) the depth of the sublimation front, *iii*) the solar input, *iv*) the bulk density, heat capacity and conductivity of the dust mantle, and *v*) the coupling mode in multi-species cases.

The spherical nucleus study with thermal conductivity aims to investigate the parameters influencing the generation of the inner-comae of comets. It was found that thermal inertia and

the depth of the sublimation front have a small effect shifting the maximum H₂O outgassing towards the sunset, while for CO₂, small changes in these parameters implied CO₂ being the main source of nightside activity for most of the model cases. This study was an important step to determine the effect of CO₂ emissions in H₂O gas field and vice versa, without the shape effects caused by the nucleus.

Once the complex shape of the nucleus is used, the study of the activity can be compared with local H₂O and CO₂ number densities measured by ROSINA, H₂¹⁶O absorption bands measure by MIRO and infrared images of H₂O and CO₂ emissions acquired by VIRTIS-M. This work is complementary to previous investigations that do not include CO₂ emissions from the nucleus [Marschall et al., 2019]. Even though the inhomogeneous distribution used for H₂O-ice sources has successfully reproduced OSIRIS and VIRTIS-M observations in the past [Marschall et al., 2019], it has been determined to have some difficulties to fit ROSINA data. Therefore, an alternative distribution with smaller regional differences needs to be done as part of future work.

Finally, for the second selected time, I have perform a similar study with H₂O emissions only, but neglecting thermal inertia effects. In this case, the objective was to determine the difficulty in detecting inhomogeneous distributions of H₂O ice sources by means of ROSINA data only. The statistical difference between model cases was not significant enough to determine the optimal ice distribution at the surface. Therefore, MIRO spectra was used to spot differences between two different thermal inputs: one that neglects the effect of a thin dust mantle, and an artificial case to test extreme cases in which a thin dust mantle transfers all thermal energy to the gas as it is being released into space from deeper layers of the nucleus. The comparison was made using LTE and non-LTE conditions, which seemed to give contradictory results in terms of the velocities required to fit the absorption band of the water isotopologue H₂¹⁶O.

6.1 Conclusions

We have built a model to simulate cometary outgassing and study in detail the influence of H₂O and CO₂ ice mixtures on the distribution of gas activity around a spherical comet nucleus and a nucleus that takes into account the complex shape of comet 67P/CG. The DSMC method was used to simulate the rarified gas in the inner-coma, and results were compared with observations from ROSINA, MIRO and VIRTIS-M in order to validate the selected distribution of ices at the surface for the real of shape of the comet.

Studies of the basic properties of the outgassing patterns of each type of gas confirmed both molecules have the same adiabatic expansion, where the normalized number density decreases with the squared of the distance from the nucleus as $(10\text{km}/r)^2$. The change of the temperature and the expansion velocity of each gas with distance from the nucleus was found to be strongly dependent on the sublimation temperature of each molecule, which clearly produced larger gas velocities for H₂O than for CO₂. The difference in gas' speeds are of about 100 m/s close to

the surface and between 300-350 m/s at distances ~ 10 km from the surface. The maximum velocity reached by each gas at ~ 10 km depends strongly on the production rates if they are below 1×10^{27} molecules/s. For production rates above this value, gas temperatures and velocities at ~ 10 km seem to converge to 50K and 700 m/s for H₂O, while for CO₂ they are 20K and 250 m/s, respectively.

By studying the small differences in number density, temperature and speed, water plumes were shown to be difficult to detect at large distances from the nucleus unless the strength of the outburst were about 100% stronger than the surrounding area. These kinds of feature in comets are more likely to be detectable by studying the dust particles being ejected by the gas on its way out, and not by studying gas emissions alone.

Different approaches to fit ROSINA/COPS and ROSINA/DFMS data have been tested. Even though ROSINA gives valuable information for the determination of abundances in the coma and the bulk composition of the nucleus, it is difficult to determine local inhomogeneities that can significantly improve the purely insolation-driven case. There are however indications that can be used to discard regions as Imhotep, Bastet or Atum as strong sources of H₂O activity on July 2015. Our results of daily variations need to be compared model results by Lauter et al. [2018] and Lauter et al. [2020], who use an inverse model to reproduce the general temporal evolution of H₂O and CO₂ abundances using ROSINA/DFMS data.

Our parameterization with a spherical nucleus comet suggests that thermal conductivity has a significant effect in the distribution of gas sources at the surface, which is especially important to generate nightside activity. Purely insolation driven models with 0 TIU, 40 TIU and 80 TIU showed us that by increasing the thermal inertia values one can shift the distribution of H₂O emission towards the evening terminator by about 20° in longitude from the sub-solar point. CO₂-ice showed much stronger shifts with respect to the sub-solar point. For shallow sublimation fronts, CO₂ emissions were on the dayside of the comet. However, for deeper sublimation fronts the direction of the maximum emission was located towards the sunset terminator and, in the most extreme cases, pointing farther into the nightside. Comparison with VIRTIS-M images on May 2015 indicates that regions with very mild illumination close to terminator on the dayside of the comet can produce strong CO₂ emissions. However, VIRTIS-M observations cannot be used to infer nightside activity, because in shadowed areas of the coma gas particles cannot be excited by solar radiation.

Contrary to expectations, H₂O inhomogeneities with strong sources at Hapi adjusted badly to ROSINA/COPS data on the spring equinox. The effect was stronger for observation geometries above the northern hemisphere for ROSINA and MIRO data, which we think is an indication of softer differences between northern regions of the comet. This new distribution has still to be tested and compare with all data sets and it will be part of future work. Regarding CO₂ sources, a single test using a mixture of strong H₂O sources at Hapi and strong CO₂-ice sources at Wosret and Khonsu was used as a first attempt to include nightside activity in a model that at the

time neglected thermal inertia. Results showed no improvement in the magnitude of the daily variations of neutral abundances in the coma. We however do not rule out yet nightside activity as a possible explanation. More work needs to be made in order to have a categorical conclusion.

Finally, we have studied the effect of a thin dust mantle in the mean expansion velocity of the gas by comparing two types of thermal inputs with MIRO's H_2^{16}O absorption band. This has been done for May and July 2015. In many cases, our model results adjust better to MIRO spectra if the gas is being released from the surface with larger initial temperatures. This results confirms previous findings that suggest some heat exchange between the dust mantle and the gas particles which would be responsible for higher temperatures of the gas leaving the nucleus [Christou et al., 2018]. Model cases that do not adjust the data are more likely to be related to underestimated production rates along MIRO's FOV.

MIRO comparison with a purely insolation-driven outgassing assuming non local thermal equilibrium

We have perform a comparison with a purely insolation-driven case for H_2O , e.g., homogeneous ice sources everywhere, assuming the gas to be in non-local thermal equilibrium (non-LTE). This has been done for July 2015, when the comet was located at 1.31AU from the sun and was approaching to perihelion. For this time, the thermal inertia is not included in the model and the sublimation front is set at the surface, where we modulate the global production rates by modifying the EAF of the surface (Equation 2.10), which is equal to 10% for the current time range. We have selected different MIRO observations, which are listed in Table A.1. All observations were done with a phase angle of approximately 89.6° and with a sub-solar latitude around -30° .

Figures A.1 to A.5 show our DSMC results of a purely insolation driven case compared to MIRO observation at different sub-solar longitudes. We can see in panel a) of all Figures that our results are significantly underestimating the central velocity of the MIRO spectra, which is associated with the expansion velocity of the gas along the FOV. This Doppler shift is large in all observations for the H_2^{16}O (left) and H_2^{18}O (right) absorption bands. The intensity of both absorption bands is larger in the model than in the observations, especially for the H_2^{18}O isotopologue. Therefore, an preliminary conclusion is that we are overestimating the production rates in the model. Absorption spectra are difficult to interpret visually, so one needs to make an iterative inversion process that give us the change of parameters one would need to do in order to fit the observations. The best fit (adjusted spectra) within 2σ of random measurement error is

APPENDIX A. MIRO COMPARISON WITH A PURELY INSOLATION-DRIVEN OUTGASSING ASSUMING NON LOCAL THERMAL EQUILIBRIUM

date	ϕ_{sun}	λ_{sun}	ϕ_{spc}	λ_{spc}	Obs. Region
2015-07-10T00:51:51	10.4	-30.5	95.0	8.2	Ash
2015-07-10T01:01:59	15.3	-30.5	100.0	8.2	Ash
2015-07-10T01:23:03	25.5	-30.5	110.2	8.1	Ash/Aten/Khepry
2015-07-10T01:32:39	30.1	-30.5	114.9	8.0	Aten/Khepry
2015-07-10T01:51:51	39.4	-30.5	124.3	7.9	Khepry/Aker
2015-07-10T02:03:20	45.0	-30.5	129.9	7.8	Aker/Anhur

Table A.1: MIRO dates selected for comparison. ϕ_{sun} is the sub-solar longitude, λ_{sun} is the sub-solar latitude, ϕ_{spc} is the sub-spacecraft longitude and λ_{spc} is the sub-spacecraft latitude. The last column indicates the region pointed by MIRO's beam.

shown by the red line in all a) panels. Then, the non-LTE code gives the best possible solution and the required vertical profiles to fit the data. These are shown in the b) panels, where the change of number density, Doppler velocity and the gas temperature with altitude are shown for our DSMC results (blue) and for the adjusted spectra (orange). All observations, except the one on 2015-07-10T01:32:39, indicate the model is overestimating the number densities along the FOV to some extent. On 2015-07-10T01:32:39, the non-LTE assumption suggest slightly larger number densities for MIRO spectra, however, the difference is not large. By looking at the Doppler velocities, the current comparison indicates that the purely insolation-driven case underestimates the speed of the flow in the first 100 m from the surface by 350 m/s to 450 m/s in all observations. Finally, in terms of the gas kinetic temperature, all the listed observations suggest larger flow temperatures close to the surface, except on 2015-07-10T00:51:51, when the model estimates similar values. However, we need to take into account that the "best fit" shown in panel a) of all figures is not a perfect fit in any case.

The previous comparison give us a strong indication that comet 67P/CG is not homogeneous in H₂O-ice sources, which agrees with results from other authors at different heliocentric distances [Fougere et al., 2016a,b; Marschall et al., 2016, 2019; Biver et al., 2019].

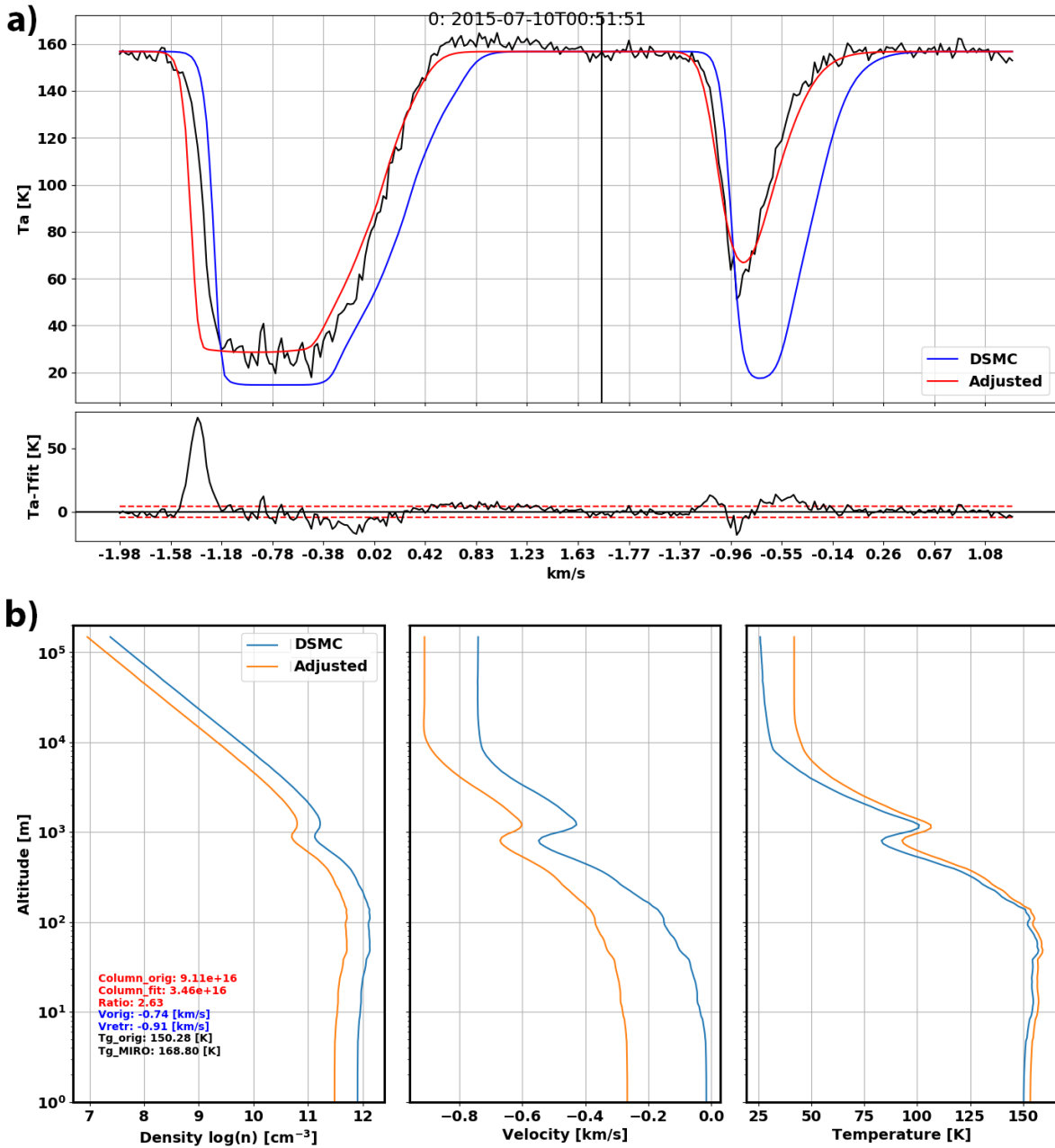


Figure A.1: Upper panel of a): Spectra for the H_2^{16}O (left) and H_2^{18}O (right) absorption bands on 2015-07-10T00:51:51. MIRO measurements (black) are compared to the DSMC results of a purely insolation driven case (blue). The best fit after iteration is shown in red. Bottom panel of a): Residual between the measurements and the best fit. Panel b): Vertical profiles of number density (left), Doppler velocity (middle) and gas temperature (right) for the DSMC results (blue) and the best fit (orange) after iteration to the measurements. The differences between the DSMC model and the adjusted spectra is given in the colored text on the bottom left.

APPENDIX A. MIRO COMPARISON WITH A PURELY INSOLATION-DRIVEN OUTGASSING ASSUMING NON LOCAL THERMAL EQUILIBRIUM

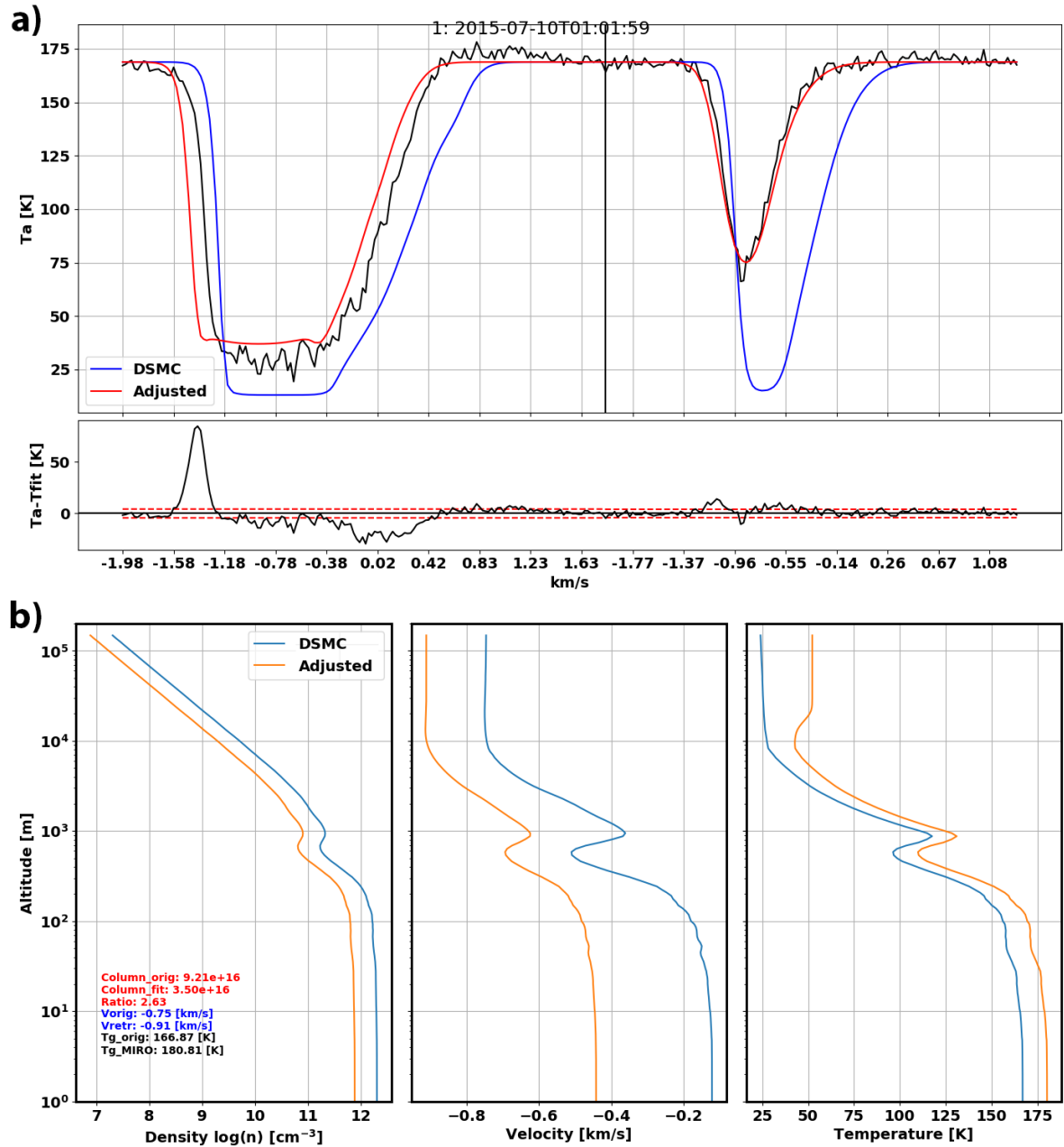


Figure A.2: Upper panel of a): Spectra for the H_2^{16}O (left) and H_2^{18}O (right) absorption bands on 2015-07-10T01:01:59. MIRO measurements (black) are compared to the DSMC results of a purely insolation driven case (blue). The best fit after iteration is shown in red. Bottom panel of a): Residual between the measurements and the best fit. Panel b): Vertical profiles of number density (left), Doppler velocity (middle) and gas temperature (right) for the DSMC results (blue) and the best fit (orange) after iteration to the measurements. The differences between the DSMC model and the adjusted spectra is given in the colored text on the bottom left.

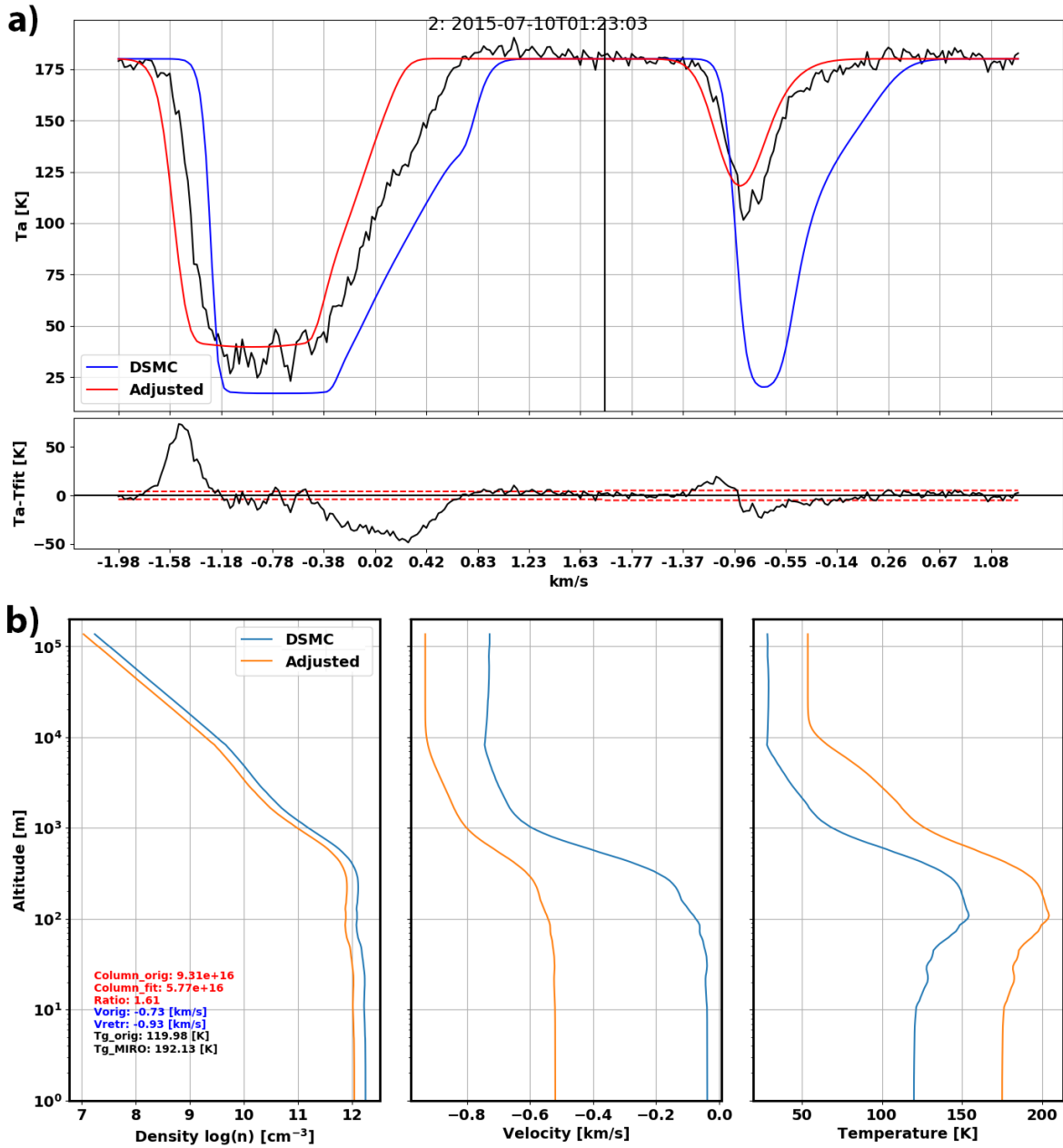


Figure A.3: Upper panel of a): Spectra for the H_2^{16}O (left) and H_2^{18}O (right) absorption bands on 2015-07-10T01:23:03. MIRO measurements (black) are compared to the DSMC results of a purely insolation driven case (blue). The best fit after iteration is shown in red. Bottom panel of a): Residual between the measurements and the best fit. Panel b): Vertical profiles of number density (left), Doppler velocity (middle) and gas temperature (right) for the DSMC results (blue) and the best fit (orange) after iteration to the measurements. The differences between the DSMC model and the adjusted spectra is given in the colored text on the bottom left.

APPENDIX A. MIRO COMPARISON WITH A PURELY INSOLATION-DRIVEN OUTGASSING ASSUMING NON LOCAL THERMAL EQUILIBRIUM

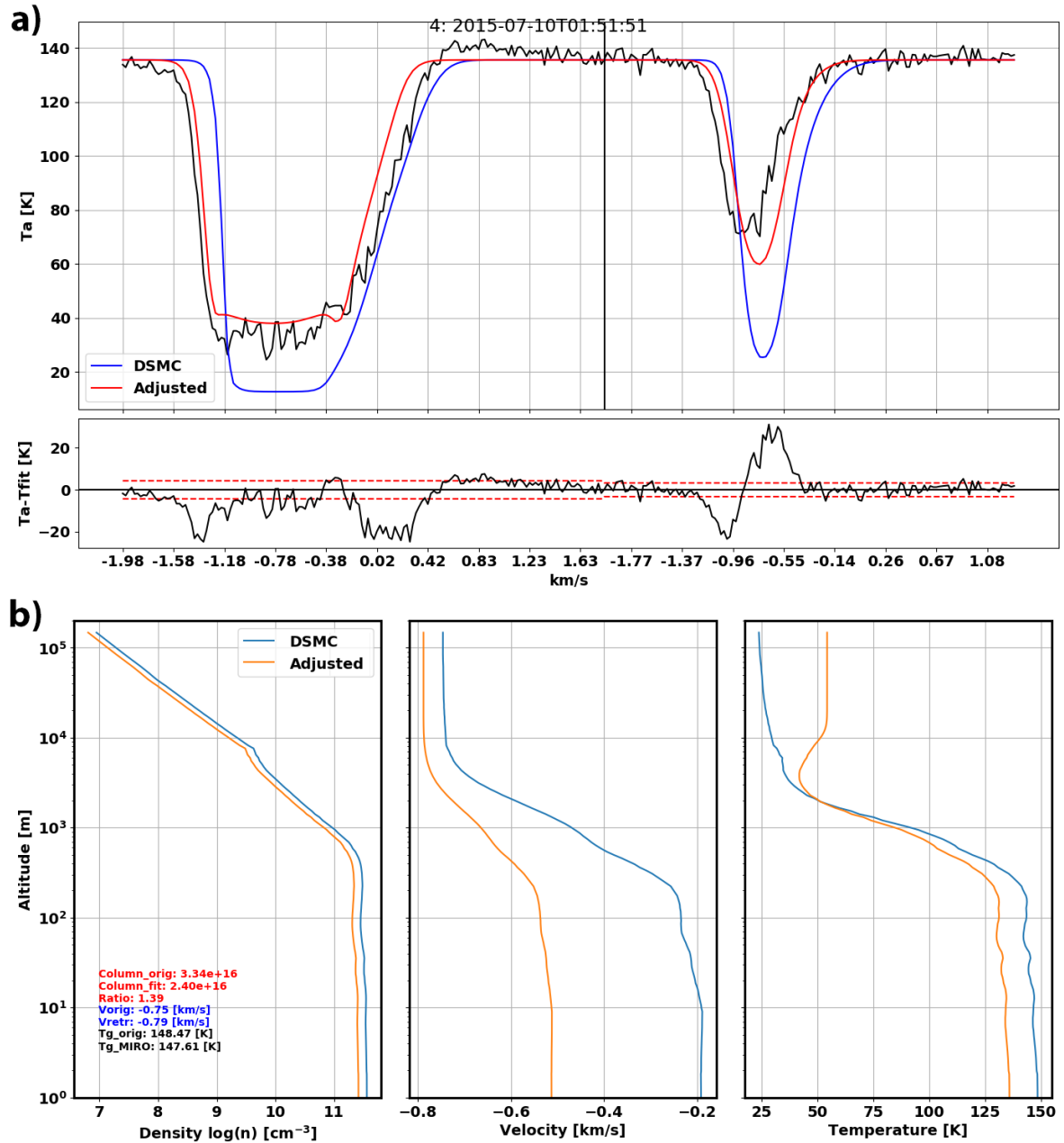


Figure A.4: Upper panel of a): Spectra for the H_2^{16}O (left) and H_2^{18}O (right) absorption bands on 2015-07-10T01:51:51. MIRO measurements (black) are compared to the DSMC results of a purely insolation driven case (blue). The best fit after iteration is shown in red. Bottom panel of a): Residual between the measurements and the best fit. Panel b): Vertical profiles of number density (left), Doppler velocity (middle) and gas temperature (right) for the DSMC results (blue) and the best fit (orange) after iteration to the measurements. The differences between the DSMC model and the adjusted spectra is given in the colored text on the bottom left.

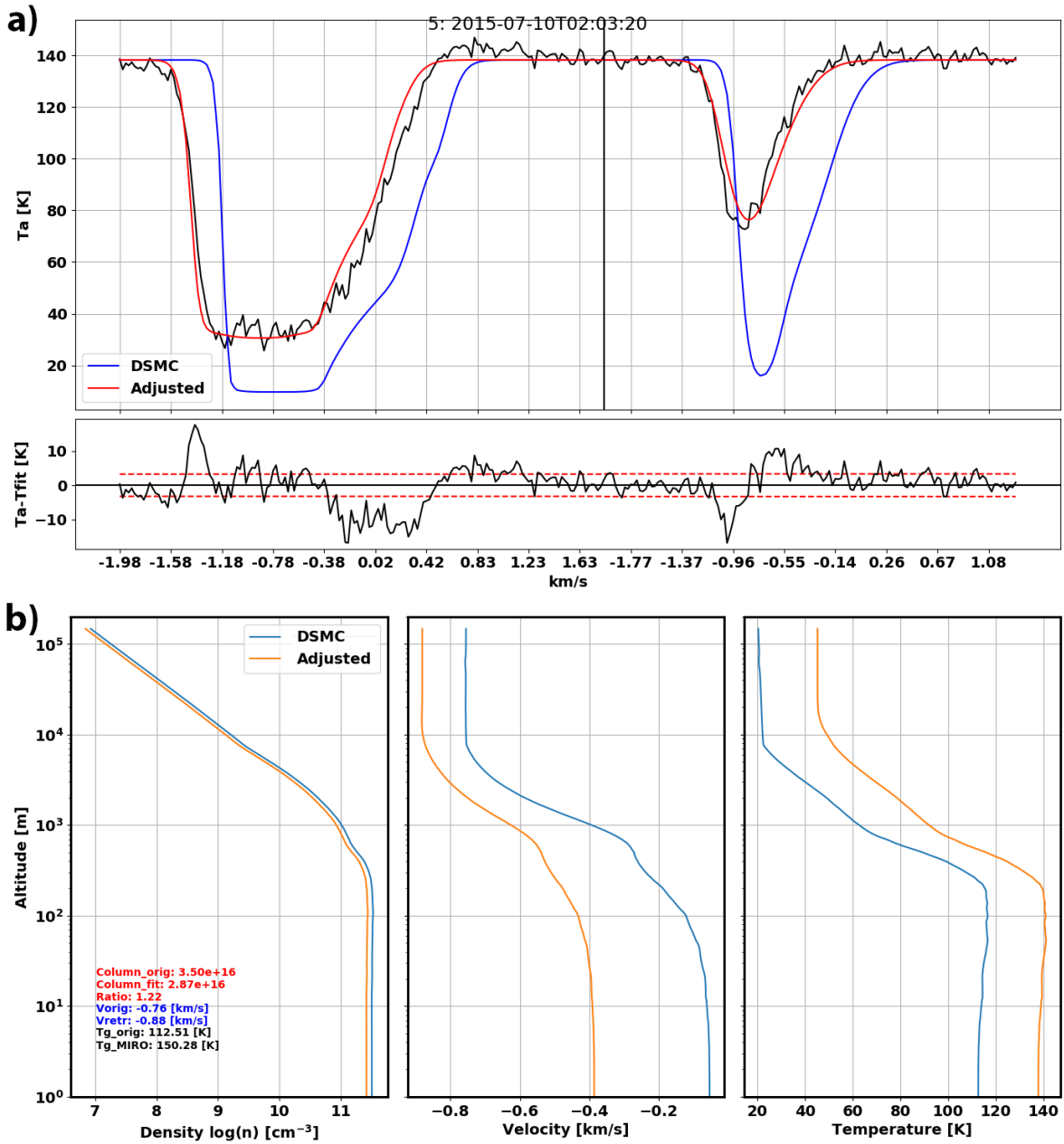


Figure A.5: Upper panel of a): Spectra for the H_2^{16}O (left) and H_2^{18}O (right) absorption bands on 2015-07-10T02:03:20. MIRO measurements (black) are compared to the DSMC results of a purely insolation driven case (blue). The best fit after iteration is shown in red. Bottom panel of a): Residual between the measurements and the best fit. Panel b): Vertical profiles of number density (left), Doppler velocity (middle) and gas temperature (right) for the DSMC results (blue) and the best fit (orange) after iteration to the measurements. The differences between the DSMC model and the adjusted spectra is given in the colored text on the bottom left.

Mapping of CO₂ sources using VIRTIS-M images

We have investigated the distribution of CO₂ emissions at the surface of comet 67P using a set of 32 VIRTIS-M IR images between February 25 to April 27, 2015. This has been done to track all possible CO₂-ice sources close to the surface. The procedure consisted in identifying CO₂ emissions with a relatively larger intensity of column density compared to the background and categorize them as "mild" or "strong" emissions. Taking into account the illuminations conditions and the observation geometry of each VIRTIS-M IR image, we estimated the regions from which emissions could have originated as it is shown as example in Figure B.1, where mild emissions are highlighted in green and strong emissions in red.

We also used some OSIRIS images in an attempt to explain some of the CO₂ emissions. The correlation of dust ejections from the nucleus with H₂O gas has been seen in multiples observations to be strong. However, for CO₂ emissions it is very difficult to determine from a visual comparison. Figure B.2, for example, shows strong CO₂ emissions from the smaller lobe of the nucleus that are clearly not observed in the dust.

Once we have estimated the total number of mild and strong emissions and their regional candidates, we have checked if mild-emission-regions were correlated with strong-emission-regions in order to discard possible outliers. The final count of strong emissions was plotted in Figure B.3, where regions are ordered from the regions with most strong CO₂ emissions to the regions with no emissions at all, and the red line indicates the cumulative total.

Finally, we have project the normalized results in a 2D map, in order to highlight the distribution of the regional CO₂ sources for the time range of the available data. In general, all the CO₂ sources shown in Figure B.4 are located towards the southern hemisphere of the comet, which for the investigated time is not illuminated. Regions Wosret and Khonsu have been

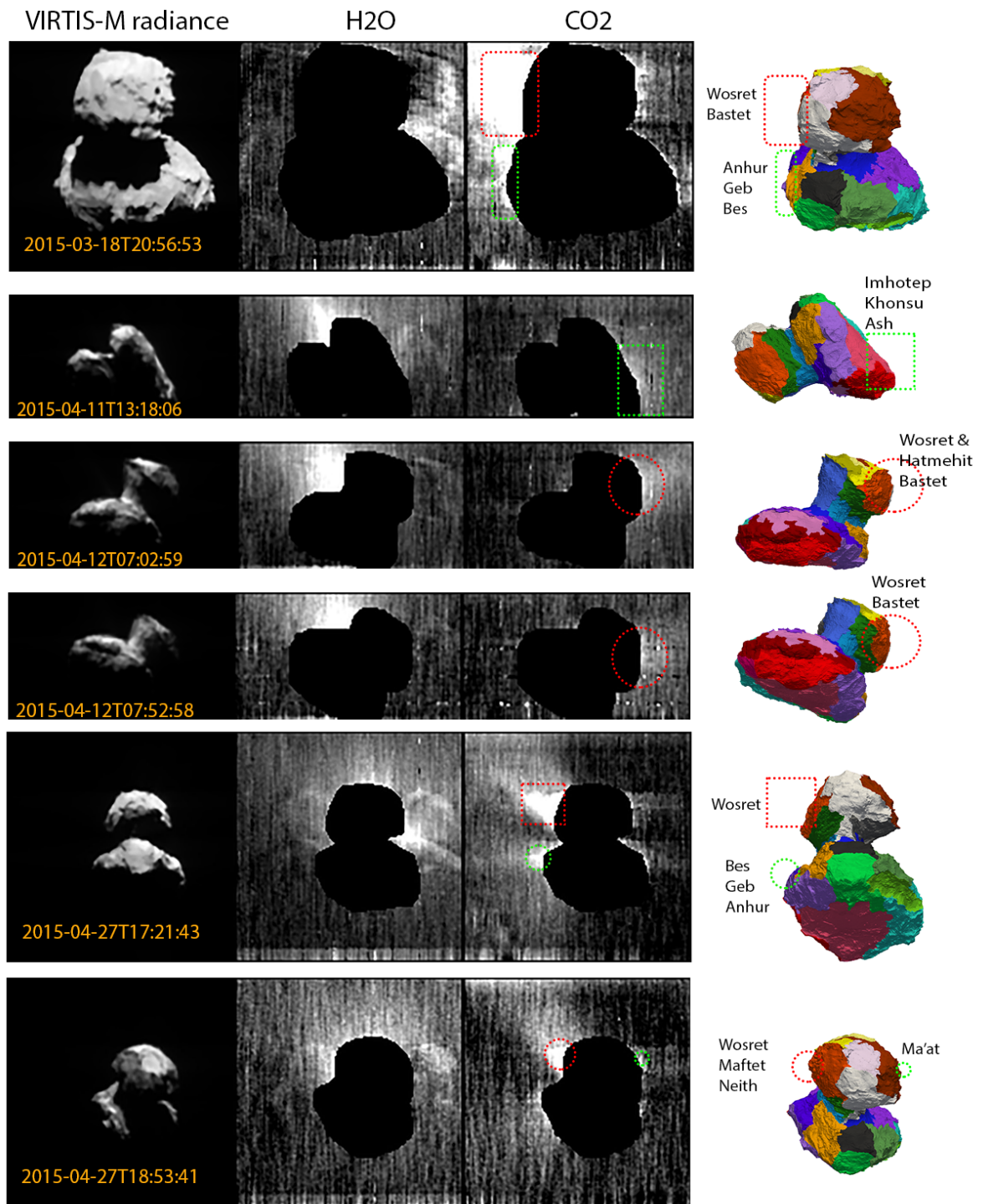


Figure B.1: On the trail of CO₂ sources using VIRTIS-M IR images.

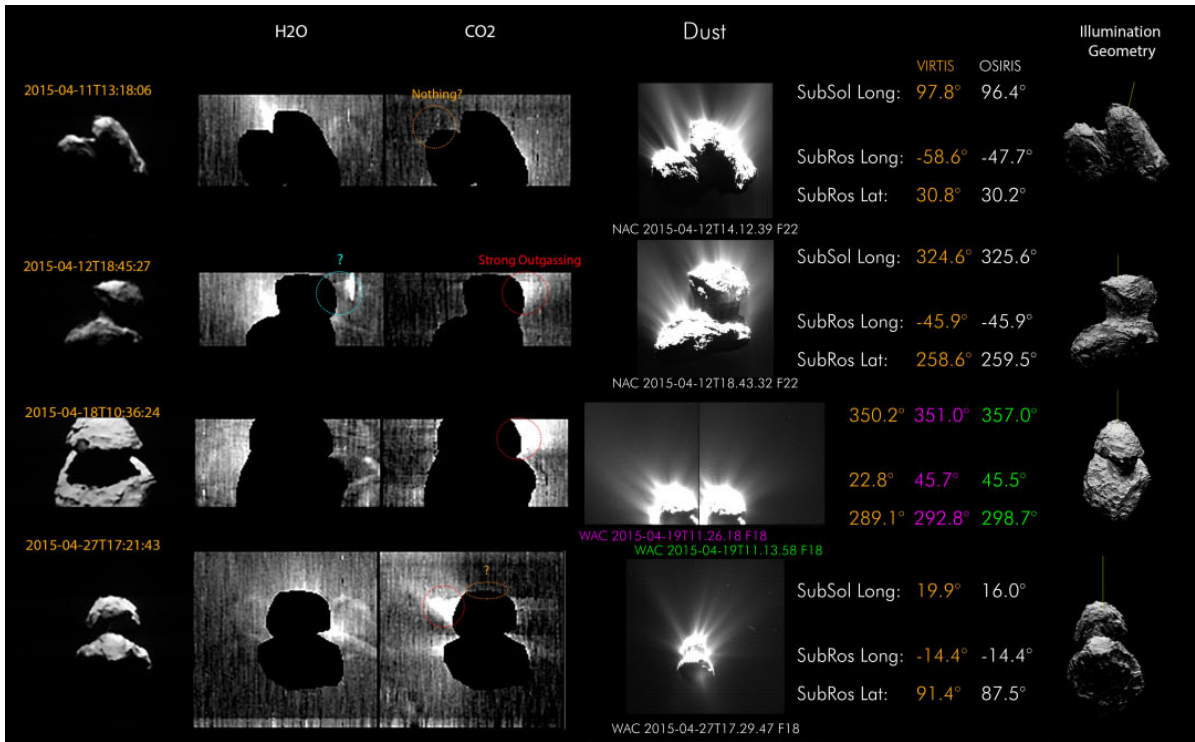


Figure B.2: On the trail of CO₂ sources using OSIRIS images.

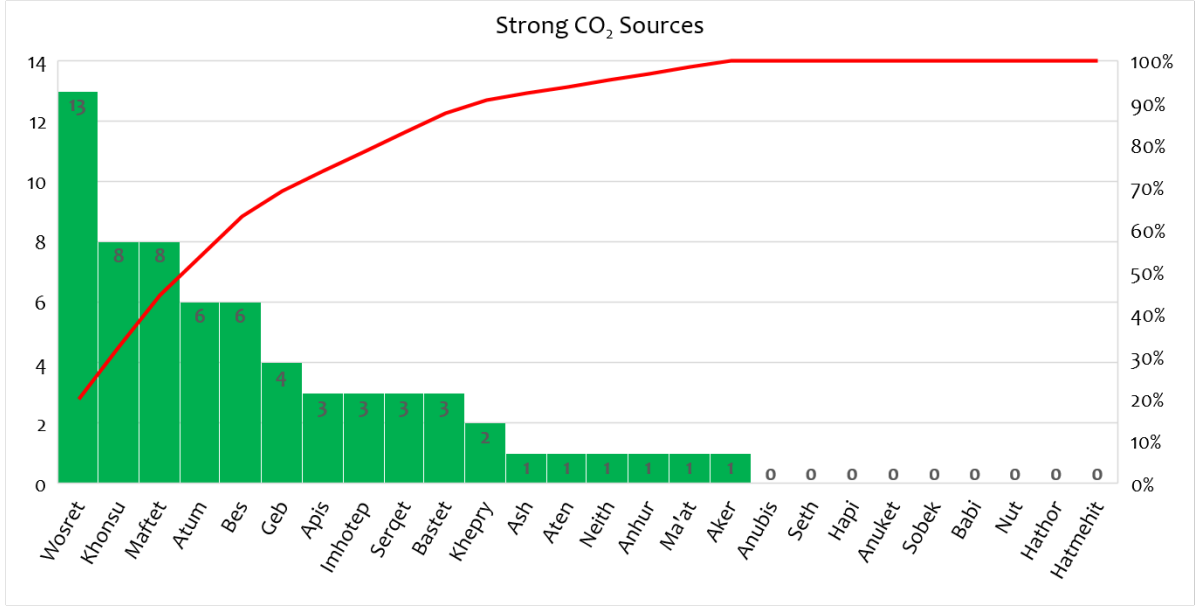


Figure B.3: Final count of CO₂ sources.

APPENDIX B. MAPPING OF CO₂ SOURCES USING VIRTIS-M IMAGES

observed more times to have the strongest emissions, followed by regions Maftet, Atum, Bes and Geb.

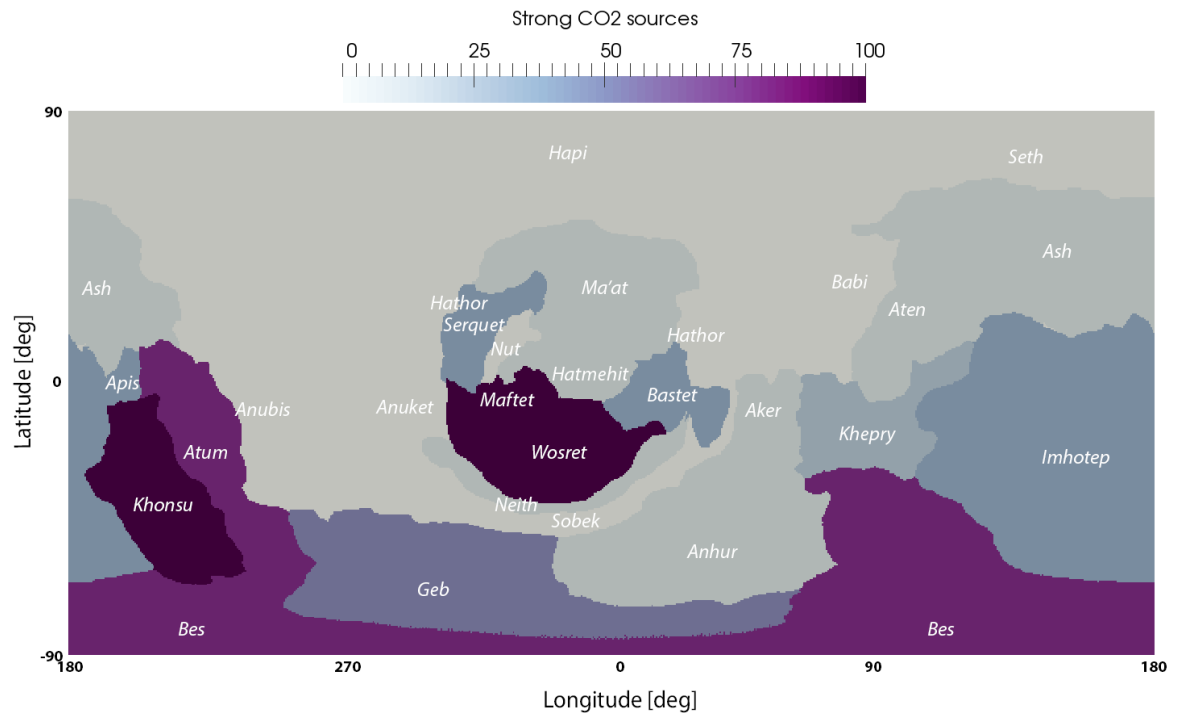


Figure B.4: CO₂ sources identified after the VIRTIS-M images analysis between February 25th to April 27th, 2015. Darker regions show the strongest outgassing in a larger amount of images. Regions in light gray showed very low or no outgassing at all. The data has been normalized in order to compare the likeliness of regions with respect to *Wosret*, which was the one with more CO₂ observations.

Bibliography

Esa science and technology web server - rosetta instruments.

<http://sci.esa.int/science-e/www/object/index.cfm?fobjectid=35061>.

Accessed: 2020-11-20.

C. Acton.

Ancillary data services of nasa's navigation and ancillary information facility.

Planetary and Space Science, 44:65–70, 1996.

URL [https://doi.org/10.1016/0032-0633\(95\)00107-7](https://doi.org/10.1016/0032-0633(95)00107-7).

C. Acton, N. Bachman, B. Semenov, and E. Wright.

A look towards the future in the handling of space science mission geometry.

Planetary and Space Science, 150, 02 2017.

URL <https://doi.org/10.1016/j.pss.2017.02.013>.

M. F. A'Hearn, R. C. Millis, D. G. Schleicher, D. J. Osip, and P. V. Birch.

The Ensemble Properties of Comets: Results from Narrowband Photometry of 85 Comets, 1976-1992.

Icarus, 118:223–270, 1995.

URL <https://doi.org/10.1006/icar.1995.1190>.

M. F. A'Hearn, M. J. S. Belton, W. A. Delamere, et al.

Deep impact: Excavating comet tempel 1.

Science, 310(5746):258–264, 2005.

doi: 10.1126/science.1118923.

M. F. A'Hearn, M. J. S. Belton, W. A. Delamere, et al.

EPOXI at Comet Hartley 2.

Science, 332(Issue 6036):1396–1400, 2011.

doi: 10.1126/science.1204054.

K. Altwegg, H. Balsiger, J.J. Berthelier, et al.

Organics in comet 67P – a first comparative analysis of mass spectra from ROSINA–DFMS, COSAC and Ptolemy.

BIBLIOGRAPHY

- MNRAS*, 469(Suppl 2):130–141, 06 2017.
URL <https://doi.org/10.1093/mnras/stx1415>.
- Y. Amelin, A. N. Krot, I. D. Hutcheon, and A. Ulyanov.
Lead isotopic ages of chondrules and calcium-aluminum-rich inclusions.
Science, 297(5587):1678–1683, 2002.
URL <https://science.sciencemag.org/content/297/5587/1678>.
- A.-T. Auger, O. Groussin, L. Jorda, et al.
Geomorphology of the imhotep region on comet 67p/churyumov-gerasimenko from osiris observations.
A&A, 583:A35, 11 2015.
doi: 10.1051/0004-6361/201525947.
- J. Baker, M. Bizzarro, N. Wittig, et al.
Early planetesimal melting from an age of 4.5662 gyr for differentiated meteorites.
Nature, 436:1127–1131, 2005.
URL <https://doi.org/10.1038/nature03882>.
- H. Balsiger, K. Altwegg, P. Bochsler, P. Eberhardt, et al.
Rosina – rosetta orbiter spectrometer for ion and neutral analysis.
Space Science Reviews, 128:745–801, 2007.
URL <https://doi.org/10.1007/s11214-006-8335-3>.
- A. Bardyn, D. Baklouti, H. Cottin, et al.
Carbon-rich dust in comet 67P/Churyumov-Gerasimenko measured by COSIMA/Rosetta.
MNRAS, 469(Suppl 2):S712–S722, 11 2017.
URL <https://doi.org/10.1093/mnras/stx2640>.
- M. A. Barucci, G. Filacchione, S. Fornasier, et al.
Detection of exposed H₂O ice on the nucleus of comet 67P/Churyumov-Gerasimenko.
A&A, 595(A102), 2016.
URL <https://doi.org/10.1051/0004-6361/201628764>.
- A. Bieler, K. Altwegg, H. Balsiger, et al.
Comparison of 3D kinetic and hydrodynamic models to ROSINA-COPS measurements of the neutral coma of 67P.
A&A, 583(A7), 2015a.
URL <https://doi.org/10.1051/0004-6361/201526178>.
- A. Bieler, K. Altwegg, H. Balsiger, et al.
Abundant molecular oxygen in the coma of comet 67P/Churyumov–Gerasimenko.

- Nature*, 526:678–681, 2015b.
URL <https://doi.org/10.1038/nature15707>.
- G. A. Bird.
The Physics of Fluids, (6), 1963.
URL <https://doi.org/10.1063/1.1710976>.
- G. A. Bird.
Molecular Gas Dynamics and the Direct Simulation of Gas Flows.
Oxford Science Publications, 1994.
- G. A. Bird.
The DS2V/3V Program Suite for DSMC Calculations.
AIP Conference Proceedings, 762(541), 2005.
URL <https://doi.org/10.1063/1.1941592>.
- N. Biver, D. Bockelée-Morvan, J. Boissier, et al.
Radio observations of comet 9p/tempel 1 before and after deep impact.
Icarus, 191(2, Supplement):494 – 512, 2007.
URL <https://doi.org/10.1016/j.icarus.2006.10.043>.
Deep Impact at Comet Tempel 1.
- N. Biver, M. Hofstadter, Samuel Gulkis, et al.
Distribution of water around the nucleus of comet 67P/Churyumov-Gerasimenko at 3.4 AU from the Sun as seen by the MIRO instrument on Rosetta.
A&A, 583(A3), 2015.
URL <https://doi.org/10.1051/0004-6361/201526094>.
- N. Biver, D. Bockelée-Morvan, M. Hofstadter, et al.
Long-term monitoring of the outgassing and composition of comet 67p/churyumov-gerasimenko with the rosetta/miro instrument.
A&A, 630(A19), 03 2019.
URL <https://doi.org/10.1051/0004-6361/201834960>.
- D. Bockelée-Morvan.
An Overview of Comet Composition.
Proceedings of the International Astronomical Union, 7(S280):261–274, 2011.
doi: 10.1017/S1743921311025038.
- D. Bockelée-Morvan and N. Biver.
The composition of cometary ices.
Phil. Trans. R. Soc. A, 375(20160252), 2017.
URL <https://doi.org/10.1098/rsta.2016.0252>.

BIBLIOGRAPHY

D. Bockelée-Morvan, V. Debout, S. Erard, et al.

First observations of H₂O and CO₂ vapor in comet 67P/Churyumov-Gerasimenko made by VIRTIS onboard Rosetta.

A&A, 583(A6), 2015.

URL <https://doi.org/10.1051/0004-6361/201526303>.

B. Bonev, M. Mumma, G. Villanueva, et al.

A search for variation in the h₂o ortho-para ratio and rotational temperature in the inner coma of comet c/2004 q2 (machholz).

The Astrophysical Journal Letters, 661:L97, 05 2007.

doi: 10.1086/518419.

A. Bouvier and M. Wadhwa.

The age of the solar system redefined by the oldest pb–pb age of a meteoritic inclusion.

Nature Geoscience, 3:637–641, 08 2010.

URL <https://doi.org/10.1038/ngeo941>.

Y. Brouet, A. C. Levasseur-Regourd, P. Sabouroux, et al.

A porosity gradient in 67p/c-g nucleus suggested from consort and sesame-pp results: an interpretation based on new laboratory permittivity measurements of porous icy analogues.

MNRAS, 462:S89–S98, 2016.

URL <https://doi.org/10.1093/mnras/stw2151>.

D. E. Brownlee, F. Horz, R. L. Newburn, et al.

Surface of young jupiter family comet 81p/wild 2: View from the stardust spacecraft.

Science, 304(5678):1764–1769, 2004.

doi: 10.1126/science.1097899.

B.J Buratti, M.D Hicks, L.A Soderblom, D Britt, J Oberst, and J.K Hillier.

Deep space 1 photometry of the nucleus of comet 19p/borrelly.

Icarus, 167(1):16 – 29, 2004.

ISSN 0019-1035.

URL <https://doi.org/10.1016/j.icarus.2003.05.002>.

Special Issue on DS1/Comet Borrelly.

R. Caflisch.

Fluid dynamics and the boltzmann equation.

Physica A: Statistical Mechanics and its Applications, 124(1):171 – 179, 1984.

ISSN 0378-4371.

URL [https://doi.org/10.1016/0378-4371\(84\)90235-8](https://doi.org/10.1016/0378-4371(84)90235-8).

F. Capaccioni, A. Coradini, G. Filacchione, et al.

- The organic-rich surface of comet 67p/churyumov-gerasimenko as seen by virtis/rosetta.
Science, 347(6220), 2015.
doi: 10.1126/science.aaa0628.
- J. W. Chamberlain.
Theory of Planetary Atmospheres. An introduction to their physics and chemistry (International geophysics series), volume 22.
Academic Press, Inc. (London), 1978.
- C. Christou, K. Dadzie, N. Thomas, et al.
Gas flow in near surface comet like porous structures: Application to 67P/Churyumov-Gerasimenko.
Planetary and Space Science, 161:57–67, 2018.
URL <https://doi.org/10.1016/j.pss.2018.06.009>.
- K. I. Churyumov and S. I. Gerasimenko.
Physical observations of the short-period comet 1969 iv.
Symposium - International Astronomical Union, 45:27–34, 1972.
doi: 10.1017/S0074180900006215.
- M. Combi.
Monte carlo particle trajectory models for neutral cometary gases. ii. the spatial morphology of the lyman-alpha coma.
Astrophysical Journal, 327:1044, 1988b.
doi: 10.1086/166260.
- M. Combi.
The outflow speed of the coma of halley's comet.
Icarus, 81(1):41 – 50, 1989.
URL [https://doi.org/10.1016/0019-1035\(89\)90124-3](https://doi.org/10.1016/0019-1035(89)90124-3).
- M. Combi.
Time-dependent gas kinetics in tenuous planetary atmospheres: The cometary coma.
Icarus, 123(1):207 – 226, 1996.
ISSN 0019-1035.
URL <https://doi.org/10.1006/icar.1996.0150>.
- M. Combi and W.H. Smyth.
Monte Carlo particle-trajectory models for neutral cometary gases. I - Models and equations.
Astrophysical Journal, 327(1026), 1988a.
- M. Combi, Y. Shou, N. Fougere, et al.

BIBLIOGRAPHY

- The Surface Distributions of the Production of the Major Volatile Species, H₂O, CO₂, CO and O₂, from the Nucleus of Comet 67P/Churyumov-Gerasimenko throughout the Rosetta Mission as Measured by the ROSINA Double Focusing Mass Spectrometer.
Icarus, 335, 2020.
URL <https://doi.org/10.1016/j.icarus.2019.113421>.
- A. Coradini, F. Capaccioni, P. Drossart, A. Semery, G. Arnold, and U. Schade.
Virtis: The imaging spectrometer of the rosetta mission.
Advances in Space Research, 24:1095–1104, 01 2007.
doi: 10.1016/S0273-1177(99)80203-8.
- H. Cottin and N. Fray.
Distributed Sources in Comets, volume 138, pages 179–197.
01 1970.
doi: 10.1007/978-0-387-85455-7_11.
- T. E. Cravens.
A magnetohydrodynamical model of the inner coma of comet halley.
Journal of Geophysical Research: Space Physics, 94(A11):15025–15040, 1989.
URL <https://doi.org/10.1029/JA094iA11p15025>.
- J.-F. Crifo.
Hydrodynamic expansion of cometary gas loaded with refractory and volatile grains.
Asteroids, comets, meteors II; Proceedings of the International Meeting, Uppsala, Sweden, pages 389–392, 1986a.
- J.-F. Crifo.
Optical and hydrodynamic implications of comet halley dust size distribution.
ESA, Proceedings of the International Symposium on the Diversity and Similarity of Comets, pages 399–408, 1987b.
- J.-F. Crifo.
Improved gas-kinetic treatment of cometary water sublimation and recondensation: application to comet p/halley.
In Michael Grewing, Françoise Praderie, and Rüdiger Reinhard, editors, *Exploration of Halley's Comet*, pages 438–450, Berlin, Heidelberg, 1988. Springer Berlin Heidelberg.
- J.-F. Crifo.
Collisional coma models: An unorthodox overview.
Advances in Space Research, 9(3):197 – 211, 1989.
URL [https://doi.org/10.1016/0273-1177\(89\)90261-5](https://doi.org/10.1016/0273-1177(89)90261-5).

J.-F. Crifo.

Water clusters in the coma of comet halley and their effect on the gas density, temperature, and velocity.

Icarus, 84(2):414–446, 1990.

URL [https://doi.org/10.1016/0019-1035\(90\)90047-D](https://doi.org/10.1016/0019-1035(90)90047-D).

J.-F. Crifo.

The correct evaluation of the sublimation rate of dusty ices under solar illumination, and its implication on the properties of p/halley nucleus.

Icarus, 130(2):549 – 551, 1997b.

URL <https://doi.org/10.1006/icar.1997.5827>.

J.-F. Crifo and A. V. Rodionov.

The dependence of the circumnuclear coma structure on the properties of the nucleus.

Icarus, 129(1):72 – 93, 1997a.

URL <https://doi.org/10.1006/icar.1997.5714>.

J.-F. Crifo and A.V. Rodionov.

The dependence of the circumnuclear coma structure on the properties of the nucleus: Iv. structure of the night-side gas coma of a strongly sublimating nucleus.

Icarus, 148(2):464 – 478, 2000.

URL <https://doi.org/10.1006/icar.2000.6495>.

J.-F. Crifo, G. Lukianov, A. Rodionov, G. Khanlarov, and V. Zakharov.

Comparison between Navier–Stokes and Direct Monte–Carlo Simulations of the Circumnuclear Coma: I. Homogeneous, Spherical Source.

Icarus, 156(Issue 1), 2002.

URL <https://doi.org/10.1006/icar.2001.6769>.

J.-F. Crifo, G. A. Loukianov, A. V. Rodionov, and V. Zakharov.

Navier–Stokes and direct Monte Carlo simulations of the circumnuclear coma II. Homogeneous, aspherical sources.

Icarus, 163(Issue 2), 2003.

URL [https://doi.org/10.1016/S0019-1035\(03\)00041-1](https://doi.org/10.1016/S0019-1035(03)00041-1).

J.-F. Crifo, M. Fulle, N. Kömle, and K. Szego.

Nucleus-coma structural relationships: lessons from physical models.

Comets II, pages 471–503, 01 2004.

J.-F. Crifo, G. A. Loukianov, A. V. Rodionov, and V. Zakharov.

Direct Monte Carlo and multifluid modeling of the circumnuclear dust coma: Spherical grain dynamics revisited.

BIBLIOGRAPHY

- Icarus*, 176(Issue 1), 2005.
URL <https://doi.org/10.1016/j.icarus.2005.01.003>.
- B. Davidsson and Y. Skorov.
A practical tool for simulating the presence of gas comae in thermophysical modeling of cometary nuclei.
Icarus, 168(Issue 1):163–185, 2004.
URL <https://doi.org/10.1016/j.icarus.2003.11.002>.
- B. Davidsson, P. Gutiérrez, O. Groussin, et al.
Thermal inertia and surface roughness of Comet 9P/Tempel 1.
Icarus, 224(Issue 1):154–171, 5 2013.
URL <https://doi.org/10.1016/j.icarus.2013.02.008>.
- M.C. De Sanctis, J. Lasue, M.T. Capria, G. Magni, D. Turrini, and A. Coradini.
Shape and obliquity effects on the thermal evolution of the rosetta target 67p/churyumov-gerasimenko cometary nucleus.
Icarus, 207(1):341 – 358, 2010.
URL <https://doi.org/10.1016/j.icarus.2009.11.009>.
- M. Delbo', A. dell'Oro, A. W. Harris, S. Mottola, and M. Mueller.
Thermal inertia of near-earth asteroids and implications for the magnitude of the yarkovsky effect.
Icarus, 190(1):236 – 249, 2007.
URL <https://doi.org/10.1016/j.icarus.2007.03.007>.
- A.-H. Delsemme and P. Swings.
Hydrates de gaz dans les noyaux cométaires et les grains interstellaires.
Annales d'Astrophysique, 15:1–6, 1952.
- P. Deshapriya, M. Barucci, S. Fornasier, et al.
Exposed bright features on the comet 67p/churyumov-gerasimenko: Distribution and evolution.
A&A, 613:A36, 05 2018.
doi: 10.1051/0004-6361/201732112.
- G. B. Donati.
Entdeckung eines cometen. schreiben des herrn prof., dr. donati an den herausgeber.
Astronomische Nachrichten, 62, 1864.
- M. Duncan, T. Quinn, and S. Tremaine.
The origin of short-period comets.
Astrophysical Journal, 328:L69–L73, 1988.

P. Eberhardt.

Comet Halley's Gas Composition and Extended Sources: Results from the Neutral Mass Spectrometer on Giotto, volume 8, pages 45–52.

Space Science Series of ISSI, 1999.

A. S. Eddington.

The envelopes of comet morehouse (1908 c).

MNRAS, 70, 1910.

URL <https://doi.org/10.1093/mnras/70.5.442>.

E. Edgeworth.

The Origin and Evolution of the solar System.

Journal of the British Astronomical Association, 53(186), 1943.

M. El-Maarry, N. Thomas, A. Gracia-Berná, et al.

Regional surface morphology of comet 67p/churyumov-gerasimenko from rosetta/osiris images: The southern hemisphere.

A&A, 598, 09 2016.

URL <https://doi.org/10.1051/0004-6361/201628634>.

C. Emerich, J. M. Lamarre, V. I. Moroz, et al.

Temperature and size of the nucleus of comet P/Halley deduced from IKS infrared Vega 1 measurements, pages 839–842.

Springer, Berlin, Heidelberg, 1988.

F. P. Fanale and J. R. Salvail.

An idealized short-period comet model: Surface insolation, H₂O flux, dust flux, and mantle evolution.

Icarus, 60(Issue 3):476–511, 1984.

URL [https://doi.org/10.1016/0019-1035\(84\)90157-X](https://doi.org/10.1016/0019-1035(84)90157-X).

F. P. Fanale and J. R. Salvail.

A model of cometary gas and dust production and nongravitational forces with application to p/halley.

Icarus, 66(1):154 – 164, 1986.

URL [https://doi.org/10.1016/0019-1035\(86\)90015-1](https://doi.org/10.1016/0019-1035(86)90015-1).

F. P. Fanale and J. R. Salvail.

The loss and depth of co₂ ice in comet nuclei.

Icarus, 72(3):535 – 554, 1987.

URL [https://doi.org/10.1016/0019-1035\(87\)90051-0](https://doi.org/10.1016/0019-1035(87)90051-0).

BIBLIOGRAPHY

F. P. Fanale and J. R. Salvail.

The influence of co ice on the activity and near-surface differentiation of comet nuclei.

Icarus, 84(2):403 – 413, 1990.

URL [https://doi.org/10.1016/0019-1035\(90\)90046-C](https://doi.org/10.1016/0019-1035(90)90046-C).

L. M. Feaga, M. F. A'Hearn, J. M. Sunshine, O. Groussin, and T. L. Farnham.

Asymmetries in the distribution of H₂O and CO₂ in the inner coma of Comet 9P/Tempel 1 as observed by Deep Impact.

Icarus, 191(Issue 2):134–145, 2007.

URL <https://doi.org/10.1016/j.icarus.2007.04.009>.

P. Feldman, M. A'Hearn, J.-L. Bertaux, et al.

Fuv spectral signatures of molecules and the evolution of the gaseous coma of comet 67p/churyumov-gerasimenko.

The Astronomical Journal, 155, 11 2017.

doi: 10.3847/1538-3881/aa9bf2.

J. A. Fernández.

On the existence of a comet belt beyond Neptune.

MNRAS, 192(3):481–491, 10 1980.

URL <https://doi.org/10.1093/mnras/192.3.481>.

Y. R. Fernández, M. S. Kelley, P. L. Lamy, et al.

Thermal properties, sizes, and size distribution of Jupiter-family cometary nuclei.

Icarus, 226(Issue 1):1138–1170, 2013.

URL <https://doi.org/10.1016/j.icarus.2013.07.021>.

M. Festou, H. U. Keller, and H. A. Weaver.

Comets II.

University of Arizona Press, 2004.

G. Filacchione, M. C. De Sanctis, F. Capaccioni, et al.

Exposed water ice on the nucleus of comet 67P/Churyumov–Gerasimenko.

Nature, 529:368–372, 2016.

URL <https://doi.org/10.1038/nature16190>.

U. Fink, M. P. Hicks, and R. A. Fevig.

Production rates for the stardust mission target: 81p/wild 2.

Icarus, 141(2):331 – 340, 1999.

ISSN 0019-1035.

URL <https://doi.org/10.1006/icar.1999.6182>.

- U. Fink, L. Doose, G. Rinaldi, et al.
Investigation into the disparate origin of CO₂ and H₂O outgassing for Comet 67P.
Icarus, 277:78–97, 10 2016.
URL <https://doi.org/10.1016/j.icarus.2016.04.040>.
- S. Finklenburg.
Investigations of the Near Nucleus Gas and Dust Coma of Comets.
PhD dissertation, Universität Bern, 2014.
- S. Finklenburg and N. Thomas.
Relating in situ gas measurements to the surface outgassing properties of cometary nuclei.
Planetary and Space Science, 93-94, 04 2014a.
doi: 10.1016/j.pss.2014.02.005.
- S. Finklenburg, N. Thomas, C.C. Su, and J.-S. Wu.
The spatial distribution of water in the inner coma of comet 9p/tempel 1: Comparison between models and observations.
Icarus, 236:9–23, 2014b.
URL <https://doi.org/10.1016/j.icarus.2014.03.032>.
- S. Fornasier, P. H. Hasselmann, and M. Barucci.
Spectrophotometric properties of the nucleus of comet 67P/Churyumov-Gerasimenko from the OSIRIS instrument onboard the ROSETTA spacecraft.
A&A, 583(A30), 2015.
URL <https://doi.org/10.1051/0004-6361/201525901>.
- S. Fornasier, S Mottola, H Keller, et al.
Rosetta's comet 67P/Churyumov-Gerasimenko sheds its dusty mantle to reveal its icy nature.
Science, 354(Issue 6319), 2016.
doi: 10.1126/science.aag2671.
- N. Fougere, K. Altwegg, J. Berthelier, et al.
Three-dimensional DSMC modeling of the coma of comet 67P observed by the VIRTIS and ROSINA instruments on board Rosetta.
A&A, 588(A134), 2016a.
URL <https://doi.org/10.1051/0004-6361/201527889>.
- N. Fougere, K. Altwegg, J.-J Berthelier, et al.
Direct Simulation Monte Carlo modelling of the major species in the coma of comet 67P.
MNRAS, 462(S156-S169), 09 2016b.
URL <https://doi.org/10.1093/mnras/stw2388>.

BIBLIOGRAPHY

- S. Gasc, K. Altwegg, B. Fiethe, A. Jäckel, A. Korth, et al.
Sensitivity and fragmentation calibration of the time-of-flight mass spectrometer RTOF on board ESA's Rosetta mission.
Planetary and Space Science, 135:64–73, 2017.
URL <https://doi.org/10.1016/j.pss.2016.11.011>.
- S.-B. Gerig, R. Marschall, N. Thomas, et al.
On deviations from free-radial outflow in the inner coma of comet 67p/churyumov–gerasimenko.
Icarus, 311:1 – 22, 2018.
URL <https://doi.org/10.1016/j.icarus.2018.03.010>.
- S.-B. Gerig, O. Pinzón-Rodríguez, R. Marschall, J.S. Wu, and N. Thomas.
Dayside-to-nightside dust coma brightness asymmetry and its implications for nightside activity at comet 67P/Churyumov-Gerasimenko.
Icarus, 351(113968), 2020.
URL <https://doi.org/10.1016/j.icarus.2020.113968>.
- A. Gicquel, D. Bockelée-Morvan, Vladimir Zakharov, M. Kelley, C. Woodward, and D. Wooden.
Investigation of dust and water ice in comet 9p/tempel 1 from spitzer observations of the deep impact event.
A&A, 542(A119), 06 2012.
URL <https://doi.org/10.1051/0004-6361/201118718>.
- T. Gombosi, T. Cravens, and A. Nagy.
Time-dependent dusty gasdynamical flow near cometary nuclei.
The Astrophysical Journal, 293, 07 1985.
doi: 10.1086/163240.
- T. Gombosi, A. Nagy, and T. Cravens.
Dust and neutral gas modeling of the inner atmosphere of comets.
Rev. Geophys., 24, 09 1986a.
doi: 10.1029/RG024i003p00667.
- T. Gombosi, D. L. De Zeeuw, R. M. Häberli, and K. G. Powell.
Three-dimensional multiscale mhd model of cometary plasma environments.
Journal of Geophysical Research: Space Physics, 101(A7):15233–15253, 1996.
URL <https://doi.org/10.1029/96JA01075>.
- O. Groussin, J. Sunshine, L. Feaga, et al.
The temperature, thermal inertia, roughness and color of the nuclei of Comets 103P/Hartley 2 and 9P/Tempel 1.
Icarus, 222(Issue 2):580–594, 2 2013.

URL <https://doi.org/10.1016/j.icarus.2012.10.003>.

O. Groussin, N. Attree, Y. Brouet, et al.

The thermal, mechanical, structural, and dielectric properties of cometary nuclei after rosetta.
Space Science Reviews volume, 215(29), 2019.

URL <https://doi.org/10.1007/s11214-019-0594-x>.

E. Grün, J. Benkhoff, R. Heidrich, P. Hesselbarth, H. Kohl, and E. Kührt.

Energy balance of the kosi 4 experiment.

Geophysical Research Letters, 18(2):257–260, 1991.

URL <https://doi.org/10.1029/90GL02523>.

S. Gulkis, M. Frerking, J. Crovisier, et al.

Miro: Microwave instrument for rosetta orbiter.

Space Science Reviews, 128:561–597, 02 2007.

URL <https://doi.org/10.1007/s11214-006-9032-y>.

S. Gulkis, M. Allen, P. von Allmen, et al.

Subsurface properties and early activity of comet 67P/Churyumov-Gerasimenko.

Science, 347(Issue 6220), 2015.

doi: DOI:10.1126/science.aaa0709.

K. C. Hansen, K. Altwegg, J.-J. Berthelier, et al.

Evolution of water production of 67P/Churyumov-Gerasimenko: an empirical model and a multi-instrument study.

MNRAS, 462(Suppl₁): S491 – –S506, 092016.

URL <https://doi.org/10.1093/mnras/stw2413>.

W. M. Harris, M. R. Combi, R. K. Honeycutt, B. E. A. Mueller, and F. Scherb.

Evidence for interacting gas flows and an extended volatile source distribution in the coma of comet c/1996 b2 (hyakutake).

Science, 277(5326):676–681, 1997.

doi: 10.1126/science.277.5326.676.

P. Hartogh, D. C. Lis, D. Bockelée-Morvan, et al.

Ocean-like water in the jupiter-family comet 103p/hartley 2.

Nature, 478:218–220, 2011.

URL <https://doi.org/10.1038/nature10519>.

L. Haser.

Distribution d'intensité dans la tête d'une comète.

Bulletin de la Classe des Sciences de l'Académie Royale de Belgique, 43, 1957.

BIBLIOGRAPHY

- K. Heng.
Exoplanetary Atmospheres. Theoretical concepts and foundations.
Princeton University Press, 2017.
- C. Herny, O. Mousis, R. Marschall, Nicolas Thomas, Martin Rubin, Olga Pinzón-Rodríguez, and I. P. Wright.
New constraints on the chemical composition and outgassing of 67p/churyumov-gerasimenko.
Planetary and Space Science, submitted for publication.
- T.M. Ho, N. Thomas, D.C. Boice, C. Kollein, and L.A. Soderblom.
Comparative study of the dust emission of 19p/borrelly (deep space 1) and 1p/halley.
Advances in Space Research, 31(12):2583 – 2589, 2003.
ISSN 0273-1177.
URL [https://doi.org/10.1016/S0273-1177\(03\)00580-5](https://doi.org/10.1016/S0273-1177(03)00580-5).
Interpretation of the Remote and In-Situ Observations of Small Bodies.
- Ho Peng Yoke and Ho Ping-Yü.
Ancient and mediaeval observations of comets and novae in chinese sources.
Vistas in Astronomy, 5:127 – 225, 1962.
ISSN 0083-6656.
URL [https://doi.org/10.1016/0083-6656\(62\)90007-7](https://doi.org/10.1016/0083-6656(62)90007-7).
- M. Hoang, K. Altwegg, H. Balsiger, et al.
The heterogeneous coma of comet 67P as seen by ROSINA: H₂O and CO₂ from September 2014 to February 2016.
A&A, 600(A77), 2016.
URL <https://doi.org/10.1051/0004-6361/201629900>.
- W.F. Huebner, J. Benkhoff, M-T. Capria, et al.
Heat and Gas Diffusion in Comet Nuclei.
The International Space Science Institute, 2006.
- W. Huggins.
Spectrum analysis of comet ii.
Astronomical register, 6:169–170, 1868.
- M. Hässig, K. Altwegg, H. Balsiger, et al.
Time variability and heterogeneity in the coma of 67P/Churyumov-Gerasimenko.
Science, 347(Issue 6220), 2015.
doi: DOI:10.1126/science.aaa0276.
- A. Ivanova and L.M. Shulman.

- The crater model of an active area as applied to comet 81p/wild-2.
New Astronomy, 11(3):185 – 196, 2005.
URL <https://doi.org/10.1016/j.newast.2005.06.009>.
- E. K. Jessberger, A. Christoforidis, and J. Kissel.
Aspects of the major element composition of halley’s dust.
Nature, 1988.
URL <https://doi.org/10.1038/332691a0>.
- D. Jewitt and J. Luu.
Discovery of the candidate Kuiper belt object 1992 QB₁.
Nature, 362:730–732, 1993.
URL <https://doi.org/10.1038/362730a0>.
- G. Jones, A. Balogh, and T Horbury.
Identification of comet hyakutake’s extremely long ion tail from magnetic field signatures.
Nature, 404:574–576, 2000.
URL <https://doi.org/10.1038/35007011>.
- L. Jorda, R. Gaskell, C. Capanna, et al.
The global shape, density and rotation of comet 67p/churyumov-gerasimenko from preperihelion rosetta/osiris observations.
Icarus, 277:257 – 278, 2016.
URL <https://doi.org/10.1016/j.icarus.2016.05.002>.
- M. Jutzi and W. Benz.
Formation of bi-lobed shapes by sub-catastrophic collisions.
A&A, 597(A62), 2016.
URL <https://doi.org/10.1051/0004-6361/201628964>.
- H. U. Keller, C. Arpigny, C. Barbieri, et al.
First halley multicolour camera imaging results from giotto.
Nature, 321:320–326, 1986.
URL <https://doi.org/10.1038/321320a0>.
- H. U. Keller, C. Barbieri, P. Lamy, et al.
Osiris - the scientific camera system onboard rosetta.
Space Science Reviews, 128:433–506, 02 2007.
URL <https://doi.org/10.1007/s11214-006-9128-4>.
- H. U. Keller, S. Mottola, Y. Skorov, and L. Jorda.
The changing rotation period of comet 67P/Churyumov-Gerasimenko controlled by its activity.

BIBLIOGRAPHY

- A&A, 579(L5), 2015.
URL <https://doi.org/10.1051/0004-6361/201526421>.
- H. U. Keller, S. Mottola, S. F. Hviid, et al.
Seasonal mass transfer on the nucleus of comet 67P/Chuyumov–Gerasimenko.
MNRAS, 469(Suppl₂): S357 – –S371, 072017.
URL <https://doi.org/10.1093/mnras/stx1726>.
- J. Kissel, K. Altwegg, B. Clark, et al.
Cosima – high resolution time-of-flight secondary ion mass spectrometer for the analysis of cometary dust particles onboard rosetta.
Space Science Reviews, 128:823–867, 02 2007.
URL <https://doi.org/10.1007/s11214-006-9083-0>.
- Y. Kitamura.
Axisymmetric dusty gas jet in the inner coma of a comet: Ii. the case of isolated jets.
Icarus, 72(3):555 – 567, 1987.
ISSN 0019-1035.
URL [https://doi.org/10.1016/0019-1035\(87\)90052-2](https://doi.org/10.1016/0019-1035(87)90052-2).
- Y. Kitamura.
A numerical study of the interaction between two cometary jets: A possibility of shock formation in cometary atmospheres.
Icarus, 86(2):455–475, 1990.
URL [https://doi.org/10.1016/0019-1035\(90\)90229-3](https://doi.org/10.1016/0019-1035(90)90229-3).
- Y. Kitamura, O. Ashihara, and T. Yamamoto.
A model for the hydrogen coma of a comet.
Icarus, 61(2):278 – 295, 1985.
ISSN 0019-1035.
URL [https://doi.org/10.1016/0019-1035\(85\)90109-5](https://doi.org/10.1016/0019-1035(85)90109-5).
- J. Knollenberg.
Modellrechnungen zur Staubverteilung in der inneren Koma von Kometen unter spezieller Berücksichtigung der HMC-Daten der GIOTTO-Mission.
PhD dissertation, Georg-August-Universität Göttingen, 1994.
- N. I. Koemle and W.-H. Ip.
A model of the anisotropic structure of the neutral gas coma of a comet.
ESA, Proceedings of the International Symposium on the Diversity and Similarity of Comets, 1987.

- W. Kofman, A. Herique, and Y. Barbin.
Properties of the 67P/Churyumov-Gerasimenko interior revealed by CONSERT radar.
Science, 2015.
- G. P. Kuiper.
On the origin of the solar system.
Proceedings of the National Academy of Sciences, 37(1), 1951.
- M. Küppers, I. Bertini, S. Fornasier, et al.
A large dust/ice ratio in the nucleus of comet 9p/tempel 1.
Nature, 437:987–990, 2005.
URL <https://doi.org/10.1038/nature04236>.
- P. Lamy, I. Toth, M.F. A'Hearn, H.A. Weaver, and P. Weissman.
Hubble Space Telescope Observations of the Nucleus of Comet 9P/Tempel 1.
Icarus, 154(Issue 2):337–344, 2001.
- P. Lamy, I. Toth, H. Weaver, L. Jorda, M. Kaasalainen, and P. Gutiérrez.
Hubble space telescope observations of the nucleus and inner coma of comet 67p/churyumov-gerasimenko.
A&A, 458:669–678, 11 2006.
doi: 10.1051/0004-6361:20065253.
- P. Lamy, I. Toth, B. J. R. Davidsson, et al.
A portrait of the nucleus of comet 67p/churyumov-gerasimenko.
Space Science Reviews, 128:23–66, 2007.
URL <https://doi.org/10.1007/s11214-007-9146-x>.
- L. Le Roy, K. Altwegg, H. Balsiger, et al.
Inventory of the volatiles on comet 67P/Churyumov-Gerasimenko from Rosetta/ROSINA.
A&A, 583(A1), 2015.
URL <https://doi.org/10.1051/0004-6361/201526450>.
- L. Lebofsky and J. Spencer.
Radiometry and thermal modeling of asteroids.
Asteroids II, 02 1989.
- J.-Y. Li, M. A'Hearn, L. Mcfadden, and M. Belton.
Photometric analysis and disk-resolved thermal modeling of Comet 19P/Borrelly from Deep Space 1 data.
Icarus, page 188, 2007.

BIBLIOGRAPHY

- Y. Liao, C. C. Su, R. Marschall, et al.
3D direct simulation Monte Carlo modelling of the inner gas coma of comet 67P/Churyumov–Gerasimenko: A parameter study.
Earth, Moon and Planets, 117:41–64, 2016.
- Y. Liao, R. Marschall, C.C. Su, et al.
Water vapor deposition from the inner gas coma onto the nucleus of Comet 67P/Churyumov-Gerasimenko.
Planetary and Space Science, pages 1–9, 2018.
- S. Lowry, A. Fitzsimmons, P. Lamy, and P. Weissman.
Kuiper belt objects in the planetary region: The jupiter-family comets.
The Solar System Beyond Neptune, 01 2008.
- S. Lowry, S. R. Duddy, B. Rozitis, et al.
The nucleus of comet 67p/churyumov-gerasimenko. a new shape model and thermophysical analysis.
A&A, 548(A12), 2012.
- G. A. Lukyanov, V. V. Zakharov, A. V. Rodionov, , and J.-F. Crifo.
Comparison between navier-stokes and dsmc simulations of the rarefied gas flow from model cometary nuclei.
AIP Conference Proceedings, 762(331), 2005.
- M. L auter, T. Kramer, M. Rubin, and K. Altwegg.
Surface localization of gas sources on comet 67P/Churyumov–Gerasimenko based on DFMS/COPS data.
MNRAS, 483(1):852–861, 11 2018.
URL <https://doi.org/10.1093/mnras/sty3103>.
- M. L auter, T. Kramer, M. Rubin, and K. Altwegg.
The gas production of 14 species from comet 67p/churyumov-gerasimenko based on dfms/cops data from 2014-2016, 2020.
- U. Marboeuf and B. Schmitt.
How to link the relative abundances of gas species in coma of comets to their initial chemical composition?
Icarus, 242:225 – 248, 2014.
URL <https://doi.org/10.1016/j.icarus.2014.07.001>.
- U. Marboeuf, B. Schmitt, J.-M Petit, O. Mousis, and N Fray.
A cometary nucleus model taking into account all phase changes of water ice: Amorphous, crystalline, and clathrate.

- A&A, 542, 06 2012.
URL <https://doi.org/10.1051/0004-6361/201118176>.
- M. L. Marconi and D. A. Mendis.
A multi-fluid model of an h₂o-dominated dusty cometary atmosphere.
Moon and the Planets, 27:431–452, 1982.
- M. L. Marconi and D. A. Mendis.
The atmosphere of a dirty-clathrate cometary nucleus - a two-phase, multifluid model.
Astrophys. J., 273, 11 1983.
doi: 10.1086/161377.
- R. Marschall.
Inner gas and dust comae of comets.
PhD dissertation, Universität Bern, 2017.
- R. Marschall, C.C. Su, Y. Liao, et al.
Modelling observations of the inner gas and dust coma of comet 67P using ROSINA/COPS and OSIRIS data: Final Results.
A&A, 589(A90), 2016.
- R. Marschall, S. Mottola, C.C. Su, et al.
Cliffs versus plains: Can ROSINA/COPS and OSIRIS data of comet 67P/Churyumov-Gerasimenko in autumn 2014 constrain inhomogeneous outgassing?
A&A, 605(A112), 2017.
- R. Marschall, L. Rezac, D. Kappel, et al.
A comparison of multiple Rosetta data sets and 3D model calculations of 67P/Churyumov-Gerasimenko coma around equinox (May 2015).
Icarus, 328, 2019.
- R. Marschall, Y. Liao, J.-S. Wu, and N. Thomas.
Limitations in the determination of surface emission distributions on comets through modelling of observational data - A case study based on Rosetta observations.
Icarus, 346, 2020.
- D. Marshall, O. Groussin, J.-B. Vincent, et al.
Thermal inertia and roughness of the nucleus of comet 67P/Churyumov–Gerasimenko from MIRO and VIRTIS observations.
A&A, 616(A122), 8 2018.
URL <https://doi.org/10.1051/0004-6361/201833104>.

BIBLIOGRAPHY

N. Masmoudi.

Chapter 3 - examples of singular limits in hydrodynamics.

volume 3 of *Handbook of Differential Equations: Evolutionary Equations*, pages 195 – 275.

North-Holland, 2007.

URL [https://doi.org/10.1016/S1874-5717\(07\)80006-5](https://doi.org/10.1016/S1874-5717(07)80006-5).

M. Massironi, E. Simioni, F. Marzari, G. Cremonese, et al.

Two independent and primitive envelopes of the bilobate nucleus of comet 67p.

Nature, 526:402–405, 2015.

K. J. Meech, M. F. A'Hearn, J. A. Adams, et al.

Epoxi: Comet 103p/hartley 2 observations from a worldwide campaign.

The Astrophysical Journal Letters, 734(1), 2011.

D.A. Mendis and G.D. Brin.

Monochromatic Brightness Variations of Comets. II: Core-Mantle Model.

The Moon, 17(Issue 4):359–372, 1977.

A. Migliorini, G. Piccioni, F. Capaccioni, et al.

Water and carbon dioxide distribution in the 67P/Churyumov-Gerasimenko coma from VIRTIS-M infrared observations.

A&A, 589(A45), 5 2016.

S. Mottola, S. Lowry, C. Snodgrass, et al.

The rotation state of 67p/churyumov-gerasimenko from approach observations with the osiris cameras on rosetta.

A&A, 569, 2014.

doi: 10.1051/0004-6361/201424590.

M. J. Mumma and S. B. Charnley.

The chemical composition of comets—emerging taxonomies and natal heritage.

Annual Review of A&A, 49(1):471–524, 2011.

URL <https://doi.org/10.1146/annurev-astro-081309-130811>.

M. J. Mumma, H. A. Weaver, H. P. Larson, D. S. Davis, and M. Williams.

Detection of water vapor in halley's comet.

Science, 232(4757):1523–1528, 1986.

doi: 10.1126/science.232.4757.1523.

M. J. Mumma, M. A. DiSanti, K. Magee-Sauer, et al.

Parent volatiles in comet 9p/tempel 1: Before and after impact.

Science, 310(5746):270–274, 2005.

doi: 10.1126/science.1119337.

- N. Ockay, J. Sunshine, M. Pajola, et al.
Comparative study of water ice exposures on cometary nuclei using multispectral imaging data.
MNRAS, 462:S394–S414, 2016.
- J. H. Oort.
The structure of the cloud of comets surrounding the Solar System and a hypothesis concerning its origin.
Bulletin of the Astronomical Institutes of the Netherlands, 11:91–110, 1950.
- A. Pommerol, N. Thomas, M.R. El-Maarry, et al.
OSIRIS observations of meter-sized exposures of H₂O ice at the surface of 67P/Churyumov-Gerasimenko and interpretation using laboratory experiments.
A&A, 583(A25), 2015.
- F. Preusker, F. Scholten, K. D. Matz, et al.
Shape model, reference system definition, and cartographic mapping standards for comet 67p/churyumov-gerasimenko – stereo-photogrammetric analysis of rosetta/osiris image data.
A&A, 583(A33), 2015.
- F. Preusker, F. Scholten, K.-D. Matz, et al.
The global meter-level shape model of comet 67p/churyumov-gerasimenko.
A&A, 607(L1), 2017.
- M. Pätzold, T. Andert, M. Hahn, S.W. Asmar, et al.
A homogeneous nucleus for comet 67p/churyumov–gerasimenko from its gravity field.
Nature, 530:63–65, 02 2016.
doi: 10.1038/nature16535.
- E. Quirico, L.V. Moroz, B. Schmitt, et al.
Refractory and semi-volatile organics at the surface of comet 67p/churyumov-gerasimenko: Insights from the virtis/rosetta imaging spectrometer.
Icarus, 272:32 – 47, 2016.
ISSN 0019-1035.
doi: <https://doi.org/10.1016/j.icarus.2016.02.028>.
URL <http://www.sciencedirect.com/science/article/pii/S001910351600097X>.
- R. Reinhard.
The giotto encounter with comet halley.
Nature, 321:313–318, 1986.
- Rezac, L., Zhao, Y., Hartogh, P., Ji, J., Marshall, D., and Shi, X.
Three-dimensional analysis of spatial resolution of miro/rosetta measurements at 67p/churyumov-gerasimenko.

BIBLIOGRAPHY

- A&A, 630:A34, 2019.
doi: 10.1051/0004-6361/201935389.
URL <https://doi.org/10.1051/0004-6361/201935389>.
- J. E. Richardson, H. J. Melosh, C. M. Lisse, and B. Carcich.
A ballistics analysis of the deep impact ejecta plume: Determining comet tempel 1's gravity, mass, and density.
Icarus, 191(2, Supplement):176 – 209, 2007.
URL <https://doi.org/10.1016/j.icarus.2007.08.033>.
Deep Impact at Comet Tempel 1.
- R. A. Robie, B. S. Hemingway, and W. H. Wilson.
Specific heats of lunar surface materials from 90 to 350 degrees kelvin.
Science, 167(3918):749–750, 1970.
doi: 10.1126/science.167.3918.749.
- B. Rozitis, S. F. Green, E. MacLennan, and J. P. Emery.
Observing the variation of asteroid thermal inertia with heliocentric distance.
MNRAS, 477(2):1782–1802, 03 2018.
URL <https://doi.org/10.1093/mnras/sty640>.
- M. Rubin, V. M. Tennishev, M. R. Combi, et al.
Monte carlo modeling of neutral gas and dust in the coma of comet 1p/halley.
Icarus, 213(2):655 – 677, 2011.
URL <https://doi.org/10.1016/j.icarus.2011.04.006>.
- M. Rubin, K. Altwegg, H. Balsiger, et al.
Elemental and molecular abundances in comet 67P/Churyumov-Gerasimenko.
MNRAS, 489(1):594–607, 07 2019.
URL <https://doi.org/10.1093/mnras/stz2086>.
- S. A. Sandford, J. Aléon, C. M. O'D. Alexander, T. Araki, et al.
Organics captured from comet 81p/wild 2 by the stardust spacecraft.
Science, 314(5806):1720–1724, 2006.
doi: 10.1126/science.1135841.
URL <https://science.sciencemag.org/content/314/5806/1720>.
- D. Sathyamoorthy and R. Palanikumar.
Linear and nonlinear approach for dem smoothening.
Discrete Dynamics in Nature and Society, 2006, 01 2006.
doi: 10.1155/DDNS/2006/63245.

- D. G. Schleicher, K. L. Barnes, and N. F. Baugh.
Photometry and imaging results for comet 9p/tempel 1 and Deep impact: Gas production rates, postimpact light curves, and ejecta plume morphology.
The Astronomical Journal, 131(2):1130–1137, 02 2006.
doi: 10.1086/499301.
- I. Schroeder, K. Altwegg, H. Balsiger, et al.
A comparison between the two lobes of comet 67P/Churyumov–Gerasimenko based on D/H ratios in H₂O measured with the Rosetta/ROSINA DFMS.
MNRAS, 489(4):4734–4740, 09 2019.
URL <https://doi.org/10.1093/mnras/stz2482>.
- P. H. Schultz, C. A. Eberhardy, C. M. Ernst, M. F. A’Hearn, J. M. Sunshine, and C. M. Lisse.
The deep impact oblique impact cratering experiment.
Icarus, 191(2, Supplement):84 – 122, 2007.
URL <https://doi.org/10.1016/j.icarus.2007.06.031>.
Deep Impact at Comet Tempel 1.
- K. Seiferlin, T. Spohn, and J. Benkhoff.
Cometary ice texture and the thermal evolution of comets.
Adv. Space Res., 15(Issue 10):35–38, 1995.
- K. Seiferlin, T. Spohn, N. Kömle, and G. Kargl.
Line heat-source measurements of the thermal conductivity of porous H₂O ice, CO₂ ice and mineral powders under space conditions.
Planet. Space Sci., 44:691–704, 7 1996.
- Z. Sekanina, D. E. Brownlee, T. E. Economou, A. J. Tuzzolino, and S. F. Green.
Modeling the nucleus and jets of comet 81p/wild 2 based on the stardust encounter data.
Science, 304(5678):1769–1774, 2004.
doi: 10.1126/science.1098388.
URL <https://science.sciencemag.org/content/304/5678/1769>.
- Y. Shinnaka, H. Kawakita, E. Jehin, A. Decock, D. Hutsemékers, and J. Manfroid.
Ortho-to-para abundance ratios of NH₂ in 26 comets: implications for the real meaning of OPRs.
MNRAS, 462(Suppl₁):S124 – S131, 09 2016.
URL <https://doi.org/10.1093/mnras/stw2298>.
- Y. Shoshany, D. Prialnik, and M. Podolak.
Monte Carlo Modeling of the Thermal Conductivity of Porous Cometary Ice.
Icarus, 157(Issue 1):219–227, 2002.

BIBLIOGRAPHY

H. Sierks, C. Barbieri, P. L. Lamy, et al.

On the nucleus structure and activity of comet 67p/churyumov-gerasimenko.

Science, 347(6220), 2015.

doi: 10.1126/science.aaa1044.

URL <https://science.sciencemag.org/content/347/6220/aaa1044>.

Y.V. Skorov and H. Rickman.

A kinetic model of gas flow in a porous cometary mantle.

Planetary and Space Science, 43(Issue 12), 1995.

Y.V. Skorov, N. Kömle, W. Markiewicz, and H.U. Keller.

Mass and Energy Balance in the Near-Surface Layers of a Cometary Nucleus.

Icarus, 140(Issue 1), 1999a.

Y.V. Skorov, N. Kömle, H.U. Keller, G. Kargl, and W. Markiewicz.

A Model of Heat and Mass Transfer in a Porous Cometary Nucleus Based on a Kinetic Treatment of Mass Flow.

Icarus, 153(Issue 1), 2001.

Y.V. Skorov, H. Keller, L. Jorda, and B. Davidsson.

Thermophysical Modelling of Comet P/Borrelly Effects of Volume Energy Absorption and Volume Sublimation.

Earth, Moon and Planets, 90, 2002a.

Y.V. Skorov, M.Y. Marov, and A.E. Korolev.

Mass transfer in the near-surface layer of a cometary nucleus: A gas-kinetic approach.

Solar System Research, 36:87–96, 2002b.

Y.V. Skorov, R. van Lieshout, J. Blum, and H. U. Keller.

Activity of comets: Gas transport in the near-surface porous layers of a cometary nucleus.

Icarus, 212(2):867 – 876, 2011.

URL <https://doi.org/10.1016/j.icarus.2011.01.018>.

L. A. Soderblom, T. L. Becker, G. Bennett, et al.

Observations of comet 19p/borrelly by the miniature integrated camera and spectrometer aboard deep space 1.

Science, 296(5570):1087–1091, 2002.

ISSN 0036-8075.

doi: 10.1126/science.1069527.

URL <https://science.sciencemag.org/content/296/5570/1087>.

T. Spohn, J. Knollenberg, A. Ball, et al.

- Thermal and mechanical properties of the near-surface layers of comet 67P/Churyumov-Gerasimenko.
Science, 349(Issue 6247), 2015.
- C.C. Su.
Parallel DSMC Methods for Modeling Rarefied Gas Dynamics, 2013.
- J. Sunshine, M. A'Hearn, O. Groussin, et al.
Exposed Water Ice Deposits on the Surface of Comet 9P/Tempel 1.
Science, 311(Issue 5766):1453–1455, 2006.
- J. M. Sunshine, O. Groussin, P. H. Schultz, et al.
The distribution of water ice in the interior of comet tempel 1.
Icarus, 190(2):284 – 294, 2007.
URL <https://doi.org/10.1016/j.icarus.2007.04.024>.
Deep Impact Mission to Comet 9P/Tempel 1, Part 2.
- P. Swings.
Molecular bands in cometary spectra. identifications.
Rev. Mod. Phys., 14:190–194, Apr 1942.
doi: 10.1103/RevModPhys.14.190.
- P. Swings, C. T. Elvey, and H. W. Babcock.
The spectrum of comet cunningham, 1940c.
Astrophysical Journal, 94:320–343, 1941.
- N. Thomas.
The nuclei of Jupiter family comets: A critical review of our present knowledge.
Planetary and Space Science, 57(Issue 10), 2009.
- N. Thomas.
An Introduction to Comets.
A&A Library, in press.
- N. Thomas, H. Sierks, C. Barbieri, et al.
The morphological diversity of comet 67p/churyumov-gerasimenko.
Science, 347(6220), 2015a.
doi: 10.1126/science.aaa0440.
URL <https://science.sciencemag.org/content/347/6220/aaa0440>.
- N. Thomas, B. Davidsson, M.R. El-Maarry, et al.
Redistribution of particles across the nucleus of comet 67P/Churyumov-Gerasimenko.
A&A, 583(A17), 2015b.

BIBLIOGRAPHY

- N. Thomas, M.R. El-Maarry, P. Theologou, et al.
Regional unit definition for the nucleus of comet 67p/churyumov-gerasimenko on the shap7 model.
Planetary and Space Science, 164:19 – 36, 2018.
URL <https://doi.org/10.1016/j.pss.2018.05.019>.
- F. Tosi, F. Capaccioni, M. Capria, et al.
The changing temperature of the nucleus of comet 67P induced by morphological and seasonal effects.
Nature Astronomy, 3:649–658, 2019.
- C. Tubiana, L. Barrera, M. Drahus, and H. Boehnhardt.
Comet 67p/churyumov-gerasimenko at a large heliocentric distance.
A&A, 490(1):377–386, 2008.
- C. Tubiana, H. Bönhardt, J. Agarwal, M. Drahus, L. Barrera, and J. L. Ortiz.
Comet 67p/churyumov-gerasimenko at a large heliocentric distance.
A&A, 527(A113), 2011.
- C.-Y. Tzou.
Calibrations of ROSINA-COPS and Observations at Comet 67P/Churyumov-Gerasimenko.
PhD dissertation, Universität Bern, 2017.
- P. Valentini, C. Zhang, and T. Schwartzentruber.
Molecular dynamics simulation of rotational relaxation in nitrogen: Implications for rotational collision number models.
Physics of Fluids, 24, 10 2012.
doi: 10.1063/1.4757119.
- D. Vokrouhlický, D. Nesvorný, and L. Dones.
Origin and evolution of long-period comets.
The Astronomical Journal, 157(5), 2019.
- A. N. Volkov.
Direct simulation monte carlo (dsmc) of gas flows [powerpoint slides].
<http://www.people.virginia.edu/~lz2n/mse627/notes/DSMC.pdf>, 2011.
Accessed: 2020–12-06.
- S. K. Vsekhsvyatskii.
The maximum length of comet tails and some considerations on their classification.
Soviet Astronomy, 13:343, 1969.

- L. V. Wallace, I. Miller, and D. Freeman.
Isophote configurations for model comets.
Astronomical Journal, 63, 1958.
- H. A. Weaver, M. J. Mumma, H. P. Larson, and D. S. Davis.
Post-perihelion observations of water in comet halley.
Nature, 324:441–444, 1986.
- H. A. Weaver, P. D. Feldman, M. F. A'Hearn, N. Dello Russo, , and S. A. Stern.
The carbon monoxide abundance in comet 103p/hartley 2 during the epoxi flyby.
The Astrophysical Journal Letters, 734(L5), 2011.
- F.L. Whipple.
A comet model. I. The acceleration of comet Encke.
Astrophysical Journal, 111:375–394, 1950.
- F.L. Whipple.
On the distribution of sernimajor axes among comet orbits.
Astrophysical Journal, 67, 1962.
- K. Willacy, C. Alexander, M. Ali-Dib, et al.
The composition of the protosolar disk and the formation conditions for comets.
Space Science Reviews, 197, 07 2015.
doi: 10.1007/s11214-015-0167-6.
- J.-S. Wu and Y.Y. Lian.
Parallel three-dimensional direct simulation Monte Carlo method and its applications.
Computers & Fluids, 32(Issue 8):1133–1160, 2003.
- J.-S. Wu, K.C. Tseng, and F.Y. Wu.
Parallel three-dimensional DSMC method using mesh refinement and variable time-step scheme.
Computer Physics Communications, 162(Issue 3):166–187, 2004.
- J.-S. Wu and K.-C. Tseng.
Parallel DSMC method using dynamic domain decomposition.
Numerical Methods in Engineering, 63(Issue 1):37–76, 2005.
- K. Wurm.
Die natur der kometen.
Mitteilungen der Hamburger Sternwarte in Bergedorf, 8:57–92, 1949.
- R.V. Yelle, L.A. Soderblom, and J.R. Jokipii.
Formation of jets in comet 19p/borrelly by subsurface geysers.

BIBLIOGRAPHY

Icarus, 167(1):30 – 36, 2004.

URL <https://doi.org/10.1016/j.icarus.2003.08.020>.

Special Issue on DS1/Comet Borrelly.

H. Yu.

Lattice boltzmann equation simulations of turbulence, mixing, and combustion.
01 2004.

V.V. Zakharov, A.V. Rodionov, G.A. Lukyanov, and J.F. Crifo.

Navier–stokes and direct monte-carlo simulations of the circumnuclear gas coma: Iii. spherical, inhomogeneous sources.

Icarus, 194(1):327 – 346, 2008.

URL <https://doi.org/10.1016/j.icarus.2007.08.038>.

V.V. Zakharov, A.V. Rodionov, G.A. Lukianov, and J.F. Crifo.

Monte-Carlo and multifluid modelling of the circumnuclear dust coma II. Aspherical-homogeneous, and spherical-inhomogeneous nuclei.

Icarus, 201(Issue 1), 2009.

V.V. Zakharov, J.-F. Crifo, A.V. Rodionov, M. Rubin, and K. Altwegg.

The near-nucleus gas coma of comet 67p/churyumov-gerasimenko prior to the descent of the surface lander philae.

A&A, 618, 07 2018.

doi: 10.1051/0004-6361/201832883.

Y. Zhao, L. Rezac, P. Hartogh, J. Ji, R. Marschall, and H. U. Keller.

Constraining spatial pattern of early activity of comet 67P/C–G with 3D modelling of the MIRO observations.

MNRAS, 494(2):2374–2384, 09 2019.

URL <https://doi.org/10.1093/mnras/stz2686>.

E. Öpik.

Note on Stellar Perturbations of Nearly Parabolic Orbits.

Proceedings of the American Academy of Arts and Sciences, 67(6):169–183, 1932.

URL <https://www.jstor.org/stable/20022899>.

Author's declaration of consent

on the basis of Article 18 of the PromR Phil.-nat. 19

Name / First Name: Pinzón Rodríguez, Olga Janeth

Registration Number: 16-138-703

Study program: PhD of Science in Physics - Dissertation

Title of the thesis: Modelling of the gas dynamics in the inner-coma and the composition of comet 67P/Churyumov-Gerasimenko.

Supervisor: Prof. Dr. Nicolas Thomas

I declare herewith that this thesis is my own work and that I have not used any sources other than those stated. I have indicated the adoption of quotations as well as thoughts taken from other authors as such in the thesis. I am aware that the Senate pursuant to Article 36 paragraph 1 litera r of the University Act of September 5th, 1996 and Article 69 of the University Statute of June 7th, 2011 is authorized to revoke the doctoral degree awarded on the basis of this thesis.

For the purposes of evaluation and verification of compliance with the declaration of originality and the regulations governing plagiarism, I hereby grant the University of Bern the right to process my personal data and to perform the acts of use this requires, in particular, to reproduce the written thesis and to store it permanently in a database, and to use said database, or to make said database available, to enable comparison with theses submitted by others.

SIGNATURE:

DATE:

Olga Janeth Pinzón Rodríguez

Date of Birth: October 1st, 1989
Place of Birth: Zipaquirá, Colombia

Education

Dec. 2016 - Feb. 2021 | **PhD of Science in Physics**

University of Bern, Switzerland

Thesis: Modelling of the gas dynamics in the inner-coma and the composition of comet 67P/Churyumov-Gerasimenko.

Advisor: Prof. Dr. Nicolas Thomas

Oct. 2013 - Feb. 2016 | **Master's Degree in Physics of the Earth and the Atmosphere**

University of Cologne, Germany

Thesis: Lyman-alpha Albedo Map of Europa with Hubble Space Telescope Observations.

Advisor: Prof. Dr. Joachim Saur

Jan. 2007 - Mar 2013 | **Bachelor of Science in Physics**

Universidad de los Andes, Colombia

Thesis: Cosmo-chronology and Radioactivity in Nuclear Astrophysics.

Advisor: Dr. Neelima Kelkar

